Novel Fluorescent probes for Analysis of Protein interactions under truly physiological conditions with real Medical devices

Marc-Krystelle Mafina

MSci Chemistry with Honours

2012

School of Engineering and Material Science

Supervisors:

Dr. Karin A. Hing & Professor Alice C. Sullivan

Queen Mary University

For the partial fulfilment of the degree of

Doctor of Philosophy

ABSTRACT

Protein adsorption under physiological conditions was recognised to be the key step in the modulation of biological responses between materials and an osseous environment. Many studies have shown variation of adsorption behaviour on medical materials but most experiments were performed under non-physiological idealised conditions with idealised samples.

The aim of this thesis was to develop a method to analyse protein adsorption on real clinically relevant samples under physiologically relevant conditions. The use of fluorescent probes was identified as a methodology which would facilitate analysis under a range of conditions including fully competitive with real samples that required no specialised surface pre-treatment. Fluoresceinthiureidoaminocaproic acid (FTCA) and a sulforhodamine derivative (SR101), were identified as suitable for coupling to proteins. FTCA labelled bovine serum albumin (BSA) was initially used to validate the technique and found to have several advantages over commercially available total protein assays; including greater sensitivity and facilitate its use under competitive conditions. These experiments also confirmed sensitivity to temperature and test media as well as demonstrating that the technique could be used on idealised dense and real porous granular (as used clinically) samples. Conformational changes associated with protein-surface interactions were observed through variation in protein auto-fluorescence and confirmed with CD analysis, therefore, care in selection of appropriate experimental conditions and fluorophore probes was required. Additionally, labelling facilitated the visualisation in differences in the morphological habit of the surface adsorbed protein species. Investigation of differential response in protein exchange with hydroxyapatite (HA) and 0.8wt% silicon substituted hydroxyapatite (SA) with more biologically relevant proteins; such as bone morphogenetic protein-2 (BMP-2), fibronectin (FN) and osteopontin (OPN) individually and/or competitively in phosphate buffered saline (PBS) or minimum Eagles medium (MEM) supplemented with 10 % foetal bovine serum (FBS) demonstrated SA to have a greater capacity to adsorb selected osteogenic proteins under competitive conditions as compared to HA.

Particularly interesting was the BMP-2 findings, which highlighted the role of media in promoting BMP-2 adsorption and the conformation sensitivity of traditional ELISA assays giving rise to unreliable results.

ACKNOWLEDGEMENTS

TABLE OF CONTENT

LIST OF FIGURES

GLOSSARY

ACA.OMe	Aminocaproate ester
BGS	Bone graft substitutes
BMP-2	Bone morphogenetic protein-2
β-TCP	Beta-Tricalcium phosphate
BSA	Bovine serum albumin
DCC	N,N- Dicyclohexylcarbodiimide
DD	Dense discs
FITC	Fluorescein isothiocyanate
FTCA	Fluoresceinthioureidocaproic acid
FN	Fibronectin
HA	Hydroxyapatite
MEM	Minimum Eagles' medium
NaOAc	Sodium acetate
OPN	Osteopontin
PBS	Phosphate buffered saline
SA	Silicate substituted hydroxyapatite
VN	Vitronectin

Chapter 1. BIOMATERIALS SCIENCE: AN OVERVIEW OF MATERIALS IN MEDICINE

1.1 Introduction

Bones are rigid organs that form part of the endoskeleton of vertebrates. Bone is made principally of the fibrous protein collagen, impregnated with a mineral closely resembling calcium phosphate (Currey 2002; Kuhn, Fink, *et al.* 1996; Weiner and Wagner 1998). Bone is produced inside the body and is usually covered with cells throughout life. Bone is a hard material, but it has the tendency to break and form with defects. When bone broke, it was most likely replaced by off the shelf materials such as wooden chair legs or metal rods (Park and Lakes 2007); which were not developed for bioactivity or biocompatibility. Scientists during that time realised how biocompatibility for better healing or repair was important; thus, they started investigating both the human bone and suitability of the material used as implants. Over the years up until the 1960s, the materials used proved inadequate, therefore, the science of biomaterials was developed (Ratner, Hoffman, *et al.* 2004).

Biomaterial science is a science that applies the properties and applications of materials (either synthetic or natural) that are used in contact with biological environments. These materials are known as biomaterials and they address aspects of chemistry, biology, material science, engineering and medicine. This science is based on the foundation of tissue engineering principles to create biological substitutes for lost or defective native tissues; the most successful approach involves generating an undeveloped but functional tissue graft *in vitro*, which will then mature after implantation *in vivo* (Vunjak-Novakovic and Freshney 2006). In tissue engineering, it is important that regeneration is provided, rather than repair, which should then lead to orderly remodelling of the tissue in response to the environmental factors, surrounding the tissue; and this principle to be applied with the use of biomaterials in biological systems. Apatite materials have been used in this manner for coating on implant or as bone grafts for bony defects. Hydroxyapatite (HA) and its other ion-substituted products are already commercially available (Apatech ltd, Biomet or CeramIsys) and have been shown to be efficient and successful as bone grafts towards bone repair. (Hing, Revell, *et al.* 2006) The material's

bioactivity and biocompatibility are linked to test environment factors such as proteins and other cells present and structural factors of the biomaterials, but also physio-chemical properties of the materials used (Hing, Annaz, *et al.* 2005) during the implantation of the engineered tissue, may inhibit or prohibit the structure and composition of the tissue, which in turn may alter the functional properties of that tissue. These key factors are important to a successful implantation, where it is essential to know how they interact and influence the engineered tissue. In addition, it is believed that if cell and/or protein adhesion is understood further, then the interface between tissue/cell/protein and material can thus be optimised.

Cell and/or protein labelling in biomaterial studies is an important part in interpreting the bioactivity and biocompatibility of the biomaterials in buffers or sera. It allows for the cells or proteins to be quantified or imaged. Monitoring protein adsorption and desorption behaviour on biomaterials' surfaces is an important factor into quantitatively and qualitatively collecting information on the mechanism and processes that occur between an implant and a material's surface (Ducheyne and Qui 1999). This can be achieved via several routes such as electrophoresis (i.e. SDS-PAGE) with staining for imaging (Matsuura , Hosokawa, *et al.* 2000), heavy metal labelling also known as radiolabelling or radioimmunoassay (Bolton and Hunter 1973; Fabrizius-Homan and Cooper "A comparison of the adsorption of three adhesive proteins to biomaterial sufaces" 1991; Fabrizius-Homan and Cooper "Competitive adsorption of vitronectin with albumin, fibrinogen, and fibronectin on polymeric biomaterials" 1991) or using assaying kits. Kits fall broadly into two categories, enzyme-linked immunosorbent assay (ELISA) or total protein type assays, where both colourimetric and fluorimetric tools can be employed. The latter assays all proteins present irrespective of species or conformations. ELISA, on the other hand, is limited to measurement of a specific protein and can be conformation dependent. Therefore, in order to carry out a competitive study multiple analyses must be performed. In addition, the two-step nature of the ELISA methodology makes it susceptible to human errors such as when aspirating solutions or loss of analyte through inverting the plate. To date the only method for true competitive analysis is electrophoresis, sodium dodecyl sulfate-polyacrylamide gel electrophoresis (SDS-PAGE) (Takami, Yamane, *et al.* 1998), often used in conjunction with staining reagents (i.e. Coomassie or silver) to image proteins (Ellingsen 1991), however, quantification by this route requires a high degree of

operating skill. Other existing methods of competitive protein analysis are ellipsometry, used for real-time adsorption kinetics, and requires no labelling of the protein (Elwing 1998), use of matrix-assisted laser desorption ionisation mass spectrometry (MALDI-MS) adapted for surface analysis determination (Griessera, Kingshottb, *et al.* 2004); this also requires no labelling of proteins. However, these methods require expensive set ups and instruments with highly skilled operator.

The objective of this thesis was to develop a method to facilitate the competitive evaluation of protein adsorption to dense and porous apatites via labelling of the species of interest with a fluorescent probe so that it may be monitored independently of other protein species in the local environment. The emphasis of the study was monitoring and recording the influences of protein species on the adsorption and desorption processes on the biomaterials in different media conditions, not its mechanistic view; but also taking into account the biomaterial's chemistry. The use of real samples representative of existing pre-clinical specimen towards osteoinduction study, further, allowed for the study to closely mimic true behaviour of the biomaterials in media, especially observed in the recombinant human bone morphogenetic protein (rhBMP-2) study in Chapter 5.

Chapter 1 of this thesis will give a short overview of bone biology, biomaterials used for the application of bone repair and remodelling, protein labelling used during biomaterial studies, along with the interactions observed and the methods of monitoring and quantifying the behaviour seen. And finally the competitive binding on biomaterials and the work done so far, which will then lead to the thesis hypotheses.

1.2   Bone Biology

A bone is made up of several different tissues working together: bone, cartilage, dense connective tissues, epithelium, adipose tissue and nervous tissue. (Tortora and Derrickson 2009) It functions to move, support and protect the organs of the body, produce red and white blood cells to act as a reservoir (Hing 2004), and stores minerals (for example, calcium) for a wide range of metabolic functions. (Weiner and Wagner 1998) Therefore it is important to know more about bone, proteins and cells involved, and their mechanism towards nourishing, maintaining and repairing bone. This is known as bone biology.

1.2.1   Structure & Histology of Bone and its tissue

The typical structure of bone is usually represented *via* analysing the macroscopic components of parts of a long bone as shown in Figure 1.1, consisting of the following parts: diaphysis, epiphyses, metaphyses, articular cartilage, periosteum, the medullary cavity and endosteum. The ***diaphysis*** is the bone's shaft (also known as body); the ***epiphyses*** are the ends of the bone known as proximal and distal, top and bottom parts, respectively. To connect both regions of the bone, the ***metaphyses*** are necessary. The thin layer covering the epiphysis is called the ***articular cartilage***. It is usually formed where bone forms a joint to reduce friction and absorb impact. When bone is not covered by articular cartilage, it is covered by the ***periosteum***, this is a tough sheet of connective tissue (most likely to be irregular) (Currey 2002; Miller, St-George, *et al.* 1989). It protects bone, assists in fracture repair, helps nourish the bone tissue and serves as an attachment point for ligaments and tendons. The space within the diaphysis is called ***medullary cavity*** or the ***marrow cavity***. It is most likely to contain yellow marrow, especially in adults. And the final component of bone is known as the ***endosteum***. It is a thin membrane, which lines the marrow cavity. It contains a single layer of bone-forming cells and small amount of connective tissue. As each bone in the body has so many components, it is usually regarded as an organ.

Looking at the histology of bone tissue allows for the microscopic components of bone to be defined. Bone is made up of a mineralised tissue known as bone tissue (or osseous tissue). This, in turn, contains an abundant extracellular matrix (ECM) which is a major

constituent of bone in which separated cells are embedded. It is produced by cells and secreted into the surrounding medium. It is extensive, where its properties depend on the properties of the tissue. There are three major components to the ECM: (1) the fibrous elements (for example, collagen, elastin or reticulin), (2) the link proteins (fibronectin) and (3) the space-filling molecules (glycosaminoglycan (Schwartz 1973)) (Lackie and Dow 1995).
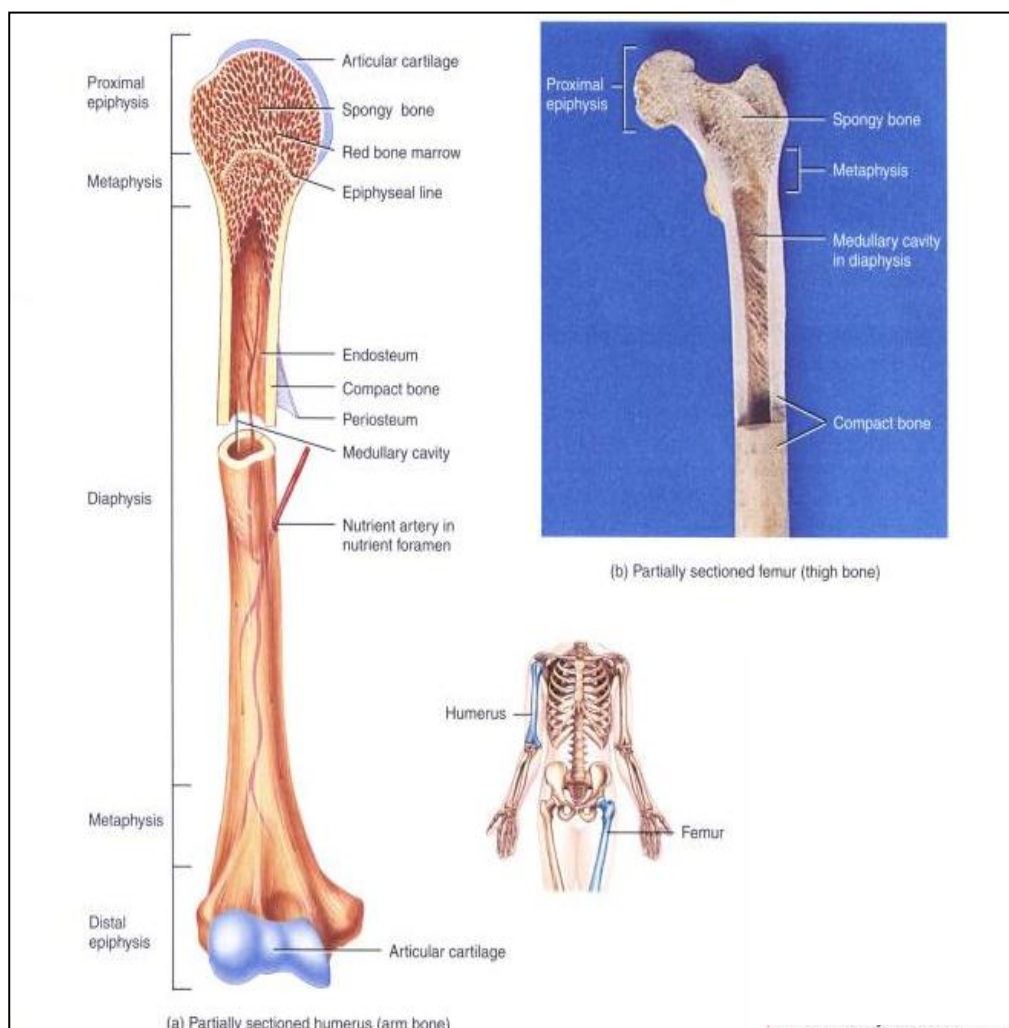
Figure 1.1 – Structure of (a) parts of long bone with spongy bone tissue of the epiphyses and metaphysic contains red bone marrow and (b) human femur copied from Tortora *et al*. (Tortora and Derrickson 2009 copyright permission granted)

The extracellular matrix (ECM) of bone is composed of 25% water and collagen fibres, and 50% crystallised mineral salts (Tortora and Derrickson 2009). Within the collagen fibres are various proteins of which 90 % are collagenic proteins (CP) containing type I collagen and type V collagen. The remaining 10 % are non-collagenous proteins (NCP)

such as osteocalcin (OC), osteonectin (ON), bone sialoproteins (BSP), proteoglycans (PG), osteopontin (OP), fibronectin (FN), vitronectin (VN), growth factors (GFs) and bone morphologenetic proteins (BMPs) (Hollinger, Einhorn, *et al.* 2005; Raynaud, Champion, *et al.* "Calcium phosphate apatites with variable Ca/P atomic ration III. Mechanical properties and degradation in solution of hot pressed ceramics" 2002)
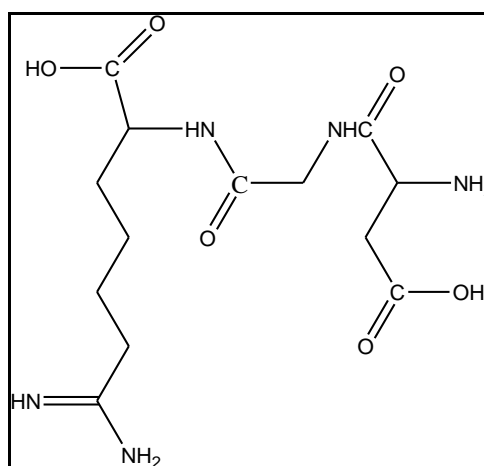
Figure 1.2- Chemical Structure of the arginine, glycine and aspartic (RGD) sequence

Some of these NCPs are known as adhesive proteins. They get their adhesive properties because they contain the Arg-Gly-Asp (RGD) sequence as shown in Figure 1.2, which is specific to the fixation of cell membrane receptors like integrin (fibronectin, vitronectin, type I collagen, bone sialoprotein) (Ruoslahti 1996; Sawyer, Hennessy, *et al.* 2005; Schaffner and Dard 2003). The matrix can be mineralised as bone or tendon, depending on the compression used on the fibres to produce the necessary tissue (Lebaron and Athanasiou 2000). As the crystals form, they combine with other mineral salts like calcium carbonate ($CaCO_3$), and ions such as magnesium (Mg^{2+}), fluoride (F^-), potassium (K^+) or sulphate (SO_4^{4-}). When the mineral salts get deposited in the framework formed by the collagen fibres of the ECM, they crystallise and the tissue becomes harder. This process is called ***calcification***, which is initiated by building cells named osteoblasts. There are four type of cells associated with bone, as they are responsible for production, maintenance and resorption of bone called osteogenic cells, osteoblasts, osteocytes (Colopy, Benz-Dean, *et al.* 2004) and osteoclasts, respectively. ***Osteogenic cells*** are unspecialised stem cells derived from mesenchyme, the tissue from which all connective tissues are formed. (Tortora and Derrickson 2009) These are the only cells that undergo cell division. The resulting cells develop into osteoblasts.

Osteoblasts are bone-forming cells (Anselme 2000; Lackie and Dow 1995), which produce and secrete collagen fibers and other components needed to build the ECM of bone tissue. They initiate calcification. As they become trapped in their secretion, they become osteocytes. ***Osteocytes*** are mature bone cells, which are the main cells in bone tissue. They maintain the bone's daily metabolism, for example, the exchange of nutrients and waste removal *via* the blood by connecting with neighbouring osteocytes. As part of the normal development of bone through growth, maintenance and repair, bone also breaks down, a process known as resorption (Alberts, Bray*, et al.* 1994). This process is controlled *via* multinuclear ***osteoclasts***. Osteoclasts, also known as bone-resorbing cells, are large cells, concentrated in the endosteum. They secrete powerful enzymes and acids that breakdown both mineral salts and collagen fibers.

1.2.2   Bone formation

Bone develops into two distinct forms: compact or cortical and spongy (cancellous or trabecular) bone (Figure 1.3). ***Compact bone*** is the strongest form of bone, found beneath the periosteum and makes up the bulk of the diaphyses. It provides protection, support and resistance to the stresses produced by weight and movement. Blood vessels, lymphatic vessels and nerves from the periosteum penetrate the compact bone through canals known as "*Volkmann's canals*". These canals then connect with those of the marrow cavity, periosteum and Haversian canals, also known as *central canals*. Around these central canals are concentric lamellae rings of calcified ECM (much like rings of a tree trunk as observed in Figure 1.3). Between those lamellae are small spaces named *lacunae* (Currey 2002) containing osteocytes. The final layer just before the periosteum is called the *circumferential lamellae.*
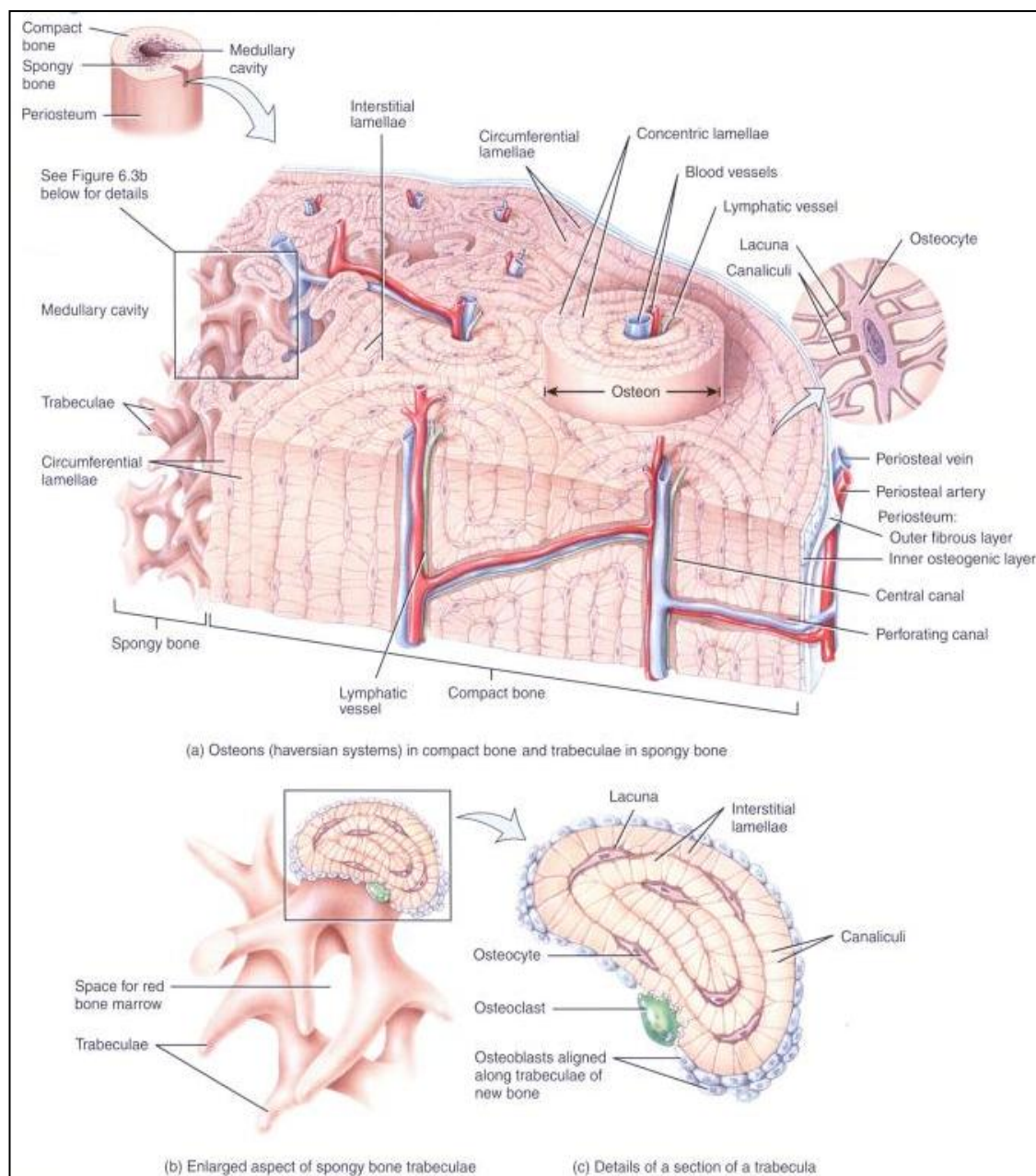
Figure 1.3 – Microscopic structure of a bone where (a) the osteons (Haversian systems) in compact bone and trabeculae in spongy bone, (b) the enlarged aspect of spongy trabeculae and (c) the detailed section of a trabeculae (Tortora and Derrickson 2009 copyright permission granted)

In contrast, the **s*pongy bone*** is a very porous form of bone. It consists of lamellae of thin columns named trabeculae. The spaces between trabeculae help make bone lighter and also can sometimes be filled with red bone marrow (or yellow in adults). Within each trabeculae are lacunae that contain osteocytes, they receive nutrients directly from circulating in the marrow cavity. In all directions from the lacunae are small canaliculi filled with ECM fluid with slender finger-like processes of osteocytes. (Colopy, Benz-

Dean*, et al.* 2004; Taylor, Hazenberg*, et al.* 2007) The components of compact bone tissue are arranged into repeating units called **osteons** (or Haversian systems). Areas between them are known as the *interstitial lamellae*, they are fragments of older osteons that have been partially destroyed during bone rebuilding and growth.

The process of bone formation occurs as described, starting with osteoblasts getting embedded in the matrix to form a random, unorganised protein mixture known as osteoid, which then mineralises to become bone. This involves the secretion of vesicles containing alkaline phosphatase, which cleaves the phosphate groups and acts as the foci for calcium and phosphate deposition. There are many elements that may play a significant role in bone formation such as calcium (Ca^{2+}), magnesium (Mg^{2+}), zinc (Zn^{2+}) and strontium (Sr^{2+}). However, it has been found that silicon is an element of particular interest. The presence of silicon in bone graft substitutes has been investigated since the early 1960s, and since, it has been shown to have some influence in bone calcification and formation. Therefore, the substitution of silicon in bone grafts can also be expected to influence porosity, chemistry of the grafts when implanted in bone defects of white rabbits, and result in improved bone healing due to its characteristic effect on bone calcification and formation (Hing 2004; Hing, Annaz*, et al.* 2005; Hing, Wilson*, et al.* 2007).

1.2.2.1   The Importance of Silicon in Bone Formation

Silicon (Si) is the most abundant element in the earth's crust; therefore it can be expected to exist at least in trace amounts, in living organisms. The effect of silicon in normal metabolism, therefore, had to be investigated to define any role in vital processes in mammals. Bone formation and restoration studies in experimental fractures` in rabbits in the work of Belous *et al.* (Belous and Skoblin 1962) have demonstrated that the relationship between silicon content and structural changes at the site of fracture can be observed and quantitatively identified, using emission spectral analysis. The study showed that the percentage of Si increased in bone callus on the 4-6th day after the fracture, corresponding to maturation of the organic matrix *via* the formation of collagenous fibers and the multiplication of cells. The study further showed that after several days, changes in the percentage of Si content corresponded

directly to the structural changes (i.e. reorganization and replacement) of the bone callus, up until the point where complete restoration of bone over the whole length of the fracture occurred. Thus from this initial study, it can be argued that silicon as an element is necessary in bone callus. Since then, further studies have been undertaken to show the importance of silicon in bone calcification and formation. It has been suggested by Carlisle that silicon could be associated with calcium in the early stages of calcification (Carlisle 1970). In 1970, she demonstrated that silicon has been localised in the active calcification site in young mice and rats bone, thus showing silicon to be an important factor in bone formation (Carlisle 1970). Her studies found that the amount of silicon was related to the maturity of the bone mineral, further confirming Belous' findings. She has shown that silicon levels falls below the detection limit once the ratio of Ca to P approaches hydroxyapatite formation. Over the years (1970-1991), her studies have confirmed the importance of silicon in bone formation. Silicon deficient chicks were found to be deformed and weak, while chicks given silicon supplement showed 50% growth and normal development (Carlisle 1972). Further experiments (Carlisle 1976; Carlisle "Biochemical and Morphological-changes associated with Long-bone Abnormalities in Silicon Deficiency" 1980; Carlisle "Silicon requirement for Normal Skul Formation in Chicks" 1980; Carlisle 1981; Carlisle 1988; Carlisle and Everly 1991) have proved that silicon is essential to bone formation, growth and development.

Furthermore, it was found that silicon appears to be present in connective tissue and its related structures by Schwartz in 1973, who found a bound form of silicon in glycosaminoglycans in the form of silanoate (ether or ester). Glycosaminoglycans consist of a repeating disaccharide unit (Trowbridge and Gallo 2002) within the family of carbohydrates, are essential and found in the extracellular matrix, which is one of the major components involved in bone formation with osteoblasts.

These findings, thus, confirm the importance of silicon in bone formation. This can then be used to suggest that silicon incorporation in biomaterials will improve bone calcification and formation *via* dissolution of Si from ECM and surface chemistry of the bone graft for cell adhesion, and thus mineralisation.

1.2.2.2   Proteins involved in Bone formation

These proteins are examples of non-collageneous proteins (NCP), which represent approximately 10% of the ECM. There are three proteins of particular interest in this respect, osteocalcin (OCN), bone sialoprotein (BSP) and osteopontin (OPN). All have the calcium (Ca)- and hydroxyapatite (HA)-binding properties (Young, Kerr, *et al.* 1992) and have been the centre of intense investigations because of their potential influence on cell attachment, Ca^{2+}, HA- binding and mineralisation of bone tissue. Osteocalcin (OCN), also known as bone Gla protein (BGP), is a polypeptide of 49 residues that contains 2 or 3 γ-carboxyglutamic acid (Gla) amino acids (Figure 1.4). (Hauschka, Lian, *et al.* 1975; Hunter, Hauschka, *et al.* 1996) It is a protein formed from a 76-77 amino acid precursor (Lackie and Dow 1995). The protein (Figure 1.5) has a strong affinity with hydroxyapatite (Hauschka, Lian, *et al.* 1989). Therefore, it plays a major role in mineralisation and calcium ion homeostasis to regulate remodelling (Dowd, Rosen, *et al.* 2003).

Osteocalcin (OCN) is one of the most abundant NCPs in bone, covering up to 20% of the total NCPs in bone. OCN binds to HA by orientating its γ-carboxyglutamic acid (Gla) residues to interact with calcium ions in the mineral lattice (Hoang, Sicheri, *et al.* 2003). It also functions in cell signalling and the recruitment of osteoclasts and osteoblasts. Hence, this protein can nucleate HA.
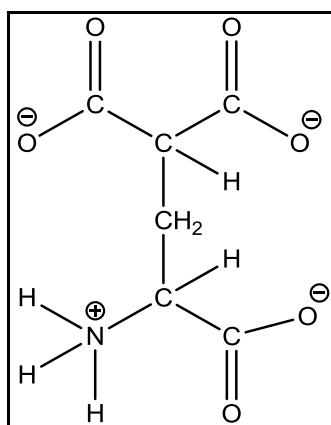
Figure 1.4 – Structure of the amino acid, γ-carboxyglutamic acid (Gla)
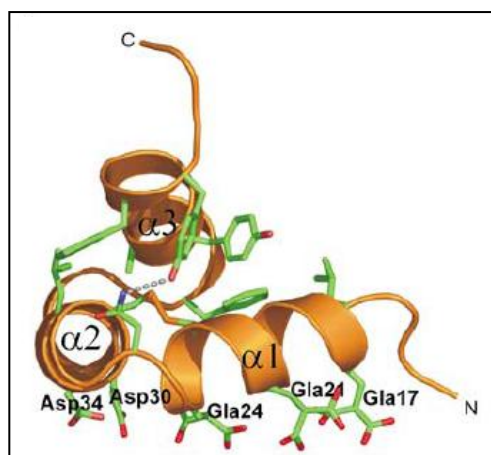
Figure 1.5 – Molecular ribbon diagram of the osteocalcin protein (Hoang, Sicheri, *et al.* 2003) where the C and N termini are labelled, the green sticks represent the side chains of Ca^{2+} coordinating residues and the orange ribbons are the 3 alpha helices.

Bone sialoprotein (BSP) is an acidic sialoprotein. It is a highly post-translationally modified protein consisting of 40-50 % carbohydrate and 13-14 % sialic acid. (Young, Kerr, *et al.* 1992) BSP constitutes approximately 15 % of the total NCPs in bone. BSP contains the RGD (see page 6) at its carboxy terminus, a region also rich in tyrosine residues, which are natural fluorophores and may be involved in autofluorescence, whereas in osteopontin (OPN), the RGD is located in the centre of the molecule (Hijya, Setoguchi, *et al.* 1994).

OPN (see Figure 1.6), also known as BSP type I or secreted phosphoprotein I (SPPI), is composed of two peptides of 57 kDa that links cells and hydroxyapatite of mineralised matrix. (Lackie and Dow 1995) OPN has calcium and hydroxyapatite binding sites for protein adsorption, to use towards bone formation (Puleo and Nanci 1999), and other components. (Fisher, Hawkins, *et al.* 1987; Oldberg, Franzen, *et al.* 1986; Reinhott, Hultenby, *et al.* 1990) OPN and BSP are both phosphorylated sialoproteins rich in acidic amino acid.
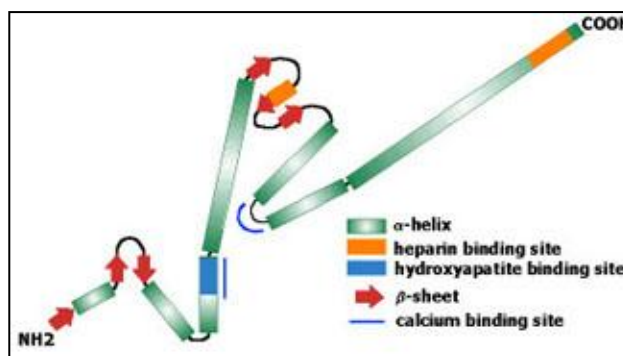
Figure 1.6 – Secondary structure of the osteopontin (Swiss Protein Database) with the key inset
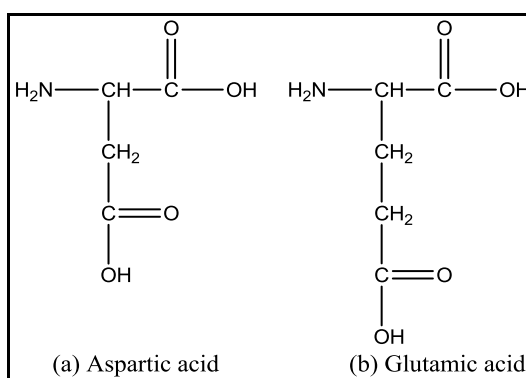
Figure 1.7 – Chemical Structures of the Amino acids: (a) aspartic and (b) glutamic amino acids

OPN is known to have a higher proportion of aspartic acid (Asp) residues (Figure 1.7a), some of which may combine and form "polyaspartate" sites, whereas BSP has more glutamic acid (Figure 1.7b) residues to form 2 or 3 "polyglutamate" sites. The structural differences observed in these three proteins, thus, result in them showing different processes in which to regulate Ca- and HA-binding, leading to HA formation and bone mineralisation. (Denhardt and Guo 1993; Hunter, Hauschka*, et al.* 1996)

The use of osteopontin for the thesis was favoured over osteocalcin due the position of the RGD sequence in the centre of the molecule. It is also considered being more important as it is secreted by the three most important bone cells osteoblasts, osteocytes and osteoclasts, (Denhardt and Guo 1993) i.e. both bone forming and bone resorbing cells and thus any effects observed from this protein could lead to better understanding and relevance to biomaterials' interactions with proteins.

Through gene expression OPN was found to be significantly up regulated compared to OCN and BSP in bone of spine fusion in rats (Zhang, Domenicucci*, et al.* 1990). It

carries the same advantages as BSP, but its calcium-binding site may compete with the hydroxyapatite calcium-binding site and mimic a truly competitive environment. OPN has various functions involved in gene expression, cell signalling and transcription, and bone-related functions (Denhardt and Guo 1993; Sodek, Ganss, *et al.* 2000), which thus lead to various effects such as influences on HA nucleation and crystal growth. (George and Veis 2008) OPN is known as a highly potent inhibitor of HA formation when phosphorylated (Denhardt and Guo 1993; George and Veis 2008; Hunter, Hauschka, *et al.* 1996), but promotes cell attachment and is involved in the regulation of osteoclast motility during bone resorption (Reinhott, Hultenby, *et al.* 1990). Therefore, it is more likely to further induce other proteins to attach on the surface of the biomaterial.

1.2.3   Proteins that lead to Cell Adhesion on Bone

Cell adhesion is involved in many natural processes in the human body. Cells in contact with a material surface will initially adhere and spread given appropriate environmental conditions. The quality of the adhesion will influence their morphology and future capacity for proliferation and differentiation. (Anselme, Noel, *et al.* 1999) Before adhesion on the material's surface, cell-cell adhesion must occur, for example a single detached fibroblast contacts an adhesive glycoprotein (fibronectin) and overlaps. This initial stage is the ***cell attachment***. (Lebaron and Athanasiou 2000; Sawyer, Hennessy, *et al.* 2005) Once attached, the cell can bind more strongly to a surface (cell-material adhesion), and starts to flatten, so as to spread across the material's surface (proliferation), and take the shape that may be peculiar to the cell type, also influenced by the surface chemistry of the material. (Hamilton, Yuan, *et al.* 2007; Kowalczynska, Nowak-Wyrzykowska, *et al.* 2005)

1.2.3.1 Proteins involved in Cell Adhesion

Blood proteins are regarded as important key factors in determining the *in vivo* acceptance of implants in hard tissue engineering (Raynaud, Champion*, et al.* "Calicum phosphate apatites with variable Ca/P atomic ratio I. Synthesis, characterisation and thermal stability of powders" 2002). During implantation, proteins are adsorbed immediately onto the surface of foreign materials, and thus determining the material's *in vivo* outcome, for example, the activation of some cells (platelet) adherence and coagulation activities can become quite a challenge.

Blood proteins such as fibronectin (FN) and vitronectin (VN), are present in blood plasma and known to interact and strongly affect several processes towards bone mineralisation, repair, regeneration and growth. All these proteins are synthesised by osteoblasts, and most are involved in adhesion. Thus, they are proteins of interest to use to help understand the competitive binding properties on biomaterial surfaces. Most adhesion proteins are characterised by their capacity to interact with a specific ligand, such as integrins. Integrins are cell-surface proteins that are involved in binding to ECM components. (Kowalczynska, Nowak-Wyrzykowska*, et al.* 2005; Lackie and Dow 1995)

Limitations to cell adhesion in bone biology often occur as a reaction to the topography of the biomaterials, i.e. surface roughness to which proteins have to adhere. Also, limitations can be observed due to the presence of other predominantly abundant proteins such as serum albumin. There are several cell types and proteins present in blood plasma, which inhibit cell adhesion, protein adsorption and even bone formation and resorption processes.

Serum albumin (SA), is a major protein component of the serum of veterbrates (Lackie and Dow 1995). It has a single polypeptide chain with multi-domain structure containing multiple binding sites. Albumin is a water-soluble globular protein (Itri, Caetano*, et al.* 2004), which is synthesised by the liver in mammals. It is the most abundant protein, corresponding to approximately 60 % of the total globular protein in blood plasma. Its function in the body is associated to the binding and transport of several small molecules such as amino acids. Serum albumin comes in various types (bovine, rat, rabbit or human). It is a protein that can be used in lab research as a diluent

or blocking agent or a standard in numerous applications. Bovine serum albumin (BSA) and human serum albumin (HSA) (see Figure 1.8) have been used to study the protein adsorption behaviour on different substrates.
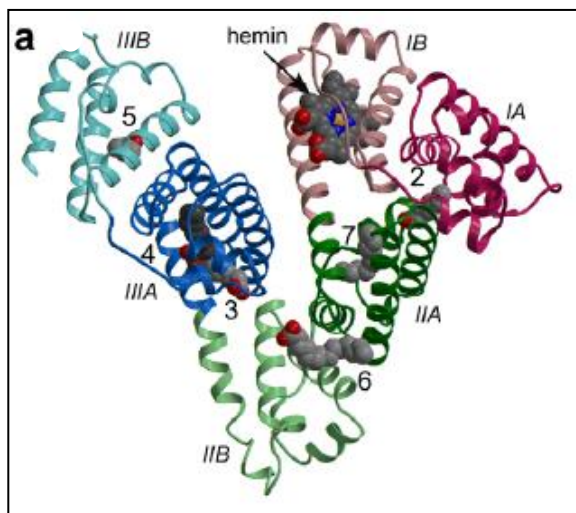
Figure 1.8 – Molecular ribbon diagram of human serum albumin (HSA) (Zunszain, Ghuman*, et al.* **2003) where the helical monomer contains 3 homologous domains where domain type I in red, type II in green and III in blue.**

Zeng *et al.* have shown that on different surfaces, such as calcium phosphate (CaP) and titanium (Ti), the protein adsorbed differently; according to how strongly it adsorbs, the protein itself may undergo some structural changes (Zeng, Chittur*, et al.* 1999). It has been suggested that these differences in protein adsorption behaviour could be accounted for the difference in the initial cellular behaviour on CaP and Ti surfaces. Other authors such as Xie *et al.*(Xie, Riley*, et al.* 2002) and Kilpadi *et al.* (Kilpadi, Chang*, et al.* 2001) have further confirmed these findings. The work of Kilpadi *et al.* has demonstrated that hydroxyapatite binds more serum proteins such as fibronectin and vitronectin than titanium or steel surfaces. This allowed for an increased accommodation of osteoblast precursors to adhere to these proteins through a suggested integrin-mediated mechanism on the different surfaces.

BSA will be used, as it is readily available and inexpensive, thus for developing a model system. BSA has a molecular weight of 66,320 Daltons and 35 lysine residues available for covalent attachment (Harlow and Lane 1988). The protein interaction with biomaterials will be initially studied individually, and then followed in competitive

conditions in the presence of 10% foetal bovine serum (FBS) with BSA, BMP-2 and OPN.

Fibronectin (FN) is a dimeric glycoprotein of high molecular mass with two subunits each 220 kDa linked by disulphide bonds near the C terminus, in total 440 kDa in size (Leahy, Aukhil*, et al.* 1996; Leahy, Hendrickson*, et al.* 1992). The subunits have identical N-terminal and C-terminal sequences, but show differences in mass due to the conditions used during protein processing (Skorstengaard, Jensen*, et al.* 1986). Fibronectin (Figure 1.9) is the most abundant extracellular matrix protein, and all connective cells produce it.
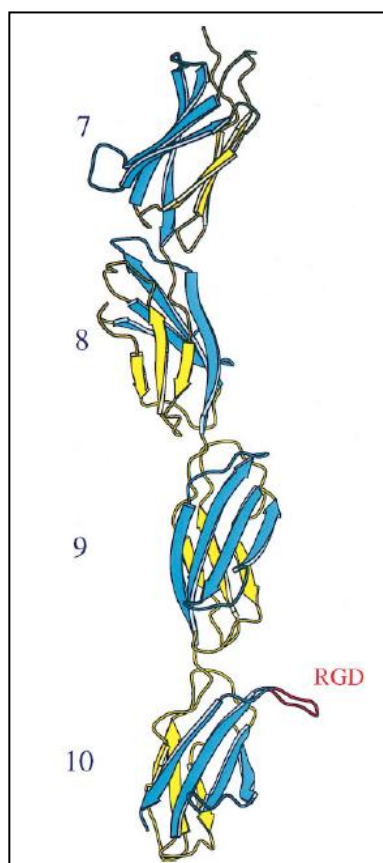
Figure 1.9 – Ribbon diagram of fibronectin type III (FN-III) protein with the blue representing the G-F-C-C' β-sheet strands of the FN7-10, yellow being the A-B-E strands and the red is the RGD loop (Leahy, Aukhil*, et al.* 1996)

FN sequence is composed of repeats of three prototypical types of domains known as type I, II and III. Type III is the most common of the repeats and the largest. FN is a multi-domain glycoprotein found in a soluble form in blood plasma with a high

concentration of 300 μg/ml (Leahy, Aukhil, *et al.* 1996), and in an insoluble form in loose connective tissue and basement membranes (Lebaron and Athanasiou 2000; Skorstengaard, Jensen, *et al.* 1986). FN has a central cell-binding domain through the RGD motif important for cell adhesion (Rosengren, Pavlovic, *et al.* 2002), recognised by integrins.

As a result, it is known to bind to many different biological compounds such as collagen and heparin. Due to the interaction properties of FN, it is therefore, involved in many biological activities, such as regulation of cellular adhesion, spreading and motility (Rosengren, Pavlovic, *et al.* 2002), wound healing and maintenance of normal cell morphology. (Mosher 1984; Yamada 1983) Fn has a molecular weight of 440 kDaltons and the presence of its 76 lysine residues available for covalent attachment to fluorescent labels (Skorstengaard, Jensen, *et al.* 1986).

Vitronectin (VN) is a serum protein, a smaller glycoprotein of 70kDa, which consists of 459 amino acid residues. It is also known as a serum spread factor protein (Lackie and Dow 1995) (or S-protein (Lakowicz 1999)) from its activity in promoting adhesion and spreading of tissue cells in culture. VN also binds through an interaction of the RGD motif in its cell-binding domain. Vitronectin consists of three domains but the one of interest is the N-terminal somatomedin b domain (SMB) with residues 1-5, (Xu, Baburaj, *et al.* 2001) also observed by other researchers (Kamikubo, De Guzman, *et al.* 2004; Kamikubo, Okumura, *et al.* 2002; Mayasundari, Whittemore, *et al.* 2004; Zhou, Huntington, *et al.* 2003). The N-terminal of vitronectin is where most processes occur, as it is the domain where the RGD sequence is most likely to be contained in. SMB of vitronectin usually crystallises with its physiological binding partner; the plasminogen activator inhibitor-1 (PAI-1) to modulate cell migration (Zhou, Huntington, *et al.* 2003).

In this thesis, fibronectin (bovine) is to be used due to its availability and its higher affinity associated with other proteins and cells, and the higher number of citations in respect to biomaterials' interaction and research potential.

1.2.3.2   Growth Factors

Growth factors (*GFs*) are polypeptide hormones that regulate the division of cells. The major type of growth factor is **transforming growth factors** (*TGFs*). These are proteins secreted by transformed cells that can stimulate growth of normal cells, regulate function and motility. There are two common forms: *TGF-α* and *TGF-β*. *TGF-α* is 50 amino acid polypeptide, containing an epidermal growth factor domain (*EGF*-domain), which binds to *EGF*-receptors, that stimulate growth of microvascular endothelial cells. *TGF-β* is a homodimer of two 112-residue amino acid chains, which is secreted by many different cell types; it stimulates wound healing. The *TGF* family includes many of the bone morphogenetic proteins (BMPs) (Klages, Kotzsch*, et al.* 2008). However, BMPs are different from *GFs*, as they are the only known *GF* to have the ability to stimulate the differentiation of mesenchymal cells towards the chondroblastic and osteoblastic phenotypes (Chen, Carrington*, et al.* 1991; Skinner, Kroon*, et al.* 2003).

Bone Morphogenetic Proteins (BMPs) are secreted from osteoprogenitor cells and mature osteoblasts, as well as many other cells. As bone formation begins through adhesion of cells into clusters or condensations, bone morphogenetic proteins (BMPs) regulate bone growth (Hollinger, Einhorn*, et al.* 2005). In bone tissue engineering, BMPs are used via three methods (1) cell therapy, (2) gene therapy and (3) cytokine therapy depicted as shown in Figure 1.10. (Saito and Takaoka 2003)
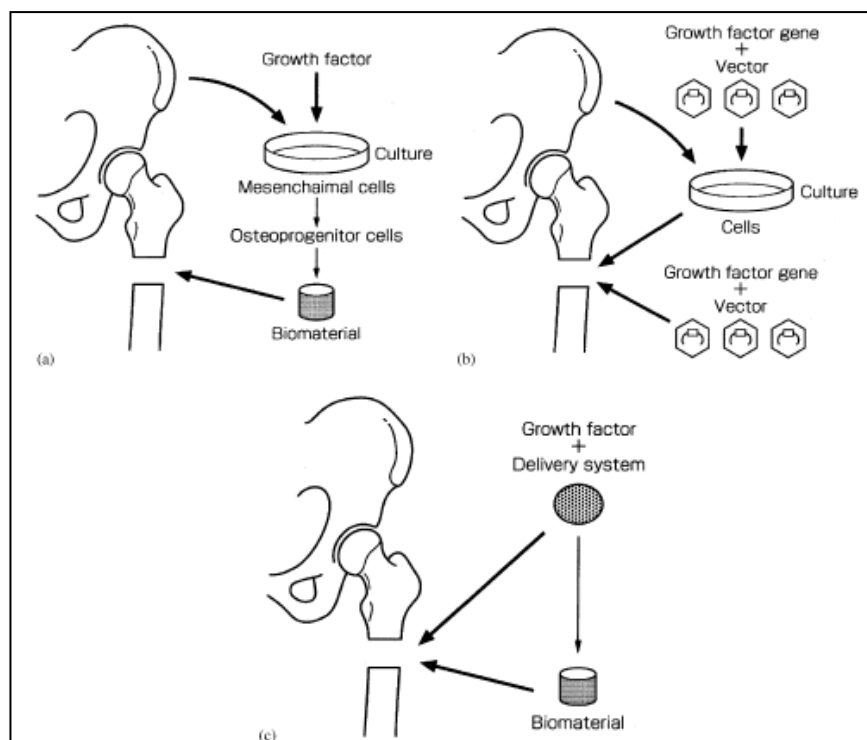
Figure 1.10 – BMPs therapies that could be used towards bone tissue engineering (a) cell, (b) gene and (c) cytokine (Saito and Takaoka 2003)

There are 20 individual BMPs that have been identified to date, as members of the *TGF-β* superfamily. BMP-7, -4 and -2 are of interest as they have been found most potent growth factors to be involved as activators in bone cell differentiation. They all have to be delivered *via* carriers such as collagen matrix, demineralised bone matrix (DBM), synthetic polymers or biomaterials to increase their efficiency towards osteoinduction. They play an important role in tissue development; growth and repair, they are mitogenic substances, which cause growth by stimulating cell division. (Tortora and Derrickson 2009) They are well established as osteoinductive proteins, especially BMP-2. (Hollinger, Einhorn*, et al.* 2005)

BMP-2 is a powerful growth factor (*GF*) (see Figure 1.11) when combined with a collagenous (Col) scaffold (Hing, Best*, et al.* 2004; Pluhar, Turner*, et al.* 2006) It is used because the proximity and quality of the local bone is less of a factor in the regeneration of new tissue; for example, it has been shown to accelerate bone formation in the periosteum cranii (Hirata, Nomura*, et al.* 2007), an area in which it is very difficult to observe natural bone mineralisation. BMP-2 has also been used successfully in clinical trials in conjunction with "Infuse" to demonstrate feasibility in a spine model

for controlled delivery and further expanding the understanding of its bioactivity in bone and other tissues (Hollinger, Einhorn, *et al.* 2005).
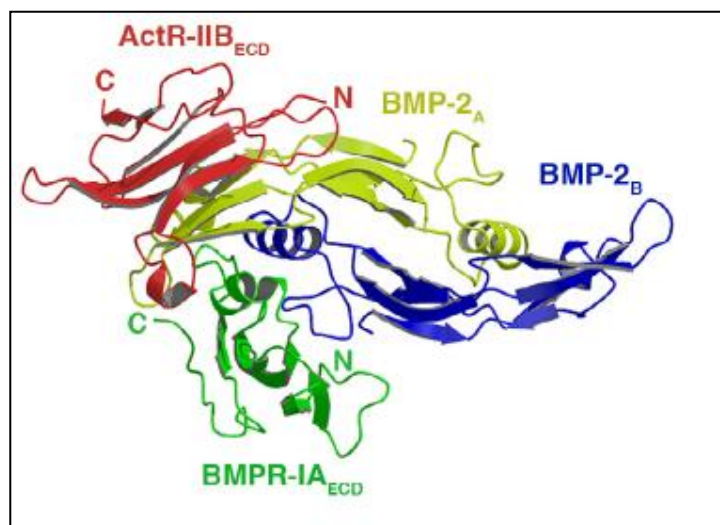
Figure 1.11 – Molecular ribbon diagram of the ligand-receptor complex of wildtype BMP-2 growth factor protein (Weber, Kotzsch, *et al.* 2007) where in yellow and blue are the wildtype representation of BMP-2, the red is the activin type IIB and in green the BMP type IA receptors

However, BMP-2 loss of function or dysregulation can lead to severe diseases, and even death (Nickel, Dreyer, *et al.* 2001; Weber, Kotzsch, *et al.* 2007). Also, pharmacological levels in the order of 0.7-17 µg per mg of Col of the *GF* are required to stimulate bone repair, compared to native BMP concentration in cortical bone (1-2 µg per kg of bone) and these levels are sometimes associated with some side effects (Weber, Kotzsch, *et al.* 2007) such as issues regarding cost, and factors affecting BMP activity *in vivo* (Hollinger, Einhorn, *et al.* 2005). The use of BMP-2 in this study is to provide evidence of its binding affinities and efficiency.

1.2.4   Characterisation Techniques for Proteins

1.2.4.1   Fluorescence Spectroscopy and Microscopy

Both these techniques rely on the fact that macromolecules (proteins) either act as fluorophores or can be attached to one to induce a fluorescent reading from the macromolecule in solution. Spectroscopy gives quantitative data, while microscopy gives qualitative data, respectively.

Fluorescence spectroscopy uses either a four-sided transparent fluorescent cuvette for samples in the form of assays (solutions) or sample holder for samples in the form of solid compounds. For both sample types, the instrument technique is the same, which result in similar data collected, a value of fluorescence in arbitrary units (Cantor and Schimmel "Part II: Techniques for the study of biological structure and function" 1980).
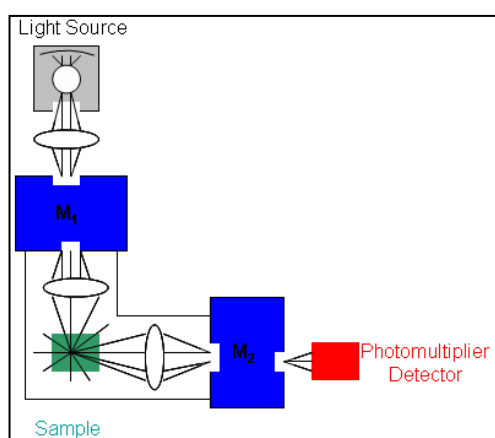
Figure 1.12 – Schematic of a Fluorimeter: cuvette reader

A fluorescence spectrometer is typically arranged as shown in Figure 1.12. M is the monochrometer where the integer 1 represents the excitation and 2, the emission, where it can be used in two modes; (1) with M_2 fixed and M_1 varying, resulting in an excitation spectrum and alternatively (2) with M_1 fixed and M_2 varied to yield an emission spectrum.

Fluorescence microscopy uses a conventional widefield microscope (see Figure 1.13) the entire specimen is bathed in light from a mercury source, and the image can be viewed directly by eye or projected directly onto an image capture device or photographic film.
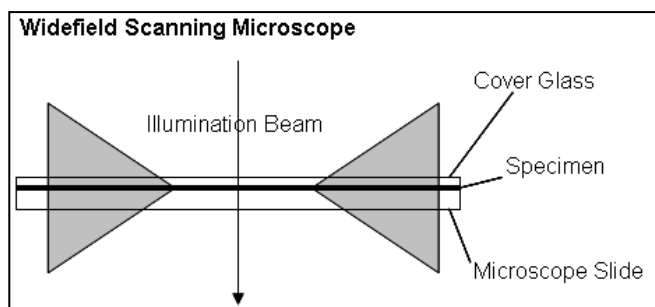
Figure 1.13 - Illustration of the widefield scanning method of Fluorescence microscopy

Specimens used are labelled protein and introduced to the biomaterial surface. The images obtained are bright and enable the protein to be seen according to the colour emitted by the tag. The image can also be used to measure the size of visible particles, as magnification and optical measuring accessories allow for accurate measurements.

1.2.4.2   Circular Dichroism (CD) Spectroscopy

This technique relies on the fact that macromolecules such as proteins have chiral centres or are optical isomers, which allow for the rotation of plane-polarised light through a solution as a function of the wavelength. (Thorpe and Thorpe 2000)

CD uses circular polarized light, obtained by superimposing two plane-polarised light waves of the same wavelengths and amplitudes but differing in the phase by a quarter of a wavelength and in their planes of polarization by 90°. (Thorpe and Thorpe 2000)

CD spectrum gives information about the relative proportions of secondary structure in a protein such as α-helixes, β-sheet and random coil in solution.

The CD information is the difference between the absorption of the left (LCPL) and right- handed circularly polarized light (RCPL) (Drake 1994) and the data obtained from CD can then be analysed using an online server to generate the secondary information of the protein under investigation (Whitemore and Wallace 2004; Whitemore and Wallace 2007)

1.2.4.3 Other Techniques

There are other techniques that could be used to further confirm protein conformation in solution and/or on the surface of the biomaterials such as ellipsometry (Elwing 1998) or matrix-assisted laser desorption ionization mass spectrometry (MALDI-MS) (Griessera, Kingshottb, *et al.* 2004) Both techniques do not require proteins to be labelled.

1.3   Biomaterials: Calcium Phosphates

Bone repair is an important subject of study as the demographic trends show a longer life expectancy of people, which may lead to higher risk of arthritis or osseous defects associated with longer life and lifestyle of these individuals. Over 300,000 hip and knee implants are used each year in the United States to replace or restore function to diseased and damaged tissues (Puleo and Nanci 1999). Due to this growth, replacing missing bone will become increasingly difficult when using either patient's own body part (known as autograft) or a donor body part (known as allograft). (Anselme 2000; Hing 2005) Therefore, the use of synthetic bone graft substitutes (BGSs) (Hing 2004) will be strongly favoured over the previous methods, especially if the resulting implant performs significantly better. Biomaterials used as BGSs can be metallic such as titanium and its alloys (Ellingsen 1991), ceramics for example apatite and bioglasses (Hench 1991; Hench and Andersson 1993; Knowles 2003) or polymers/copolymers (Kowalczynska, Nowak-Wyrzykowska, *et al.* 2005) like polyethylene oxide (PEO) (Fabrizius-Homan and Cooper "A comparison of the adsorption of three adhesive proteins to biomaterial sufaces" 1991; Fabrizius-Homan and Cooper "Competitive adsorption of vitronectin with albumin, fibrinogen, and fibronectin on polymeric biomaterials" 1991). Several researchers have shown that surface physio-chemical properties such as surface roughness (Thomas, McFarland, *et al.* 1997), surface area (Harding, Rashid, *et al.* 2005), surface charge (Yin, Liu, *et al.* 2002), porosity (Hing, Best, *et al.* 1999) and chemistry (Gibson, Best, *et al.* 2002; Hing 2005; Thomas, McFarland, *et al.* 1997), of the implant (BGS) to be of great importance as well as the composition of the surrounding environment in generating observed differences in cell

adhesion processes. Each factor affects the bioactivity, and thus biocompatibility of the material *in vivo* and *in vitro* in different ways (Ducheyne and Qui 1999).

1.3.1 Hydroxyapatite (HA)

HA is a bioactive biomaterial, also known as a bioceramic material, specifically, calcium phosphate. It is important for biological applications such as coatings, porous implants and fillers. Stoichiometric HA is used as a bioceramic due to its excellent biocompatibility, bioactivity, osteointegration and osteoconductivity properties *in vivo*; and its ability to bond directly to bone. HA has a hexagonal structure, see Figure 1.14, with a space group, $P6_3$/m, made up of PO_4 tetrahedra, and CaO_6 and CaO_7 polyhedra with channels containing the hydroxyl anions running parallel to the c-axis, where its general empirical formula is $Ca_{10}(PO_4)_6(OH)_2$. (Cazalbou, Combes, *et al.* 2004)
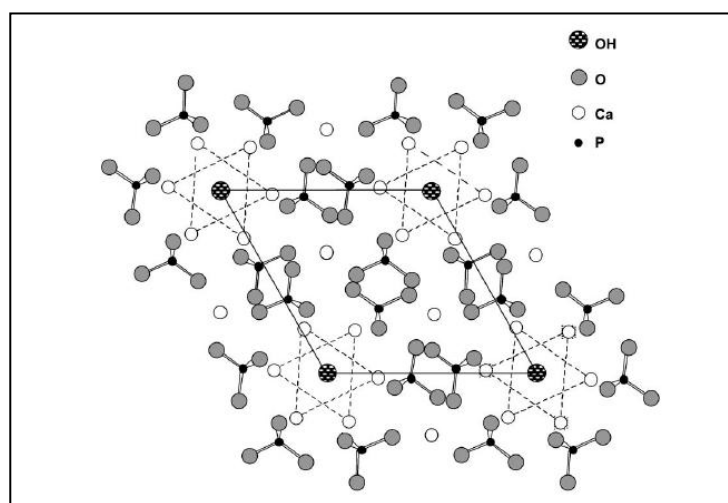
Figure 1.14 - Crystal lattice of Stoichiometric HA (Cazalbou, Combes, *et al.* 2004)

There are four ways in which HA can be synthesized, described as follows according to the review of LeGeros *et al.* (LeGeros and LeGeros 1993); from calcium hydroxide and phosphoric acid; in alkaline conditions from calcium nitrate; *via* a sol-gel method or by mechanochemical process, and final by solid state.

The preferred way is the first i.e. synthesise of HA is *via* an aqueous precipitation as it results in the formation of a one-phase product, when sintered at the optimum temperature for research or clinical applications. This consists of using calcium

hydroxide ($Ca(OH)_2$) and orthophosphoric acid (H_3PO_4). The orthophosphoric acid is added dropwise to an aqueous solution of calcium hydroxide at high pH (Equation 1.1). Then the resulting precipitate is filtered, dried at 80 °C overnight and then ground, milled and sieved.

$$10Ca(OH)_2 + 6H_3PO_4 \rightarrow Ca_{10}(PO_4)_6(OH)_2 + 18H_2O$$
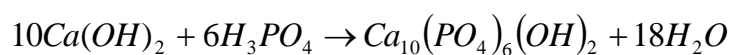
Equation 1.1

This results in the production of the hydroxyapatite in the form of a salt. Using ammonium hydroxide, known as the alkaline reaction condition, can further modify this method, and help in producing a phase pure compound. The main advantage of using HA is its chemical similarity to the inorganic component of the bone. However, it has its limitations. HA lacks the mechanical properties for use in monolithic load-bearing implants. (Gibson, Best, *et al.* 1999) It is brittle and usually needs to be used as a coating or filler within another device rather than as a whole implant. While synthesising HA, the pH of the resulting suspension needs to be kept at pH 10.30 because it will result in changes in the Ca/P ratio of 1.67. If the Ca/P ratio falls below or above 1.67, β-tri-calcium phosphate (β-TCP), $Ca_3(PO_4)_2$, and other phases will be produced, which then lowers the phase purity of the HA, increases its solubility, and thus introduces other factors to consider when using that particular material in a research investigation. When the Ca/P ratio is higher than 1.67, calcium oxide (CaO) will be present in the HA, which will also alter the crystal structure of HA and result in changes to the surface chemistry of the material. Also, due to these slight changes, there could be minor and trace elements from the original reagents used to make the apatite powder.

1.3.2 Silicate-Substituted Hydroxyapatite (SA)

Silicate-substituted hydroxyapatite (SA) was produced and can exist in varying weight percentage of silicon content (0.2, 0.4, 0.8 and 1.5 wt%); knowing the empirical formula, $Ca_{10}(PO_4)_{6-x}(SiO_4)_x(OH)_{2-x}$, the actual weight percentage of the silicate (SiO_4^{4-}) groups which substitute site specifically for the phosphate groups in HA can be determined. The synthesis and characterisation of SA of different weight percentage

level has been researched and characterised by Gibson *et al.* (Gibson, Best, *et al.* 1999) and in the work of Hing *et al.* (Hing, Revell, *et al.* 2006) The incorporation of a small amount of silicon (0.8 wt%) was introduced in the structure of hydroxyapatite lattice $Ca_{10}(PO_4)_6(OH)_2$ using an aqueous precipitation reaction. This consists of using silicon acetate $(Si(OAc)_4)$ to retain the charge balance (Gibson, Best, *et al.* 1999) (Equation 1.2):

$$10Ca^{2+} + (6-x)PO_4^{3-} + xSiO_4^{4-} + (2-x)OH^- \rightarrow Ca_{10}(PO_4)_{6-x}(SiO_4)_x(OH)_{2-x}$$
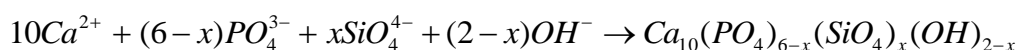
Equation 1.2

The appropriate quantities of the reactants to quantitatively produce stoichiometric HA, compared to SA are shown in Table 1.1

Table 1.1 – Molar Quantities of Reactants needed for HA & SA material & Molar ratio of *Ca/P* equivalent (Gibson, Best, *et al.* 1999)

Materials	Wt% Si	No. of moles			Molar Ratio
		$Ca(OH)_2$	H_3PO_4	$Si(OAc)_4$	
HA	-	0.500	0.2970	-	1.67
SA	0.8	0.500	0.2850	0.0150	1.67 Ca/(Si+P)

It was very important that the ionic substitution did not result in thermal instability of the material as this would affect the sintering of the material, which may result in decomposition to undesirable by-products. According to the review of Gibson several attempts have been made to produce a silicon-substituted hydroxyapatite by different methods such as sol gel found by Ruys *et al.* in 1993, hydrothermal methods in 1994 and solid state in 1997by Tanizawa *et al.*, however, none resulted in the formation of a single-phase silicon-substituted hydroxyapatite (Gibson, Best, *et al.* 1999).

These different phases introduced further difficulties in clearly obtaining evidence that the silicon was incorporated site specifically for the phosphorus site in the HA lattice. The silicon-substituted hydroxyapatite formed by Gibson was one phase pure sample with no presence of decomposition or phase changes upon the sintering of the material into derivatives such as β-TCP or presence of impurities such as calcium oxide (CaO) compared to previous works. The work of Marques *et al.* have further demonstrated that single-phase silicon-substituted apatites with the crystal and chemical structure of HA

have been formed with silicon contents of up to 0.15 wt% by wet chemical route. (Marques, Magalhaes, *et al.* 2000)

1.3.3   Other substitutions

It is well known that bone has many apatite phases (Cazalbou, Combes, *et al.* 2004; Kuhn, Fink, *et al.* 1996), which may have different type and amount of ionic substitution (Ca^{2+}, Mg^{2+}, Sr^{2+} and CO_3^{2-}). These ions play an important role in bone mineralisation and other related functions. (Meyer and Wiesmann 2006) Therefore, using a synthetic apatite and other forms of ionic-substituted apatites, such as silicate (SiO_4^{4-}), carbonate (CO_3^{2-}) (Barralet, Best, *et al.* 2000; Landi, Tampieri, *et al.* 2004; Takemoto, Kusudo, *et al.* 2004) and/or fluoride (F^-), will have an effect on the surface structure, surface charge, and solubility of the material; result in changes in the biological performance *in vitro* and *in vivo*.

The work of Barralet *et al.* has investigated the effect of water, vapour during sintering, on the density and microstructure of varying carbonate content in HA to show that upon different sintering conditions the biomaterial will topographically be different. (Barralet, Best, *et al.* 2000) This could then lead to differences in protein adsorption as the material was modified to be more hydrophilic than hydrophobic. Heavy metal substitutions have been incorporated into HA to investigate cell adhesion and quantify the enhanced bioactivity of these new biomaterials. Magnesium (Mg^{2+}), cadmium (Cd^{2+}), zinc (Zn^{2+}) and yttrium (Y^{3+}) have been used to dope HA and found that osteoblast adhesion was increased significantly on HA doped with 2-7 mol% Y^{3+} (Webster, Ergun, *et al.* 2002). Other researchers have incorporated up to 2 wt% ion content of silicon and 1 wt% of magnesium, as a co-substitution to investigate sintering behaviours, which could lead to enhanced biocompatibility and bioactivity. (Kim, Lee, *et al.* 2003) Using about 5 % zinc doped in HA found an increased formation of a biologically active layer on its surface, which permitted a stronger chemical bond between the bone and ceramic work (Jallot, Nedelec, *et al.* 2005).

Composites of hydroxyapatite and phosphates such as β-tricalcium phosphate may also be an advantageous biomaterial. These are usually known as biphasic calcium phosphates (*BCPs*). They combine the excellent bioactivity of HA with the good bio-

resorbability of *β-TCP*, and are interesting materials for use in medical applications such as bone replacement. *β-TCP* and HA characterisation and behaviour upon protein adsorption has been investigated (Gregori, Kleebe, *et al.* 2006). This team of researchers has demonstrated using electron energy-loss spectroscopy (EELS), that characterisation properties such as hydrophobicity/hydrophilicity, and heat-treatment strength, and resorption of the individual grains of the bioceramic material differ from when compared to composites made of the mixture. The composite had revealed to be an improvement to mechanical properties, where the work of Raynaud's group showed that a *BCP* containing just 10 wt% of *β-TCP* exhibits double tensile strength compared to stoichiometric HA ceramics. (Raynaud, Champion, *et al.* "Calicum phosphate apatites with variable Ca/P atomic ratio I. Synthesis, characterisation and thermal stability of powders" 2002; Raynaud, Champion, *et al.* "Calcium phosphate apatites with variable Ca/P atomic ration III. Mechanical properties and degradation in solution of hot pressed ceramics" 2002)

1.3.4   Characterisation Techniques for Ceramic Biomaterials

1.3.4.1   *X-ray Diffractometry (XRD)*

XRD involves the scattering of X-rays with $\lambda \sim 1$ Å by the repeating elements of a crystal lattice resulting in a diffraction from the crystal planes. XRD is also used for determining the crystal structure of a specimen.

Bragg's Law indicates that diffraction is only observed when a set of planes make a very specific angle with the incoming X-ray beam (Callister and Rethwisch 2007; Cantor and Schimmel "Biophysical Chemistry Part II: Techniques for the study of Biological Strucutre and Function" 1980); a constructive interference (Figure 1.15). This angle depends on the inter-plane spacing d, which itself depends on the size of the atom which make up the structure. During XRD, diffraction is measured for a range of different angles, theta (θ), see Figure 1.16 for the schematic of a powder diffractometer. The amount of beam scattered depends on the atomic number of the element(s) present in the sample (specimen). The crystallographic directions and planes are expressed in

'Miller' indices where (x,y,z) indicates the location of a point, [hkl] indicates the direction from (0,0,0) to (x,y,z) in whole numbers. (Park and Lakes 2007)
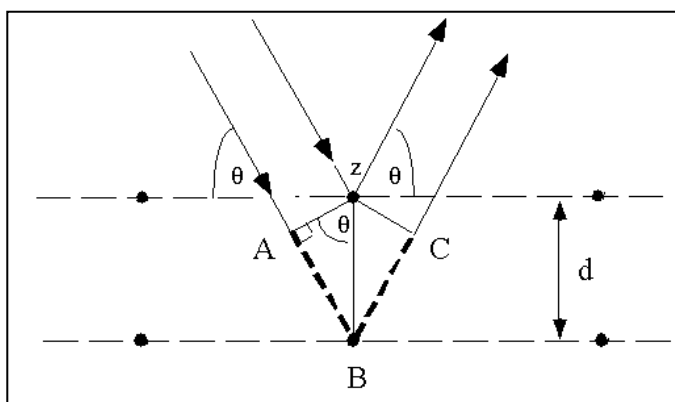
Figure 1.15 - Schematic diagram of Bragg's Law
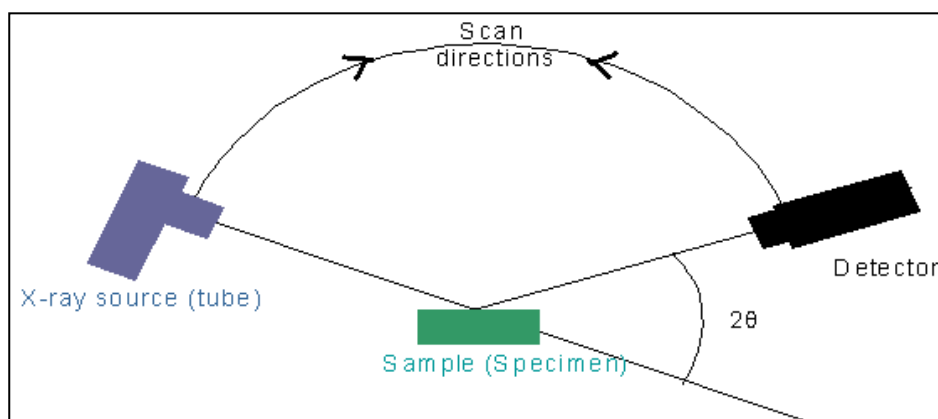
Figure 1.16 - Schematic of a Powder Diffractometer

$$n\lambda = 2d_{hkl}Sin\theta_{hkl}$$

Equation 1.3

This relationship is further explained *via* Bragg's equation (see Equation 1.3) where the path difference between coherently reflected beams is related to the d-spacing between the crystal planes, d_{hkl}, and the particular Bragg angle, θ_{hkl}, at which reflections from these planes are observed, the latter is detected and recorded against intensity as a XRD pattern.

1.3.4.2 Fourier Transform Infrared- Photoacoustic Spectroscopy (FITR-PAS)

Photoacoustic spectroscopy (PAS) is commonly used in the analysis of a variety of materials. It is a non-destructive technique that is applicable to almost all types of samples, powder, films and even polymers. It offers minimal or no sample preparation and the capability to perform depth-profiling experiments. PAS can be used for both qualitative and quantitative analysis.

In PAS, the transformation of an optical event to an acoustic one occurs. Initially, modulated light is absorbed by the sample located in a sealed chamber. The non-radiative decay of this absorbed light produces a modulated transfer of heat to the surface of the sample. This modulated thermal gradient produces pressure waves in the gas (helium, He) inside the cell that can be detected by the attached microphone (Figure 1.17). This microphone signal, when plotted as a function of wavelength, will give a spectrum proportional to the absorption (or transmittance or photo-acoustic unit) spectrum of the sample.
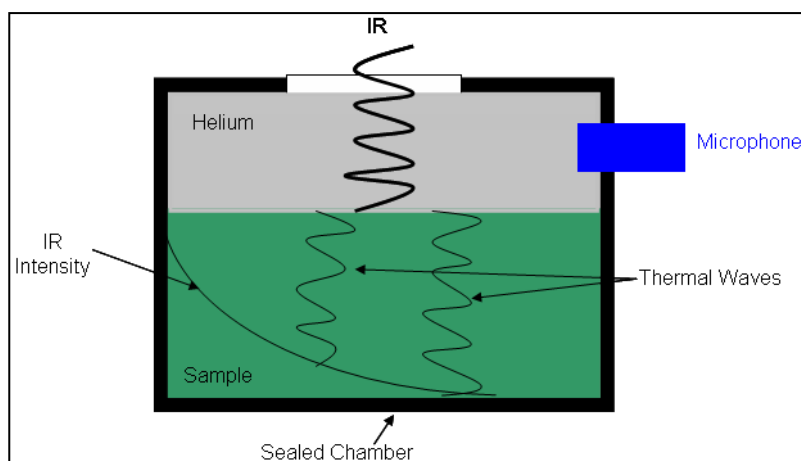
Figure 1.17 - Depiction of a Photoacoustic Spectrometer (PAS) signal

For PAS experiment conditions, a FT-IR spectrometer capable of operating in both continuous scan mode and in step-scan mode is used. A photo-acoustic cell is used as an accessory for containing the sample within the sample chamber. Helium gas is used as the transfer medium in the cell and to purge water vapour and carbon dioxide, and a 60 % carbon black-filled polymer is often used as a reference sample.

1.3.4.3   X-ray Fluorescence (XRF)

X-ray fluorescence (XRF) spectroscopy is another characterisation technique, which has been used extensively to further quantify constituent distribution of calcium phosphate (CaP) biomaterials in order to determine the calcium to phosphate ratio or silicate ratio in the biomaterials under investigation. (Best, Sim, *et al.* 1997) It works on the basis of measuring the individual component wavelengths of the fluorescent emission produced by a sample when irradiated with X-rays. It is also a non-destructive technique.

It works on the principle that excited atoms produced from a sample hit by high-energy electrons, will emit a x-ray fluorescence signal, which is characteristic to those elements present in the irradiated sample (Chen, Gibson, *et al.* 2008).

1.3.4.4   Surface Area Analysis & Porosity

Surface Area (S.A.) analysis of the powder and porous specimens is to be determined by performing multi-point analysis via helium intrusion into degassed specimens. This method involves measuring the amount of helium required to intrude into a sample at a particular rate, and using the Brunauer-Emmett-Teller (BET) equation, so as to measure the surface area.

Strut porosity of the porous granules is usually measured using mercury intrusion porosimetry (MIP). This usually involves measuring how much pressure is required to push mercury through the specimen initially at low pressure, then followed at high pressure, calculated using a known standard of the pycnometer and its constant.
Other methods require samples to be embedded in resin and imaged by SEM, and then the strut porosity will be determined by the scale of the image dimensions.

1.3.4.5   Scanning Electron Microscopy (SEM)

SEM is a technique that uses electrons instead of light to form an image. A probe scans the surface of the object, under investigation. SEM has a large depth of field, which allows more of a specimen to be in focus at one time.

It also has a high resolution with more control over the magnification due to the use of electromagnets rather than lenses, as a result, producing clear images. This technology is based on the television technique all in vacuum (see Figure 1.18 & Figure 1.19).

The method is suitable for specimens with conductive surfaces. For imaging only of specimens, preparation of the surface needs to be made, where the specimen is coated with gold, for example palladium and gold/palladium also.

Figure 1.18 – SEM Instrument in Nanovision Centre at QMUL (F.E.I., UK)

Further analysis, such as ***energy dispersive spectroscopy (EDS)*** can be used in conjunction with SEM to obtain elemental composition of the material under investigation. *EDS* is a microanalysis technique that is performed by measuring the energy and intensity distribution of X-ray signals generated by a focused electron beam on the sample material. (Goldstein, Newbury*, et al.* 2003)
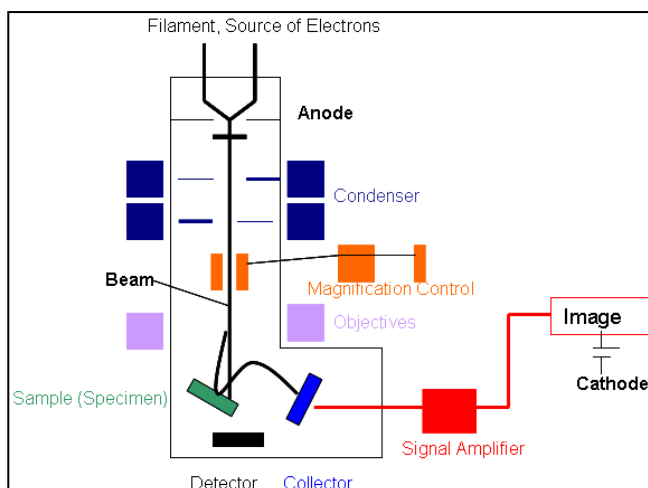
Figure 1.19 - Schematic of an SEM, slightly modified (Rochow and Tucker 1994)

The surface of the object is scanned with the electron beam point by point, whereby the resultant signals are then fed to the amplifier. Various signals can be collected by the amplifier such as secondary electrons, back-scattered electrons, incident beam, visible light and X-rays. All can be monitored separately or simultaneously by the means of the appropriate detector. SEM thus constructs a pattern or map of the chosen resultant signals that can be interpreted as an image of the object under investigation.

1.3.4.6   Other Techniques

Atomic force microscopy (AFM) is a versatile technique (Figure 1.20 and Figure 1.21) that has been applied to a large number of research topics, and therefore, can be modified for specific application requirements.

The technique has several modes of operation with the most commonly used one being the tapping mode, which is more of interest to this study. The tapping, also known as *dynamic force or the intermittant-contact mode* of AFM is a method used widely as it is advantageous over the others as it improves lateral resolution on soft samples, and eliminates lateral forces such as drag (obtained in contact mode) (Li, Xi*, et al.* 2006; Micic, Chen*, et al.* 1999; Smith, Connell*, et al.* 2003). It involves close proximity of the stiff cantilever as it oscillates closer to the sample than in a non-contact mode.

As part of the oscillation extends into the repulsive region, the tip is known to intermittently touch the surface of the sample. A laser is placed at the tip of the

cantilever, as a way to accurately determine the oscillating measurements of the cantilever against the sample in any environment.

Figure 1.20 – Atomic Force Microscope (AFM) at the Nanovision Centre at QMUL, London, UK
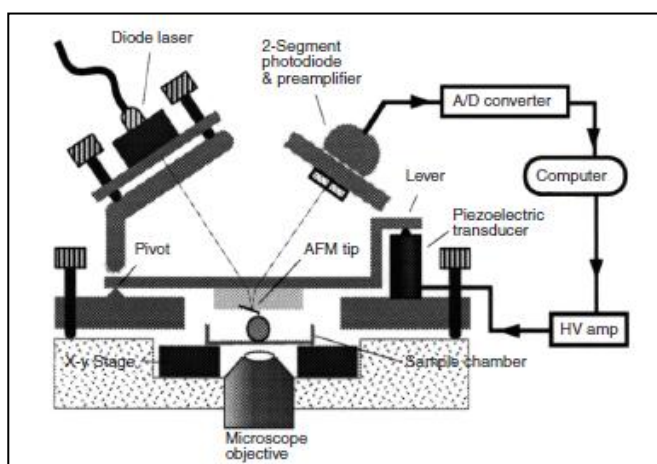
Figure 1.21 – A schematic of the atomic force apparatus (Micic, Chen*, et al.* 1999)

As the tip of the cantilever oscillates across the surface, the differences obtained from the laser are recorded. The data is then collected and from this, force constants, surface morphology and surface area can be determined.

On biomaterials, AFM is usually used to show surface roughness and chemical homogenous or heterogeneous activity of the surface *via* phase analysis. It can also be used in a wet environment, i.e. with samples submerged into solutions, which may require tips to be functionalized for better resolution(Micic, Chen*, et al.* 1999).

1.4   Cell/ Protein Adhesion on Biomaterials

1.4.1   Cell/Protein and Bone-Implant Interactions

Cell adhesion is important in various natural physiological processes such as embryogenesis, maintenance of tissue structure, wound healing, immune response, and metastasis as well as tissue integration of biomaterials (Anselme 2000). In terms of biomaterials, adhesion covers different domains; (1), the attachment phase which occurs rapidly and involves short-term events like physicochemical linkages between cells and materials involving ionic forces, or van *der* Waals forces, for example; and (2), the adhesion phase occurring in the longer term and involving various biological molecules such as extracellular matrix proteins, and cytoskeleton proteins, which interact together to induce signal transduction, promoting the action of transcription factors, and consequently, regulating gene expression. These processes are devised to improve wound healing and efficient remodelling of the engineered implant.

The bone-implant interface has been investigated to better understand the events that occur at the interface, as reviewed by Puleo and Nanci (1999). The study has enabled the determination of the host response *via* an assumption that the bone-implant interaction comprises of two components; (1) the response of the host to the implant and (2) the behaviour of the material in the host, summarized in Figure 1.22.

This mechanism was further confirmed and observed by Anselme, when using osteoblast on different materials. (Anselme 2000; Anselme, Noel*, et al.* 1999) The study demonstrated that cells and proteins do not interact with pure material. The material needs to be conditioned by biological fluid components, first, which determine protein adsorption. Factors such as pH, as well as ionic composition and strength of solution (for example, the use of PBS or HEPES), temperature and the functional group of the proteins and other cells present used (for example, which type of bonding will they be forming with the surface) are also important in deriving a mechanism in protein adsorption.
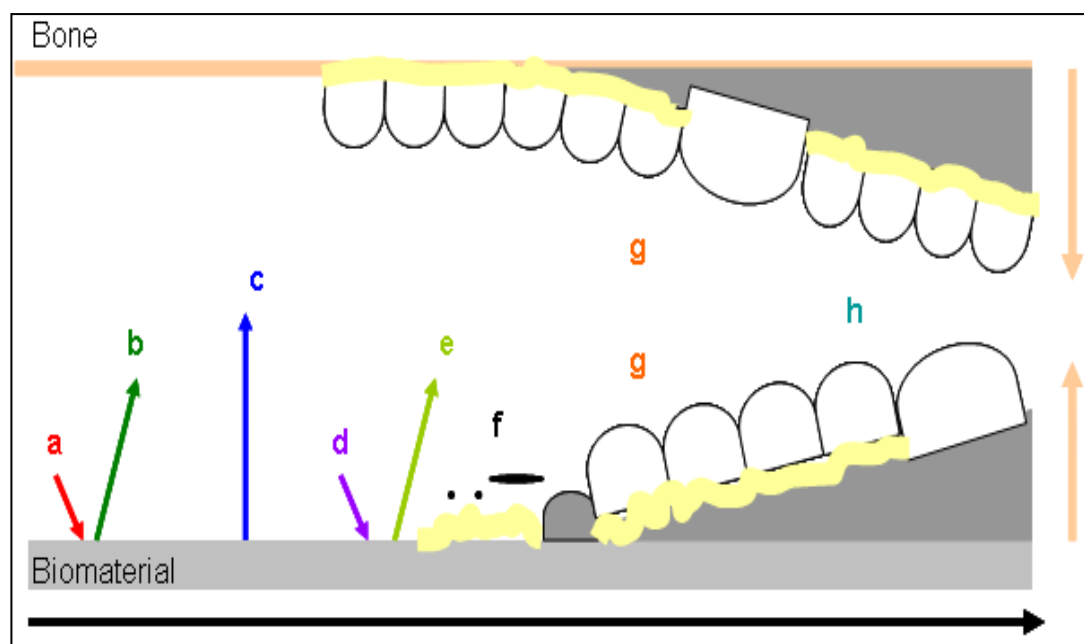
Figure 1.22 – Modified representation of the events occurring at the bone-implant interface. The protein adsorption (a) from blood and tissue fluids begins the process, followed by the proteins desorption (b). This leads to surface changes and material release (c), which prepare the material to further changes and responses. The inflammatory and connective tissue cells (d) approach the implant where possible targeted release of matrix proteins and selected adsorption of proteins such as BSP and OPN (e) occurs. The formation of *lamina limitans* (f) and adhesion of osteogenic cells and bone deposition (g) on both the exposed bone and implant surfaces results in (h) the remodelling of newly formed bone. (Puleo and Nanci 1999)

The interaction also depends very much on the surface aspects of the material used (titanium alloys, bioglass, hydroxyapatite and substituted-hydroxyapatite), which can be described according to their chemistry, surface energy or topography. These surface characteristics determine how biological molecules will adsorb to the surface, and more particularly determine the orientation of adsorbed molecules. Surface roughness of materials does affect the behaviour of different cells or proteins on the material, where generally it has been demonstrated that roughness modify greatly cell processes compared to smooth surfaces (Roach, Farrar, *et al.* 2005; Sawyer, Hennessy, *et al.* 2005; Thomas, McFarland, *et al.* 1997).

1.4.2 Physiological, Morphological and Ionic Influences of HA and SA on Cell/Protein Adhesion

Adsorption of protein on apatite depends largely on surface area and properties of the apatite before and during the sintering processes; the sample form (granules or discs), its density and porosity, its surface packing (microstructure) and the crystallinity of material. The chemistry occurs at the surface interface between the apatite material and the protein, solid-lipid (or liquid) interface, very much like for the metallic and bioglass surfaces. Grain structure, size and boundaries should be very similar.

Another important factor for cell or protein adhesion is how the HA or SA has been produced and the *Ca/P* ratio in the material when sintered. In HA, it was shown that a ratio of 1.67 is the optimum ratio to which a stoichiometric HA forms as a single phase product, this was also found to be true when forming SA, (Gibson, Best, *et al.* 1999; Hing, Gibson, *et al.* 1998) where enhanced bioactivity was achieved. For a lower ratio both types form with beta-tricalcium phosphate (*β-TCP*), whereas for a higher ratio calcium oxide (CaO) becomes present in the samples. This may also result from poorly calcined materials (Patel, Gibson, *et al.* 2001) or sintered conditions used on the materials (Gibson, Ke, *et al.* 2001), which further may lead to changes in the biomaterials' hydrophobicity and hydrophilicity. These will, in turn, lead to changes in the surface charge and packing of the grain of the materials, which will subsequently affect the adsorption property of the proteins on the surface due to differing grain size and boundaries (Barralet, Best, *et al.* 2000).

Introducing porosity into the HA and SA production has increased cell and protein adsorption due to differences in surface area. (Hing, Annaz, *et al.* 2005; Hing, Best, *et al.* 1999) It also allowed for the samples to achieve micro- and macro-porous properties that introduce interconnectivity and ultimately enabling the sample to behave more like real bone, i.e. a good candidate to use as a synthetic bone graft substitute (BGS). Looking at Figure 1.23, it is evident that increased porosity increases volume of bone ingrowth.

As a result, the protein attachment will be affected to these various heat-treatments and forms, as the surface chemistry would be different from the optimum condition for protein adsorption to occur. Secondary behaviours may occur, where due to the changes

on the surface, i.e. production of *β-TCP* instead of HA, results in the sample being more soluble, thus protein would react differently as they adsorb on the surface (Hing, Annaz, *et al.* 2005). The affinity may be lower or higher depending on the side chains available on the protein under investigation.
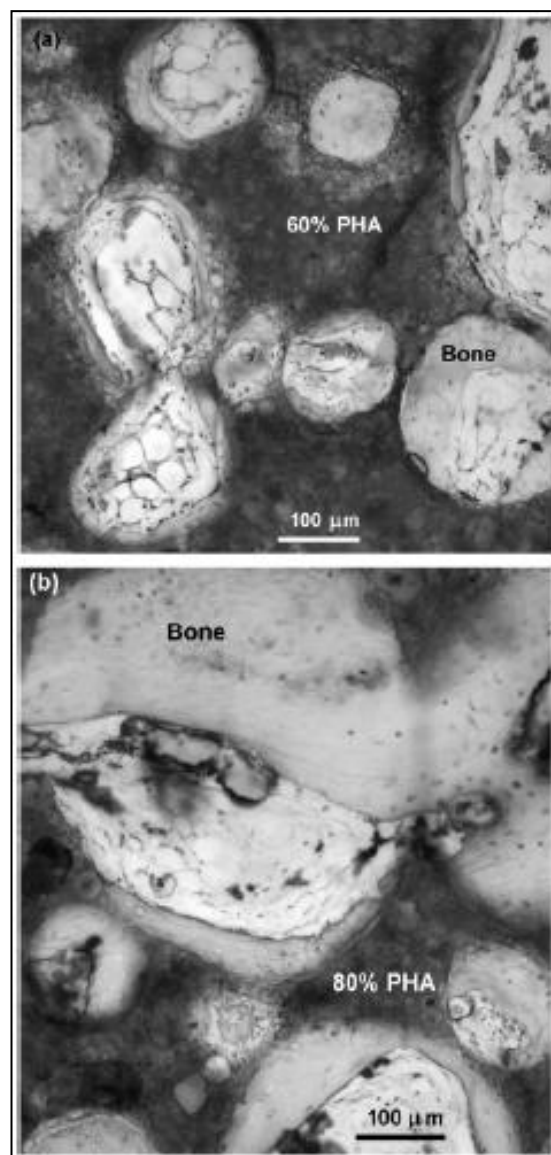
Figure 1.23 – Variation in bone volume and morphology within the central porosity of (a) 60% and (b) 80% porous hydroxyapatite (HA) bone graft substitutes after 12 weeks in vivo (lapine femoral condyle defect model) (Hing 2005)

To conclude, the phenomenon of cell adhesion on biomaterials can be summarised in terms of the mediation of the biomaterial-cell interactions by the adsorbed proteins. Implanted materials are immediately coated with proteins from blood and fluids, and it is through the adsorbed protein layer that cells then sense the foreign surfaces. Surface

composition, pH and morphology thus interact with protein in the appropriate mechanism, depending also on temperature and time, which then result in proteins adopting particular conformations, which cells then respond to. This suggests that it is the adsorbed proteins, rather than the surface itself, to which cells initially respond, as reviewed by Wilson *et al.* (Wilson, Clegg, *et al.* 2005).

1.5   Competitive Binding of Proteins on Biomaterials

Adsorption of proteins onto biomaterials does not occur randomly or sequentially. The binding is competitive, very much depending on the adhesive proteins present, their molecular weight, concentration, and the contact time the proteins have to adsorb onto a surface.

Adsorption characteristics of adhesive proteins such as fibronectin (FN), vitronectin (VN) and others have been of special interest. Due to their abundance in plasma and their varying molecular weight and involvement in bone related functions, these adhesive proteins will always be present in and around any implant and thus may be involved in wound healing processes.

So far protein competitive binding studies have been investigated using SDS-PAGE, known as sodium dodecyl sulfate polyacrylamide gel electrophoresis (Ellingsen 1991), in conjunction with enzyme-linked immunoadsorbent assay (ELISA); the first is used to analyse the proteins, while the other to identify specific proteins. Another method is *via* labelling, also known as radiolabelling, for example iodination with iodine isotopes (^{125}I or ^{131}I ions) (Fabrizius-Homan and Cooper "A comparison of the adsorption of three adhesive proteins to biomaterial sufaces" 1991; Fabrizius-Homan and Cooper "Competitive adsorption of vitronectin with albumin, fibrinogen, and fibronectin on polymeric biomaterials" 1991). This method both analyses and identifies the proteins under investigation. All methods have been used to quantify and study the potential mechanism of protein adsorption on biomaterials' surfaces.

Radiolabelling has been more favoured over the others for the competitive studies, especially in the work of Fabrizius-Homan *et al.* They demonstrated that VN competitively adsorbed in the presence of human serum albumin (HSA), fibrinogen (FGN) and FN in very different ways compared to their relative individual affinities on polymeric biomaterials. The study was monitored by incubating radio-labelled protein solutions contained inside tubing fabricated from the polymeric biomaterials. The experiment revealed VN adsorbed more readily when competitively adsorbed at equal mass concentrations. However, when competitively adsorbed in the presence of increasing amounts of HSA, FGN and FN, the amount on VN adsorbed diminished. When HSA, FGN and FN were competitively adsorbed in the presence of increasing

amounts of VN, VN diminished their adsorption on weight basis in the following trend: HSA > FN > FGN (Fabrizius-Homan and Cooper "A comparison of the adsorption of three adhesive proteins to biomaterial sufaces" 1991; Fabrizius-Homan and Cooper "Competitive adsorption of vitronectin with albumin, fibrinogen, and fibronectin on polymeric biomaterials" 1991). However, reproducing this type of study with more dense materials such as HA or SA could be problematic, where the overall idea is to mimic as close as possible the human bone environment.

Further studies have shown that due to proteins being highly surface active, they must exhibit high affinity for interfaces. Adsorption can be promoted or opposed by a number of factors such as dehydration of proteins, or surfaces, redistribution of charged groups at the interface and the conformational changes of the protein molecule itself (Wilson, Clegg, *et al.* 2005). Adsorption may be seen to increase over time and protein concentration increases until a monolayer coverage is obtained on the material surface (Noh, Yohe, *et al.* 2008), this may be true of individual protein adsorption, thus intuitively can be expected for the adsorption of multiple proteins upon a surface. In the work of Noh *et al.* adsorption was also confined to the number of available binding sites that each protein would adhere to in preference to other sites on the material surface. As a result the adsorption rate would be affected over time, depending on how many binding sites are present. Given these factors, the relationship between adsorption rate and proteins is difficult to define when many proteins are present.

1.5.1 The *"Vroman"* Effect

During competitive binding and in the absence of cellular interactions, proteins are usually known to displace over time rather than simply desorb from the surface. This is known as the *"Vroman"* Effect (Green, Davies, *et al.* 1999; Gugala and Gogolewski 2004). Proteins such as vitronectin (VN), fibronectin (FN) and fibrinogen (FBN) are believed to exhibit this behaviour, which occurs when the composition of the adsorbed layer changes as faster diffusing molecules (such as albumin) are displaced by proteins with higher affinity for the surface (such as FN or VN or BMP-2); this phenomenon being most pronounced on hydrophilic surfaces (Wilson, Clegg, *et al.* 2005).

1.5.2   Characterisation & Monitoring Techniques for Competitive Binding

1.5.2.1   Principle of Colourimetry (Absorbance)

Colourimetry involves the measurement of a compound or group of compounds present in a complex mixture by making use of the property that when light passes through a particular solution, some wavelengths are absorbed more than others. (Plummer 1987) It is a method widely used for determining the concentration of compounds, and when the compounds themselves are not coloured, they can be made to absorb light in the visible region by reaction with suitable reagents (Gordon 2000). These reactions can be very specific and sensitive.

The depth of colour is proportional to the concentration of the compound being measured, while the amount of light absorbed is proportional to the intensity of colour and hence the concentration (Plummer 1987). This is expressed in terms of the Beer-Lambert law, depicted in Figure 1.24.

$$A = \varepsilon cl; \; A = log_{10}\frac{I_o}{I}$$

Equation 1.4

A is the absorbance, where I_o is the incident beam and I is the emerging beam; ε is the molar extinction coefficient, c is the concentration of the compound in solution and l is the optical pathway in cm.
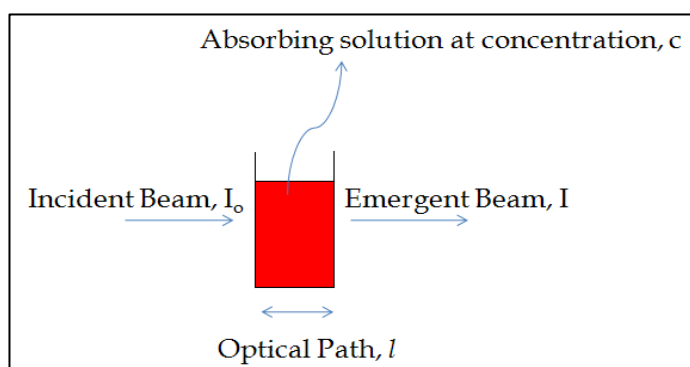
Figure 1.24 – Schematic of the colourimetric analysis

There are several colourimetric assays available to analyse proteins, in terms of determining their concentration, most common ones are Lowry method, also known as Folin-Ciocalteau method, and which also includes the Biuret reaction, BCA reagent

(bicinchoninic acid) and Coomassie brilliant blue, also known as the Bradford method; each have distinct wavelengths, 660, 562 and 595 nm, respectively, thus will react specifically with particular proteins (Gordon 2000).

All bind to proteins *via* an ionic bond to form strongly coloured complexes from blue-purple, strong purple and dark blue, respectively, which then are quantified.

But due to the ionic bond formed all three may be prone to interferences from zwitterionic buffers or media, which is then reflected on their individual sensitivity in the following trend: BCA > Lowry > Bradford; 0.5, 10 and 20 µg cm^{-3}, respectively (Walker "Protein structure, purification and characterisation" 2000).

1.5.2.2 Principle of Fluorimetry

Fluorescence occurs spontaneously in numerous organic molecules, and the decay depends on the time, pH and temperature within the surrounding environment of the fluorescent molecule, which can affect quantum yield, Q (Equation 1.5) and fluorescence intensity (Equation 1.6) and lifetime.

The fluorescence spectra give information about events that occur in less than 10^{-8} s, this ratio is known as the quantum yield, its efficiency, and is expressed as follows:

$$Q = \frac{Amount\ Fluoresced}{Amount\ Absorbed}$$

Equation 1.5

This technique is most accurate at very low concentration, where the intensity of the fluorescence (I_f) is related to the intensity of the incident radiation (I_o), expressed as follows:

$$I_F = 2.3 I_0 \varepsilon_\lambda c d Q$$

Equation 1.6

where c is the concentration of the fluorescing solution, *d* is the light path in cm, ε_λ is the molar extinction coefficient for the absorbing material at wavelength (λ) in dm^{3}mol^{-1}cm^{-1}(Gordon 2000).

It is a process that occurs upon transitions from the lowest spin singlet energy level (S_1) to the ground state (S_0), illustrated as **F** in Figure 1.25.
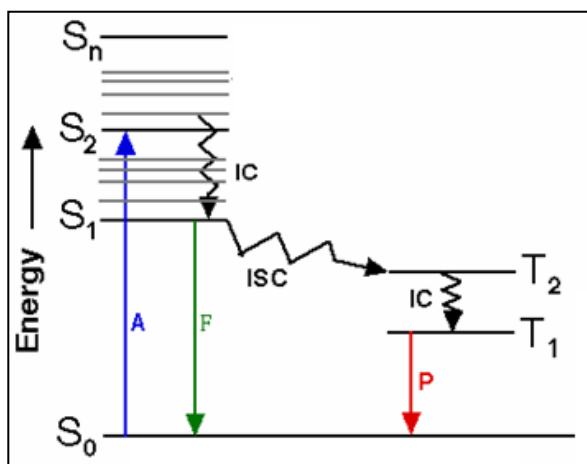
Figure 1.25- Modified & Simplified Jablonski diagram, the blue line is the photon adsorption (A), the green line represents the fluorescence emission (F), the red line represents the phosphorescence (P; a rare event), S is the singlet state, T is the triplet state, IC is the internal conversion and ISC is the intersystem crossing. (Herman 1998)

Fluorescence is also prone to quenching, which decreases quantum yield, Q. It can occur by interaction with the solvent and other molecules in the solution. Another event, which can occur, is called "delayed fluorescence", which involves the transition from T_1 back to S_1 and relaxing back to S_0 (also known as G_0). **IC** and **ISC** are non-radiative deactivation processes.

Fluorochromes, commonly used with proteins, are chosen as to readily form covalent links with amine groups on lysine residues (Thorpe and Thorpe 2000). Others may also be used depending on the kind of bond formed with the protein under investigation. The fluorescein and its derivative, fluorescein isothiocyanate (FITC) (Abuelyaman, Hudig, *et al.* 1994), or the rhodamine and its derivative, Texas red (TXR) (Titus, Haugland, *et al.* 1982) both illustrated in Figure 1.26 have been extensively used because of their reactive groups, which covalently form to make thiourea and sulfonamide bonds, respectively. FITC emits in the green, while TXR emits in the red regions of the visible spectrum. They are non-destructive to proteins and non-toxic to cells during *in vitro* or *in vivo* studies. Also, they have high quantum yields, in the order of 0.85 and 0.88, respectively, compared to their respective precursor, fluorescein and rhodamine B at 0.79 and 0.71 (Myers 1980; Umberger and Lamber 1945). Both fluorophores can be

stored for a long period of time without any loss of fluorescent intensity under appropriate conditions.
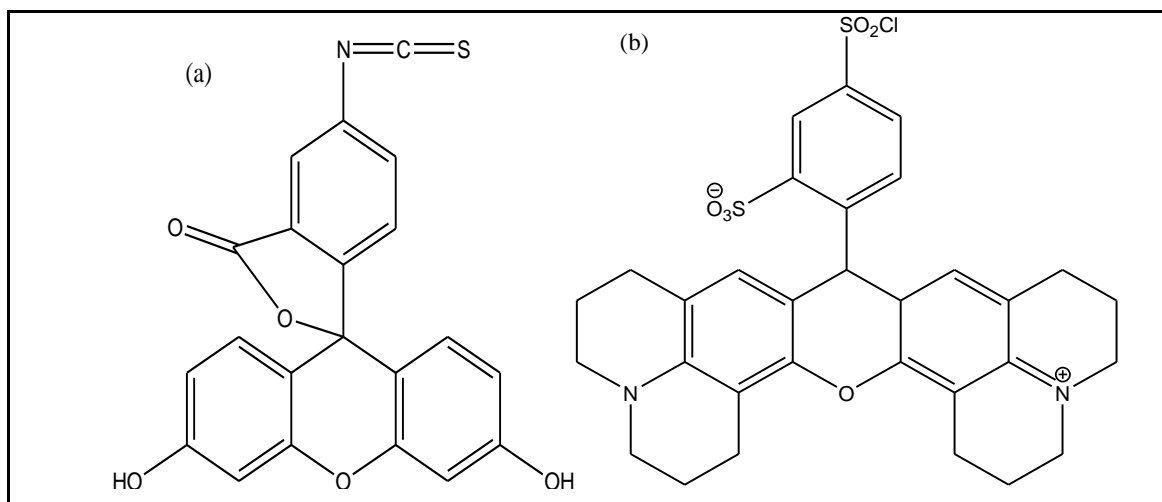
Figure 1.26- Chemical Structures of (a) Fluorescein isothiocyanate-FITC & (b) Texas red-TXR

Other available fluorochromes are fluorescent proteins, also known as the visible fluorophores. The most common and widely used of these are green fluorescent proteins (GFPs) (dos Remedios and Moens 1999; Megley, Dickson, *et al.* 2009). They usually emit in the green region of the visible spectrum and require little synthesis, which allows for good quantitative data to be collected for *in vivo* or *in vitro* work (Maddalo and Zimmer 2006). Natural fluorophores are also available; again they require very little synthesis, they include the fluorescent amino acids tyrosine, (Massip, Riollet, *et al.* 2002) tryptophan and phenylalanine found in proteins, as well as some enzyme cofactors. They can be used to study cellular dynamics and proteins; however the presence of these residues in proteins means they can also give unwanted background emission known as "auto-fluorescence", which then needs to be separated from the desired signal, if other labels are used. All three have low quantum efficiencies in the order of 0.14, 0.13 and 0.02 (Lakowicz 1999), respectively, which can be seen as insignificant when quantum efficiency ranges from 0 to 1. Also they emit in the ultra-violet region (280-350 nm), which can be very difficult to work with. Therefore, they are not useful for this study, as it is a time-dependent study with the necessity for strong fluorescence properties.

Monitoring and characterising protein adsorption and desorption behaviour on surfaces is an important factor into quantitatively and qualitatively collecting information on the mechanism and processes that occur between an implant and a material's surface. It allows improving and increasing the biocompatibility of the material as an implant, further expanding our understanding of the processes during protein adsorption. In this sub-section, electrophoresis, radiolabelling and assaying kits will be discussed, as they are the most commonly used methods. There are other methods of competitive proteins analysis such as ellipsometry which requires no labelling of the protein (Elwing 1998), however adsorbed antigens are required to detect the proteins. This type of quantification also requires a high degree of operating skill and the expensive instrument, or cell detachment method (Anselme, Noel, *et al.* 1999; Ellingsen 1991).

1.5.2.3 Principle of Electrophoresis

To date the only method for true competitive analysis is electrophoresis (Matsuura , Hosokawa*, et al.* 2000; Takami, Yamane*, et al.* 1998), often used in conjunction with staining reagents (i.e. coomassie or silver) to image proteins (Ellingsen 1991) for microscopic work, however, quantification by this route requires a high degree of operating skill.

Electrophoresis is a simple and highly sensitive tool. The separation by electrophoresis is based on the fact that biological molecules carry an electric charge, the magnitude of which depends on the molecule under investigation, and the pH and composition of the supporting medium (Plummer 1987).There are several supporting media such as paper or agar gel, but the most frequently used is polyacrylamide gel, often referred to as PAGE, (Plummer 1987; Walker "Electrophoresis techniques" 2000) used in conjunction with sodium dodecyl sulfate (SDS) an anionic detergent. SDS-PAGE is extensively used as a method to analyse protein mixtures, depending on the percentage of PAGE used separating proteins ranges depending on the molecular size of the proteins. This process, however, requires the denaturation of proteins to be fully analysed.

1.5.2.4   Principle of Radiolabelling

It is a method, also known as radioimmunoassay (RIA) (Kao 1999; Kao, Hubbell, *et al.* 1999), that involves labelling cells or proteins with radioactive elements such as iodine isotopes (^{125}I- and ^{131}I-labels) bound to proteins (Fabrizius-Homan and Cooper "A comparison of the adsorption of three adhesive proteins to biomaterial sufaces" 1991; Fabrizius-Homan and Cooper "Competitive adsorption of vitronectin with albumin, fibrinogen, and fibronectin on polymeric biomaterials" 1991). This kind of labelling is most commonly used for antigens used as tracers in the radioimmunoassay applications, quite precise, accurate and economical. However, the iodination solution conditions are considered harsh, and only available for proteins containing tyrosine residues. (Bolton and Hunter 1973) Also it is difficult to automate, takes relatively long time and dose-response curve covers only a relatively narrow range of the analyte concentration. (Thorpe and Thorpe 2000) This shows that only a few selected proteins can be used and there is also a danger that protein damage may occur, which may lead to loss of sensitivity of the assay system.

1.5.2.5   Assaying Kits

Another method is using kits prepared by manufacturers such as Invitrogen (Quant-IT kit), R&D Systems (Quantikine: a BMP-2 specific kit) and others, which have detection limits and set procedures. Kits fall broadly into two categories, enzyme-linked immunosorbent assay (ELISA) or total protein type assays, where both colourimetric and fluorometric tools are employed. The latter assays all proteins present irrespective of species or conformations. ELISA, on the other hand, is limited to measurement of specific protein and can be conformation dependent. Therefore in order to carry out a competitive study multiple analyses must be performed. In addition the two-step nature of the ELISA methodology makes it susceptible to human errors such as pipetting stages and aspiration steps.

1.6   Thesis Hypotheses

The hypothesis of this thesis is that physiochemical differences in SA and HA modulate competitive protein adsorption in a manner which contributes to the enhanced osteogenic activity of the SA material. In order to test this hypothesis a series of sequential studies were planned and are presented in this thesis as chapters 2 to 6.

Chapter 2: Materials Production.

The total characterisation of the biomaterials in all the morphological forms, powders, dense discs and porous granules is to be determined. The aim is to show that hydroxyapatite (HA) and silicate-substituted hydroxyapatite (SA) have similar densities when in the dense discs and porous granules forms. They both have the chemistry that is expected of them to be confirmed by powder composition characteristics with the correct position of the phosphate or silicate group, surface analysis and the surface topography of the specimens. Samples produced here closely represent those of pre-existing specimen used for clinical procedures (i.e. Apatech), and thus represent real samples that would gave rise to analysis and trend that could be related to real situations.

Chapter 3: Probe Manufacture.

The synthetic route for the fluorescent labels is to be decided using compounds that are non-toxic to proteins or cells, strongly fluorescent and able to covalently attach to proteins.
The synthetic route needs to be simplistic and reproducible for each of the fluorescent labels. The fluorescent labels need to show strong fluorescence in different media, and a similar fluorescence once covalently attached to proteins.

Chapter 4: Single species probe validation.

This work is to be done using bovine serum albumin (BSA), as it is an inexpensive protein, present in abundance in the body at a physiological level in the working range

of most commercial kits such like the Quant-IT kit and involved in many bone processes. Experiments are to be set up against the probe labelled BSA at various conditions. Also, having the protein directly attached to the probe will allow for the qualitative analysis to be undertaken. The protein morphology on the dense discs surface, at several immersion time points, can be discerned and help show the possible differences that may occur on the two different biomaterials in the different media.

Chapter 5: Methodology refinement.

Bone morphogenetic protein-2 (BMP-2) is to be set up in 2 experiments using a growth factor specific kit (Quantikine, R&D systems) and the probe, and determine the binding affinity on the biomaterials' porous granular form. Here the kit works on the basis of colourimetry compared to the Quant-IT kit in Chapter 4, which works on the basis of fluorescence, the same as the probe. This study is to be undertaken to determine the influences and preferences of BMP-2 adsorption and desorption processes on the different biomaterials; and the media used; to establish what the important or pronounced factors to the behaviour are?

Chapter 6: Competitive Binding Studies.

In this chapter, all proteins are to be evaluated at their respective physiological amounts in various media at 37 ^{o}C.

The initial set up involved two independently labelled proteins in solution. However, unexpected results obtained when performing competitive studies with dual labelled probes lead to additional studies into the protein conformation and necessitated modification of the methodology for the studies.

All research findings and conclusions can then be found in Chapter 7 for a summary of the behaviour of the physiochemical differences observed in SA and HA modulated to competitive protein adsorption.

Chapter 2.   SYNTHESIS & CHARACTERISATION OF THE BIOMATERIALS

2.1   Background

Hydroxyapatite (HA) and its other ion-substituted products such as silicate-substituted hydroxyapatite (SA) are already commercially available (Apatech ltd, Biomet or Ceramisys) and have been shown to be efficient and successful as bone grafts substitutes (BGS) towards bone repair (Hing, Revell*, et al.* 2006). The material's bioactivity and biocompatibility are linked to environmental factors such as proteins and other cells present and structural factors, but also the physiochemical properties of the materials itself (Hing, Annaz*, et al.* 2005).

The work of several researchers has shown that the surface physiochemical properties such as surface roughness (Thomas, McFarland*, et al.* 1997), surface area (Harding, Rashid*, et al.* 2005), surface charge (Yin, Liu*, et al.* 2002), porosity (Hing, Best*, et al.* 1999) and chemistry (Gibson, Best*, et al.* 2002; Hing 2005; Thomas, McFarland*, et al.* 1997), of the implant (BGS) to be of great importance as well as their interactions with the composition of the surrounding environment. These studies have generated observed differences in cell adhesion as each factor affected the bioactivity and thus biocompatibility of the material *in vivo* and *in vitro* in different ways (Ducheyne and Qui 1999). For example, a Ca/P ratio of 1.67 is the optimum ratio to which stoichiometric HA forms as a one phase product, which was also found to be true when forming SA (Gibson, Best*, et al.* 1999; Hing, Gibson*, et al.* 1998) where enhanced bioactivity was achieved (Patel, Best*, et al.* 2002). Lower or higher ratios resulted in impurities, which often lead to poorly calcined or sintered samples (Gibson, Ke*, et al.* 2001; Patel, Gibson*, et al.* 2001), that changed the biomaterials' surface area and charge, the packing of the crystallites, the roughness, and density, which subsequently have an effect on the adsorption property of the proteins to that surface (Barralet, Best*, et al.* 2000).

Thus, it will be of great importance to characterise HA and SA so that microstructure is similar.

2.2   Experimental Methodology

Silicate-substituted hydroxyapatite (SA) and stoichiometric hydroxyapatite (HA) powders were synthesised at Apatech ltd. The powders were characterised as received and calcined. The powders were then processed in the form of dense discs and porous granules with matched densities and surface morphologies between the SA and HA specimens.

2.2.1   Materials Synthesis

HA and SA Powder production

Deionised water (DIW, 100 L) was added to the precipitation vessel with a 300 rpm overhead stirrer.

For the preparation of SA powder; $Si(OAc)_4$ was weighed, added to DIW vessel, left to stir completely before the addition of $Ca(OH)_2$ (see Table 2.1) to the reaction vessel and left stirring (see Figure 2.1) at room temperature (RT). Ensuring all $Ca(OH)_2$ was transferred, the equipment was washed down. Both 25 L mixing vessels were filled with DIW (20 L) with a 150 rpm mechanical stirrer. The ammonia was added before the phosphoric acid (H_3PO_4) addition, the mass added was recorded and the volume of ammonia added calculated, using the density value of 0.89 g/ml.

Table 2.1 – Amount required of reactants to synthesise HA and SA powder

Biomaterials	Reactants	Mass required (g)
HA	Calcium hydroxide, $Ca(OH)_2$	3,927
	Orthophosphoric acid, H_3PO_4	3,709
SA	Calcium hydroxide, $Ca(OH)_2$	3,928
	Orthophosphoric acid, H_3PO_4	3,441
	Silicon acetate, $Si(OAc)_4$	395.0

For the preparation of the HA powder; $Ca(OH)_2$ was added to the reaction vessel, again, ensuring all $Ca(OH)_2$ was transferred, the equipment was washed down. Both 25 L mixing vessels were filled with DIW (20 L) with a 150 rpm mechanical stirrer.

After 15 minutes, the stirrers were turned off and tubing was run from the 25 L vessels through a peristaltic pump (5001-5004 type, Heidolph) into the precipitation vessel with the pump rate set at 20 arbitrary units and the acid addition was begun. A bottle of ammonium hydroxide (2.5 L) was placed on a balance and the tubing was inserted into the bottle and fed through the peristaltic pump head to the precipitation vessel, then the balance was tarred. Using the calibrated time switch, the ammonia was set to be added at an arbitrary rate of 200, for a period of 4 minutes, starting 10 hours and 40 minutes after the start of the phosphoric acid addition

Figure 2.1 – Experimental set up for the manufacture of HA/SA Powder (Pilot plant in Apatech ltd)

After the phosphoric acid solution addition was completed (next day for HA), the mixing vessels were rinsed with DIW (250 ml), and the tubing was flushed.

The precipitation vessel was then left to stir for a further 2 hours, followed by the ageing process for a minimum of 10 hours.

Filtering, Drying, Disc Milling and Calcining Powder

The process is depicted in Figure 2.2 top left image shows the precipitate being filtered, using a horizontal filter with a compression system and pump at a pressure of 600 MPa.

The cakes were then retrieved and chopped into 2 cm cubes to be placed in separate trays of equal weigh compared to the bulk sample. Once all trays were filled, they were placed in the drying oven for over 4 days set at 80 ^{o}C (see Figure 2.2, top right image).

The chunks of dried HA/SA from the oven were crushed into smaller pieces, using a pestle and mortar and passed through a sieve. The small pieces were then fed to the disc mill machine 1 kg at a time to be crushed to HA/SA powder of a particle size of 300 µm. The HA powder was then collected into a plastic container (10 L), labelled with a batch number and dated (see Figure 2.2, bottom images).

Figure 2.2 – Visual scheme of the filtering, drying, disc milling process of the powder

For the calcination, 200 g of material (SA/HA) were transferred into a ceramic dish, which was then placed in a Carbolite Muffle RHF furnace (Carbolite, UK) set at 700 ^{o}C. The powder was then left to calcine for up to 4 hours. Once cooled, the powder was transferred to glass-sealed containers, labelled and dated.

Porous granules (PG) Samples Preparation

To a mill pot, the calcined (500 ^{o}C) powdered HA or SA (509-511 g) was transferred into a plastic container (2.5 kg) along with DIW (798-802 g) and mixed into a paste. To

this mixture milling media (4363-4437 g) were added. The container was sealed shut using nuts and bolts to avoid leaking, and the whole container was transferred onto a ball mill machine and spun at a rate of 270 rpm for 30 minutes. After the 30 minutes, the mill pot was opened in order to add the PVA (90-92 g) and sealed shut again. (see Figure 2.3, top images).The container was once again placed on the ball mill machine and spun at a rate of 270 rpm for 3 hours. After 3 hours, the spinning was stopped. The foam was sieved to remove all milling media. Once removed, the foam, porous material was transferred to moulds and dried for over 48 hours. Once dried, the foams were removed from the mould and transferred into ceramic deep trays to be sintered at 1260 ^{o}C for HA and 1300 ^{o}C for SA in a eurotherm furnace (Lenton, UK) for a dwell time of 4 hours (see Figure 2.3, bottom left image).

Figure 2.3 – Visual scheme for the foaming process for the production of PG

Granulation of HA foams was achieved using 3 sets of sieves (5 mm, 2 mm and 1 mm). Each batch was weighed and transferred into the top of the sieve column, vigorously shaken until no further granules went anywhere (see Figure 2.3, bottom right image). The larger chunks, which did not sieve through, are then transferred into a bowl. A little at a time, they were crushed to smaller pieces and passed through sieve again. This process was then repeated until no further large chunks of HA or SA were left in the top

sieve tray. When completed, each layer (2-5 mm; 1-2 mm; <1 mm) was weighed and volume recorded of the final porous granules (PG).

Dense Disc (DD) Samples Preparation

Dense discs (DD) were prepared by pressing 1.00 g or 1.60 g of SA/HA powder in a 16 mm or 20 mm steel die, respectively (as illustrated in Figure 2.4). The force used ranged from 1.50, 1.75 and 2.00-tonne pressure, corresponding to powders pressed at loads of 15KN, 18 KN and 20 KN. Using Equation 2.1, these loads can be expressed in terms of MPa for both steel die systems as shown in Table 2.2, where r is the radius of the die system.

$$Pressure = \frac{Load \; (1016.046)}{\pi r^2}$$

Equation 2.1

Table 2.2 –Pressures used on the pressed discs for each steel die system

Load / KN	Pressure / MPa	
	16 mm steel die	20 mm steel die
15	75.8	48.5
18	90.9	58.2
20	101.1	64.7

The discs were then sintered in Carbolite Furnaces (RHF1600 or RHF1400, Carbolite, UK) at temperatures ranging from 1200-1375 ^{o}C for the SA and 1150-1300 ^{o}C for the HA samples with a ramp rate of 2.5 ^{o}C per minute, dwell time of 120 minutes and a cooling rate of 10 ^{o}C per minute to ambient temperature.

Figure 2.4 – Visual scheme of the compressing of biomaterial powder into DD

2.2.2   Materials Characterisation

X-ray Diffractometry (XRD)

XRD patterns were obtained using a XPERT-PRO PW3064/60 (Philips, UK) with CuK$_{\alpha1}$ (λ = 1.5406 nm) and CuK$_{\alpha2}$ (λ = 1.5444 nm) radiation operating at 45 kV and 40 mA. Data were collected over a 2θ range of 5° to 120°, with a step size of 0.03° and a dwell time of 200 s.

Crystallography Parameters were obtained using the XRD patterns in conjunction with 3 programs. Xpert HighScore Plus software along with the ICDD database was used to obtain the unit cell volume, and the values for the *a*, *b* and *c* axes using the peak list with the Miller indices of known stoichiometric HA. Pickpx2 software (developed in-house, UK) enabled *xrdml* and *uxd* files of the XRD data to be converted into corresponding 2-theta values and their d-spacing along with peak intensities. And the UnitCellWin software (developed by T.J.B. Holland (Holland and Redfern 1997), UK) evaluated all information (Miller indices and 2-theta data) and calculated the unit cell parameters ($a = b \neq c$ and cell volume).

In order to quantify the unit cell parameters, two methods were used, where one involved using the best fit values to that of stoichiometric HA and its Miller indices (method 1), and the other involved using the first 50 values from the XRD patterns of the samples and the HA Miller indices, as template (method 2).

Fourier Transform Infrared Spectroscopy (FTIR)

FTIR-Photoacoustic spectroscopy (PAS) spectra were obtained using a Thermo Nicolet 8700 spectrometer in conjunction with a PA Cell-MTEC Model 200 with KRS-5 sample chamber window. Spectra were obtained at a resolution of 4 cm^{-1}, averaging 128 scans, operating from 4000 to 400 cm^{-1}. The sample chamber of the PAS cell was purged with helium gas prior to analysis.

Reference samples for HA and SA sintered at 1250 and 1300 ^{o}C were analysed using a Spectrum GX (Perkin Elmer, UK) with the spectrum v5.3 software and a SpecAc attachment. These spectra were obtained at a resolution of 4 cm^{-1}, averaging 10 scans, operating from 2000 to 450 cm^{-1} in transmittance (% T) at an interval of 1 cm^{-1}.

X-ray Fluorescence (XRF) Spectroscopy

For the XRF analysis, samples were sent to CERAM Research (Stoke-on-Trent, UK), as sintered granular samples. Samples were analysed using the XRF Panalytical (Axios).

Surface Area Analysis & Porosimetry

A micromeritrics FlowPrep060 degaser, multipoint analyser was used to measure the surface area (S.A.) of both powdered and granular samples of the biomaterials, as shown in Figure 2.5. Surface area values were obtained using helium (He) at 15 psi with an evacuation rate of 300 mmHg/min. Prior to the analysis samples were dried at 200 ^{o}C overnight with nitrogen (N_2) at 15 psi.
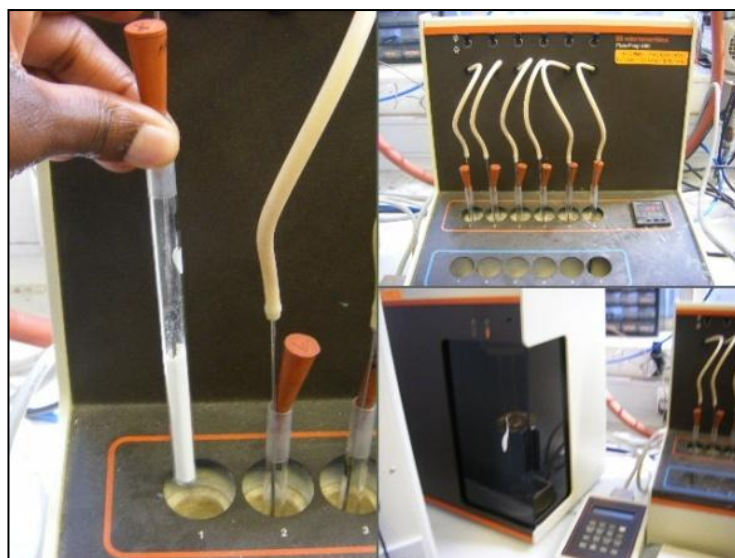
Figure 2.5 – BET instrument set up in the IRC at QMUL

Strut porosity of the porous granules was confirmed by embedding porous specimens in resin mixture; 15 parts resin (EpoFix Resin, Struers, UK) for 2 parts hardener (EpoFix Hardener, Struers, UK) and left to slowly set for 8 hours. The specimens were then polished on diamond paper from P80 to P220, and then imaged using SEM. The strut porosity was then determined using ImageJ 1.44i (National Institute of Health, USA).

Scanning Electron Microscopy (SEM)
and Energy Dispersive Spectroscopy (EDS)

An INSPECT F (FEI, UK) field emission gun scanning electron microscope (FE-SEM) equipped with an energy dispersive X-ray spectrometer (EDS) was used to observe morphology and determine elemental distribution of silicon (Si) at a high resolution and accelerating voltage of 10 kV with samples coated with gold for SEM imaging only, while carbon was used for the analysis of samples for EDS.

Density Measurements

Two methods were used for the density measurements, in order to obtain precise and accurate data from both biomaterials. Method-One involved using a micrometer; and method -Two involved using Archimedes' principle.

Method-One: The dense discs were measured using a micrometer (RS, Mitutoyo, Japan), along the diameter and height in triplicates, followed by weighing on an analytical balance.

Method-Two: The specimens were weighed in a dry condition (W_{dry}) in triplicate using an analytical plus electronic balance (Ohaus, Leicester, UK). The specimens were then placed in boiling deionised water for 30 minutes (60 minutes for porous samples) to ensure all open pores were filled with water and left to cool, still submerged in water. The specimens were weighed using the density AP solids kit (Ohaus, Leicester, UK), three times submerged in deionised water (W_{sub}) of known temperature, and then three times in the wet state (W_{sat}). The apparent and real densities of specimens were calculated using Equation 2.2 and Equation 2.3, respectively. The former takes into account both the open and closed porosity of the material, while the latter only considers closed pores.

$$D_{apparent} = \left(\frac{W_{dry}}{W_{sat} - W_{sub}} \right) \rho H_2 O$$

Equation 2.2

$$D_{real} = \left(\frac{W_{dry}}{W_{dry} - W_{sub}} \right) \rho H_2 O$$

Equation 2.3

Equation 2.4 and Equation 2.5 were used to determine the closed and total porosity, respectively.

$$CS\mu = \left(1 - \frac{D_{real}}{\rho HA} \right) \times 100$$

Equation 2.4

$$TP = \left(1 - \frac{D_{apparent}}{\rho HA} \right) \times 100$$

Equation 2.5

An accepted value of 3.156 g/cm^3 (Akao, Aoki, *et al.* 1981) was used for the theoretical apatite density (ρHA); although in silicate substitution a slight shift in the density of SA may be expected, equal values were used for both. For all equations described above: *D* is density, *W* is weight, ρH_2O is the density of deionised water at a given temperature, *CSμ* is the closed strut porosity and ρHA is the theoretical density of the apatite. For dense specimens, W_{dry} should equal W_{sat} (as there should not be significant amounts of open porosity) thus measuring W_{dry} and W_{sat} only is needed to calculate the real density (D_{real}) to determine the percentage of closed porosity.

Atomic Force Microscopy (AFM)

Atomic force microscopy (AFM, NTegra with NT-MDT set up, Russia) of the samples was performed using a silicon, N-type cantilever with a working range of 0.01-0.025 ohm/cm, a frequency range of 145-230 kHz and a spring constant range of 20-95 N/m.

2.3   Results

2.3.1   Chemical Analysis

The biomaterials' phase purity and crystallinity, the presence of silicate and phosphate groups and the design level of silicate incorporation were confirmed using XRD, FTIR and XRF, respectively.
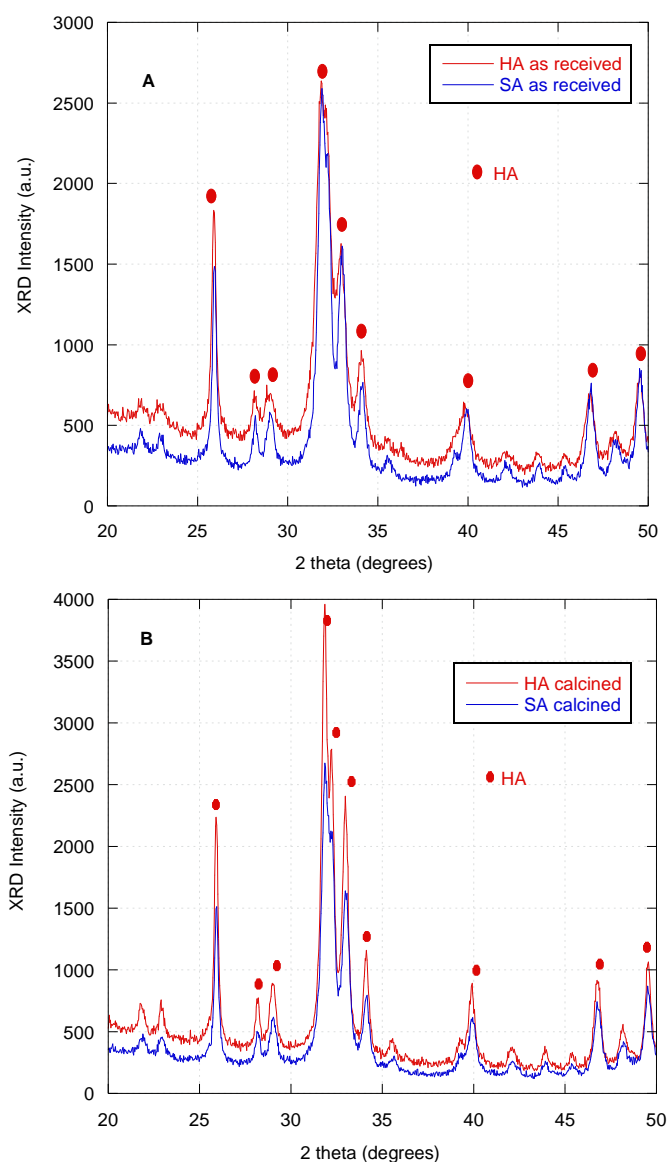
Figure 2.6 - Comparative XRD Patterns of SA & HA samples (a) as-received and (b) calcined in the range of 25 to 40 degrees

XRD (Figure 2.6 A and B) confirmed the phase purity of both the HA and SA (A) as-received and (B) calcined samples. There was no presence of either *β-TCP* or CaO

impurities, as they should be observed at around 31.2 ^{o} and 37.8 ^{o}, respectively. (Hing, Gibson, *et al.* 1998; Mostafa 2005)
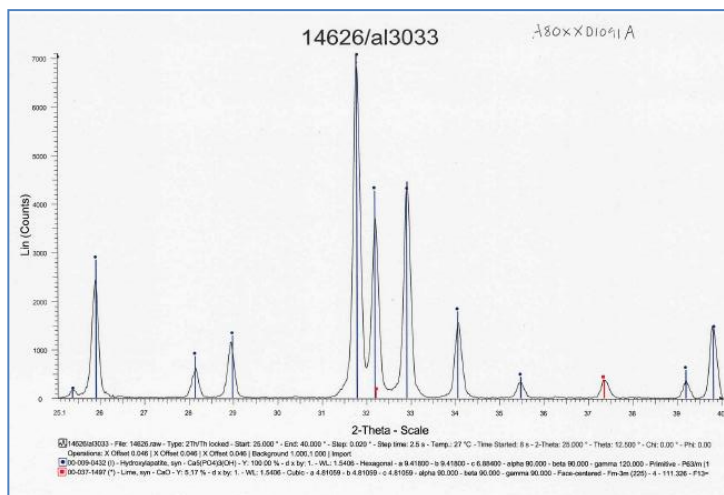
A
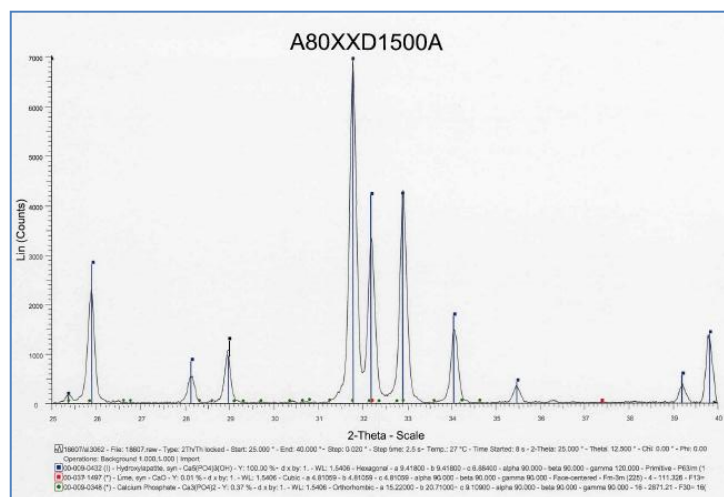
B

Figure 2.7 – XRD spectra of the (a) A80XXD1091A and (b) A80XXD1500A hydroxyapatite sample with and without impurities present, respectively.

Figure 2.7 A and B show the XRD patterns obtained of the HA synthesised at Apatech ltd, where the first batch (A) resulted in a HA product with a 5% CaO impurity, and the

latter (B) with the use of a corrected protocol resulting in the optimum stoichiometric HA produced. (Appendix 1for all raw data from CERAM)

The phase purity was further confirmed by the XRF analysis, as shown in Table 2.3, where for HA #1 sample (A) the Ca/P was higher at 1.75 than the expected value of 1.68 for HA #2 sample (B).

Table 2.3 – XRF data obtained for HA and SA powders

	wt %			Molar ratio	
Sample	CaO	P_2O_5	SiO_2	Ca/P ratio	Ca/(P+Si)
HA #1	57.36	41.47	-	1.75	-
HA #2	53.70	40.57	-	1.68	-
SA	56.37	40.47	1.73	1.76	1.68

XRF of the powders further confirms that the substitution occurred due to the presence of 0.8 wt% silicon for the SA sample as it allowed for the Ca/P ratio to be determined (see Table 2.3), which is very important when the powder undergoes further heat-treatments for the formation of the two morphological forms of the biomaterials.
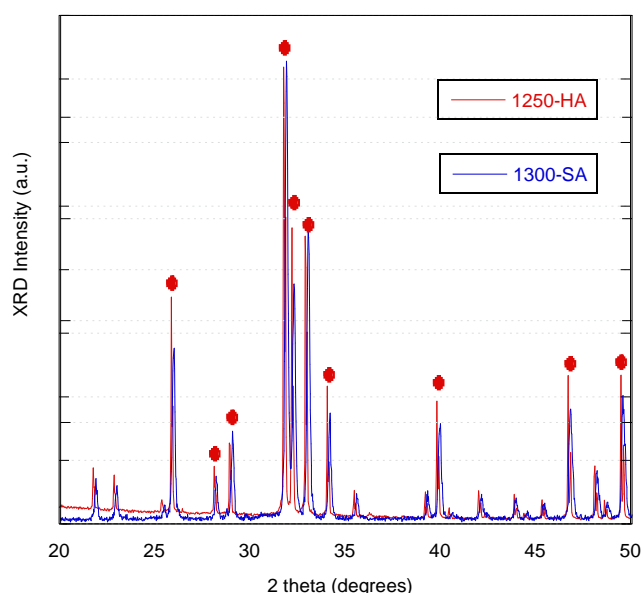
Figure 2.8 - XRD pattern of HA and SA over the range of 20 to 50 2θ

Figure 2.8 shows the XRD patterns of HA and SA sintered at their optimum sintering temperatures of 1250 and 1300 ^{o}C, respectively. No second phases could be identified

in both materials, where position, intensity and peak widths were not noticeably different, suggesting similarity in the level of crystallinity in the biomaterials.

Further XRD patterns were obtained at different sintering temperatures and all depicted in Figure 2.9 and Figure 2.10, both for SA and HA powdered samples.
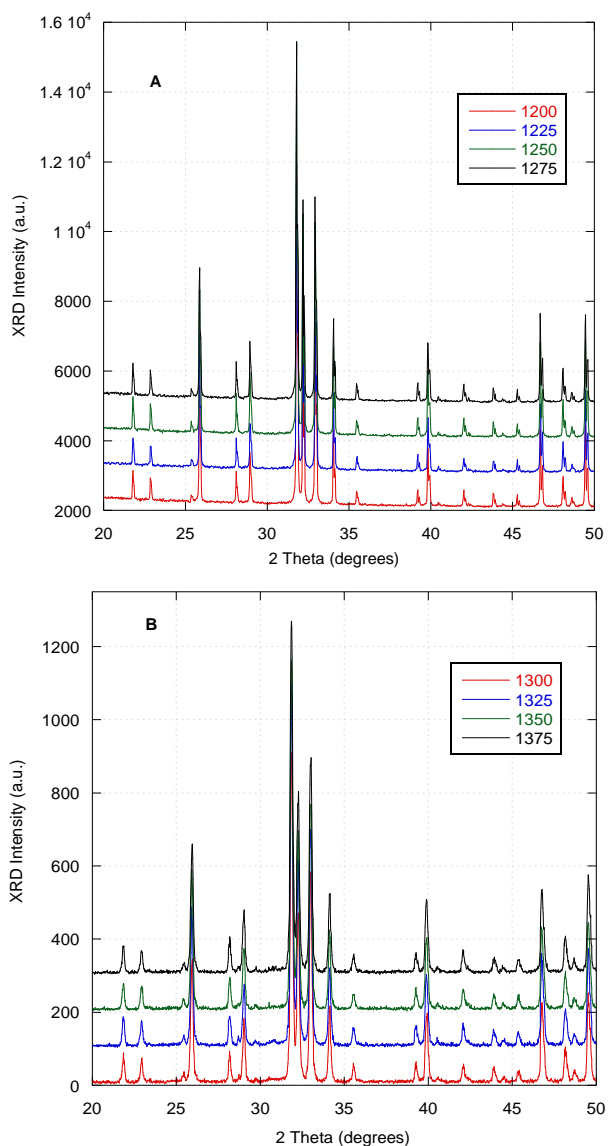
Figure 2.9 – XRD spectra of SA in the range of 20 to 50 2θ at all sintered temperatures (a) 1200-1275 ^{o}C and (b) 1300-1375 ^{o}C
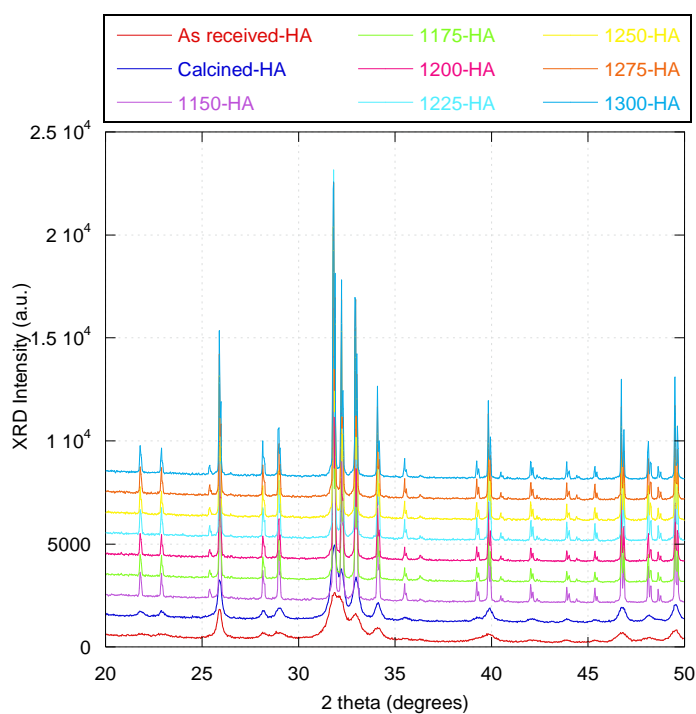
Figure 2.10 – XRD spectra of HA between 20-50 degrees at all sintered temperatures (1150-1300 ^{o}C)

The XRD spectra obtained show little differences in peak pattern as sintering temperature was increased to produce a more crystalline material. The differences were more evident, when the crystallographic parameters were determined.

For the crystallographic parameters, two methods were used, where method-1 involved using the first 30 to 50 values from the XRD patterns of the samples against the HA Miller indices, while method-2 involved using the best fit data against the HA Miller indices as template.

SA crystallographic parameters at all sintered temperatures ranging from 1200 to 1375 ^{o}C are tabulated in Table 2.4 and Table 2.5 for method 1 and 2, respectively.

And for the HA crystallographic parameters at all sintered temperatures ranging from 1150 to 1300 ^{o}C are tabulated in Table 2.6 and Table 2.7, for method 1 and 2, respectively.

Table 2.4 – Unit Cell parameters for all sintered samples of SA using method-1

Sintered Temperature / $^{\circ}$C	a/ Å	c / Å	Unit Cell Volume / Å^3
1200	9.29	6.79	507.63
1225	9.41	6.89	528.18
1250	9.40	6.83	522.39
1275	9.30	6.77	507.52
1300	**9.41**	**6.88**	**527.89**
1325	9.36	6.91	524.90
1350	9.41	6.87	527.00
1375	9.41	6.89	528.38

Table 2.5 – Unit Cell parameters for all sintered samples of SA using method-2

Sintered Temperature / $^{\circ}$C	a / Å	c / Å	Unit Cell Volume / Å^3
1200	10.11	7.33	648.50
1225	10.50	7.56	721.51
1250	9.79	7.09	588.69
1275	9.80	7.08	588.36
1300	**11.39**	**8.02**	**901.40**
1325	11.82	8.45	1023.11
1350	11.25	8.02	879.64
1375	11.81	8.49	1025.90

Method 1 for SA specimen was the better method to use (see Table 2.4 and Table 2.5), as it gave rise to values comparable to the literature (Balas, Perez-Pariente, *et al.* 2003; Gibson, Best, *et al.* 1999; Hing, Revell, *et al.* 2006; Thian, Huang, *et al.* 2006). At 1300 $^{\circ}$C, the appropriate unit cell volume and the axes were calculated; the optimum characteristic of the sample was reached by comparison the values found in literature.

Again method 1 for HA specimen (see Table 2.6 and Table 2.7), was the better method, as it allowed a trend to be observed as temperature increased for the sintering process of the HA material. The crystallographic parameters confirmed that at 1250 $^{\circ}$C the appropriate unit cell volume and the axes were determined; the optimum characteristic of the sample was reached.

Table 2.6 - Unit Cell parameters for all sintered sample of Stoichiometric HA using method-1

Sintered Temperature / ^{o}C	a / Å	c / Å	Unit Cell Volume / Å^{3}
1150	9.42	6.86	527.66
1175	9.41	6.86	526.10
1200	9.42	6.87	527.49
1225	9.41	6.87	527.22
1250	**9.41**	**6.88**	**527.09**
1275	9.41	6.85	525.48
1300	9.41	6.86	526.44

Table 2.7 – Unit Cell parameters for all sintered samples of Stoichiometric HA using method-2

Sintered Temperature / ^{o}C	a / Å	c / Å	Unit Cell Volume / Å^{3}
1150	10.28	7.39	676.91
1175	10.56	7.49	723.59
1200	10.79	7.70	775.62
1225	10.37	7.42	690.43
1250	**10.61**	**7.55**	**736.29**
1275	10.58	7.53	730.57
1300	10.52	7.53	722.70

Following the XRD and XRF analysis, the FTIR was undertaken to show the peak position of the phosphate and silicate groups in the biomaterial samples.

Figure 2.11 shows the FT-IR PAS of HA and SA sintered at their optimum temperatures, across the range of 4000 to 400 cm^{-1}. The spectra depict the characteristic hydroxyl group (OH^{-}) at 3570 cm^{-1} on both materials, and a band of adsorbed water on the SA spectra at 3417 cm^{-1}, expected from the substitution within the HA lattice and release of hydroxyl group from the system. Figure 2.12 shows the spectra across the 1400 to 400 cm^{-1}, which is the characteristic region for both the phosphate and silicate ions to be present in. Both are depicted here in red dots for the phosphate and blue dots for the silicate groups.
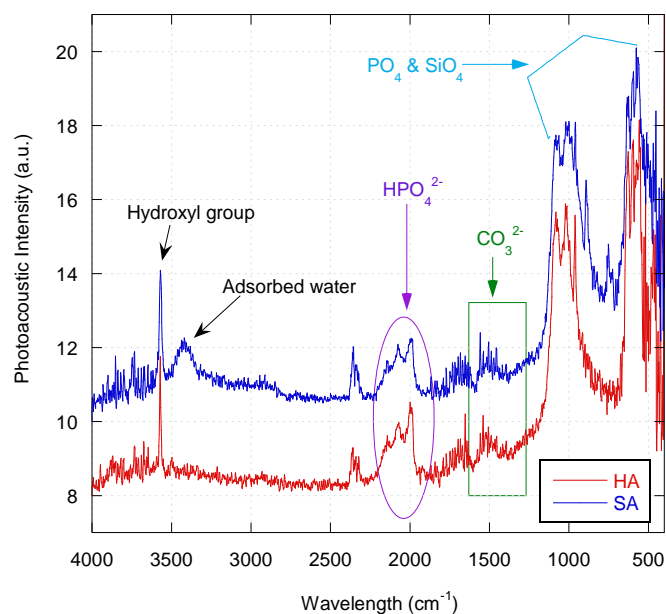
Figure 2.11 – FT-IR spectra of HA and SA between 4000 and 400 cm^{-1}
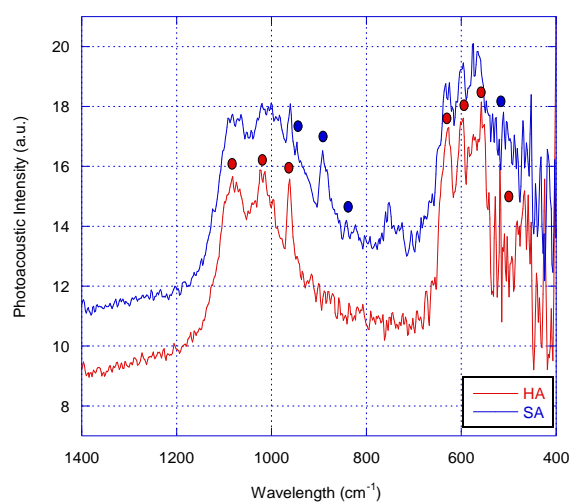
Figure 2.12 – FT-IR spectra of HA and SA between 1400 and 400 cm^{-1} (red and blue dots are associated with phosphate groups in HA and SA, respectively)

Peak assignments can be clearly seen in Table 2.8, in terms of groups, bands and remarks, which are further confirmed through the reference samples analysis, as shown here in Figure 2.13.

Table 2.8 – FTIR peak assignments for silicate-substituted hydroxyapatite, with associated peaks for hydroxyapatite

Groups	Band (cm^{-1})	Notes
Phosphate	507,682	υ_4 PO_4^{3-}
	962	υ_1 PO_4^{3-}
	1032, 1046, 1080	υ_3 PO_4^{3-}
Phosphate	474	υ_1 PO_4^{3-}
Associated with HA	632, 600, 578	υ_3 PO_4^{3-}
Silicate	510	SiO_4^{4-}
	970, 915, 850	SiO_4^{4-}
Carbonate	1250-1500	CO_2^{3-}
Surface adsorbed phosphate	2000-2250	HPO_4^{3-}
Adsorbed water	3300-3500	H_2O
Hydroxyl	3575	υ_1 ^-OH notes
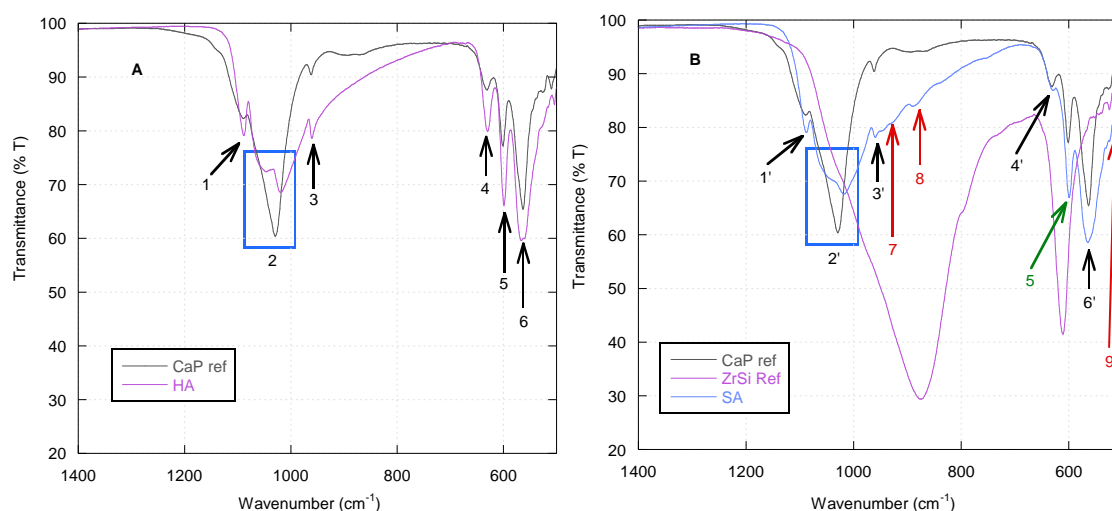
Figure 2.13 – FTIR spectra of reference samples in the range 1400 and 500 cm^{-1} for (a) calcium phosphate with HA and (b) zirconium silicate and calcium phosphate with SA

Figure 2.13A clearly shows where the phosphate group in the calcium phosphate ($Ca_3(PO_4)_2$) sample overlapped with HA at peak positions of 1, 3, 4, 5 and 6 with a broader peak at position 2. While for SA (see Figure 2.13B) there were similarities in phosphate groups at peak positions 1, 2, 3 and 6, but with some ambiguities in peak positions 4 and 5, may be due to the presence of the silicate group. The zirconium silicate ($ZrSiO_4$) reference sample showed a broad peak between 800 and 1000 cm^{-1},

which may result in the presence of the silicate groups at peak positions 7 and 8; the smaller size may be due to the relatively small amount of silicon present at 0.8 wt%. Peak positions 5 and 9 may also result from the presence of the silicate. Overall, the phosphate and silicate group positions shown in Figure 2.12 seemed to correspond to those observed in the reference samples.

FTIR at all sintering temperatures, including as-received and calcined, were performed and shown here in Figure 2.14 for the SA and Figure 2.15 for the HA samples, respectively.

The calcined and as-received SA samples, show broad spectra compared to the samples sintered at higher temperatures, clearly showing the change in the samples' morphology, which was expected as the samples crystallinity increased with increasing temperature. Once the samples were sintered beyond 1200 ^{o}C, it was hard to distinguish a peak position differences between samples.

A similar observation was seen for the HA samples with the calcined and as-received samples also having a broad spectra as shown in Figure 2.15, but overall higher photoacoustic intensities were observed compared to SA samples.
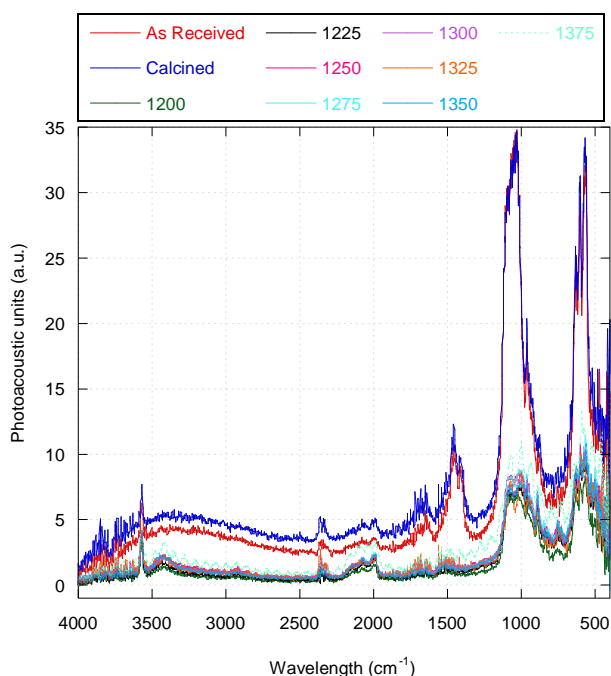
Figure 2.14 – FT-IR spectra of SA between 4000 and 400 cm^{-1} at all sintered temperatures (1200-1375 ^{o}C)
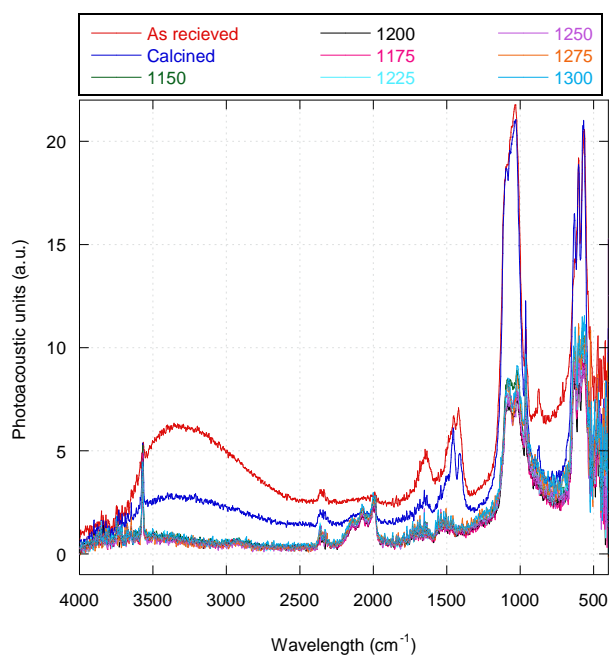
Figure 2.15 – FT-IR spectra of HA between 4000 and 400 cm^{-1} at all sintered temperatures (1150-1300 ^{o}C)

2.3.2 Powder Morphology

The powder morphology was characterised in terms of surface area analysis, particle size and topography *via* SEM. Particle analysis of HA and SA were obtained and tabulated below in Table 2.9 and Table 2.10, as-received and calcined biomaterials, respectively. HA and SA particle sizes were very similar between samples for both treatments, which range agrees with values found in the literature(Gibson, Best*, et al.* 2002; Gibson, Ke*, et al.* 2001).

Table 2.9 – Particle size obtained for the as-received samples

Sample	Particle size (μm)		
	d_{10}	d_{50}	d_{90}
HA	3.97	12.22	108.5
SA	3.82	12.89	114.3

Table 2.10 – Particle size obtained for the calcined samples

Sample	Particle size (µm)		
	d_{10}	d_{50}	d_{90}
HA	3.95	13.10	112.6
SA	3.75	11.93	107.4

The surface area was measured *via* BET and tabulated above (see Table 2.11) for the as-received and calcined samples.

Table 2.11 – BET Surface Area values for the powder apatites

Sample name	Surface Area / m^2g^{-1}
HA as-received	51
SA as-received	68
HA calcined	31
SA calcined	37

The values obtained were lower to the HA values found in the literature (Gibson, Ke, *et al.* 2001) for the precipitate (as-received) samples, but with a similar pattern where SA had a larger surface area than HA. Once calcined, the surface area of the powders was dramatically reduced for both samples with the SA still having the higher value possibly due to the presence of silicon compared to HA. The as-received samples have larger surface area compared to the calcined (700 ^{o}C) samples.

To further characterise the powdered samples, SEM images were obtained to show powders' morphology, as heat-treatment increased as shown in Figure 2.16.
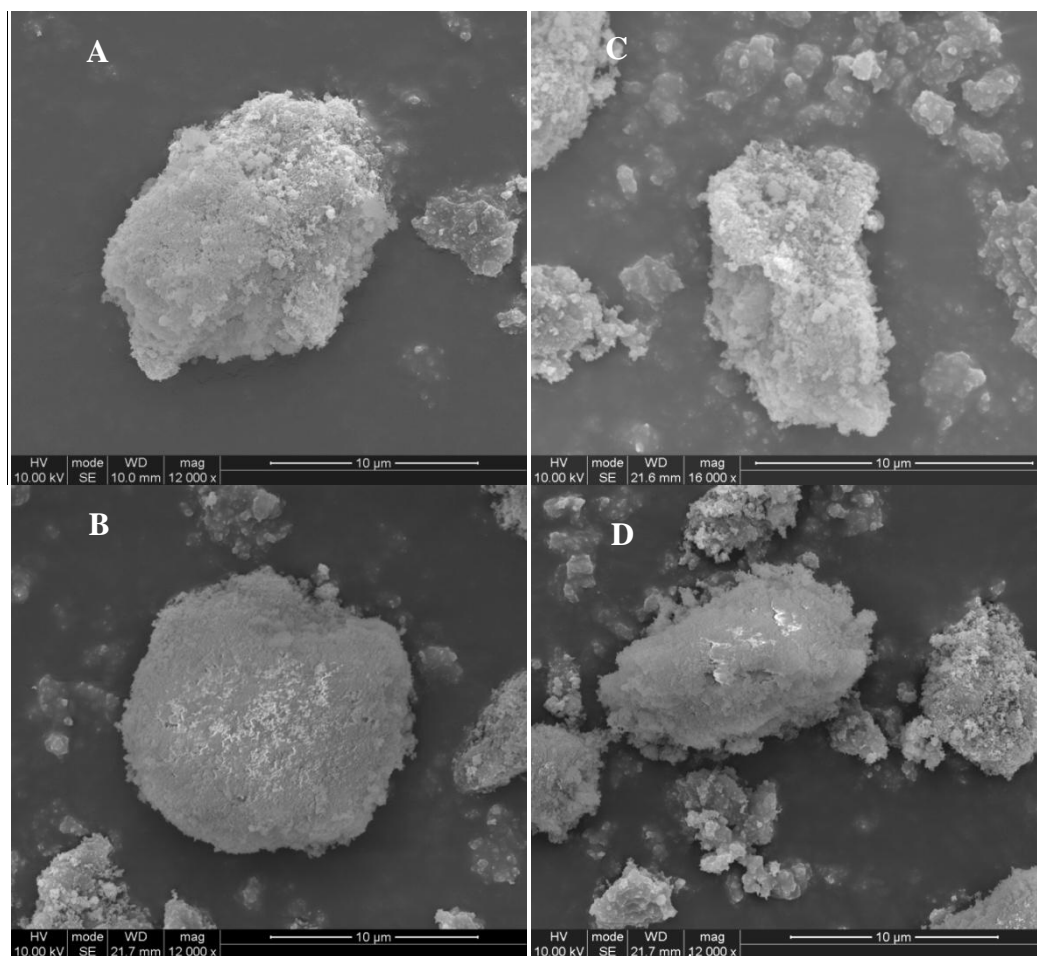
Figure 2.16 – SEM of as-received powders of (a) HA and (c) SA, and calcined (b) HA and (d) SA

2.3.3   Dense Discs (DD) Morphology

The density of the materials was investigated *via* two methods. The first method involved using a micrometer, while the second method, the Archimedes' principle. All measurements made using the micrometer gave rise to inconsistent data, this may reflect the fact that this method assumed that each disc were perfect cylinders (all raw data available in Appendix 2 to Appendix 10). Therefore, the values showed here are all from the Archimedes' principle method, see Table 2.12, and illustrated in Figure 2.17 ; and a summary at the optimum sintering temperature of 1300 ^{o}C shown in Table 2.13 including values for the total porosity of the samples.

Table 2.12 – SAD density at all sintering temperatures, using the Archimedes' principle

Sintering Temperature / ^{o}C	Density at 75.8 MPa ($\pm\sigma$) / gcm^{-3}	Density at 90.9 MPa ($\pm\sigma$) / gcm^{-3}	Density at 101.1 MPa ($\pm\sigma$) / gcm^{-3}
1200	3.049 ($\pm$0.01)	3.057 ($\pm$0.01)	3.092 ($\pm$0.06)
1225	3.064 ($\pm$0.01)	3.085 ($\pm$0.03)	3.086 ($\pm$0.01)
1250	3.070 ($\pm$0.03)	3.085 ($\pm$0.01)	3.092 ($\pm$0.01)
1275	3.086 ($\pm$0.01)	3.090 ($\pm$0.01)	3.106 ($\pm$0.01)
1300	**3.065 ($\pm$0.01)**	**3.089 ($\pm$0.01)**	**3.100 ($\pm$0.01)**
1325	3.068 ($\pm$0.01)	3.100 ($\pm$0.02)	3.098 ($\pm$0.01)
1350	3.067 ($\pm$0.01)	3.097 ($\pm$0.01)	3.121 ($\pm$0.01)
1375	3.073 ($\pm$0.02)	3.098 ($\pm$0.02)	3.109 ($\pm$0.01)
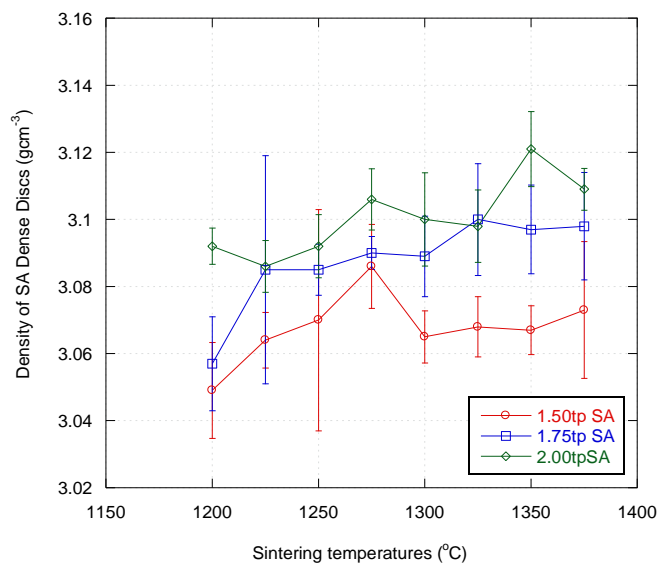
Figure 2.17 – Density of sintered SA at different pressures 75.8 (1.50), 90.9 (1.75) and 101.1 (2.00) MPa, calculated using the Archimedes' principle

Table 2.13 – Average SA-D density sintered at 1300 °C, using the Archimedes' principle

Pressure / MPa	Density ($\pm\sigma$) / gcm^{-3}	Total porosity / %
75.8	3.065 ($\pm$0.01)	3.2
90.9	3.089 ($\pm$0.01)	2.6
101.1	3.100 ($\pm$0.01)	2.9

The density of the HAD produced at 101.1 MPa were not included as the discs produced were brittle and broke up either on removal from the die or during sintering. Therefore only the data of the discs pressed at 75.8 and 90.9 MPa are included, as shown in Table 2.14 and Figure 2.18, with a summary shown in Table 2.15 with values for the total porosity of the samples at the two different pressures.

Dense discs made at the applied pressure of 90.9 MPa resulted in the formation of the best discs with appropriate densities, showing no sign of breakage prior and after the sintering process. As a result, all required discs for all experiments in the following chapters were pressed at 90.9 MPa.

Table 2.14 – HAD density at all sintering temperatures, using the Archimedes' principle

Sintering Temperature / ^{o}C	Density at 75.8 MPa ($\pm\sigma$) / gcm^{-3}	Density at 90.9 MPa ($\pm\sigma$) / gcm^{-3}
1150	3.083 ($\pm$0.01)	3.102 ($\pm$0.01)
1175	3.110 ($\pm$0.01)	3.118 ($\pm$0.02)
1200	3.116 ($\pm$0.01)	3.135 ($\pm$0.01)
1225	3.126 ($\pm$0.01)	3.125 ($\pm$0.02)
1250	**3.120 ($\pm$0.01)**	**3.136 ($\pm$0.01)**
1275	3.126 ($\pm$0.02)	3.131 ($\pm$0.01)
1300	3.117 ($\pm$0.01)	3.128 ($\pm$0.01)
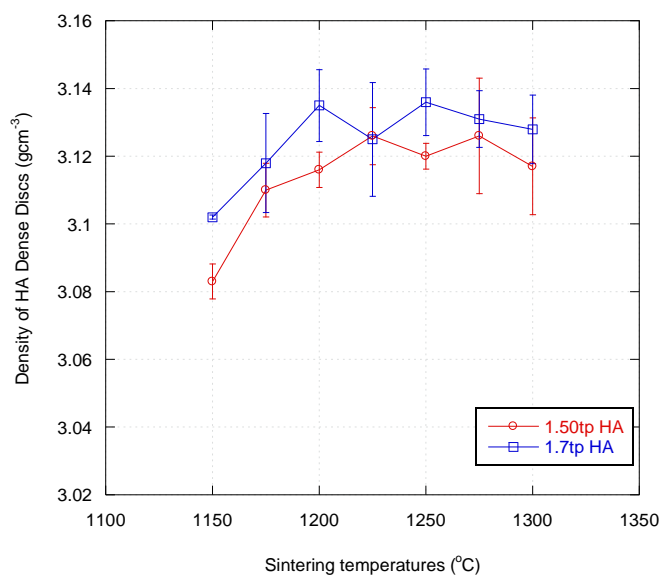
Figure 2.18 – Density of sintered HA at different pressures 75.8 (1.50) and 90.9 (1.75) MPa, calculated using the Archimedes' principle

Table 2.15 – Average HA-D density sintered at 1250 ^{o}C, using the Archimedes' principle

Pressure / MPa	Density ($\pm\sigma$) / gcm^{-3}	Total porosity / %
75.8	3.120 ($\pm$0.01)	2.0
90.9	3.136 ($\pm$0.01)	1.5

Grain size of the specimens was investigated using SEM in conjunction with EDS to confirm elemental distribution on the surface of the biomaterials. The figures below correspond to the SEM imaging of the biomaterials, followed by the EDS analysis.
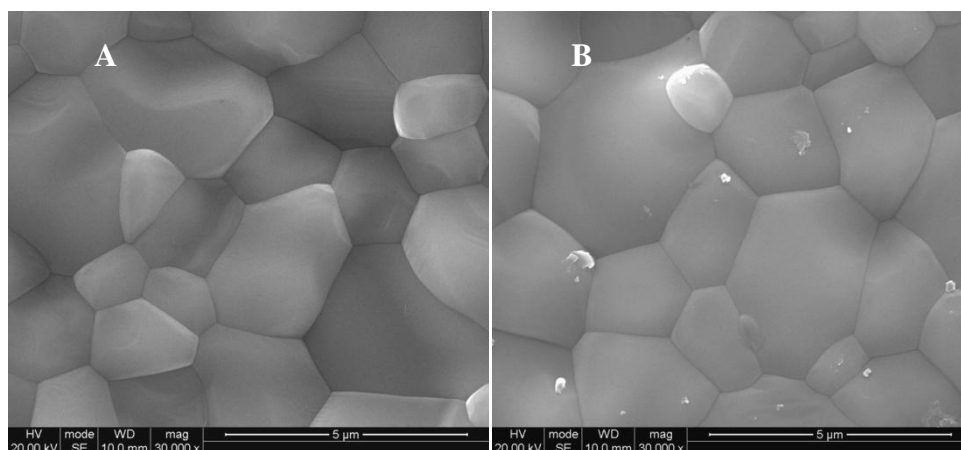
Figure 2.19- SEM imaging of (a) SA and (b) HA dense disc sintered at 1300 and 1250 ^{o}C, gold coated

Figure 2.19A shows SA samples at its optimum sintering temperature showing no sign of degradation. Figure 2.19B depicts the crystal morphology of HA sintered at 1250 ^{o}C. The images showed a very crystalline structure with clear grain boundaries of an average grain size of 1-2 μm.

The EDS analysis showed the content of element present on the surface of the samples under investigation in terms of percentages.

Table 2.16 – EDS Analysis of HA & SA in terms of weight and atomic percentage of element present

Elements	HA		SA	
	Weight %	Atomic %	Weight %	Atomic %
Ca	37.6	22.0	34.4	19.4
P	19.1	14.5	17.6	12.9
O	43.3	63.5	47.2	67.0
Si	-	-	0.8	0.7

Table 2.16 shows the elemental distribution as a percentage on the surfaces of the two biomaterials. SA has 0.8 % silicon and HA has none. Figure 2.20A and B are the EDS

spectra, clearly showing the absence and presence of the silicon as an element in the biomaterials' surface of the dense discs.
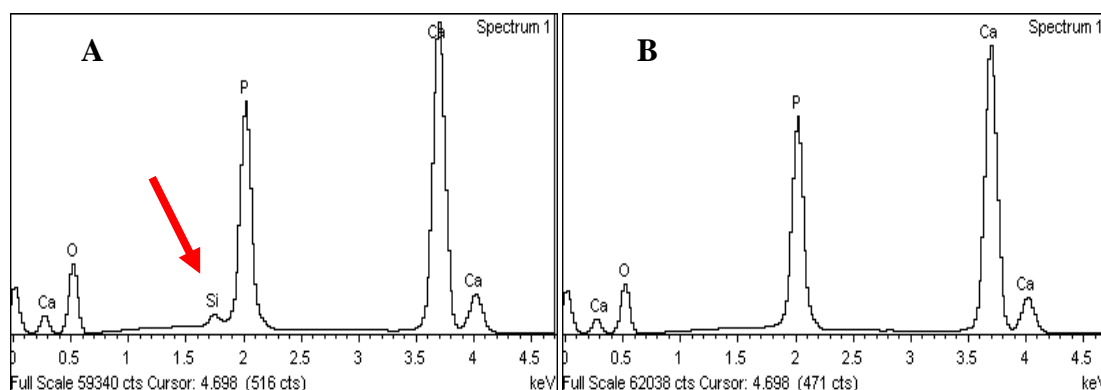
Figure 2.20 – EDS spectrum of the (a) SA and (b) HA sintered at 1300 and 1250 ^{o}C, respectively

AFM was used to measure surface roughness (see Table 2.17) and confirm dense disc's material morphology and phase homogeneity.

Table 2.17 – Average Surface Roughness of biomaterials calculated using AFM statistical analysis

Materials	Surface Roughness ($\pm\sigma$) / nm
SA	360 ($\pm$ 80)
HA	330 ($\pm$ 40)
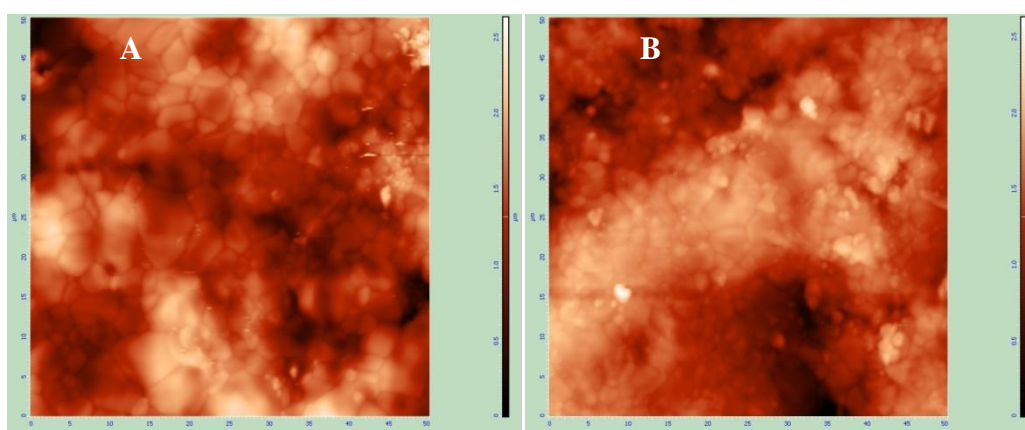
Figure 2.21 – AFM images of (a) HA and (b) SA dense disc sintered at 1250 ^{o}C

The AFM images in Figure 2.21 show different colours from light to dark, these represent how shallow or deep the surface is, taking this into account, it can be said that

HA has deeper surfaces than SA. These images also show that SA surface is more homogeneous that HA. And finally, some of the grain sizes observed may be comparable to the ones observed *via* SEM.

2.3.4 Porous Granules (PG) Morphology

Porous samples of the biomaterials were investigated using the Archimedes' principle for the density and total porosity (see Table 2.18). The surface area of the samples was confirmed *via* BET (see Table 2.19) and the strut porosity, also known as the pore interconnectivity was calculated and values tabulated below (see Table 2.20) *via* samples embedded in resin, imaged by SEM (see Figure 2.22).

Table 2.18 –Archimedes' principle data for the porous materials

Material	Density ($\pm\sigma$) / gcm^{-3}	Total porosity / %
SAG	2.874 ($\pm$ 0.08)	80.8
HAG	2.567 ($\pm$ 0.04)	81.0

Table 2.19 –Surface area data for the porous materials using BET

Sample name	Sample Weight / g	Surface Area / m^{2}g^{-1}
SAG	1.1162	0.169
HAG	1.1566	0.134

Table 2.20 –Strut porosity in the biomaterials

Sample name	Strut Porosity ($\pm\sigma$) / %
SAG	19.8 ($\pm$ 0.52)
HAG	19.6 ($\pm$ 3.5)

The porous samples were imaged further to show grain boundaries and sizes to be similar to those found on the dense discs surface in section 2.3.3.

SA porous sample (see Figure 2.23) sieved through particle size of 2 < PG < 5 mm show clear and clean grain boundaries with a average grain size of 1 -2 μm, while the HA porous sample (see Figure 2.24) shows a similar pattern. Images on the SA showed smaller grains than HA, but overall they look similar.
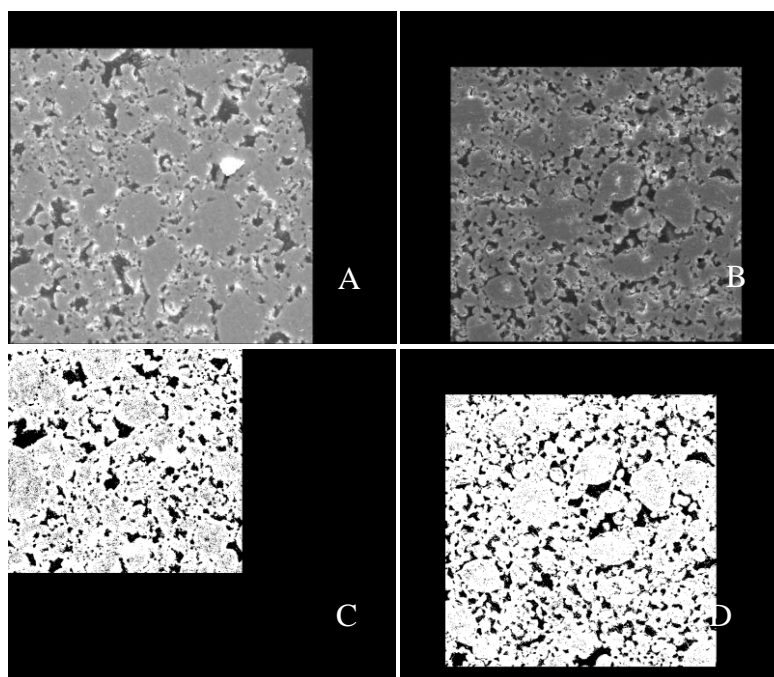
Figure 2.22 – SEM images of (a) porous SA and (b) porous HA embedded in resin and polished used to determine the strut porosity *via* (c) SA and (d) HA thresholds
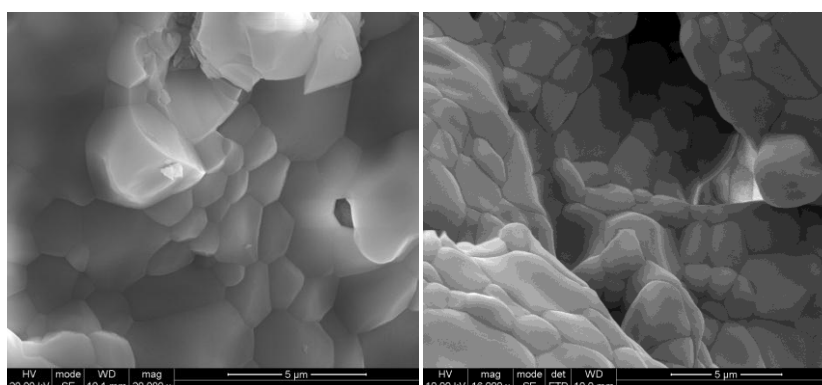
Figure 2.23- Porous SA granules (sieve size of 2-5 mm) sample at a high and low kV, gold coated
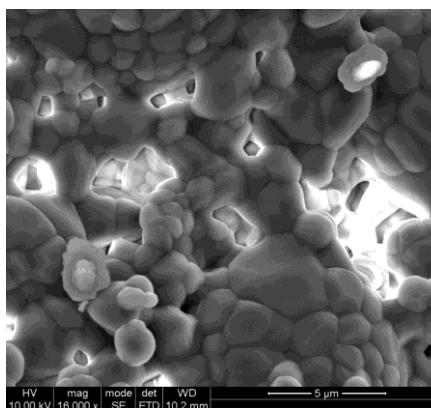
Figure 2.24 – SEM imaging of Porous HA (granular size sieve through 2-5 mm) gold coated

2.4 Discussions

Chemical Analysis

XRD pattern of the powdered HA samples, as shown in Figure 2.6, had larger intensity values than that of SA pattern on both patterns. For both biomaterials, the calcined patterns were more intense than those observed for the as-received patterns (see Figure 2.6A and B). The XRD patterns overall were very similar between the biomaterial powders. The unit cell volume and axes (*a* and *c*) for the as-received and calcined samples were determined and showed inconsistency, which was found to agree with the findings in Gibson *et al.* (2001). Samples heated at and below 500 ^{o}C were found to be difficult to assess any effect of chemical changes on the phase composition and structure of HA, especially when prepared *via* the aqueous precipitation route was difficult (Gibson, Rehman*, et al.* 2000; Osaka, Miura*, et al.* 1991). The XRD pattern of the powders show that phase pure products were made as no impurities were found compared to the HA sample #1 formed as shown in Figure 2.25A.

The differences in the intensity of the XRD pattern from HA to SA were known to be due to the presence of silicon (Si), as silicon is known to act as a sintering aid, which results in SA samples having lower crystallinity at the same calcination temperature than HA. Hence, lower intensity was observed. (Gibson, Best*, et al.* 2002; Kim, Lee*, et al.* 2003) This agreed with the findings and supported by the SEM images obtained, as shown in Figure 2.16 that showed a change in structure of the samples' edges with more change observed on SA than HA.

The XRD patterns of the SA and HA samples with increasing sintering temperature illustrated in Figure 2.9 and Figure 2.10, showed very little difference in peak position in both samples. The effect of increasing temperature on the biomaterials was more apparent when looking at the crystallographic parameters in Table 2.4 and Table 2.6 generated through the XRD patterns in Figure 2.9 and Figure 2.10, for SA and HA respectively. Using the patterns and a refinement software, the structural parameters of the HA and SA have been determined and found in the literature to show a certain tendency, where for all SA samples, the unit cell parameters were slightly greater than those obtained for HA. Thus, showing a trend in which the incorporation of Si in the

HA lattice increases the a- and c- axes , as well as the unit cell volume, this possibly due to silicon's larger atomic size and the change on the surface charge of the biomaterial, as the phosphate ions are replaced. Before and beyond the optimum sintering temperature for SA and HA was reached, the crystallographic parameters in Table 2.5 and Table 2.7, analysed using method-2, did not correspond to expected data found in the literature, and method 1 was found to be more reliable in generating the expected data. The differences in crystallographic parameters can also be due to the way the hydroxyapatite: stoichiometric and substituted, have been synthesized (Balas, Perez-Pariente, *et al.* 2003; Gibson, Best, *et al.* 1999; Thian, Huang, *et al.* 2006).

In this investigation, the unit cell parameters obtained from the samples made, should be ideally within the data obtained from Gibson, as the samples would be quite similar in nature due to the process used to manufacture them, with an emphasis on SA unit cell parameters being larger than those obtained from HA. Therefore, this would be an expected observation when characterising samples for this investigation, which was observed in this study.

Following the XRD, XRF of the powders further confirmed the difference in the biomaterial's composition due to the presence of silicon, but also established that the substitution had occurred with no changes to the Ca/P ratio, suggesting that upon sintering a single phase product was formed, as described by the work of Hing and Gibson *et al.* It is important to have the correct Ca/P ratio in order to have the optimum specimen (see Figure 2.25 , CaP2 sample) (Hing, Gibson, *et al.* 1998).
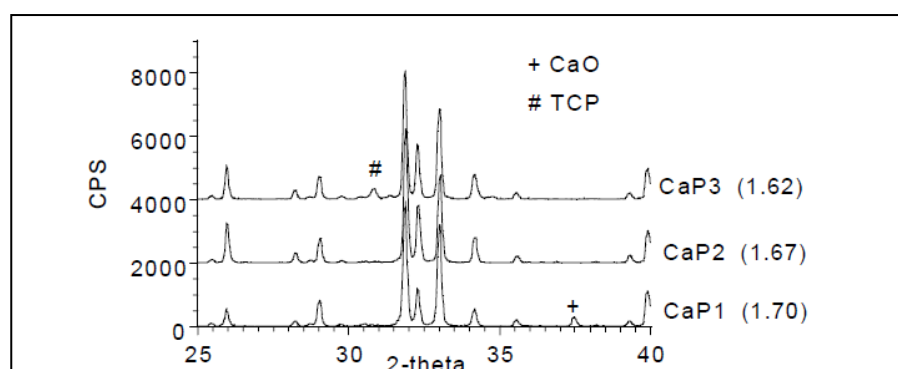
Figure 2.25 – XRD pattern indicating the position of impurities in hydroxyapatite, where calcium oxide is present in CaP1, tricalcium phosphate in CaP3, and the optimum sample composition in CaP2. (Hing, Gibson, *et al.* 1998)

Higher than the expected ratios result in the formation of calcium oxide (CaO) impurities within the samples, as shown on the initial HA produced (see Figure 2.7A) which agreed with Hing *et al.* (see Figure 2.25 sample CaP1) (Hing, Gibson*, et al.* 1998), while a lower ratio gives rise to the beta-tricalcium phosphate to form upon sintering above 1200 ℃ as in the CaP3 sample, as shown in Figure 2.25. This observation was further confirmed by others as well as the importance of the Ca/P ratio (Mostafa 2005).

XRD and XRF analyses, together, confirmed the biomaterial powders to be phase pure and silicate substituted.

Analysing the powders *via* FTIR showed a broader spectrum for the SA material, probably due to the loss of the hydroxyl through the substitution compared to HA, as shown in Figure 2.11 at the full range of 4000 to 400 cm^{-1}, which was expected and agreed with by others.(Balas, Perez-Pariente*, et al.* 2003; Gibson, Best*, et al.* 1999; Hing, Revell*, et al.* 2006; Thian, Huang*, et al.* 2006). For the characteristic phosphate and silicate group peak position, a more specific range was used at 1400-400 cm^{-1}, as shown in Figure 2.12, in order to identify the individual groups. The assignments made in , agreed with those found in the work of Gibson, Best *et al.* (Gibson, Best*, et al.* 1999), where the peak positions observed showed phosphate peaks at 950, 890 and 840 cm^{-1} in SA compared to HA between 960 and 1100 cm^{-1}, which have moved due to the presence of silicate. Further confirmed by peak assignment found in the work of Hing *et al.* (Hing, Revell*, et al.* 2006) and Thian *et al.* (Thian, Huang*, et al.* 2006).

The peak positions were then compared to crystalline sample references obtained in Figure 2.13, calcium phosphate (Ca$_3$(PO$_4$)$_2$) and zirconium silicate (ZrSiO$_4$), clearly showing corresponding positions to those observed in the SA or HA samples, which was in agreement with assignments found in the work of Rashid *et al.* (Rashid, Harding*, et al.* 2008)

Increasing sintering temperature of the powders during the FTIR, just like the XRD analysis, showed little differences between samples sintered above 1150 ^{o}C.

Powder Morphology

The particle size distribution of the as-received (precipitate) and calcined powder samples were within the normal range reported in the literature for HA synthesised using the same general production route. HA and SA particle sizes were fairly similar, especially once calcined at 700 ^{o}C, with slightly higher particle sizes observed from the HA samples, which was described by Gibson *et al.* (Gibson, Best, *et al.* 2002; Gibson, Ke, *et al.* 2001)

Table 2.11 clearly showed SA to have the higher surface area values measured *via* BET compared to HA, as the temperature increased. SA surface area of the as-received material was found to be lower in values compared to that found in the literature, but still higher than HA. The higher surface area in SA has been known to be indicative of the presence of silicon (Si) as a substituted element, which inhibits the crystal growth where smaller but a larger amount of crystallites are formed, in the SA precipitate compared to HA precipitate (Gibson, Best, *et al.* 2002).

The work of Raynaud and his co-workers showed that with increasing Ca/P ratio from 1.50 to 1.71 on HA powder sintered at 1000 ^{o}C, there was a decrease of the specific surface area from 88 ± 2 to 55 ± 1 m^2/g. This observation demonstrated the importance of acquiring the appropriate Ca/P to achieve the corresponding surface area from the biomaterials. This suggests a possible trend that with increasing temperature, a decrease of surface area will also be evident, which would make temperature an important factor in obtaining a biomaterial specimen with an appropriate surface area, which agreed with findings in this study. This was further exhibited when working with the dense disc morphological form of the biomaterial. When the Ca/P reached the optimum ratio at 1.667 for HA, the specific surface area obtained was 58 ± 1.5 m^2/g, close to the value obtained in this work (Raynaud, Champion, *et al.* "Calicum phosphate apatites with variable Ca/P atomic ratio I. Synthesis, characterisation and thermal stability of powders" 2002).

The surface area and particle size of HA biomaterials are strongly affected by the Ca/P ratio and sintering temperatures of the starting materials, thus it was very important to get the chemical analysis right.

Figure 2.16A and C showed the SEM of the as-received samples of HA (A) and SA (C) respectively, at the micron level. The samples depicted are an agglomeration of the needle-like crystalline structure of hydroxyapatite, which is usually found in the literature as T.E.M. images at the nano-level (Weiner and Wagner 1998). Thus, samples showed less sharp the edges for both HA and SA, compared to clear crystal needles, and once calcined this effect was lessened, as shown in Figure 2.16B and D. This effect was more apparent on the SA biomaterial, reflecting the smaller crystallite formation in the precipitate powder possibly due to its higher surface area.

Dense Discs (DD) Morphology

SA sintering temperatures can be as high as 1400 ^{o}C to reach optimum density of the material, depending on the weight percent amount of silicon substituted. At low temperature (1000-1150 ^{o}C) low densities of the samples were observed as compared to that of stoichiometric HA (Gibson, Best, *et al.* 2002). This observation agreed with observation found in this work also. Beyond 1400 ^{o}C, the SA samples are prone to undergo a second phase change to calcium silicate as its melting point is within this temperature region. Thus, the sintering experiment for the SA samples was investigated from above 1150 ^{o}C to below 1400 ^{o}C, to optimise the production of a highly dense biomaterial, and avoid the low densities sample production and second phase formation of the biomaterial.

In the case of hydroxyapatite (HA; calcium phosphate ceramics), the sintering temperature has been established in the range between 1000 ^{o}C to 1500 ^{o}C, following compaction of the powder into the desired shape (Hench 1991). However, it was also found that beyond 1250 ^{o}C, HA has a tendency to degrade into its derivative (β-TCP) and decompose, or have calcium oxide impurities, depending on the Ca/P ratio of the powder produced. Also, the influence of heat on HA has been investigated extensively to demonstrate that calcination of HA powder at temperatures between 400 and 1000 ^{o}C influenced its properties towards a material more crystalline (Patel, Gibson, *et al.* 2001). Thus, the sintering experiment was undertaken above 1000 ^{o}C up to 1400 ^{o}C to achieve a more crystalline product, no impurities and highly dense material.

Observed densities were comparable to values found in the literature with HA exhibiting higher densities than those observed for SA, which corresponded to an

average 98 % density for SA compared to 99 % for HA dense discs pressed at 90.9 MPa. Dense apatite can also be described as microporous, where the materials have a total porosity of less than 5 % by volume, as shown for SA in Table 2.13 and HA in Table 2.15, to be true. (LeGeros and LeGeros 1993) Table 2.13 and Table 2.15 show the average densities determined using the Archimedes' principle, at the optimum sintering temperature for the biomaterials.

The low microporosity observed during the analysis for samples pressed at 90.9 MPa was another advantage in using this applied pressure for the formation of the dense discs. According to previous work (LeGeros and LeGeros 1993), the applied pressure used was within the range found in that work, which was also dependent on the sintering temperature used and heating duration. In other work, an applied pressure of 200 MPa was used to compress 2 g of sample, however, the size and silicon content differed from that under investigation compared to Gibson's samples, which contained only 0.4 wt% Si in HA to form 12 mm diameter and 6 mm thickness discs (Gibson, Best, *et al.* 1999). This may suggests that with reduced silicon content a higher applied pressure may be required to achieve a similarly microporosity.

SEM images of SA (A) and HA (B) shown in Figure 2.19 indicated that the biomaterial produced was not decomposing, showed clear grain and grain boundaries. Clean grain boundaries were observed with relatively similar grain sizes on both surfaces, but SA having on average smaller ones than HA. This was further confirmed by the AFM and agreed with findings in previous studies, where the incorporation of the silicate group in the HA lattice showed to produce smaller grain size in the biomaterials.(Balas, Perez-Pariente, *et al.* 2003; Gibson, Ke, *et al.* 2001)

The differences seen in the EDS shown in Figure 2.20 further confirm the XRF and thus the presence of silicon in the biomaterials and its composition, as a substituted biomaterial.

AFM confirmed the differences in grain size of the two biomaterials' surfaces, where SA shows smaller grain size (see Figure 2.21B) compared to HA (see Figure 2.21A), thus leading to more boundaries forming that may have resulted in the increase in surface roughness of the SA biomaterial, as shown in Table 2.17, but also the increased presence of triple junctions at the grain boundaries. For the purpose of this study and using proteins instead of cells, i.e. larger molecular weights, and concentration

increased roughness on the biomaterials may lead to increased protein adsorbed. This will be further discussed in the following chapters.

Porous Granules (PG) Morphology

The density of the porous samples was lower than the calculated density of the dense discs, however, the overall trend of SAG having the higher value compared to HAG was still observed, as shown in Table 2.18. This observed lower density was also found by others (Hing, Best, *et al.* 1999) for the porous specimens, which were cylindrical in shape with a length of 8.8 mm and a diameter of 4.6 mm.

Using the Archimedes' principle also allowed for the total porosity of the samples to be determined at an average 80 % for both samples, which was as expected. This would represent the macroporosity of the samples *via* density and SEM (in mm), while the microporosity (the strut) can be visualised using SEM (in μm), but sometimes also measured using intrusion porosimetry. (Rosengren, Pavlovic, *et al.* 2002)

The surface area for the porous granules has been determined using BET as shown in Table 2.19. SAG had a higher surface area compared to HAG, which was expected as for the chemical and powder analyses, confirming the influence of Si in the biomaterial. The introduction to porosity should not affect the surface chemistry of the samples compared to the powder or dense disc specimens, as in principle only the interconnectivity would have increased (Shors and Holmes 1993) which was observed here also.

Strut porosity of the porous samples was observed in Figure 2.22 to be the same for both biomaterial, and valued at around 19.6 %, shown in Table 2.20, which was about 0.4 % lower than expected but similar in both samples. Figure 2.22 clearly showed samples to have very similar topographies when visualised at the 100 μm range.

Other SEM images of the porous samples (not embedded in resin) in Figure 2.23 and Figure 2.24 for SAG and HAG, respectively, confirmed specimen similarity in the grain structure and boundaries.

2.5   Summary & Conclusions

The biomaterials SA and HA were characterised and found to correspond to characteristics found in the literature, with densities of 98 % and 99 %, respectively. The photo-acoustic spectra confirmed the peak positions of key functional groups of the samples; the XRD confirmed the formation of a one phase pure biomaterial with a high degree of crystallinity, in addition it gave rise to corresponding crystallographic patterns and parameters. The XRF in conjunction with EDS confirmed the composition and silicon substitution, while the SEM and AFM confirmed surface topography.

Further characterisation of the porosity of the samples, both dense and porous, revealed the expected trends of the samples where the dense samples had 100 % closed porosity, while the porous samples showed an average of 80 % total porosity with a closed strut porosity of 19.8 and 19.6 % for SA and HA, respectively.

BET confirmed higher surface area values observed for SA compared to HA due to the presence of the silicon.

Differences in samples are now accounted for, and hence differences seen in the adsorption/desorption profiles can be explained due the presence or not of the silicate ions substituted which replace the phosphate ions.

Chapter 3. SYNTHESIS AND CHARACTERISATION OF FLUORESCENTLY LABELLED PROTEINS

3.1 Background

The use of fluorescent tags (or labels) has been previously mentioned and researched specifically for staining antigens since the 1950s (Coons and Kaplan 1950; McKinsey, Spillane, *et al.* 1962). They are also commonly used for microscopy or as clinical immunoassays to monitor or quantify several biological processes. The fluorophores are usually labelled to antigens, which would then be used to detect fluorescent signals when bound, for example to proteins, cells and other biological samples. Several steps are required, highly skilled (or trained) operators are needed as well as expensive reagents or kits; therefore the process is complex which limits the possibility of automating this system of analysis, (Wei, Blumenthal, *et al.* 1994) but also could hinder the possibility of detection in a competitive environment.

The most common fluorophores used are the fluorescein and rhodamine derivatives, such as fluorescein isothiocyanate (FITC) or the sulforhodamine 101 (SR101) or Texas red (TXR). (Abuelyaman, Hudig, *et al.* 1994; Little, Paquette, *et al.* 1997) These fluorophores have excitation and emission spectra at different characteristic wavelengths, which can permit simultaneous detection.

The aim in this chapter was to develop a method to facilitate the competitive evaluation of protein adsorption on silicate-substituted hydroxyapatite (SA) and stoichiometric hydroxyapatite (HA). Thus we set out to establish a method based on the use of proteins individually covalently modified with fluorescent tags emitting at different wavelengths. This required selection of suitable labels and methods for their covalent attachment to the proteins.

3.2   Experimental Methodology

3.2.1   General Procedures

Glassware was cleaned with soapy lukewarm water, and rinsed with enough water, acetone and followed by dichloromethane (DCM). The glassware was then dried in an oven at 110 ^{o}C overnight. Syringes, syringe needles and stainless steel transfer tubes (also known as cannulae) were all cleaned by passing concentrated nitric acid and distilled water through them. Some of the reagents used in the synthesis were considered to be air and moisture sensitive, in such cases, all manipulations were carried out under inert atmosphere of nitrogen using standard cannula techniques.

All solvents were dried over the appropriate drying agent, for example, magnesium sulphate (Abuelyaman, Hudig, *et al.* 1994). All solvents were stored in reservoirs equipped with Young's taps over the appropriate molecular sieves under nitrogen atmosphere and degassed prior to use.

Dichloromethane (DCM), dimethylformamide (DMF) and chloroform (CHCl$_3$) were purified by refluxing for 4 hours over calcium hydride (CaH$_2$). Methanol (MeOH) was distilled in the presence of a small quantity of magnesium. The solvents were then transferred under N$_2$ into flasks and stored over activated 4 Å molecular sieves. Hydrochloric acid (HCl) of a concentrated form of 11.1 M was used. Deuterated solvents (DMSO-d$_6$ and CDCl$_3$) were purchased from Cambridge Isotopes, UK and used as received. Solvents used for fluorometric analysis, ethanol, were of spectroscopic grade purchased from HP, and used as received.

Fluorescein isothiocyanate isomer I (FITC), methyl-6-Aminocaproate hydrogenchloride (ACA-OMe.HCl), bovine serum albumin (BSA), N, N'-Dicyclohexylcarbodiimide (DCC), phosphorus oxychloride (POCl$_3$) and 4-methylmorpholine (NMM) were purchased from Sigma-Aldrich, UK and used as received. Sulforhodamine 101 (SR101) (free acid) was purchased from ACROS Organics, prior to use the sample was vacuum dried at 100 ^{o}C, overnight.

3.2.2   Instrumentation parameters

Nuclear Magnetic Resonance (NMR)

NMR spectra were obtained using a JEOL 270 (^{1}H, 270 MHz; ^{13}C-(Dowd, Rosen, *et al.*), 67.88 MHz) and Bruker AMX400 (^{1}H, 400 MHz; ^{13}C-{^{1}H}, 100.61 MHz). Spectra were obtained operating from δ 0-10 ppm chemical shift (δ) reported relative to the position of the solvent signal.   For ^{1}H NMR, chloroform δ 7.26, DMSO δ 7.25, methanol δ 3.34 and water δ 4.31 were used as internal references, while for ^{13}C NMR, chloroform δ 77.36, DMSO δ 40.45 and methanol δ 49.86 were used.

Fourier Transform Infrared (FITR) - Attenuated Total Reflectance (ATR)

ATR spectra were obtained using an ATR (Bruker) and Hitachi IR spectrometer. Spectra were obtained at a resolution of 4 cm^{-1}, averaging 16 scans, operating from 4000 to 400 cm^{-1}. All samples were analysed neat.

Ultraviolet-Visible Spectroscopy

UV-visible spectra were obtained using a Hewlett Packard Spectrophotometer (Hewett Packard, UK) operating from 200 to 1100 nm.

Fluorescence spectra were obtained using the Fluoro-Max-3 Spectrometer (Yvon-Jobin Horiba, UK) with a xenon lamp. The spectra were obtained at an excitation wavelength of 494 nm for the FITC and its derivative, and 586 nm for the SR101 fluorophores under investigation, operating from 250 to 750 nm with slit widths of 1.5 were employed.

Mass Spectroscopy

Mass Spectra were obtained from the EPSRC National Service at Swansea. The spectra were measured using LTQ Orbital XL (Thermofisher Scientific, UK) high resolution instrument across the full range in electrospray.

3.2.3   Synthesis of the fluorophores

In the following sub-sections, the synthetic route to producing the fluorophore will be explained from their precursor reagent to the final product via a two-step manufacturing process; (1) a coupling with a spacer and (2) a conversion from an ester to a carboxylic acid. Using, the extended fluorophore, individual protein species were coupled via the lysine residue through the carbolic acid reactive group of the fluorophore.

3.2.3.1   Preparation of Fluoresceinthiureidocaproic acid (FTCA)

(i) Coupling the Aminocaproic acid Ester to the Fluorophore Fluorescein isothiocyanate

The synthesis followed the work of Abuelyaman *et al*. (1994) FITC (197.9 mg, 0.508 mmol) was dissolved in DMF (5 ml), a solution of ACA-OMe (153.2 mg, 0.843 mmol) in DMF (1 ml) was added at RT to the FITC mixture and stirred for 30 minutes. (Abuelyaman, Hudig, *et al.* 1994) The solvent was removed *in vacuo*. The collected residue was purified on a silica gel column eluted with chloroform: methanol (4:1), the fractions were collected and combined with Rf values of 0.33-0.51 measured on TLC chromatographic paper, depending on the height of the column made, then concentrated to give a dark orange oily residue. This residue was then vigorously stirred (or triturated) with distilled water (5-10 mL) to give the crude fluoresceinthioureidocaproic methyl ester (FTCE) solid (155.6 mg, 0.291 mmol, 57.3 % yield).
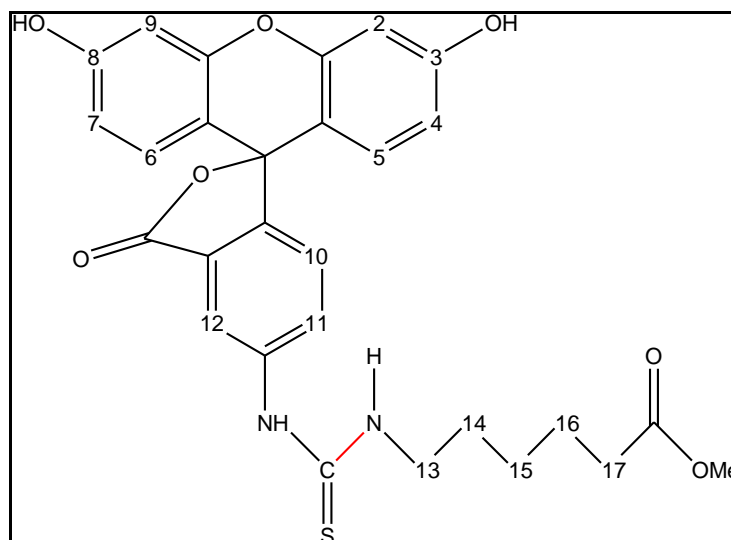
Figure 3.1 – Structure of the FTCE compound

NMR assignments corresponding to proton position shown in Figure 3.1 δ_H (270MHz, DMSO-d$_6$) 10.17 (2H, br s, OH), 8.32, (1H. bs, H12), 6.70-6.58 (6H, m, xanthene moiety, H2 to H9), 3.59 (3H, s, COO<u>Me</u>), 3.43 (2H, bs, H13), 2.31 (2H, t, H17), 1.54-1.51 (4H, m, H14 and H16) and 1.33-1.24 (2H, m, H15).

(ii) Converting the FTCE to its Acid Derivative FTCA

The water was decanted away from the FTCE orange sheet-like compound from part (i); once the water was removed, sodium hydroxide (NaOH, 3 ml, 1.0 M) was added, followed by a minimum volume of methanol (a few drops) to give a clear solution. The mixture was stirred at RT for 1 hour. The solvent was concentrated *in vacuo* and the remaining aqueous solution was placed in an ice bath. Hydrochloric acid (concentrated HCl, 11 M) was added dropwise with stirring to the solution until it became acidic (pH~3-4). The orange suspension formed was then cooled for an additional 3 hours; the solid was isolated by filtration using a Buchner funnel and flask, and dried to give crude FTCA (155.0 mg, 0.2978 mmol, 58.6 % yield).
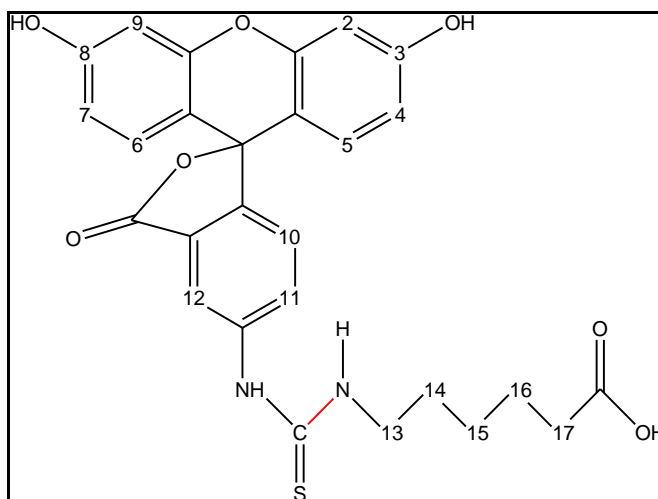
Figure 3.2 - Structure of the FTCA compound

NMR assignments corresponding to proton position shown in Figure 3.2 δ_H (400MHz, DMSO-d_6) 11.56 (1H, bs, OH), 10.15 (2H, s, OH), 7.78-7.92 (1H, d, H11), 7.24 (1H, d, H10), 6.70-6.52 (6H, m, xanthene moiety, H2 to H9), 3.72-3.58 (2H,br s, H13), 2.30 (2H, t, H17), 1.62-1.50 (4H, m, H14 and H16) and 1.38-1.24 (2H, bs, H15)

IR assignments: ν_{max} /cm^{-1} (KBr) 3735.9 (O-H), 2945.1 (C-H), 2478.4 9 (N-H), 1701.1 (C=C) and 1596.9 (C=O).

UV-Vis (2.845x 10^{-6} M in water and ethanol): 493 λ/nm, Absorbance of 0.8, equivalent to a extinction coefficient (ε) value of 281,000 Lmol^{-1}cm^{-1}.

Fluorescence (2.845x 10^{-6} M in water and ethanol): Excitation 494 λ/nm and Emission 521.6 λ/nm with an intensity of approximately 2.7 x 10^6 (AU)

Mass Spec: The spectrum clearly shows that FTCA with its corresponding molecular ion found m/z 521.1364 (20) M$^+$

3.2.3.2   Preparation of the Texas red sulfonylamidocaproic acid (TSCA) via Texas
RED (TXR)

(i)   Synthesising the TXR fluorophore

Sulforhodamine 101 (SR101, 259.9 mg, 0.4283 mmol) was treated with phosphorus oxychloride (POCl$_3$, 3 ml, 4.935 g, 32.19 mmol) according to work of Titus *et al.* (Titus, Haugland*, et al.* 1982) After standing for 12 hours under nitrogen, the dark solution was poured onto a minimal amount of crushed ice. After 15 minutes, the product was extracted into chloroform, washed several times with cold water and dried with magnesium sulfate (Mg$_2$SO$_4$). The material was then dried by evaporation *in vacuo*. The material was re-dissolved in chloroform (25 ml), and precipitated with an excess of hexanes (PET 40-60 ^{o}C). The dark blue-green product (410.7 mg) was then filtered, vacuum dried under nitrogen, and stored in a container in the fridge freezer.
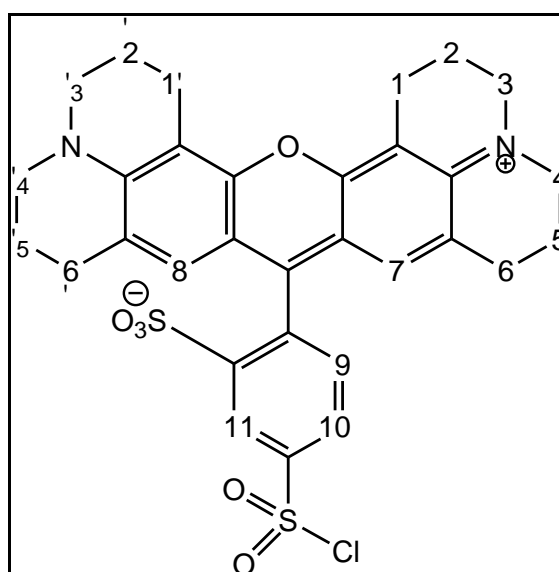
Figure 3.3 – Structure of the Texas red (TXR) compound

NMR of this product was inconclusive, and other characterisation including mass specrometry and IR of the material also showed inconsistencies with the expected product. Due to the colour of the product indicating presence of the target, the next synthetic step was undertaken, assuming that further processing would allow for a better separation of the by-products during analysis.

(ii)   Adding an Aminocaproic acid methyl ester spacer to the TXR fluorophore

Dry product from part (*i)* (410.7 mg, 0.6573 mmol) was dissolved in chloroform (15 ml) and to this solution 6-aminocaproic acid methyl ester (120.4 mg, 0.6627 mmol) was added in the presence of NMM (72.4 µl, 66.6 mg, 0.6585 mmol). The final solution was stirred at 0 °C for 30 minutes, followed by further stirring at RT overnight. The reaction mixture was then concentrated *in vacuo* to give a dark red solid (241.4 mg). The NMR showed this to be a mixture including the capote ester and possibly the TCSE compound, see Figure 3.4A. This particular mixture was further purified by recrystallisation and taken to the next step.
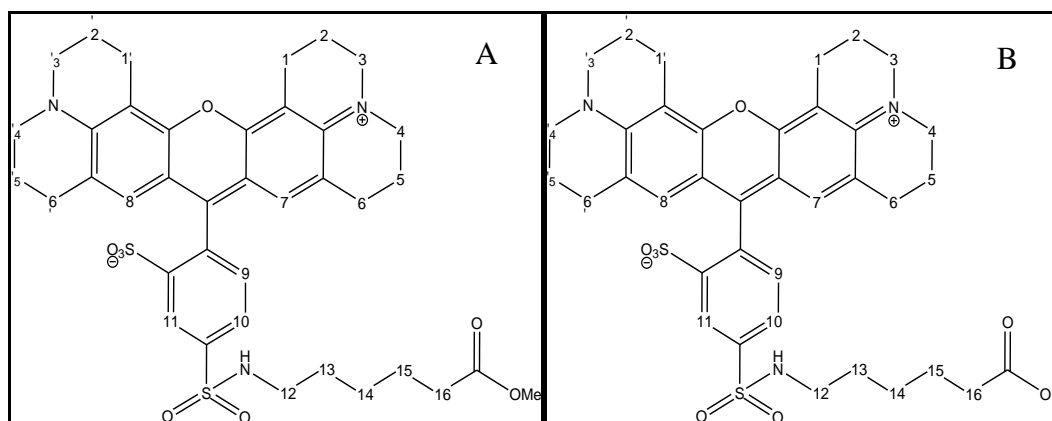
Figure 3.4 - Structure of the (a) TSCE and (b) TSCA compounds

(iii)   Conversion of the Ester TSCE to the Acid TSCA

NaOH (10 ml, 1M) was pipetted into a round bottom flask (25 ml) containing the TSCE reaction mixture, followed by a few drops of methanol. The mixture was stirred for 2 hours at RT and then cooled in an ice bath. Concentrated HCl (11 M) was added dropwise carefully until the dark solid completely precipitated. The product, pale pink crystals when isolated, was collected and dried by vacuum filtration (59.2 mg). The mother liquor remained deeply purple but no solid TSCA (see Figure 3.4B) product could be obtained from this. The whole process was repeated again with the same result.

3.2.4 Coupling Fluorophore labels to Proteins

(i) *FTCA, the GREEN emitting Fluorophore*

Fluorophore (FTCA, 13.5 mg, 0.0259 mmol) was diluted in water (1 ml); DCC (130.0 mg, 0.6304 mmol) was added in water (1 ml). The fluorophore mixture was then incubated for 5 minutes at RT with the DCC solution, where NaOH (3-5 drops, 1 M) was added to maintain reaction solution at pH 5. BSA (48.0 mg) was added to yield a final molar ratio of approximately 1 mole of fluorophore to each available 50 amino acids of the protein for coupling. The reaction was left to incubate for 4 hours in the dark, for the conjugation to occur, with continuous stirring (460 rpm). The reaction was then stopped by adding sodium acetate (NaOAc; 29.6 mg, 0.3608 mmol) to achieve a final concentration of 100 mM and incubated for a further 1 hour. The FTCA-BSA conjugate was separated from free fluorophore by direct dialysis against PBS (pH 7.4, 0.01 M), where two changes overnight had been sufficient (Harlow and Lane 1988). The freeze dried solution gave a bright orange filamentous material (15.8 mg) that was stored in the fridge and readily redispersed when required.
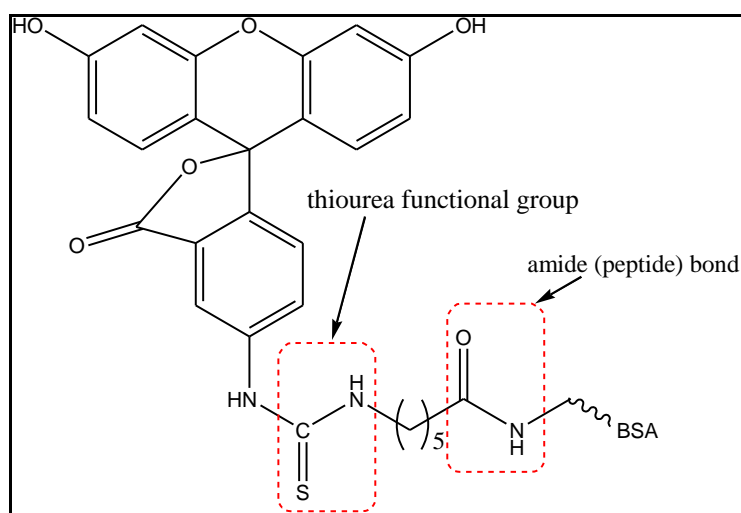
Figure 3.5 – Structure of the FTCA coupled to BSA via the lysine residue

UV-Vis (8.131 x 10^{-6} M in PBS): 494 λ/nm, Absorbance of 0.3, equivalent to a extinction coefficient (ε) value of 37,000 Lmol^{-1}cm^{-1}.

Fluorescence (8 .131 x 10^{-6} M in PBS): Excitation 494 λ/nm and Emission 518 λ/nm with an intensity of 3.10 x 10^6 (AU)

(ii)   Identification and coupling of a RED emitting Fluorophore

Given that we were unable to isolate any solid red emitting TSCA (see experimental), direct labelling with the precursor (SR101) alone was attempted, although sulfonic acid coupling analogous to the carboxylic acid coupling used for FTCA is rare. Given that SR101 is a strong acid, it was assumed that no coupling reagent would be necessary for it to attach to protein covalently; hence, two methods were explored. Method one (M1) was carried out without coupling reagent, while method two (M2) employed a coupling reagent following the same protocol as for the FTCA coupling process.

Method One (M1)*:* Fluorophore (SR101, 15.6 mg, 0.0257 mmol) was diluted in water (2 ml), where NaOH (5 drops, 1 M) was added to maintain the mixture at pH 5. BSA (47.4 mg) in water (1 ml) was added, and then the reaction mixture was left to incubate for 4 hours in the dark with continuous stirring (460 rpm). In an attempt to separate the target SR101-BSA (M1) conjugate (Figure 3.6) from free fluorophore by direct dialysis against PBS, none of the fluorophore remained in the dialysis tube.

Method Two (M2): Fluorophore (SR101, 14.5 mg, and 0.0239 mmol) was diluted in water (1 ml) and mixed with a solution of DCC (124.4 mg, 0.6033mmol) in water (1ml). The fluorophore mixture was then incubated for 5 minutes at RT, where NaOH (3-5 drops, 1M) was added to maintain the solution at pH 5. BSA (51.3 mg) and the reaction solution were left to incubate for 4 hours with continuous stirring (460 rpm). The reaction was stopped by adding sodium acetate (NaOAc; 29.2 mg) to achieve a final concentration of 100 mM and incubated for 1 hour. The SR101-BSA (M2) conjugate was separated from free fluorophore by direct dialysis against PBS. The freeze dried dialysed solution afforded a dark red solid (14.9 mg). This was stored in the fridge and redispersed as required.
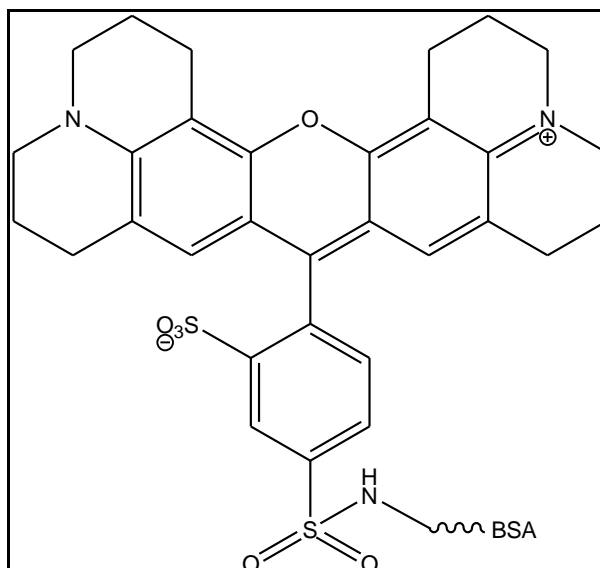
Figure 3.6 – Structure of SR101 coupled to BSA via the lysine residue

UV-Vis (8.008 x 10^{-6} M in PBS): 587 λ/nm, Absorbance of 0.5, equivalent to an extinction coefficient (ε) value of 62,000 Lmol^{-1}cm^{-1}.

Fluorescence (8 .008 x 10^{-6} M in PBS): Excitation 586 λ/nm and Emission 608 λ/nm with an intensity of 3.75 x 10^{6} (A.U.)

Other attempted syntheses of target labels for coupling to proteins are tabulated in 68 to 70 in Appendix 11.

3.3   Results and Discussions

The aim of the work in this chapter was to establish protocols whereby fluorescent probes with different colours could be covalently attached to a model protein BSA without significant quenching of fluorescence intensity. The fluorescence from proteins having the different labels attached could subsequently be used to monitor competitive adsorption events on biomaterial surfaces. Thus the covalent attachment should ensure that mixtures of proteins or batches of proteins having different labels attached should be stable to under the conditions of experiments.

Fluorescein Derivative (FITC)

Fluorescein isothiocyanate is the original fluorescein molecule functionalized with an isothiocyanate group (-N=C=S-), replacing a hydrogen atom on the benzene ring of the fused ring structure. It has similar and improved properties to its precursor, fluorescein, which can exist in the form of various species (see Figure 3.7) in solution due to its sensitivity to pH.
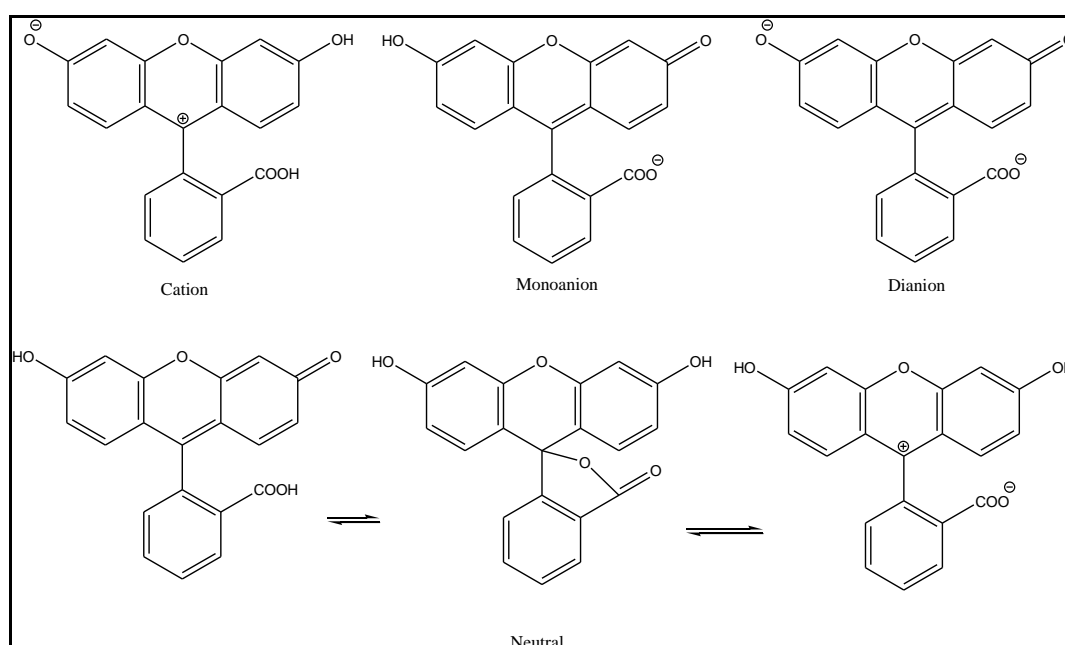
Figure 3.7 – pH dependent species of Fluorescein

This reactive group can then react with amine groups on proteins, the sulfur group is known to be responsible for modulating fluorescence properties of the chromophore

through a dynamic quenching mechanism (Klonis and Sawyer 2003), therefore the FITC further requires a spacer to avoid this phenomenon.

The synthetic approach used for the coupling of BSA labelled with the fluorophore fluoresceinthiureidocaproic acid, FTCA, is shown in Scheme 3.1.
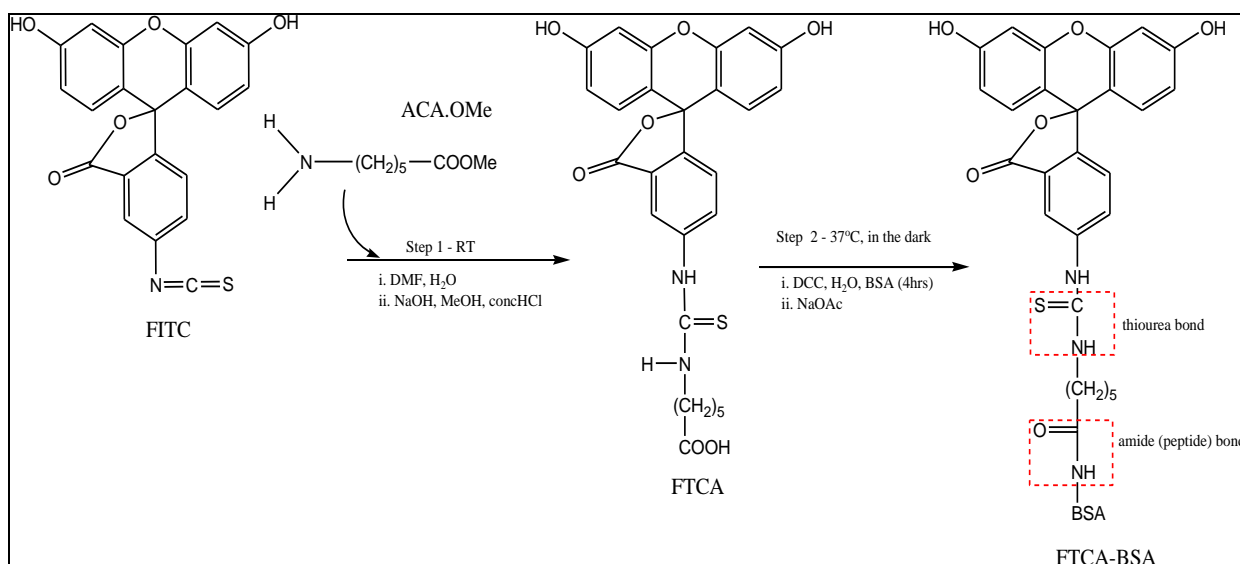
Scheme 3.1– Synthetic approach to BSA coupled to FTCA

This approach was previously published (Abuelyaman, Hudig, *et al.* 1994). The synthesis of FTCA is shown in step 1, while the coupling to BSA is shown in step 2. The coupling reaction was prepared as described and slightly modified by Harlow *et al.* in 1988 (Harlow and Lane 1988) in order to allow for a physiological amount of BSA saturated with fluorophore. During the synthesis of FTCA (Figure 3.2) pH 5 was maintained for the formation of the fluoresceinthiureidocaproic acid.

Isothiocyanate groups are very reactive groups, but are stable at low pH and they do not easily hydrolyse. They form upon coupling with amine groups a thiourea link via a nucleophilic addition due to their electrophilic character, and the thiourea link is very stable both in aqueous neutral solution, but also in alkaline media (Valentine, Amarnath, *et al.* 1992). This reaction was aided by the fact that amine groups in proteins are reactive nucleophiles.

This affects the distribution of mono and dianion in the product. The FTCA compound was isolated in a crude form. This was observed from the ^{1}H NMR spectrum, where there were a number of resonances (solvent and water) in addition to those reported in the literature (Abuelyaman, Hudig, *et al.* 1994). The IR obtained for both the ester and

carboxylic acid of FTCA showed characteristic peaks such as hydroxyl vibration at 3350 cm^{-1} and carboxylic acid vibration at 1590 cm^{-1}, but this method did not give conclusive structural information.

Mass spectroscopic analysis of the FTCA fluorophore was undertaken and of its precursor, fluorescein isothiocyanate (FITC) and showed the expected molecular ions for the parent compounds (see Table 3.1).

Table 3.1 – Mass Spectrum fragmentation patterns of the FCTA and FITC

m/z	Corresponding ion of FTCA	m/z	Corresponding ion of FITC
348.09	Fluorescein.NH_4^+	388.02	$[C_{21}H_{11}NO_5SH]^+$
422.07	$[C_{21}H_{15}N_2O_5NH_4]^+$	777.06	$[C_{21}H_{11}NO_5SH]_2^+$
521.14	$[C_{27}H_{24}N_2O_7SH]^+$		

The appearance of some higher molecular weight fragments suggested occurrence of dimer formation in the case of FITC but this may have also occurred during ionisation. The fragmentation patterns of the FTCA showed the presence of the caproic acid spacer, which confirmed derivitisation of the FITC.

The crude FTCA isolated was used without further purification and used to label BSA. It was conjugated via the lysine residue as it is the amino acid most frequently used for this purpose to lead to a successful covalent attachment to macromolecules. (Klonis and Sawyer 2003). It was reasoned that any uncoupled fluorophore would be removed in the dialysis step of the coupling protocol. This was proved to be successful as a limited amount of free fluorophore was observed in the dialysis fluid after the process. Also, a very intense orange coloured protein solution was isolated for the adsorption and desorption studies.

The average fluorescence emission wavelength observed with the labelled-protein is very similar to that of the free FTCA at an average of 516.67 nm (Table 2 and Figure 10). This value closely corresponds to value found in the literature at 517 nm (Titus, Haugland, *et al.* 1982).

A shift might have been expected after conjugation to BSA but the spacer group would hinder interaction between the label and the protein surface as expected and possibly minimize effects of the protein on the fluorophore.

Table 3.2 - Excitation & Emission of the FTCA-BSA in phosphate buffered saline (PBS)

Sample	Concentration / M	Excitation / nm	Emission / nm
FTCA-BSA	8.131×10^{-6}	494	519
FTCA	8.131×10^{-7}	494	518
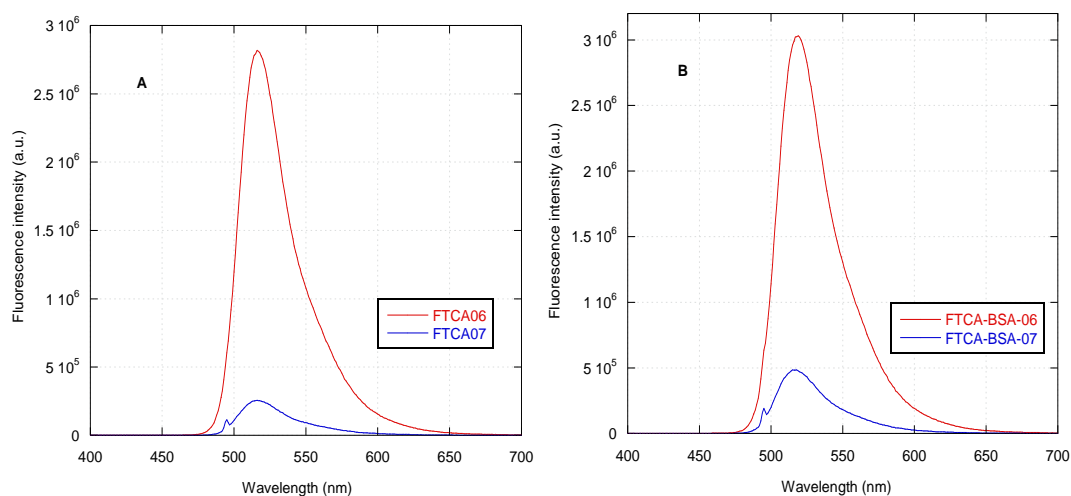
Figure 3.8 – Emission Spectra at 2 distinct concentrations of the (a) FTCA and (b) FTCA-BSA in PBS
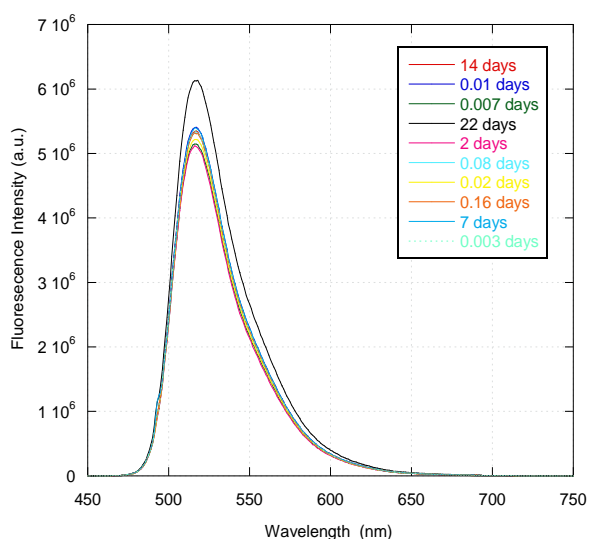
Figure 3.9 – Fluorescence Spectra of FTCA-BSA at different time intervals

A fluorescence stability study of FTCA-BSA confirmed that fluorescence intensity was stable over several days (Figure 3.9).

Fluorescein isothiocyanate and its precursor, fluorescein, are known to couple specifically to N-terminal of a peptide or amino acids of proteins. (Wei, Blumenthal, *et al.* 1994) They are also known to form dimers readily in aqueous solution, which would explain the inconsistencies observed during IR and NMR analysis, but also the extra fragments in the mass spectrum analysis. High concentration or close proximity of the dyes induces this phenomenon, which can result in fluorescence quenching; as a result a spacer is used to minimize this effect.

Rhodamine Derivative (SR101)

The rhodamine derivaties, which emit in the red region of the visible spectrum, are another commonly used type of fluorophore for fluorescence based analytical applications. Sulforhodamine 101 (SR101), specifically Texas red (TXR), has been the label of choice for this purpose. Texas red is known to form covalent links with amino groups on proteins when the appropriate reagent and protein are mixed. (Titus, Haugland, *et al.* 1982) The following synthetic approach describes the process towards the synthesis of the red emitting fluorescent label called Texas red (TXR) as shown in step 1 of Scheme 3.2.

Step 1 of this scheme turned out to be somewhat challenging and no evidence of conversion could be observed as indicated by NMR, IR and mass spectroscopy on the isolated material. Part of the challenge was related to the moisture sensitivity of the reagents; according to Titus *et al.*, the free sulfonic acid renders the TXR more hydrophilic and more soluble (Titus, Haugland, *et al.* 1982). It must be kept as dry as possible prior to addition to the protein solution, but also the protein solution is to be kept quite cold on ice to enhance coupling relative to the hydrolysis process with rapid mixing.
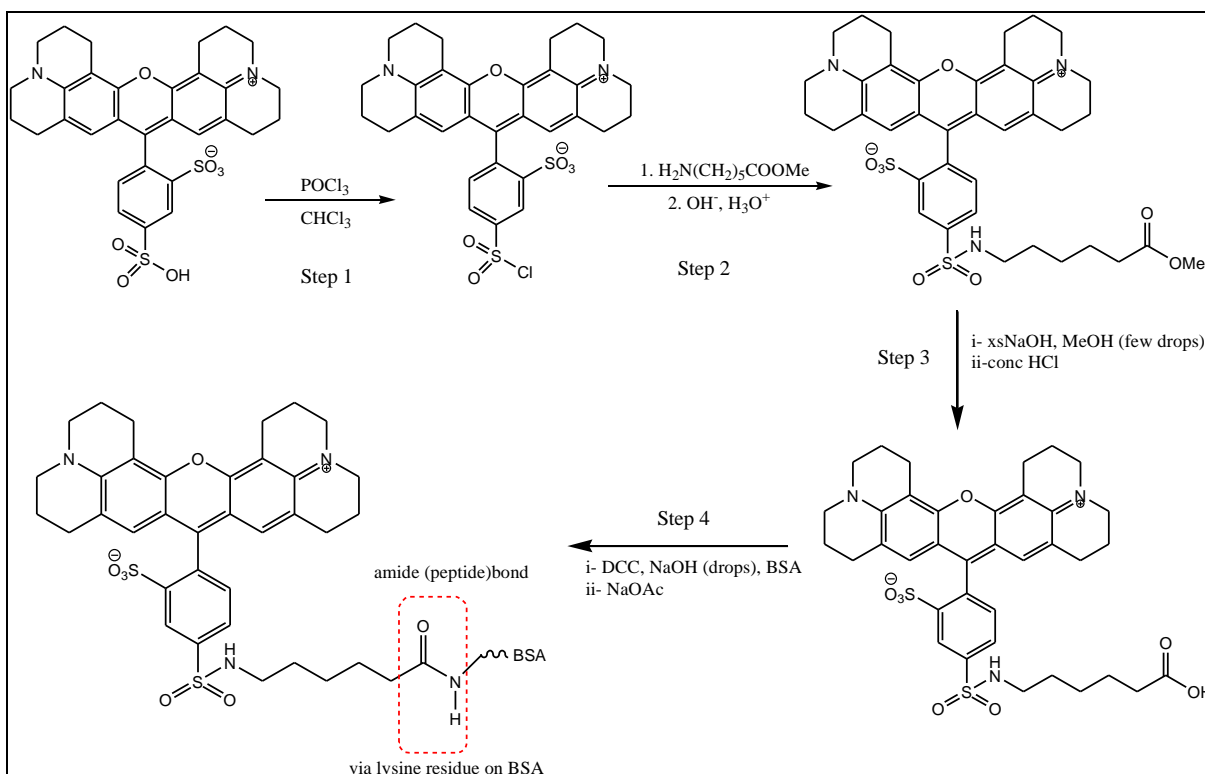
Scheme 3.2 – Synthetic route to the formation of TXR

The mass spectrum showed that the TXR compound was not isolated although it may have been produced judging by the colour of the product solutions; it may have been subsequently hydrolysed during attempted isolation. According to Lefevre and his co-workers, it has been reported that Texas Red sulfonyl chloride (TR-SC) which is a very popular red emitting dye, is also unstable to moisture during storage and prone to hydrolysis in the conjugation reaction (Lefevre, Kang, *et al.* 1996), due to the presence of the sulfonyl chloride. Apparently, a higher pH of 9-9.5 is also required for the conjugation to occur successfully compared to pH 5 used for the conjugation of FTCA. However pH 9-9.5 is much too high for proteins, which often leads to the denaturation of the protein in solution.

The TXR was needed to introduce the caproate spacer but in view of the difficulty in synthesising this it was decided to use the precursor SR101 as shown in Scheme 3.3 without a spacer for further studies in this investigation rather than pursuing the target TSCA in Scheme 3.2.
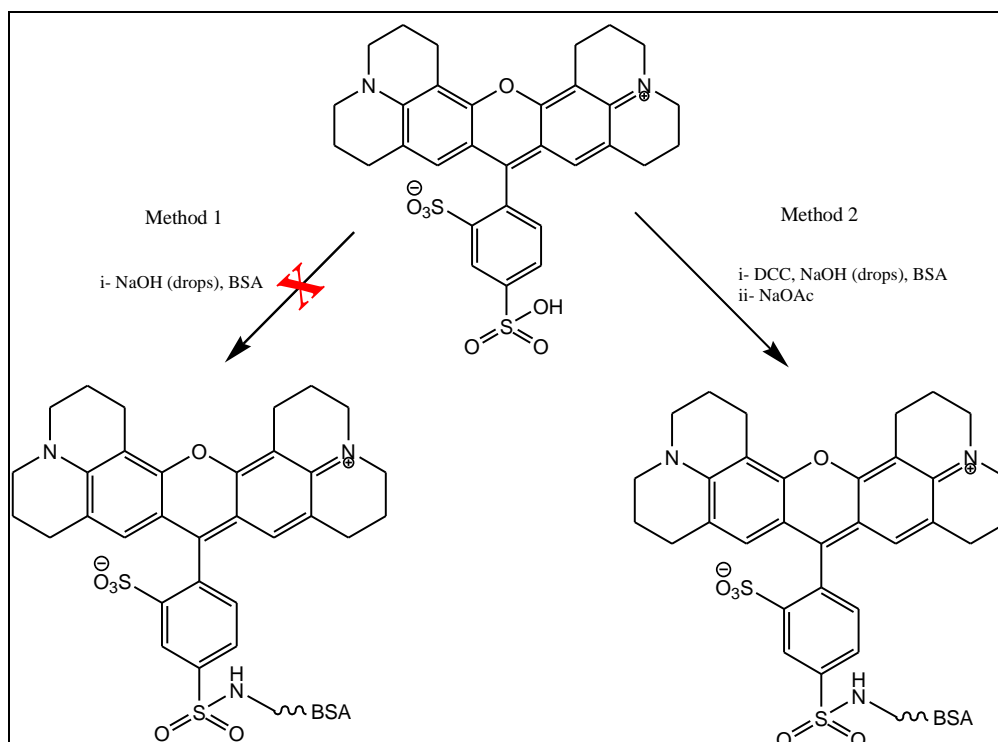
Scheme 3.3 – Synthetic route for the coupling of SR101 to BSA

Coupling to BSA using SR101 allowed lower pH to be used, at room temperature and with good reproducibility. The sulfonic acid group (SO_3H) present in SR101 facilitated and improved the conjugation of this red emitting dye to the protein. Thus, this process was favoured and the compound was stable in an aqueous solution (Ishizaka, Habuchi, *et al.* 1999) as shown in the life-time study in Figure 3.10, and also in a serum and serum-free media shown in Chapter 6.
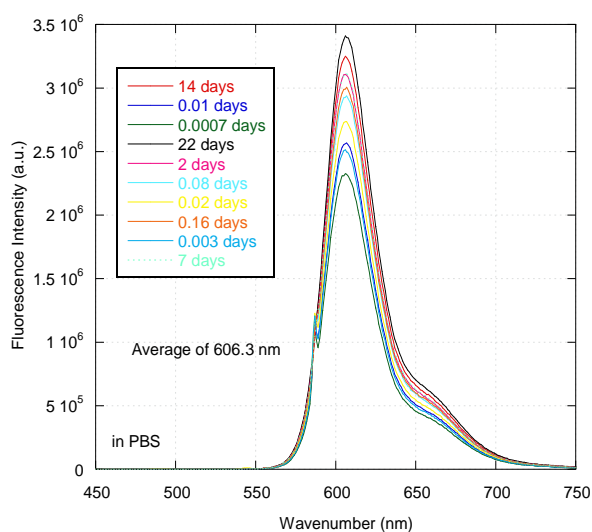
Figure 3.10 – Fluorescence Spectra of SR101-BSA at different time intervals

It was originally thought, that as a strong acid, SR101 may not need the use of a coupling reagent such as DCC to couple to the lysine residue present on the protein, as shown in method (1) of Scheme 3.3. However, when the SR101-BSA solution was dialysed in PBS to separate the unbound/free SR101, all of the coloured (deep purple) SR101 leached out of the tube to leave behind the uncoupled BSA.

Further characterisation through fluorescence (Table 3.3 and Figure 3.11) and life-time study (Figure 3.10) confirmed SR101 to have formed a covalent attachment to BSA.

Table 3.3 - Excitation & Emission of the labelled-protein SR101-BSA in phosphate buffered saline (PBS)

Sample	Concentration / M	Excitation / nm	Emission / nm
SR101-BSA	8.008×10^{-6}	586	608
SR101	8.008×10^{-7}	586	605

This confirmed that the strong acid alone may have only formed some kind of weak interactions rather than a covalent amide link with BSA.
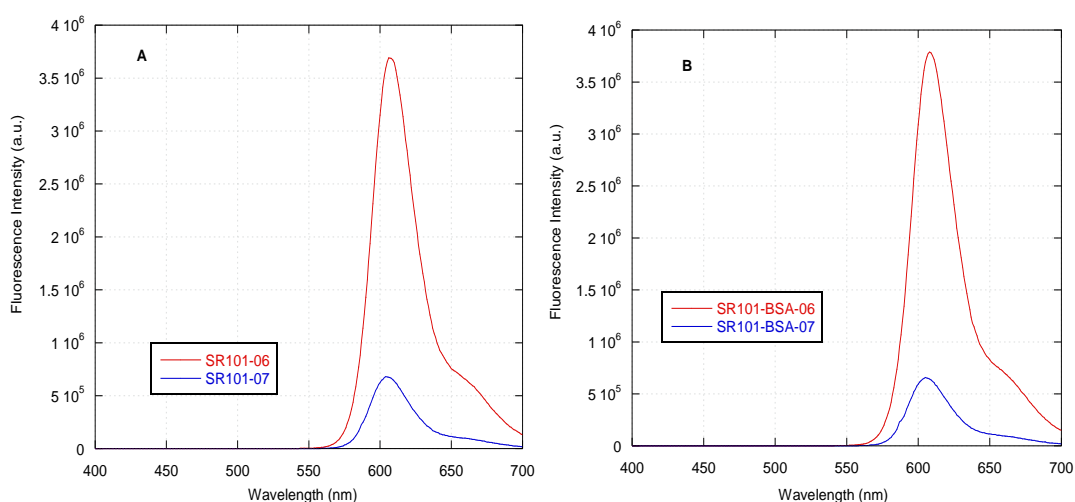
Figure 3.11 – Emission Spectra at 2 distinct concentrations of the (a) SR101 and (b) the SR101-BSA in PBS

As a result, the experiment was repeated with the use of DCC (as described in method two) and when the SR101-BSA solution was dialysed, very little unbound SR101 leached out, confirming the presence of a covalent attachment.

SR101-BSA fluorescence emission wavelength at 606 nm showed little difference to that of the free SR101 fluorophore, which was as expected (see Figure 3.12).

Figure 4. Normalized absorption of sulforhodamine 101 (B) and TR-X (C) (panel a) and normalized emission spectra (panel b) of fluorescein (A), sulforhodamine 101 (B), and TR-X (C) in PBS. The patterns of the absorption and emission of both Texas Red dyes are very similar and well distinguished from that of fluorescein.
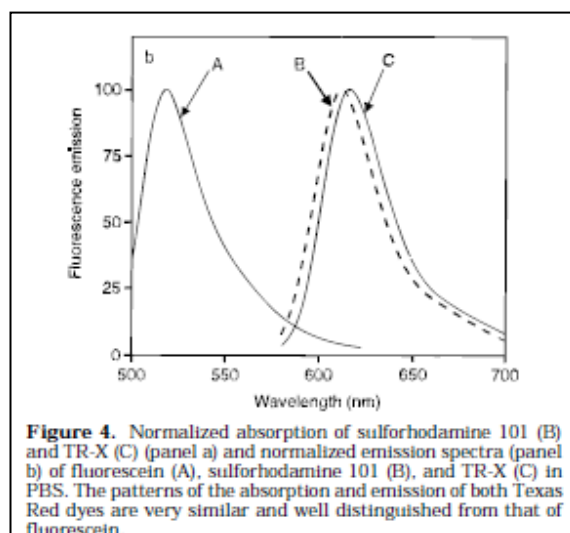
Figure 3.12 – Expected Fluorescence for the (b) SR101 and (c) TXR compared to (a) Fluorescein spectra (Lefevre, Kang, *et al.* 1996)

In this case, the sulfonamide group attached to the xanthenes moiety may act as a space between the fluorophore and the protein. As shown in Scheme 3.3, the xanthene moiety is more sterically demanding than the fluorescein isothiocyanate shown in Scheme 3.1 and as such interactions with the protein leading to fluorescence quenching might be less of an issue in this case rendering the presence of a spacer less critical.

Sulfonamide groups have quite an importance in medicinal chemistry applications (Caddick, Wilden*, et al.* 2004), constituting the largest class of anti-microbial agents. According to the work of Caddick and Wilden *et al.* the formation of sulfonamides mostly relied on the presence of the sulfonyl chlorides (SO_2Cl), however due to their disadvantages, the route through the sulfonic acids (SO_3H) has been investigated. So far, there is no current procedure that transforms sulfonic acid to sulfonamide in one synthetic step. In the work of Caddick *et al.,* however, activation of the sulfonic acid is required by triphenylphosphine ditriflate (Ph_3P^+-O-$^+PPh_3$2OTf$^-$) to create an

intermediate (e.g. compound 7 in Scheme 3.4) that would be suitable towards the following nucleophilic reaction with the amines to form the sulfonamide (see Scheme 3.5).
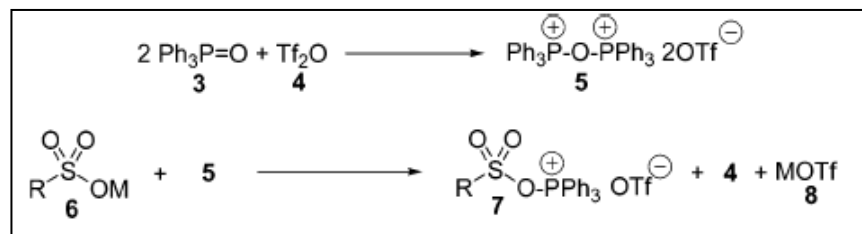
Scheme 3.4 – Activation of sulfonic acid by Triphenylphosphine Ditriflate (Caddick, Wilden, *et al.* 2004)
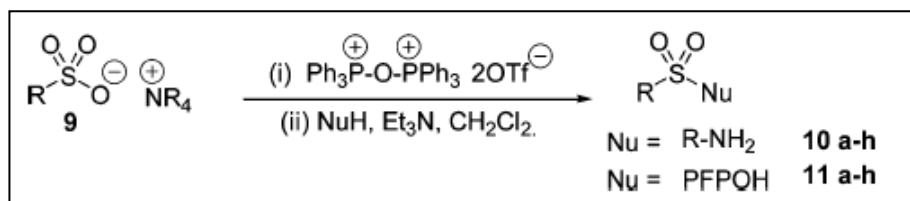
Scheme 3.5 – Sulfonamides and Sulfonate esters from Activated sulfonic acid. (Caddick, Wilden, *et al.* 2004)

Triphenylphosphine oxides are known to be troublesome to remove at the end of the reaction, thus may cause concern, but again the Caddick's group worked on replacing the need for this by using solid-supporter variant, which can be removed by washing.

This is not too different to the synthetic route used in this study, where DCC was also used to activate the sulfonic acid towards the addition of the amine group form the BSA, as shown in Scheme 3.3. The only difference would be the ease at which DCC was removed at the end of the reaction, as it drives the reaction forward to form an oxide complex, leaving behind the sulfonamide link to the protein.

The novelty, here, could be in the reagent used for the intermediate formation before the coupling reaction to the amine, as this was successful with minimum loss of fluorophore, and thus fluorescence intensity.

3.3.1   The Labelling Protocol

The final labelling route could then be described. The relationship between the moles of the fluorophore and protein was calculated with the assumption according to Harlow (Harlow and Lane 1988) that for every 1 mg of fluorophore, 50 peptides would be labelled per mole of proteins expressed as follows, where 10 is an integer factor for the coupling reaction to saturate all lysine residue present;

$$moles\ of\ FTCA\ or\ SR101$$
$$= moles\ of\ proteins\ \times\ number\ of\ lysine\ residues \times 10$$

Equation 3.1

It was very important to take into account the amount of lysine residues available for coupling, value found in the literature. Using Equation 3.1 the mass of fluorophore for the protein under investigation can then be determined, and made up into the protein solution in water, usually made as a stock solution three times larger than the original.

Fluorophore (FTCA or SR101) was diluted in water (1 ml); DCC was added in water (1 ml). The fluorophore mixture was then incubated for 5 minutes at RT with the DCC solution, where NaOH (3-5 drops, 1 M) was added to maintain reaction solution at pH 5. BSA, FN, BMP-2 or OPN was added. The reaction was left to incubate for 4 hours in the dark, for the conjugation to occur, with continuous stirring (460 rpm). The reaction was then stopped by adding sodium acetate (NaOAc) to achieve a final concentration of 100 mM and incubated for a further 1 hour. The labelled protein conjugate was separated from free fluorophore by direct dialysis against PBS or water, where two changes overnight had been sufficient (Harlow and Lane 1988).

Figure 3.13 summarises the schematic route to labelling BSA or rhBMP-2 with FTCA, while Figure 3.14 shows the route to labelling FN or rmOPN to SR101. Amounts of fluorophore would vary according to the molecular weight and final protein concentration required for the investigation.
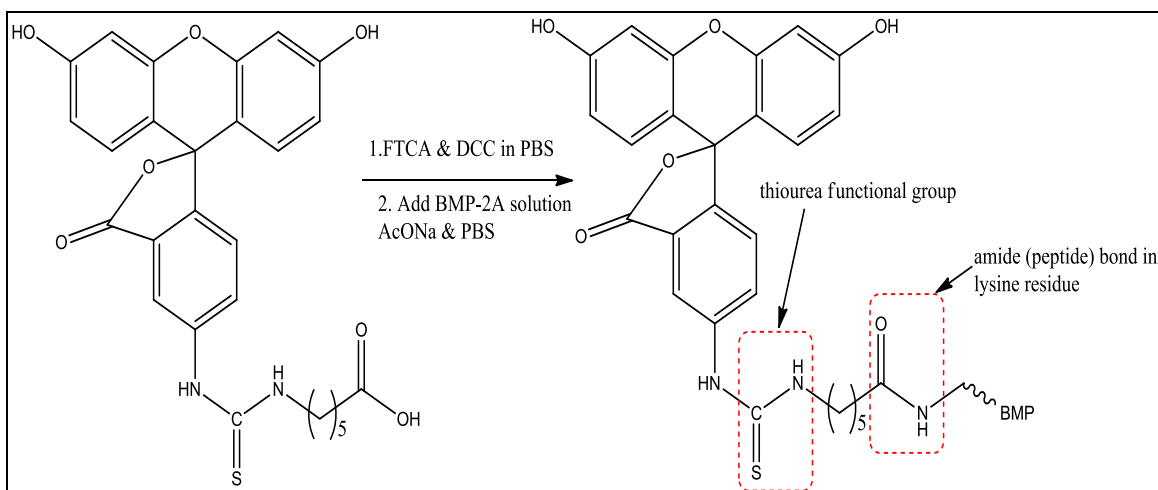
Figure 3.13 – Coupling reaction scheme of the BSA or rhBMP-2 with FTCA
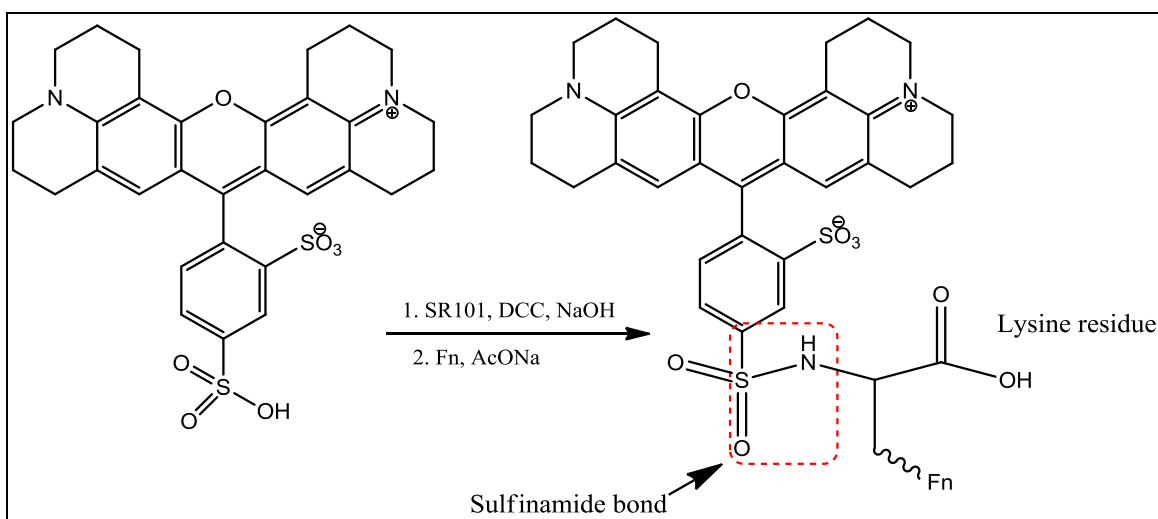
Figure 3.14 – Coupling reaction scheme of the FN or rmOPN with SR101

3.4   Summary & Conclusions

FTCA was prepared and coupled to BSA. There were difficulties in making the TXR and thus TSCA with finally no conclusive chemical analysis to indicate the compound was present among the product mixture. As a result, its precursor (SR101) was used.

Initially, the SR101 compound (used as received) was reacted with BSA without coupling reagent (DCC). When this method (one) proved to be unsuccessful, the process was repeated using method (two) including the DCC. Subsequent dialysis clearly indicated that a covalent amide link to BSA was introduced. This suggests that the role of DCC in this reaction was crucial to achieve covalent bonding.

The simplicity of this direct coupling route from the relatively cheap SR101 by-passing the need for tortuous synthesis of TSCA was a very useful discovery, however sulfonamide formation from sulfonic acid has already been demonstrated by Caddick *et al* (Caddick, Wilden*, et al.* 2004).

Further chemistry on simple lysine containing model compounds could confirm the role of DCC in effecting the covalent coupling of SR101 but this is beyond the scope of this work.

Therefore, in this study the use of SR101 as the red emitting fluorophore will be favoured over the TXR, and used along with the green emitting FTCA to label proteins for the competitive binding studies to be undertaken.

Chapter 4.   PROTEIN ADSORPTION AND DESORPTION STUDIES

4.1   Background

Protein adsorption to a biomaterial surface is one of the earliest events that occurs post implantation (Anselme 2000; Baxter, Frauchiger, *et al.* 2002; Green, Davies, *et al.* 1999), occurring within seconds of introduction into the body. The adsorbed protein layer subsequently influences host response by acting as an intermediary between the implant surface and the surrounding tissue through its ability to facilitate cell motility, attachment and development. In the case of bone graft substitute materials, modulation of the species and conformation of proteins that adsorb to the surface have been demonstrated to be critical in promoting osteogenic cell attachment (Bumgardner, Wiser, *et al.* 2003; McFarland, Thomas, *et al.* 2000; Thomas, McFarland, *et al.* 1997; Yang, Cavin, *et al.* 2003), spreading (Sawyer, Hennessy, *et al.* 2005; Yang, Roach, *et al.* 2001), proliferation (Rouahi, Champion, *et al.* 2006; van Wachem, Vreriks, *et al.* 2006), morphology (Allen, Tosetto, *et al.* 2006; Gugala and Gogolewski 2004; Kilpadi, Chang, *et al.* 2001) and development (Kilpadi, Sawyer, *et al.* 2004; Rouahi, Gallet, *et al.* 2006; Wilson, Clegg, *et al.* 2005)

In the quest to develop bone graft substitutes with enhanced bioactivity or osteoinductivity monitoring protein adsorption and desorption behaviour on surfaces has increasingly been recognised as vital to understanding the mechanisms and processes that occur between a material's surface and the host environment. (Anselme, Noel, *et al.* 1999; Ducheyne and Qui 1999; Ellingsen 1991; Guth, Campion, *et al.* "Effect of Silicate-Substitution on Attachment and Early Development of Human Osteoblast-Like Cells Seeded on Microporous Hydroxyapatite Discs" 2010)

In many studies, protein adsorption or depletion is quantified indirectly using enzyme-linked immunosorbent assays (ELISAs) or total protein type assays, where radioactive, colourimetric or fluorimetric probes are employed. (Fabrizius-Homan and Cooper "Competitive adsorption of vitronectin with albumin, fibrinogen, and fibronectin on polymeric biomaterials" 1991; Rosengren, Pavlovic, *et al.* 2002; Wilson, Clegg, *et al.* 2005) Total protein assays quantify all proteins present irrespective of species or conformation, ELISAs on the other hand are limited to measurement of a specific

protein and as a result of the reliance on antibodies can also be conformation dependent. Therefore, in order to carry out a competitive study multiple analyses must be performed. To date the truly competitive analysis are restricted to sodium dodecyl sulfate-polyacrylamide gel electrophoresis (SDS-PAGE) methodologies, ellipsometry, for analysis of real-time adsorption kinetics, (Elwing 1998), or matrix-assisted laser desorption ionisation mass spectrometry (MALDI-MS) adapted for surface analysis determination (Griessera, Kingshottb, *et al.* 2004). All of these methodologies require a high degree of operator expertise and skill to obtain truly quantitative data in addition to specialised equipment.

The aim of this chapter was to validate the use of the fluorophore probes as protein labels for tracking protein adsorption and desorption in a competitive environment. In order to validate the use of direct protein labelling with the fluorophore probes in quantitative monitoring of adsorption and desorption two sets of experiments were performed. In addition, adsorption isotherms for BSA to HA and SA were constructed in order to observe BSA behaviour and calculate the BSA surface coverage to the two materials.

(1) In the first set of experiments BSA adsorption and desorption was monitored using an established commercially available total protein assay kit.

(2) In the second set of experiments BSA adsorption and desorption was monitored directly through analysis of fluorescence intensity of the fluorophore labelled BSA.

Details of the fluorescent labelling can be found in Chapter 3, section 3.3.1. Both protocols utilise the phenomenon of fluorescence spectroscopy to monitor sample concentration.

4.2   Experimental Methodology

Bovine serum albumin (BSA) was used as a model protein, due to its relative cost effectiveness and abundance in blood plasma making it a useful comparator when studying the competitive environment. Protein adsorption and desorption on both hydroxyapatite (HA) and silicate-substituted apatite (SA) materials were investigated. Two morphological forms of the specimen were used making four groups of test specimen: silicate-substituted dense discs (SAD), silicate-substituted porous granules (SAG), hydroxyapatite dense discs (HAD) and hydroxyapatite porous granules (HAG). Details of the materials synthesis and characterisation can be found in Chapter 2.

All chemicals were supplied by Sigma-Aldrich unless otherwise specified. The commercial total protein assay kit used was a Quant-IT kit (Invitrogen, UK).

4.2.1   Specimens and Test solutions

Tabulated below are the type of specimens in Table 4.1 and test solutions in Table 4.2 used for the experiments undertaken in Table 4.3 and Table 4.4.

Table 4.1 – Specimen description and acronyms used throughout study

Specimen description	Acronyms
Silicate-substituted apatite dense discs	SAD
Silicate-substituted apatite porous granules	SAG
Hydroxyapatite dense discs	HAD
Hydroxyapatite porous granules	HAG

Test solutions of unlabelled (BSA) were generated from a stock solution of 50 mg/mL, and then diluted to the appropriate concentration with PBS or MEM to the required volume. A similar protocol was followed for the labelled (FTCA-BSA) from a stock solution of 15.8 mg/mL, as previously prepared and described in Chapter 3 section 3.3.1.

Table 4.2 – Test solutions: buffer, medium and protein solutions

Test solutions	Details	Concentrations
Phosphate Buffered Saline	PBS: dissolve one tablet in 200mL deionised water pH 7.4 (product code: P4417)	0.01 M
Minimum essential Eagles' medium	MEM: containing inorganic components, amino acids and vitamins (product code:M3024)	9.3 g/L
Bovine Serum Albumin (BSA)	BSA: lyophilised powder dissolved in PBS or MEM to produce stock solution of 50 mg/mL (product code:A9647)	Several from 0.002 to 20 mg/mL

Table 4.3 – Specimen and experiments undertaken in PBS

Specimens	SAD		SAG		HAD		HAG	
Temperature (^{o}C)	RT	37	RT	37	RT	37	RT	37
20 mg/mL BSA	√	√	√		√	√		
4 mg/mL BSA	√	√			√	√		
0.004 mg/mL BSA	√	√	√		√	√	√	
20-0.002 mg/mL BSA	√	√			√	√		
4 mg/mL FTCA-BSA	√	√		√	√	√		√

Table 4.4 – Specimen and experiments undertaken in MEM (at 37 ^{o}C only)

Specimen	SAD	SAG	HAD	HAG
8 mg/mL BSA	√		√	
4 mg/mL BSA	√		√	
2 mg/mL BSA	√		√	
1 mg/mL BSA	√		√	
0.5 mg/mL BSA	√		√	
4 mg/mL FTCA-BSA	√	√	√	√

RT is room temperature, which was 19 (± 2.0) ^{o}C. Dilutions were chosen in order to mimic BSA physiological concentration at 4 mg/mL, the pharmacological amounts

often used towards osteoinduction study of 4 µg/mL; and finally the other to represent BSA saturation levels above 4 mg/mL.

4.2.2   Adsorption and Desorption Protocol

For the quantitative data, BSA or FTCA-BSA solutions of different concentrations were prepared, and each of the protein solutions (1.5 mL) was then placed in a clean glass vial. A biomaterial, dense or porous, HA or SA was added to analyse **adsorption**, where 100 µL of protein solution was removed at the following intervals (1, 5, 10 and 15 minutes). After 15 minutes, the samples were removed and the original soaking solution stored. The samples were placed in PBS (1.5 mL), shaken for 5 minutes, then removed and the washing solution stored. The samples were then placed in fresh PBS or MEM (1.5 mL) to analyse **desorption**, where 100 µL of the solution was removed at the following intervals (5, 60, 240, 1440 minutes). The samples were kept in clear glass vials.
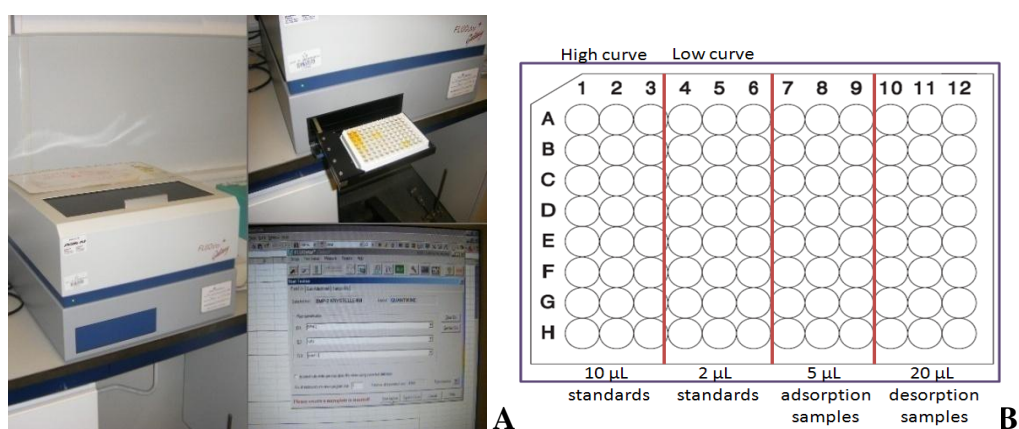
Figure 4.1 – (a) Picture of the FluoStar Instrument used for the analysis of adsorption and desorption and (b) plate layout

For the qualitative data, adsorbed FTCA-BSA from PBS at RT and MEM at 37 $^{\circ}$C were imaged (see section 4.2.5) on dense discs of the biomaterials after samples were incubated for time intervals of 1, 5, 10, 15, 30 and 60 minutes in solutions containing 4 mg/mL FTCA-BSA.

Instrument parameters: FluoStar Galaxy Microplate Reader: 96 –well plate reader (BMG laboratories, UK) with fluorescence intensity and time resolved settings with excitation and emission set at 485 and 520 nm, respectively. A cycle time of 120 seconds with 10 flashes, 0.5 seconds delay with orbital shaking set for 10 seconds before each cycle was used.

4.2.3   Analysis using the Quant-IT kit

The manufactures' standard protocol was followed, according to the leaflet provided. The components of the Quant-IT™ Protein Assay Kit were equilibrated at room temperature or 37 $^{\circ}$C for a few hours. A working solution was prepared by diluting Quant-IT™ protein reagent (1:200) in Quant-IT™ protein buffer in a plastic container, where for example, for 100 assays, 100 µL of Quant-it protein reagent (Component A) was diluted in 20 mL of Quant-it protein buffer (Component B) and mixed well. Glass containers were not used, as the protein reagent is known to adsorb to glass. Once mixed, the working solution is stable for up to 3 hours, if protected from light. 200 µL of the working solution was then loaded into each microplate well with a kit detection limit of 0.25-5.00 µg of protein. Despite this detection limit, calibrations were run at lower levels to accommodate the comparison with the novel FTCA-BSA probe developed in this work. Thus, using the standards provided by the Quant-IT protein assay kit, and the methodology as described by the manufacturer, two low calibration curves were prepared, one for the generation of the 0-5 µg standard curve, which required 10 µL of each BSA standards added in triplicate to wells containing the 200 µL of the working solution, and the second, for the generation of the 0-1 µg standard curve, where 2 µL of each BSA standards was added in triplicate to wells.

Two high calibration curves were also prepared to cover the higher concentration range of the adsorption study, in which the protein was found to crash out of solution unless vigorous stirring was applied immediately before the data was collected. For the generation of the 0-500 µg standard curve, 10 µL of each BSA standard was added in triplicate to wells containing the 200 µL of the working solution, and for the generation of the 0-100 µg standard curve, 2 µL of each BSA standard was added in triplicate to

wells. Table 4.5 shows the expected BSA amount observed per well for all 4 calibration curves, two low and two high, which were prepared in PBS and MEM.

Table 4.5 – Amounts of the BSA in serial dilutions used for the Calibration curves

Amount of BSA per well in µg			
5-0	1-0	500-0	100-0
5.0	1.0	500.0	100.0
4.0	0.8	250.0	50
3.0	0.6	125.0	25
2.0	0.4	62.50	12.5
1.0	0.2	31.30	6.25
0.5	0.1	15.60	3.13
0.25	0.05	7.810	1.56
0	0	0	0

Protocol for the determination of the BSA surface coverage

Adsorption isotherms of unlabelled-protein (BSA) on SAD and HAD both at 19 (± 2.0) ^{o}C (room temperature: RT) and at 37 ^{o}C were investigated in order to determine the average monolayer coverage of BSA on the dense biomaterials. Assumptions were made in order to determine the surface area of both the albumin and the discs. Albumin was calculated using the assumptions that it has a molecular weight of 66,320 Daltons (Harlow and Lane 1988) and is a globular protein (prolate ellipsoid) with dimensions of 140 x 40 x 40 Å (Hirayama, Akashi, *et al.* 1990), resulting in a cross-sectional surface area of 5.03 x10^{-17} m^{2}. It was also assumed that only the top side and side of the dense disc would be available for protein adsorption, tabulated below.

Table 4.6 – Calculated Surface Area for the dense biomaterials using micrometer measurements

Biomaterials	Surface area (±σ) / m^{2}
SA	2.24 x10^{-4} (±0.001)
HA	2.22 x10^{-4} (±0.001)

The surface area of the dense discs was determined by taking the average disc dimensions and calculating the area by assuming each disc to be a smooth perfect cylinder with top and side most exposed to protein under investigation. Previous work (in Chapter 2) had demonstrated that these assumptions were not strictly true as the discs are known to have a surface roughness of 0.3-0.4 μm and were not perfect cylinders, however this proved to be the most practical method available, as surface area was found to be below the detection limits of both the BET porosimeter and He pycnometer.

Using these surface area values, the theoretical number of binding sites for both biomaterials can thus be calculated with Equation 4.1 and tabulated in Table 4.7.

$$Theoretical\ Number\ of\ Binding\ sites\ per\ protein\ unit = \frac{Disc\ Surface\ Area}{BSA\ Surface\ Area}$$

Equation 4.1

Table 4.7 – Theoretical Number of Binding Sites; a ratio of the surface area values

Biomaterials	Theoretical Number of Binding Sites
SA	4.46×10^{12}
HA	4.41×10^{12}

The surface area values were then used to calculate the adsorption surface coverage in terms of molecules per dense disc, while using the Quant-it kit protein assay allowed for the amount of BSA adsorbed to be obtained.

$$\Gamma = \left(C_o - C_{eq}\right) \times (V/m)$$

Equation 4.2 – Adsorbed (Γ) amount equation (D'Andrea and Fadeev 2003)

The adsorbed amounts were calculated using Equation 4.2, where Γ is the adsorbed amount in mol per g, C_o is the original protein concentration in mol dm^{-3}, C_{eq} is the equilibrium concentration after adsorption in mol dm^{-3}, V is the total protein volume of the solution in L and *m* is the mass of the sample in g. Using this equation, a relationship in the adsorption isotherm can thus be determined quantitatively, in terms of BSA surface coverage in percentages adsorbed on the surface of the biomaterials.

4.2.4   Analysis using the Fluorophore

All FTCA-BSA buffer and medium solutions were equilibrated at RT (19 ($\pm$ 2.0) ^{o}C) on the bench top or at 37 ^{o}C in an incubator for a few hours. 200 µL of the freshly made PBS or MEM was then loaded into each microplate well. For the analysis: 5 µL of original and adsorbed samples were placed in the wells according to the layout (see Figure 4.1B) followed by 20 µL of the wash and desorbed samples, and the standards for each method where 10 µL and 2 µL were added to separate wells.

FTCA-BSA (15.8 mg/mL) in PBS or MEM was used to construct calibration curves. Serial dilutions (1 mL) were prepared, from which, high and low standards were generated following a similar protocol to that of BSA only protein solution.

Table 4.8 – Amounts of the BSA in the FTCA-BSA serial dilutions used for the Calibration curves

BSA Concentrations / µg		
Original/ µg/mL	10 µL	2 µL
15800	158	31.6
7900	79.0	15.8
3950	39.5	7.90
1975	19.6	3.95
988	9.88	1.96
494	4.94	0.988
247	2.47	0.494
0	0	0

The two calibration curves generated were 0-158 µg high standard curve, which required 10 µL of FTCA-BSA standard added in triplicates to wells containing fresh PBS or MEM (200 µL). The low 0-32 µg standard curve was generated using 2 µL of the FTCA-BSA. To make the calibration curves, the protein concentration was plotted against fluorescence intensity; a line of best fit was generated to obtain an equation of the linear line along with the R^2 value. Using the equation of the line in the form of $y =$

mx + C with the intercept set at 0 when the data was best fitted, the actual protein amount per well can be calculated, and thus the amount in the total volume deduced.

To test the calibration curves a series of FTCA-BSA solutions were prepared and fitted. For this test analysis FTCA-BSA (15.3 mg/mL) in MEM stock solution was used to make eight different concentrations including stock, 12, 10, 8, 4, 2, 1 and 0.5 mg/mL. 5 µL of each solution were then placed in wells, containing 200 µL of MEM, according to the layout as shown in Figure 4.1B, done in triplicate at 37 $^{\circ}$C.

4.2.5   Fluorescence Microscopy

Fluorescence microscopy was performed using a Zeiss Axioskop microscope, employing a mercury lamp UV source, and three filters with excitation/emission wavelengths of 450-490/515 nm, 365/395 nm and 546-512/598 nm which enable imaging of dyes that fluoresce in the green, blue or red, respectively. The images (micrographs) were taken at magnifications of 50, 100 or 200 and used for qualitative analysis of the protein adsorption on dense discs of the biomaterials with a working fixed exposure of 695 milliseconds.
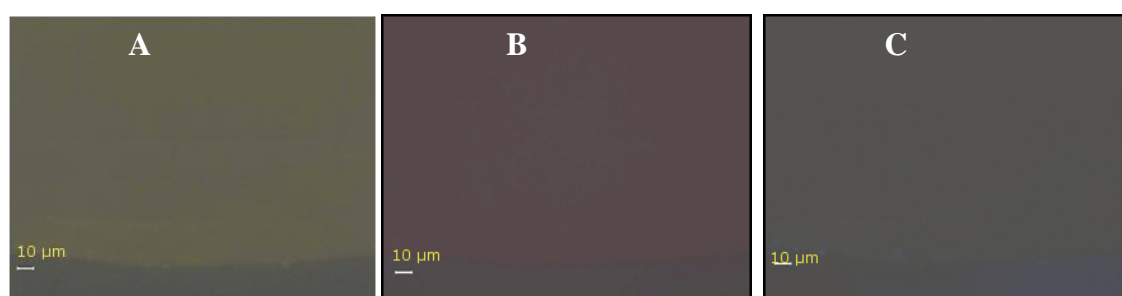
Figure 4.2 – FM background images of HAD emitting (a) green, (b) red and (c) blue fixed at an exposure of 695 ms, scale shown to represent 10 µm.

Initially, the HA and SA dense discs were imaged blank for the background fluorescence (Figure 4.2 and Figure 4.3) at a fixed exposure of 695 and 3930 ms, respectively, with a 50X magnification through three distinct filters. The main interest to these FM images was the green and red emission observed, so the following images were focused on these and compared between biomaterials in terms of adsorption time at 200X magnification with a scale shown to represent 10 µm.
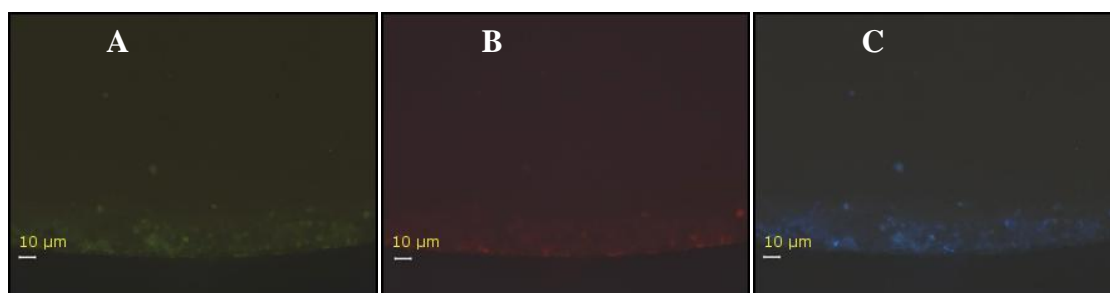
Figure 4.3 – FM background images of SAD emitting (a) green, (b) red and (c) blue fixed at an exposure of 3930 ms, scale shown to represent 10 μm.

The BSA coated samples were prepared as follows: 1 mL aliquots of FTCA-BSA at 4 mg/mL in PBS or MEM at 37 $^{\circ}$C was transferred in to 24-well plate containing dense disc of the biomaterials, and left submerged for 1, 5, 10, 15, 30 and 60 minutes. After immersion time, the discs were rinsed in PBS or MEM then imaged, and transferred into a clean 24-well plate containing formaldehyde.

4.3   Results

4.3.1   Quant-IT analysis

Calibration curves for the unlabelled BSA study at room temperature (RT, 19 ($\pm$ 2.0) ^{o}C) and 37 ^{o}C in PBS and MEM were generated using both the Quant-IT kit supplied BSA standards for the low ranges and in house prepared protein solutions for high ranges. This resulted in the generation of two low protein range calibrations at levels of 0-1 and 0-5 µg BSA per well, and two high protein range calibrations at levels of 0-100 and 0-500 µg BSA per well.

Table 4.9 – R^2 values of the BSA calibrations in PBS at RT

Range	BSA / µg	R^2 values obtained
Low	0-5	0.996
	0-1	0.948
High	0-500	0.904
	0-100	0.882

Table 4.10 – R^2 values of the BSA calibrations in PBS at 37 ^{o}C

Range	BSA / µg	R^2 values obtained
Low	0-5	0.995
	0-1	0.987
High	0-500	0.967
	0-100	0.922

The calibration values obtained, using the Quant-IT Kit at RT and 37ºC, are shown in Table 4.9 and Table 4.10 respectively. For the low range the R^2 values were lower at 37 ^{o}C compared to RT, while for the high range the opposite behaviour was observed. Overall, the correlation was good, more polynomial than linear for any of the ranges (Appendix 19 to Appendix 22 in Figure 129 to Figure 132) from the point of origin and thus the kit had inherent detection limits set by the calibration range selected, to a minimum of 0.2 µg per well.

A change in medium (MEM) improved correlation moderately for the low and high ranges, as shown in Table 4.11, however, relationships remained non-linear (Appendix 19 to Appendix 22 in Figure 129 to Figure 132).

Table 4.11 – R^2 values of the BSA calibrations in MEM at 37 degrees

BSA	Range µg	R^2 values obtained
Low	0-5	0.995
	0-1	0.933
High	0-500	0.922
	0-100	0.907

Using the Quant-IT kit, the analysis of the low concentration at 0.004 mg/mL BSA was not possible as expected. Protein amounts in 5 and 20 µL corresponded to 2 and 8 ng per well, respectively, which are lower than that of the manufacturers recommended low range of 0.25 µg per well, which agreed with our findings.

Analysis of the median concentration at 4 mg/mL, which is also the physiological concentration of BSA, was successful, see Figure 4.4. The time-dependent adsorption profiles showed porous granules adsorbed less BSA than dense discs in an overall trend as follows SAD > HAD > SAG > HAG with more affinity towards the silicate samples. Dense disc (DD) samples showed a faster rate of adsorption compared to the porous granular (PG) samples, which showed a slower rate which could be due to the diffusion in the pores of the protein in solution, followed by a plateau of BSA adsorption. Desorption, in contrast, was instantaneous from porous granules (PG) with extensive desorption from HAG and very little desorption occurred from HAD, giving rise to a desorption trend as follows: HAG > SAG >> HAD = SAD.
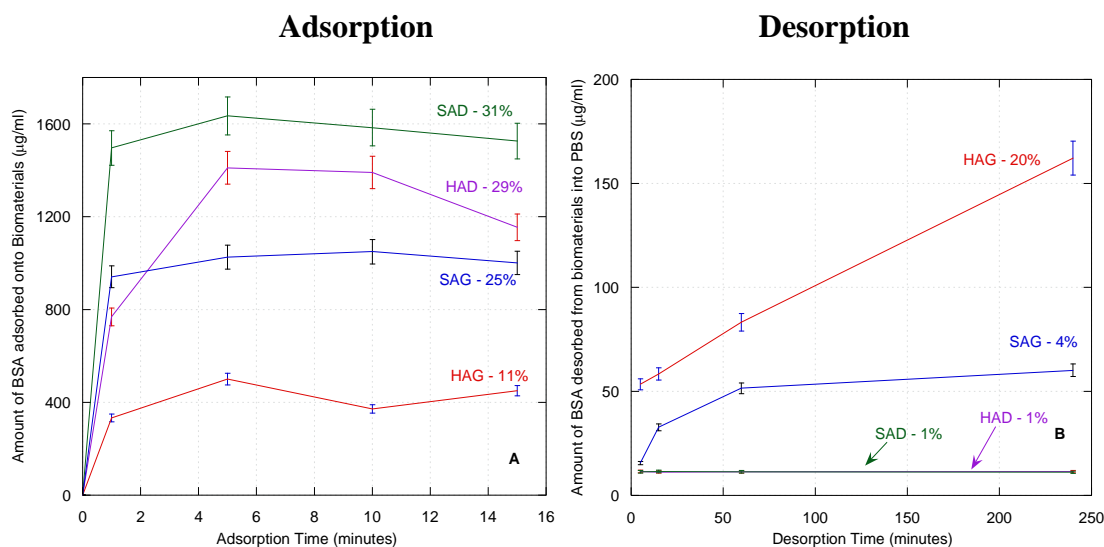
Figure 4.4 –BSA (a) adsorption and (b) desorption profiles on biomaterials at RT analysed using the Quant-it kit at an initial concentration of 4 mg/mL in PBS (n= 3 ±s.d.)

At high concentration (40 and 20 mg/mL), the analysis was unreliable as the Quant-IT kit reagent instigated precipitation of the protein from solution at this high concentration.

Adsorption profiles on silicate-substituted hydroxyapatite showed a similar behaviour between dense discs and porous granules to the physiological concentration, where DD adsorbed more than PG with larger adsorbed amounts. The desorption also showed a similar pattern to that observed at physiological concentration, in the following trend HAG >> SAG >> HAD > SAD.

Determination of BSA surface coverage on dense discs (DD)

As there appeared to be some temperature effect, adsorption isotherms were investigated on dense discs of the biomaterials, at RT (19 ($\pm$ 2.0) ^{o}C) and 37 ^{o}C.

Figure 4.5 and Figure 4.6 depict the raw time-dependent data observed on SAD and HAD, respectively, at RT and 37 ^{o}C at around the physiological BSA concentration.

Adsorption on SAD showed BSA adsorbing more with increasing initial concentrations at RT with the exception of the 5 mg/mL solution, Figure 4.5A. At the 15 minutes time point more BSA was adsorbed from the 4 mg/mL protein solution compared to the others, followed by the 2, 5 and finally 1 mg/mL solutions. Past this time point for all

concentrations except the 5 mg/mL solution, a slow decrease or plateau of the adsorbed amounts was observed.

At 37 ^{o}C, there was more BSA adsorbed from the smaller protein concentrations compared to the larger ones, where at the 15 minute time point, more BSA was adsorbed from the 2mg/mL solution compared to the 1, 5 and 4 mg/mL solutions, Figure 4.5B. However, beyond that for all concentrations except the 5 mg/mL solution, a slow increase or plateau of the adsorbed amounts was observed.
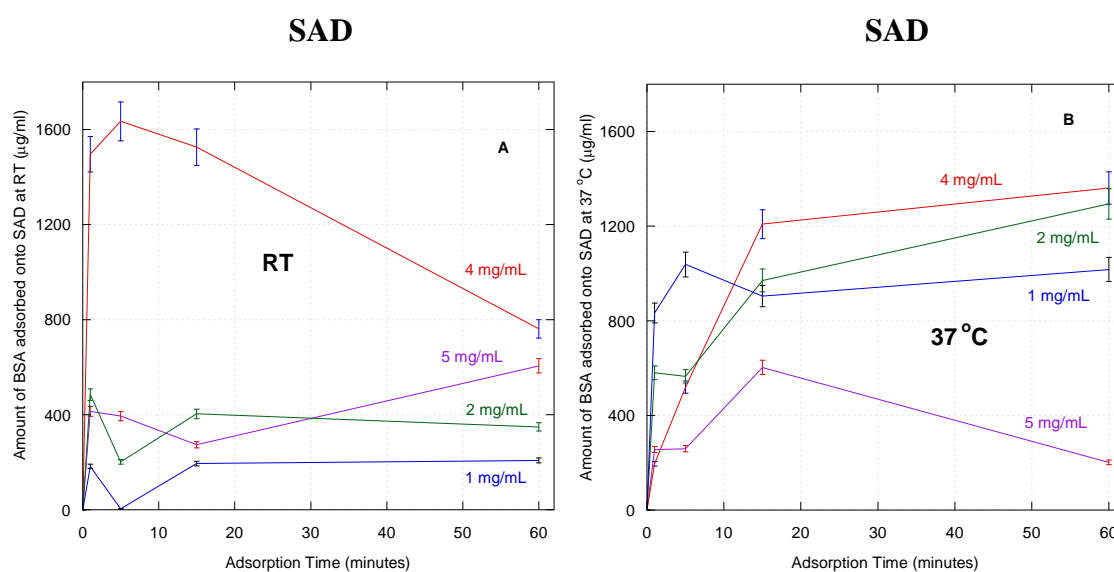
Figure 4.5 - Adsorption profiles of BSA protein at around physiological concentrations on SAD at (a) RT and (b) 37 ^{o}C using the Quant-it kit in PBS (n= 3 ±s.d.)
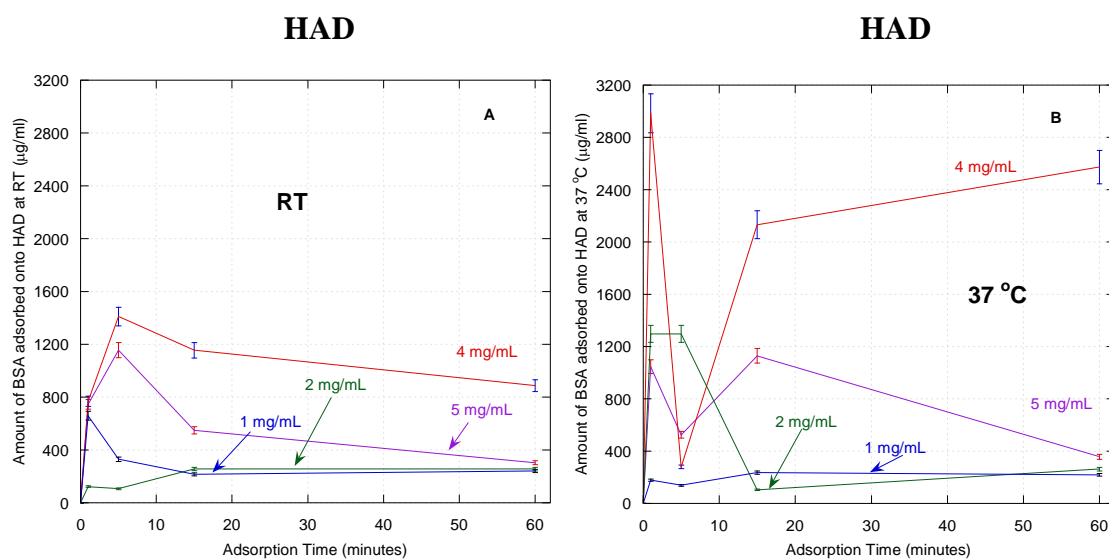
Figure 4.6 - Adsorption profiles of BSA protein at around physiological concentrations on HAD at (a) RT and (b) 37 ^{o}C using the Quant-it kit in PBS (n= 3 ±s.d.)

Adsorption on HAD showed BSA adsorbing more from the higher concentrations compared to the lower ones, where more BSA was adsorbed from the 4 mg/mL solution (the physiological level). At the 15 minute time point compared to the others, see Figure 4.6A. Beyond the 15 minutes, less BSA was adsorbed, decreasing with time, from the higher concentrations, while for the lowers one the amount adsorbed seemed to have reached a plateau.

At 37 ^{o}C, the initial BSA adsorption seemed fast with a dynamic behaviour, see Figure 4.6B. At the 15 minute time point, significantly more BSA was adsorbed from the physiological level (4 mg/mL) protein solution compared to the other protein solutions with an observed dip at the 5 minute point.

The other concentrations adsorbed less than the 4 mg/mL protein solution, they also go through a dip at 5 minutes with the exception of the 2 mg/mL solution, but not as drastic as the physiological concentration solution. Overall more BSA was adsorbed at 37 ^{o}C, compared to at RT for the 5 and 4 mg/mL solution, and less for the 2 mg/mL protein solution, and no significant difference for the 1 mg/mL solution.

Figure 4.7 and Figure 4.8 depict the raw data on SAD and HAD, respectively, at higher BSA concentrations.

Adsorption on SAD show more BSA adsorbed with increasing concentrations at RT (Figure 4.7A). However, the adsorption was not significantly different from the two concentrations for the first two time points. Beyond the 5 minutes time point, there was a further increase in BSA adsorbed from the 20 mg/mL solution compared to an observed decrease from the 10 mg/mL solution. Beyond the 15 minutes time point, both protein solutions show a slow and steady decrease of BSA adsorbed on the biomaterial's surface.

At 37 ^{o}C in Figure 4.7B, different adsorption patterns were observed from both BSA concentrations. For the first two time points, more protein was adsorbed from the 20 mg/mL solution, however past that point there was a sharp decrease from that protein solution, which was then adsorbing less than the 10 mg/mL BSA solution for the remainder of the adsorption period.
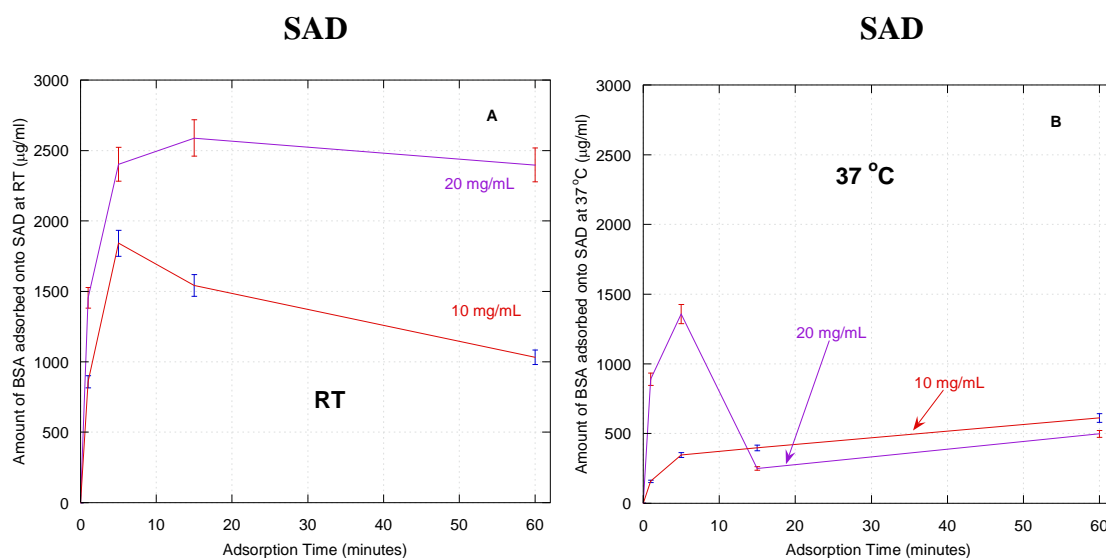
Figure 4.7 - Adsorption profiles of BSA protein at high concentrations on SAD at (a) RT and (b) 37 ^{o}C using the Quant-it kit in PBS (n= 3 ±s.d.)

Adsorption on HAD show at both temperatures more BSA adsorbed with increasing BSA concentrations, see Figure 4.8A. At RT, the patterns for 20 and 15 mg/mL concentrations show a dip at the 15 minutes time point compared to a dip seen at the 5 minutes time point for the 10 mg/mL concentration.
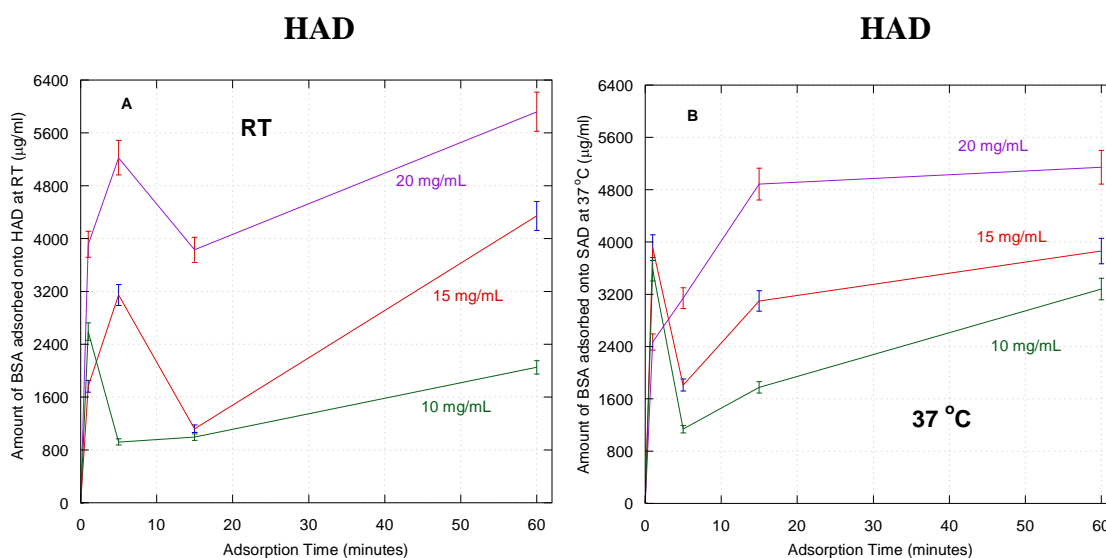
Figure 4.8 - Adsorption profiles of BSA protein at high concentrations on HAD at (a) RT and (b) 37 ^{o}C using the Quant-it kit in PBS (n= 3 ±s.d.)

Beyond the 15 minutes, all concentrations showed increased BSA adsorption. At 37 ^{o}C, there was no significant adsorption difference between the 15 and 10 mg/mL concentrations at the 1 minute time point. An observed dip was also seen at these

131

concentrations at the 5 minutes time point. For the 20 mg/mL concentration, an increasing BSA adsorption pattern was seen up until the 15 minutes time point was reached, then beyond that, the rate of adsorption was reduced but still increasing. A similar observation was depicted here for the 15 and 10 mg/mL BSA concentrations.

Using the raw time-dependent data in Figure 4.5, Figure 4.6, Figure 4.7 and Figure 4.8, and the methodology in conjunction with Equation 4.1 and Equation 4.2 copied here below (1) and (2), respectively, the concentration-dependent adsorption isotherms for HAD and SAD were calculated at RT and 37 ^{o}C, see Figure 4.9.

$$(1) \ Theoretical \ Number \ of \ Binding \ sites \ per \ protein \ unit = \frac{Disc \ Surface \ Area}{BSA \ Surface \ Area}$$

$$(2) \ \Gamma = \left(C_o - C_{eq}\right) \times (V/m)$$

Adsorption isotherms on HAD both at RT and 37 ^{o}C clearly showed three different patterns in the three regions (A, B and C), as shown in Figure 4.9A and B, compared to only 2 patterns of behaviour on SAD across the three regions.

On HAD at RT, Region A occurred over the lower concentrations with no significant change in BSA adsorbed with time and increasing equilibrium concentration. In region B, as the equilibrium concentration increased more BSA was adsorbed, the highest levels being achieved between the 5 and 60 minute time points. And finally in Region C, the physiological BSA level of 4 mg/mL, which is the equivalent of an equilibrium concentration of 6.03 x 10^{-8} mol/L, the highest adsorbed amount was observed at the 15 minute time point, following a dipped trend for all other time points. At 37 ^{o}C, the three regions of behaviour were similarly identified in Figure 4.9B, again region A was consistent with the behaviour of a monolayer, as seen at RT, with an increased adsorbed amount of BSA observed. Region B remained the highest of the regions, but slightly less adsorbed amounts compared to RT; however, more BSA was adsorbed at 15 and 60 minute time points. In Region C, higher levels of BSA were adsorbed at all time points except at 5 minutes.

On SAD only 2 adsorption patterns were observed across the three regions both at RT and 37 ^{o}C, as shown in Figure 4.9C and D, respectively, compared to HAD. At RT, the monolayer formation (Region A) was reached faster, rapidly forms into the next step in

Region C, then closely followed by Region B, the highest region of adsorbed amount of BSA. While at 37 ^{o}C, Region A showed an increased amount of BSA adsorbed on the surface at all time points, little change in Region C except at the 15 minute time point was observed, and a decreased amount of BSA was adsorbed in Region B. Figure 4.9D BSA adsorption did not rise with increasing equilibrium concentration.
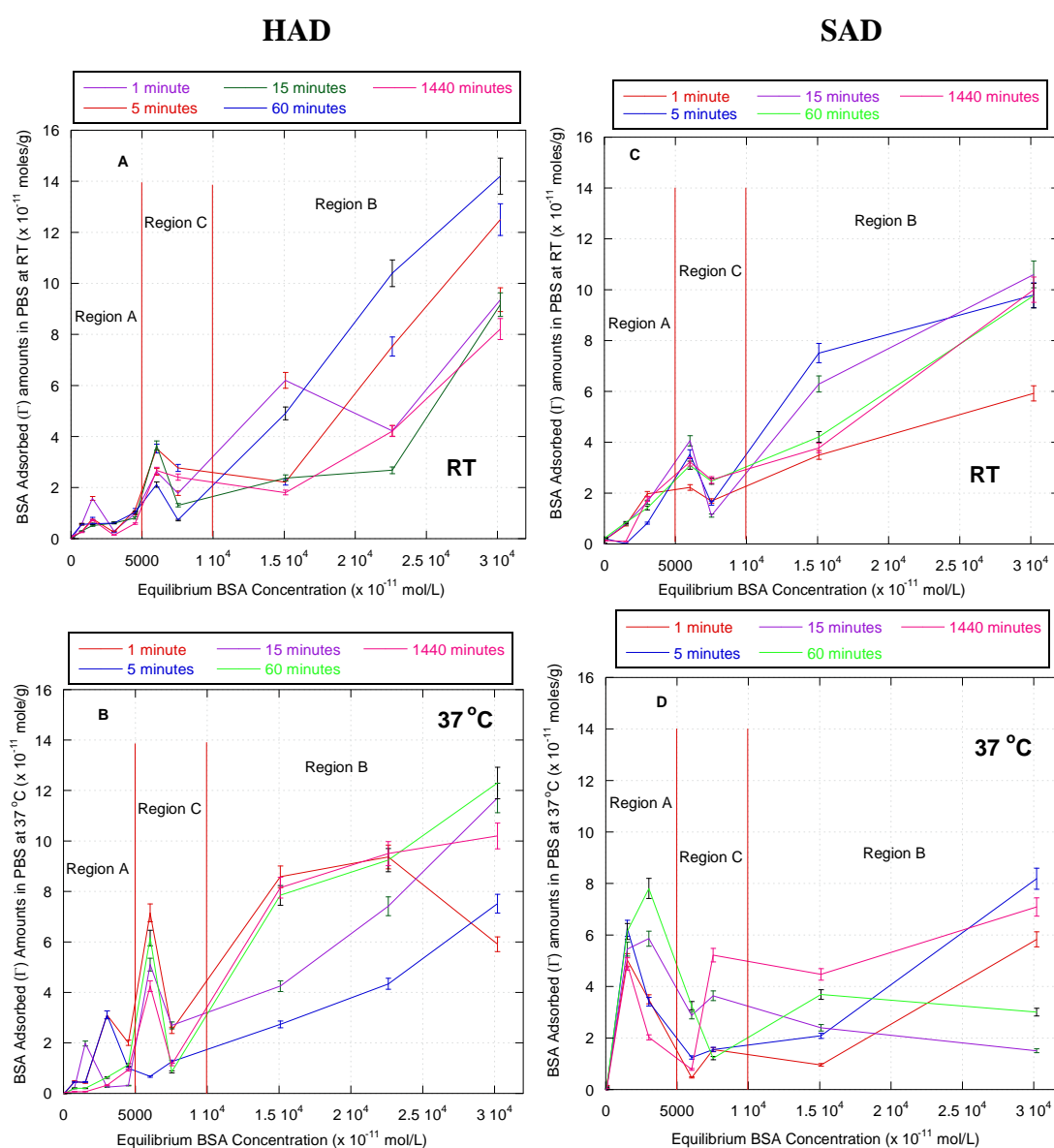
Figure 4.9 - Adsorption Isotherms of BSA in PBS on HAD at (a) RT and (b) 37 ^{o}C and SAD (c) RT and (d) 37 ^{o}C using the Quant-it kit (n= 3 ±s.d.)

The BSA surface coverage at 6030 x 10^{-11} mol/L, which is equivalent to the physiological concentration of BSA at 4 mg/mL, was then calculated.

At RT, HAD had a BSA surface coverage of more than 100 % from the first time point of immersion at its highest and decreasing with time, suggesting the rapid formation of multi-layer BSA sheets on the surface of the biomaterials. A similar observation was seen on SAD, where the BSA surface coverage was also more than 100 % starting from its lowest and increasing with time until the 15 minute time point, then slowly decreasing with time.

At 37 ^{o}C, higher BSA surface coverage was observed from HAD, except at the 5 minute time point where only 91.4 % was calculated, this was lower than 100 %, suggesting that at that time point a BSA monolayer might be present. Again on SAD, the BSA surface coverage started low at 63.6 %, then increased with time up until the 1440 time point, with a similar magnitude to RT values found. This may suggest that at 37 ^{o}C, the BSA coverage on the SAD surface was accumulative, starting with the monolayer, saturating just before the 5 minute time point (169 %), and increasingly forming the multi-layer with time.

4.3.2   Analysis using the Fluorophore (FTCA)

Calibration graphs were generated over two ranges using FTCA directly labelled on the BSA at RT (19 ($\pm$ 2.0) ^{o}C) and 37 ºC, in PBS and MEM demonstrated a linear relationship between the fluorescence intensity and the amount of protein present per well (Appendix 23 and Appendix 24 in Figure 133 and Figure 134) and correlation coefficients were much improved compared to the Quant-IT kit calibrations.

Table 4.12 – R^2 values of the FTCA- BSA calibration curves in PBS at RT

Range	BSA µg	R^2 values obtained
Low	0-31	0.997
High	0-158	0.968

Table 4.13 – R^2 values of the FTCA-BSA calibration curves in PBS at 37 ^{o}C

Concentration	Curves generated µg	R^2 values obtained
Low	0-31	0.962
High	0-158	0.927

Table 4.14 – R^2 values of the FTCA-BSA calibration curves in MEM at 37 ^{o}C

Concentration	Curves generated µg	R^2 values obtained
Low	0-32	0.926
High	0-159	0.942

In order to test the use of the fluorescent label as a quantitative monitoring tool known samples were prepared and analysed in MEM at 37 ºC. The results of this analysis demonstrated the technique to have an average error level of 6.7 % which was assumed to be acceptable as average error observed using the Quant-IT kit was 5.6 %.

Having identified that the technique was suitable for quantitative analysis the adsorption/desorption experiments performed with the Quant-it kit were duplicated with FTCA-BSA in PBS at RT at an initial BSA concentration corresponding to the physiological level of 4 mg/mL to ensure that addition of FTCA-BSA did not significantly affect the adsorption/desorption behaviour of BSA.

Table 4.15 – Values of the FTCA- BSA calibration curves in MEM at 37 °C

Known Sample Concentration (mg/mL)	Intensity Obtained	Calculated Concentration (mg/mL)	Percentage Error
15.3	35950	14.6	4.6%
12.0	32527	12.8	-6.6%
10.0	29316	11.2	-12%
8.0	26657	7.6	5%
4.0	19859	4.2	-5%

Figure 4.10 shows the amount of BSA adsorbed from HAD (A) and SAD (B) at RT as analysed using the Quant-it kit and FTCA-BSA, clearly showing similar quantities adsorbed at the end of the adsorption period, with very different adsorption trends obtained on both materials.

Desorption data (Figure 4.11), while indicating similar ultimate magnitudes of desorption from HAD and SAD, there was no significant difference, varied in that use of the FTCA-BSA enabled more accurate analysis of the pattern of release, reflecting the fact that these levels were approaching the detection limits of the Quant-it assay.

FTCA-BSA was then used to study the effect of test conditions on protein adsorption and desorption. Experiments were performed in PBS at 37 °C and in MEM at 37 °C to deconvolute the effect of changing both test environment and temperature.

HAD SAD
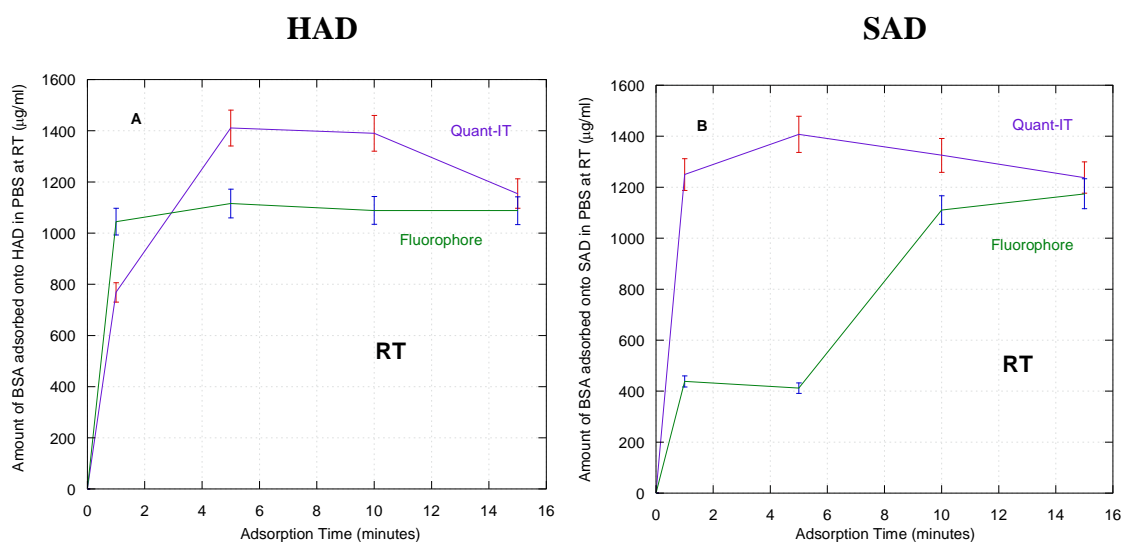
Figure 4.10 – Adsorption profiles of (a) HAD and (b) SAD at RT in PBS at an initial 4 mg/mL concentration, using Quant-IT kit and FTCA-BSA (n= 3 ±s.d.)

HAD SAD
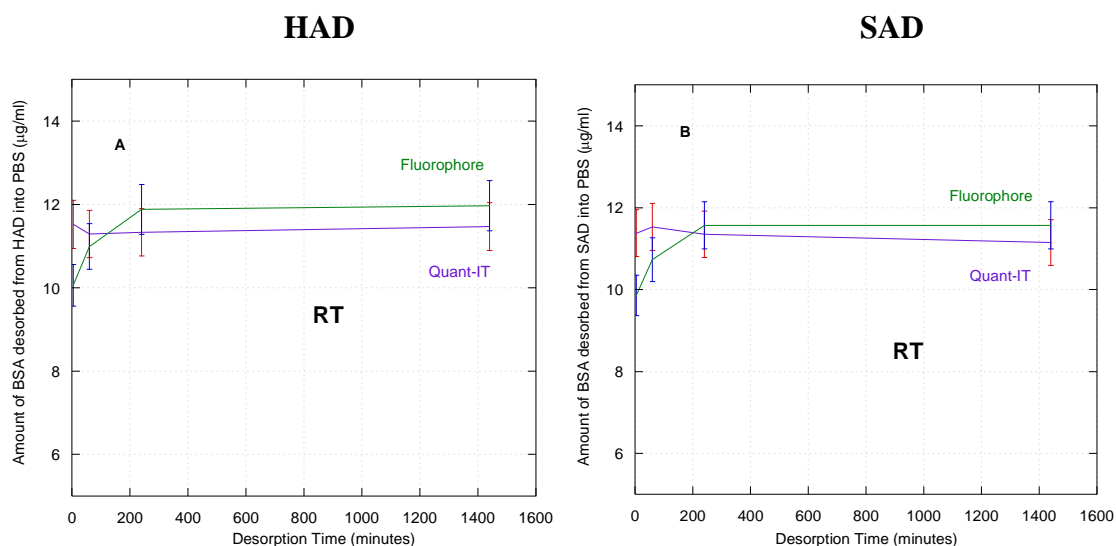
Figure 4.11 – Desorption profiles of (a) HAD and (b) SAD at RT in PBS at an initial 4 mg/mL concentration, using Quant-IT kit and FTCA-BSA (n= 3 ±s.d.)

FTCA-BSA was then used to study the effect of test conditions on protein adsorption and desorption. Experiments were performed in PBS at 37 ºC and in MEM at 37 ºC to deconvolute the effect of changing both test environment and temperature.

Figure 4.12 shows the effect of temperature on the adsorption and desorption of FTCA-BSA in PBS on the dense discs. More BSA was adsorbed at RT than at 37 $^{\circ}$C for both biomaterials at the end of the adsorption period.

Adsorption Desorption
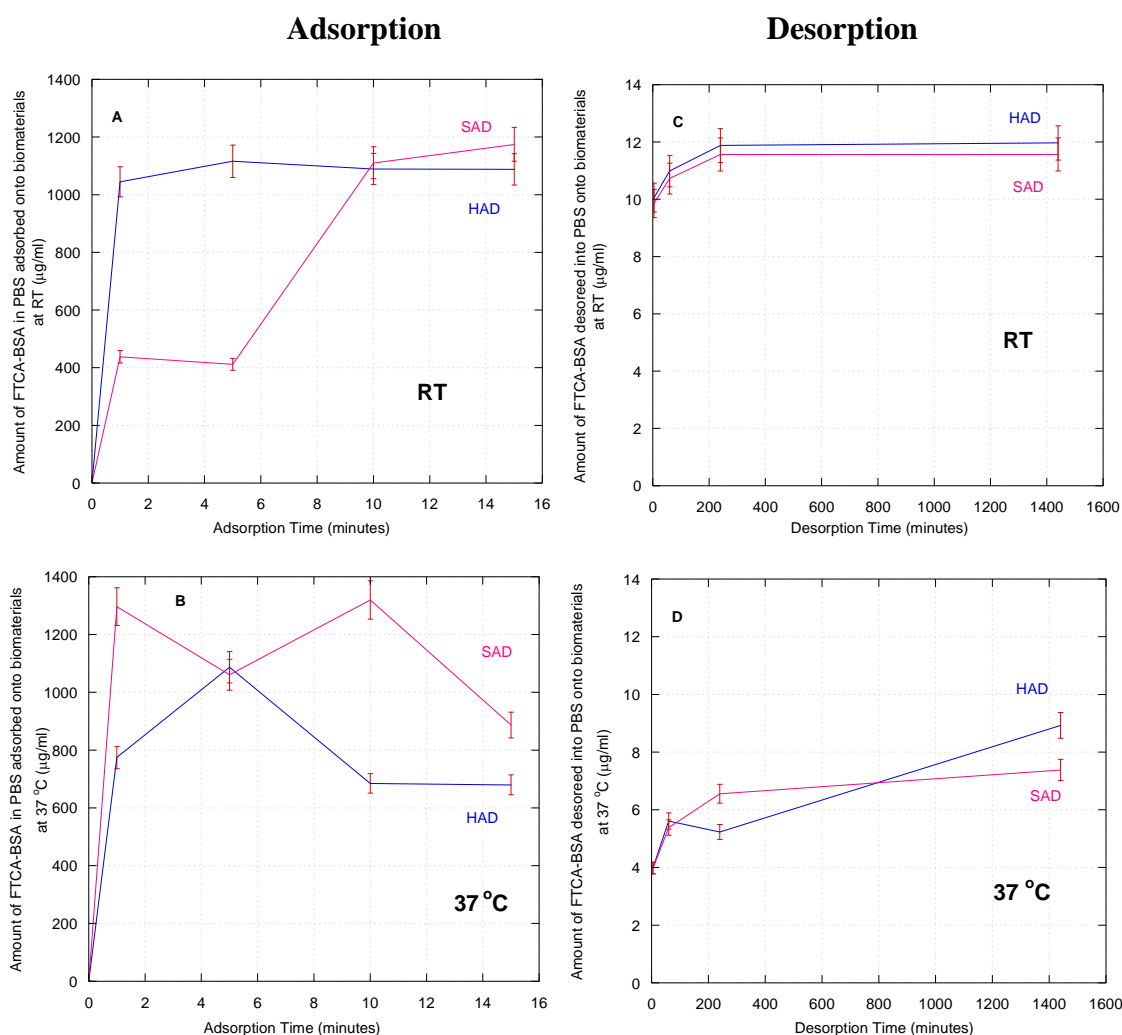
Figure 4.12 – FTCA-BSA (4 mg/mL) Adsorption at (a) RT and (b) 37 ^{o}C and desorption at (c) RT and (d) 37 ^{o}C profiles of the dense biomaterials in PBS (n= 3 ±s.d.)

In Figure 4.12A, the adsorption rate of HAD was much faster than that observed for SAD, and at the end of the adsorption time SAD and HAD adsorption were not significantly different. In Figure 4.12B, at 37 ^{o}C, the adsorption rate for both HAD and SAD was much faster with SAD significantly adsorbing more than HAD.

More BSA was desorbed at RT compared to 37 ^{o}C, however at RT the desorption was not significantly different between HAD and SAD (see Figure 4.12C). The increase in temperature on the desorption allowed for a distinctive behaviour to be observed, see Figure 4.12D, where HAD desorbed more than SAD, as seen previously by the Quant-IT data.

Figure 4.13 shows the effect of changing test environment at the same temperature (37 ^{o}C) from PBS to MEM on the dense discs.
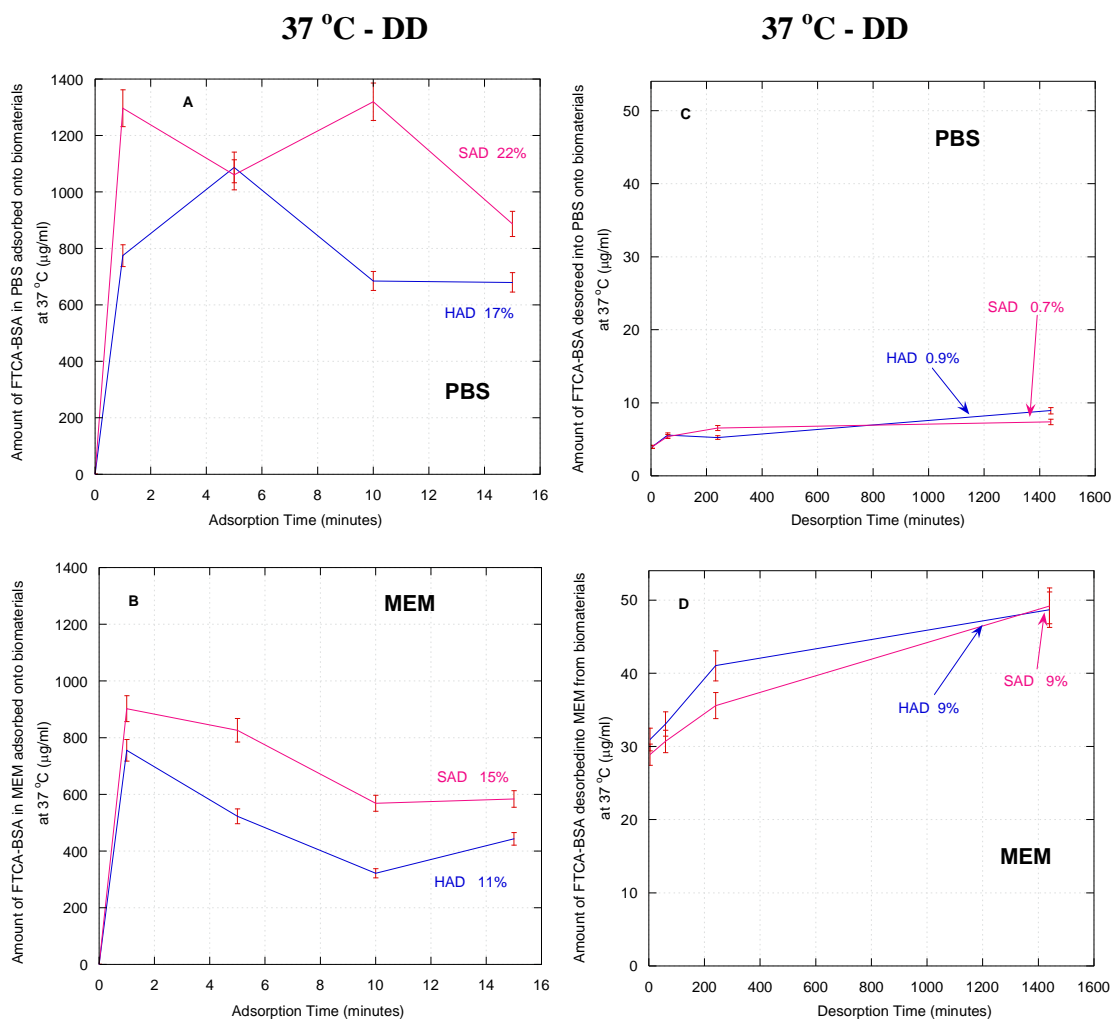
Figure 4.13 – FTCA-BSA (4 mg/mL) Adsorption in (a) PBS and (b) MEM and desorption in (c) PBS and (d) MEM profiles of the dense biomaterials in at 37 °C (n= 3 ±s.d.)

Figure 4.13A and B show that more FTCA-BSA adsorbed on the biomaterials in PBS than MEM with SAD adsorbing more than HAD. In both media the initial adsorption rate was fast with not significantly different between the biomaterials for the first minute of adsorption. Beyond that point, FTCA-BSA adsorbed more on the SAD specimen with some dynamism in PBS (Figure 4.13A), and a decreased behaviour in MEM, see Figure 4.13B.

Figure 4.13C and D show the effect of media on the desorption behaviour from the dense discs. The difference in media seemed to have induced a change in desorption pattern and amount of FTCA-BSA desorbed from the biomaterials. It appeared that more FTCA-BSA was desorbed in MEM to PBS with no significant difference at the end of the desorption period. Figure 4.13C shows a similar pattern in PBS to that

observed by the Quant-IT analysis. A slow and steady desorption rate for both biomaterials with a further increase seen from HAD, however, not so significant.

Figure 4.13D shows a different behaviour for both, where the rate was much faster in MEM than PBS and still increasing past the 240 minutes time point. HAD desorbed more than SAD, but the converged trend with desorbed amounts for both biomaterials being similar at the end of the desorption period.

The following graphs will show the effect of changing the biomaterial's morphological form from dense disc (DD) to porous granules (PG) in PBS and MEM at 37 ^{o}C. This would be comparable to the data found in Figure 4.13 for DD.
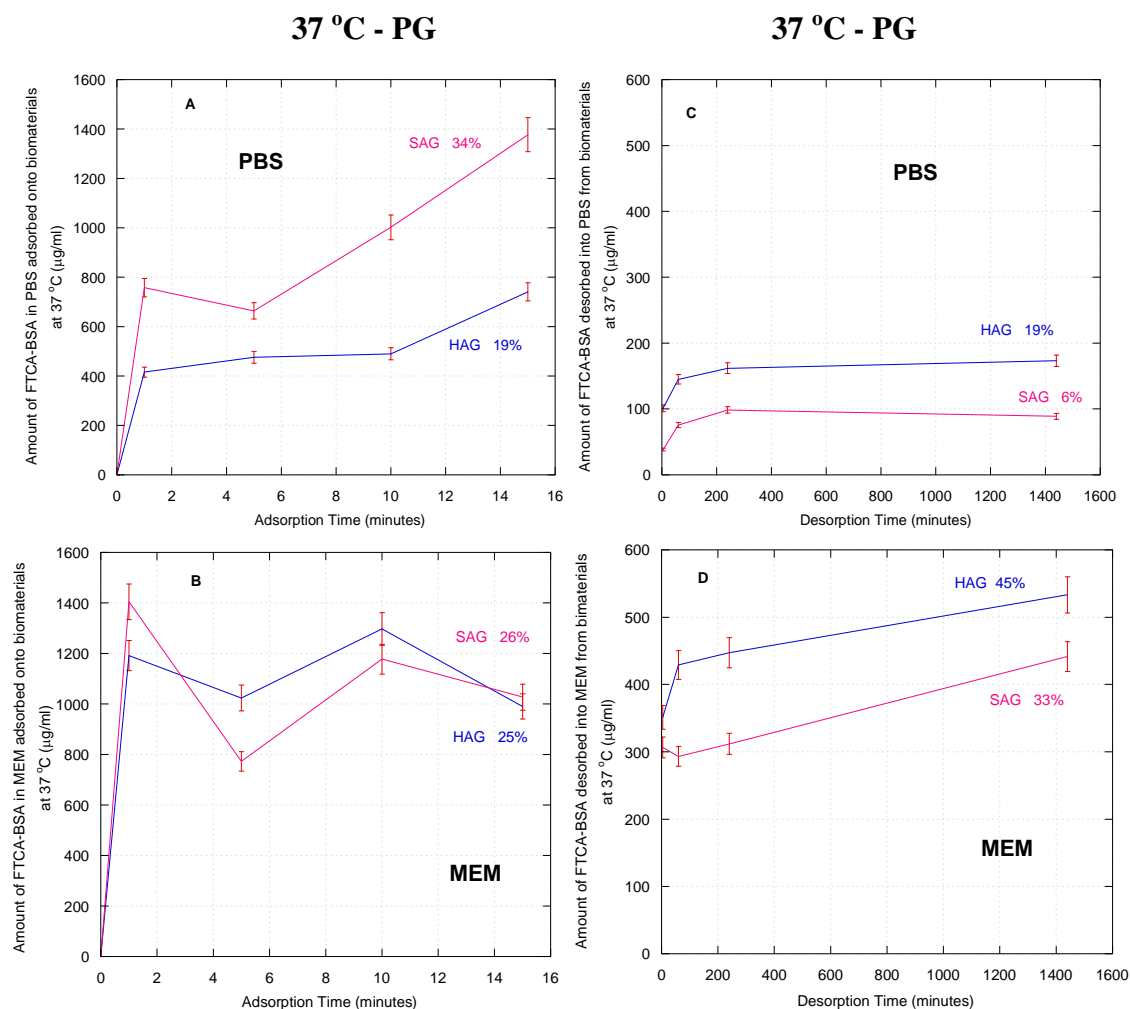
Figure 4.14 – FTCA-BSA (4 mg/mL) Adsorption in (a) PBS and (b) MEM at 37 ^{o}C and desorption in (c) PBS and (d) MEM at 37 ^{o}C profiles of the porous biomaterials (n= 3 ±s.d.)

Figure 4.14 shows more BSA was adsorbed in PBS than MEM with SAG adsorbing more than HAG at the end of the adsorption period. In MEM, SAG adsorbed less after 5 minutes, and then caught up in adsorption amount with HAG with no significant difference between the samples. Overall more FTCA-BSA was adsorbed on PG compared to DD as shown in Figure 4.13 with SA adsorbing more than HA with different patterns in MEM, but not in PBS.

Figure 4.14A shows a fast rate of adsorption from SAG than HAG in PBS with amounts of FTCA-BSA increasing with time, significantly more on SAG compared to HAG. In MEM, there was also a fast rate (see Figure 4.14B), but amount of adsorbed FTCA-BSA beyond the 1 minute adsorption period decreased in a dynamic manner.

Figure 4.14C and D show the effect of porosity on the desorption of FTCA-BSA from the biomaterials. More FTCA-BSA was desorbed in MEM than PBS from PG compared to DD(see Figure 4.13C and D) with the expected trend of HA desorbing more than SA, similarly seen throughout the study.

In conclusion, the study FTCA-BSA study showed both decreased adsorbed and desorbed FTCA-BSA amounts on DD in PBS with increasing temperature, a change in media also decreased the amount of FTCA-BSA adsorbed, but showed an increase in the desorption process. The introduction of porosity increased both the amount of FTCA-BSA adsorbed and desorbed, especially in MEM, where the small components may have helped in the protein diffusion into the porous biomaterials. Overall, more FTCA-BSA was adsorbed on SA compared to HA, and less desorbed on SA compared to HA.

4.3.3   Fluorescence Microscopy (FM)

A significant advantage of using FTCA-BSA (4 mg/mL) for analysis of protein adsorption/desorption behaviour was the ability to study the bulk morphology of BSA in contact with HA and SA, which was found to be very different on the biomaterials, yet similar in the different media.

The work was set up in two experiments. Initially in PBS at RT (19 ($\pm$ 2.0) ^{o}C) on HAD and SAD to help interpret the data obtained from the isotherms and the fluctuating adsorption pattern observed. And the other experiment at 37 ^{o}C in MEM to assess the BSA morphology in a different media.

Experiment One

Figure 4.15, Column A showed a fluctuating fluorescent intensity with increasing time that may suggest a dynamic FTCA-BSA adsorption on the surface at RT. Globular FTCA-BSA clusters were present heterogeneously spread across the surface. There was a change in morphology resulting in regions, where dual morphology was observed, up until the 60 minute time point was reached, where the protein clusters were again predominantly globular on the surface.

In contrast, the BSA morphology on SAD, as shown in Figure 4.15, Column C, showed more clusters from the first minute, more fluorescent with smaller globules. The protein was spread out more homogeneously across the surface, especially on the ten minute specimen, creating a mesh like effect. The protein still retained a globular shape as more time elapsed on the surface of the SA biomaterial in PBS.

Figure 4.15, Columns B and D showed the images when excited within the red emitting region, to observe if any autofluorescence has occurred, where HAD showed to have more autofluorescence than SAD.

Columns: A.   B.   C.   D.

HAD   **SAD**
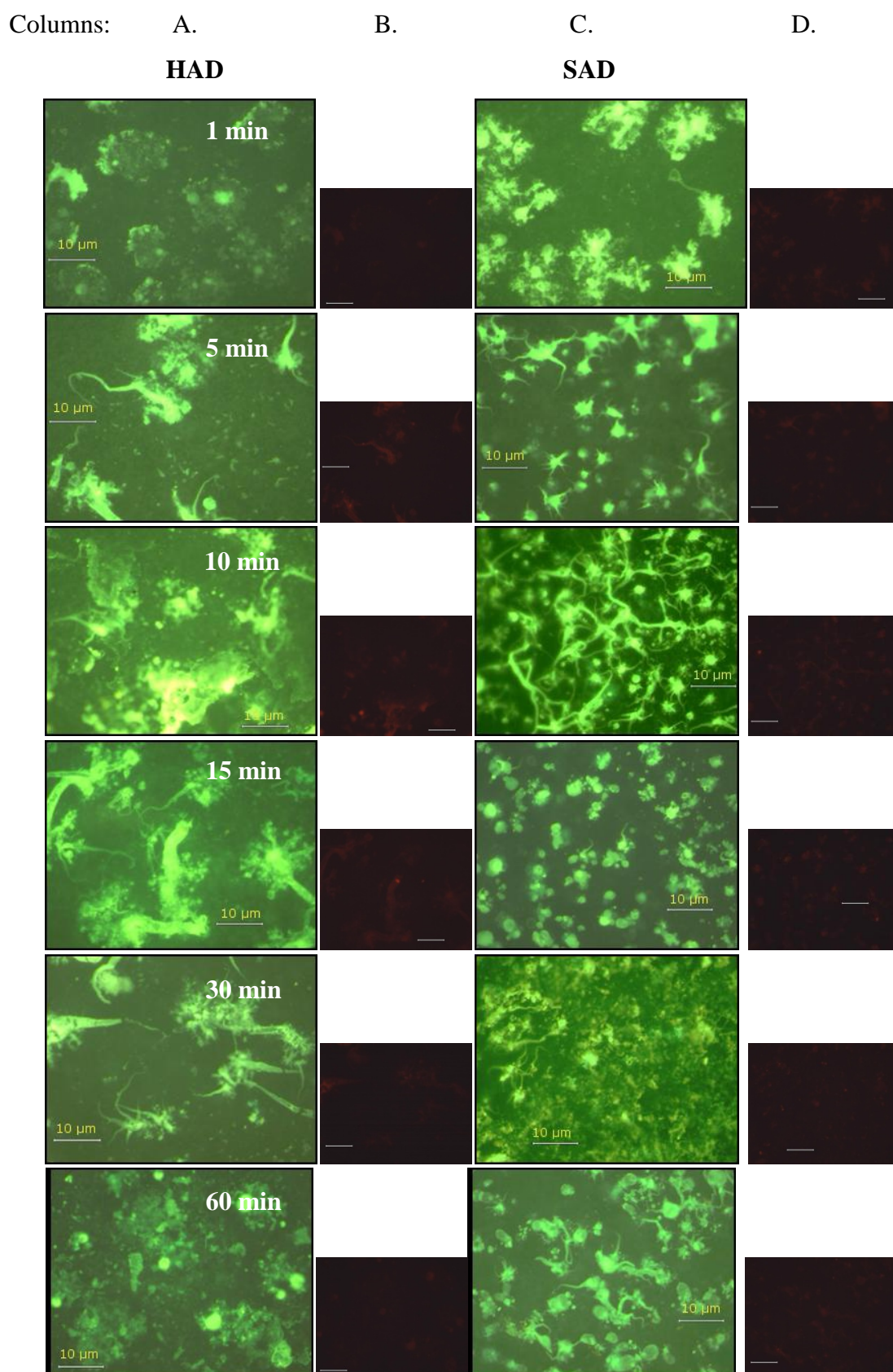
Figure 4.15 – FM images of FTCA-BSA demonstrating the protein morphology on (a) HAD and (c) SAD; and the black images which should show minimum amount of red emitting protein (b) on HAD and (d) on SAD at all time intervals in PBS at RT

Experiment Two

The second experiment set up involved looking at the morphology of the BSA in MEM at 37 ^{o}C on both biomaterials, HAD (see Figure 4.16, Column A) and SAD (see Figure 4.16, Column C). In MEM, no protein 'fingers' like morphology was observed. The adsorption was slower and the globules were smaller than those observed in PBS.

On HAD, smaller clusters were formed across the surface, which eventually accumulated to form larger clusters as time elapsed, heterogeneously spread on the surface. Thus, the fluorescence also increased with time.

While on SAD, the protein morphology was very similar to that observed in PBS. Smaller globules of protein were present on the surface compared to HAD surfaces. The globules began to cluster only after the fifteen minute time point, which then further continued after an hour.

Columns: A   B   C   D

HAD   **SAD**

Figure 4.16 – FM images of FTCA-BSA demonstrating the protein morphology on (a) HAD and (c) SAD; and the black images which should show minimum amount of red emitting protein (b) on HAD and (d) on SAD at all time intervals in MEM at 37 ºC

4.4   Discussions

Quant-IT kit calibrations showed a more polynomial rather than linear pattern both in PBS and MEM at RT (19 ($\pm$ 2.0) ^{o}C) and 37 ^{o}C (see Appendices 19 to 22). The graphs of the provided BSA standards and the two generated curves at 0 to 5 and 0 to 1 μg BSA per well were non-linear below 1.0 and 0.6 μg, respectively. Similar observation patterns were seen for the in-house BSA standards for the higher curves of 0 to 500 and 0 to 100 μg BSA per well, where the data was non-linear below 50 and 20 μg, respectively, even though the standards were repeated at different time in triplicate. Thus, in contrast, with the calibrations observed from the FTCA-BSA that gave rise to linear plot across the complete concentration range, throughout the repeats, suggesting reliability of the curves for the analysis of adsorption and desorption. (Appendices 23 and 24) This was a surprising observation as the commercial assay kits are expected to be more reliable than that; this may suggest that only a short range is used, as these would definitely show a more linear trend.

The FTCA-BSA was validated in two experimental set ups. Set up one consisted of making known concentrations of the FTCA-BSA, measuring their fluorescence intensity and fitting them to the calibration curves to calculate the actual concentrations. The results shown in Table 4.15 confirmed the validity of the method with an average error of 6.7 %, which could in part be due to operator handling. The second set up involved duplicate analyses of the adsorption and desorption behaviour on dense discs at RT using both the Quant-IT kit and FTCA. The results for this were depicted in Figure 4.10 for the adsorption and Figure 4.11 for the desorption, clearly showing similarities in amounts adsorbed and desorbed at the end of the designated period with distinct behavioural patterns.

4.4.1   Quant-IT kit Study

During the initial analysis, the Quant-IT kit proved to be only useful at RT (19 ($\pm$ 2.0) ^{o}C) and the physiological levels compared to the higher and lower concentrations, shown in Figure 4.4 with an adsorption trend was observed where SAD > HAD > SAG > HAG in PBS with a desorption trend of HAG > SAG >> HAD = SAD. Clearly

showing that silicate-substituted hydroxyapatite (SA) has a stronger binding affinity than stoichiometric hydroxyapatite (HA) measured by the commercial kit and further confirmed by previous studies, where in the work of Patel *et al.*, Hing and Guth *et al.* showed SA to enhance bioactivity and biocompatibility towards improved bone repair. (Guth, Campion*, et al.* "Effect of Silicate-Substitution on Attachment and Early Development of Human Osteoblast-Like Cells Seeded on Microporous Hydroxyapatite Discs" 2010; Hing 2004; Patel, Best*, et al.* 2002)

At low BSA levels, it was assumed, then verified *via* the calibrations non-linearity, that the detection limit of the kit was reached. Therefore, another kit would have been necessary to quantitatively measure protein at this level, which would mean adding on a further expense and probably another time-consuming manufacturer's procedure.

At high BSA levels, the working reagent solution made the protein crash out of solution, during plate-reading. It often required additional vigorous agitation to determine the protein concentration. Dilution of the samples could have been undertaken, so that protein was within the kit working range, however it would not have mimicked the desired adsorption-desorption environment. Also, the kit, being a total protein kit, means that the analysis would involve all proteins in any given sample and the specific discernment of proteins would therefore not be possible in a competitive environment.

Determination of the BSA coverage through the adsorption isotherms using the Quant-IT kit

At around the physiological level, the effect of temperature on SAD showed BSA adsorbing in the following trend 4 > 5 > 2 > 1 mg/mL protein solutions at RT (19 (± 2.0) ^{o}C) compared to the patterns seen at 37 ^{o}C, 2 > 1 > 4 > 5 mg/mL (see Figure 4.5). On HAD, a different behaviour was seen where at both RT and 37 ^{o}C, the adsorption trend was the same 4 > 5 > 2 = 1 mg/mL protein solutions (see Figure 4.6). More BSA was adsorbed on SAD compared to HAD at RT, while curiously the effect was reversed at 37 ^{o}C. At the higher concentrations the adsorption trend showed that at RT, HAD adsorbed more BSA than SAD from the 20 mg/mL BSA concentration, while the opposite effect was seen when 10 mg/mL BSA concentration was analysed. The overall adsorption pattern on SAD suggested that significantly more BSA was adsorbed from the 20 mg/mL protein solution compared to the 10 mg/mL, while the trend on HAD

showed proportionality to the protein concentrations used, where from the 20 > 15 >> 10 mg/mL more BSA was adsorbed with increasing protein concentrations measured at the end of the adsorption period. At 37 ^{o}C, HAD adsorbed more BSA than SAD for all concentrations, with an overall pattern of 20 > 15 > 10 mg/mL for HAD and 10 > 20 mg/mL for SAD at the end of the adsorption period.

The adsorption on the biomaterials was a dynamic process especially on SAD, often related with accelerated cell adhesion as well. This observation has been observed by others, especially in the work of Hing *et al.* (Hing, Annaz*, et al.* 2005), Rashid *et al.* (Rashid, Harding*, et al.* 2008) and Guth *et al.* (Guth, Campion*, et al.* "Effect of Silicate-Substitution on Attachment and Early Development of Human Osteoblast-Like Cells Seeded on Microporous Hydroxyapatite Discs" 2010; Guth, Campion*, et al.* "Surface Physiochemistry Affects Protein Adsorption to Stoichiometric and Silicate-Substituted Microporous Hydroxyapatites" 2010), showing that cell adhesion was affected by protein adsorption. The dynamic behaviour of cell adhesion was observed on the biomaterials, possibly due to their sensitivity to the dynamic behaviour of adsorbed protein layer on the surface, which agreed with this work and the work of Allen *et al.* (Allen, Tosetto*, et al.* 2006)

Using the methodology described in section 4.2.3, the adsorption isotherms were constructed with the raw data as shown in Figure 4.5, Figure 4.6, Figure 4.7 and Figure 4.8 was converted into adsorbed amounts (Γ) in moles/g against the equilibrium concentrations in mol/L.

Figure 4.9A showed three regions on the HAD surface. The pattern seen in Region A at RT suggested that the adsorption was limited by the formation of one layer, however values calculated for the BSA surface coverage were more than 100%, suggesting the formation of a multi-layer. In Region B, the pattern seen suggested a dynamic formation and rearrangement of a multilayer at the higher concentrations, as the values calculated fluctuated beyond the 100 % threshold. Region C, which occurred at the physiological concentration, also showed to have more than 100 % BSA surface coverage at all time points, but at a lower magnitude compared to the other concentrations, suggesting that the surface of the dense discs may be saturated with proteins, which would then explain the need for the formation of the multi-layer as equilibrium concentration increases. The work of Zeng *et al.* (Zeng, Chittur*, et al.* 1999) has shown that a higher BSA adsorption

rate was observed on HA compared to different surfaces. Although, the work was achieved using thin films of the materials, similar observations were obtained on different forms of the biomaterials. At the 5 and 10 minute time points, their work did suggest a change in the speed of the adsorption rate, which could explain the differences observed here. However, the pattern observed closely resembled that found in the work of Mavropoulos *et al.* (Mavropoulos, Costa*, et al.* 2011). Although they did not include higher concentrations beyond 2 mg/mL BSA solutions, it can be assumed that the possibility of a dynamic process on the surface may occur also. At 37 ^{o}C (Figure 4.9B) the three regions were still observed with Regions A and C being larger compared to values previously seen at RT. Region B showed an increased degree of dynamic behaviour with increasing levels of protein adsorption at lower magnitude, still suggesting a continual cycle of rearrangement and exchange on the surface.

For SAD, (see Figure 4.9C and D) the adsorption isotherms showed different patterns to HAD with only two distinct patterns across the three regions both at RT and 37 ^{o}C. Lower adsorbed amounts were observed on SAD compared to HAD, but a more dynamic behaviour was obtained at the two temperatures, suggesting a faster formation of BSA multilayers.

Previous studies have been performed using ELISA and have shown greater amounts of BSA, FN or VN adsorption on HA as compared to titanium or steel, which are less hydrophobic; this is in agreement with the observations here for HA and SA, suggesting that the hydrophobic nature is not a limiting factor (Kilpadi, Chang*, et al.* 2001). Due to the presence of the ions in the lattice of the ceramic, HA is more hydrophobic than SA in nature and both overall are less hydrophobic than metals, followed by polymers (hydrophilic).

4.4.2   FTCA-BSA Studies

Validation with Dense Discs in PBS at RT (19 (± 2.0) ^{o}C)

Initially, the FTCA-BSA study was undertaken in PBS at RT, where the adsorption trend was as follows: SAD > HAD after the 15 minutes adsorption time, the same as for the BSA only study, confirming that the label did not affect the adsorption behaviour of the protein on the biomaterials. The dynamics during that period of time may have been

slightly different, but overall, it seemed to suggest an accumulative protein adsorption process compared to the dynamic process seen when analysed using the kit. The desorption profiles also highlighted very little desorption from DD. The observed desorption trend HAD > SAD, again was similar to that of BSA with Quant-IT study.

Having validated the use of the FTCA-BSA, further work was then centered on demonstrating the differences in adsorption and desorption profiles between the biomaterials, stoichiometric HA and SA, two morphological forms; dense disc (DD) and porous granules (PG), and the effect of temperature (Figure 4.12), media (Figure 4.13) and porosity (Figure 4.14).

Effect of Temperature; Room Temperature (RT: 19 (± 2.0) ^{o}C) and 37 ^{o}C

The effect of temperature on DD showed that more BSA was adsorbed at RT compared to 37 ^{o}C on the DD surfaces with SA adsorbing more than HA (see Figure 4.12). Historically temperature has not been standardised in protein adsorption experiments and ranged from 4 to 37 ^{o}C. (Grinnell and Feld 1982; Kilpadi, Chang, *et al.* 2001; Steele, Johnson, *et al.* 1992) The change in temperature seemed to affect the affinity of the protein depending on the chemistry of the biomaterials. For example, in the work of Guth *et al.* (Guth, Campion, *et al.* "Surface Physiochemistry Affects Protein Adsorption to Stoichiometric and Silicate-Substituted Microporous Hydroxyapatites" 2010) half the amount of fibronectin was adsorbed to the HA surface at 37 ^{o}C compared to RT, while for SA the amount tripled at 37 ^{o}C. This may suggest that a change in energy in the protein solution, may have affected the protein dynamic behaviour, and thus its interaction with the biomaterials. The fact that FN is a protein of 440,000 Daltons compared to the BSA (66,320 Daltons), and the energy (increased temperature) may dissipate differently in a smaller protein, and hence the behaviour would be different, as observed in this work. The overall pattern was found to be true, in the work of Guth *et al.* where SA adsorbed more than HA, which then further lead to more cell adhesion. (Guth, Campion, *et al.* "Effect of Silicate-Substitution on Attachment and Early Development of Human Osteoblast-Like Cells Seeded on Microporous Hydroxyapatite Discs" 2010)

Effect of media; PBS and MEM at 37 ^{o}C

Changing media on DD at 37 ^{o}C (see Figure 4.13) showed that more BSA was adsorbed from PBS solutions compared to MEM on the DD surfaces, 15-20 % compared to 10-15 % with SA adsorbing more than HA in MEM. However, this observation clearly showed that MEM, which has both inorganic and amino acid constituents affected the interactions of the BSA with the biomaterial surfaces similarly to results found in the work of Dong *et al.* (Dong, Wang*, et al.* 2007) with a growth factor. In this work, although the protein here investigated was rhBMP-2, they demonstrated that the presence of amino acids can influence the adsorption behaviour of the growth factor to HA. These amino acids, also termed fulcrum-adsorption residues, such as asparagine (Asn) or glutamic acid (Glu) are all present in the MEM at an average concentration of 0.0134 g/L, and therefore could have influenced the BSA adsorption on the biomaterial's surface. However, in this instance, the trend was more towards inhibiting adsorption compared to enhancing it as observed in the rhBMP-2 study, and further confirmed in Chapter 5 of this thesis. The differences in behaviour could be due to the size of the proteins, where BSA is approximately three times larger than rhBMP-2, and additionally the physiological concentrations being larger (4 mg/mL compared to 300 ng/mL). In the work of Green *et al.* albumin was shown to exhibit the Vroman effect over two other proteins on polymeric surfaces in the presence of other organic components. (Green, Davies*, et al.* 1999)

Effect of Porosity Porous Granules (PG) at RT and 37 ^{o}C

The introduction of porosity at RT showed a slower BSA rate of adsorption on PG compared to the DD surfaces with lower adsorbed amount, but increased desorbed amounts detected in PBS using the Quant-IT kit, as shown in Figure 4.4.

At 37 ^{o}C, the behaviour was different when using the probe. Higher adsorbed amounts of FTCA-BSA were detected on PG compared to DD in both media. The rate of adsorption, however, induced a slower rate of adsorption due to the introduction of porosity. This could be due to the rate of diffusion of the protein, water and the other component of the medium interacting with the larger surface area and pores of the biomaterials, which agrees with the work of Rashid *et al.* (Rashid, Harding*, et al.* 2008) and Guth *et al.* (Guth, Campion*, et al.* "Effect of Silicate-Substitution on Attachment

and Early Development of Human Osteoblast-Like Cells Seeded on Microporous Hydroxyapatite Discs" 2010) There is a form of ion exchange that changes the surface charge of the material and with increased surface area, i.e. increased porosity, that process influences the speed at which a protein may adsorb on the biomaterial surface. This may further suggest the lower adsorbed amounts detected in MEM, 5 to 10 % lower as shown in Figure 4.13 and Figure 4.14, as there are more components of this media to interact with this process. Hence, less FTCA-BSA was adsorbed on SAG in MEM compared to PBS (26 % compared to 34 %), but overall more was adsorbed on SAG compared to SAD in a dynamic fashion (34 % and 26% in Figure 4.14A and B compared to 22% and 15% in Figure 4.13A and B in PBS and MEM, respectively), only the pattern and rate of adsorption differed in the different media. This observation was expected as shown from the work of Guth *et al.* (Guth, Campion*, et al.* "Effect of Silicate-Substitution on Attachment and Early Development of Human Osteoblast-Like Cells Seeded on Microporous Hydroxyapatite Discs" 2010; Guth, Campion*, et al.* "Surface Physiochemistry Affects Protein Adsorption to Stoichiometric and Silicate-Substituted Microporous Hydroxyapatites" 2010) clearly suggested that the introduction of porosity in polymeric membranes and calcium phosphates enhances adsorption behaviours and cell attachment.

In HA, the change in porosity in PBS showed similar adsorbed amounts detected but different rate and pattern of adsorption, as shown in Figure 4.13A and Figure 4.14A, respectively. Adsorption on DD showed lower adsorbed amounts from PBS to MEM (17 % to 11%), as seen with SA, but not from DD to PG in MEM (11 % to 25%), as shown in Figure 4.13B and Figure 4.14B. More FTCA-BSA was adsorbed on HAG in MEM in comparison to PBS, and overall pattern observed with SA. This may suggest that the effect of morphology enhanced FTCA-BSA adsorption on HA in MEM towards a similar reactivity to SA irrespective of biomaterial's chemistry.

Overall, SA specimens adsorbed more than HA specimens, suggesting a stronger affinity between FTCA-BSA and silicate-substituted specimens compared to the stoichiometric apatite, further demonstrated when taking into account the desorption pattern HAG > SAG in both media, with more desorbing in MEM than PBS (see Figure 4.14C and D) compared to values obtained from DD (Figure 4.13C and D).

Desorption values obtained from dense disc (DD) in both media showed no significant difference between biomaterials, other than less than 1 % was desorbed in PBS

compared to less than 10 % in MEM. Introduction of porosity resulted in higher desorbed amounts in both media with a significant difference between biomaterials possibly due to their chemistry. Following on the previous observations, more FTCA-BSA was desorbed from MEM compared to PBS. 45 % was desorbed from HAG compared to 33 % from SAG as shown in Figure 4.14D in MEM; compared to 19 % from HAG and 6 % from SAG in PBS. This further suggests that SA enhances BSA adsorption on its surface, dense discs or porous granules, as it retains more through the desorption process.

Both morphological forms have been the subject of extensive research due to their different biological response to bone growth when incorporated as implants both *in vitro* and *in vivo* models. (Hing, Best*, et al.* 1997; Ripamonti 1996) Bone implants are more likely to be moulded or pressed (Rouahi, Gallet*, et al.* 2006) as dense or porous materials (Hing, Best*, et al.* 2004; Hing, Revell*, et al.* 2006), rather than left as fine powders, especially for bony defects, therefore trends that would be observed here, may differ slightly from previous studies in terms of the chemical composition and physical properties of hydroxyapatite powders (Best, Sim*, et al.* 1997) to initiate bone ingrowth. HA mimics very closely the composition of mineral bone, thus studies using its lattice as a base to enhance its bioactivity and biocompatibility, have been undertaken extensively and successfully by researchers. (Botelho, Lopes*, et al.* 2002; Gibson, Best*, et al.* 1999; Gibson, Best*, et al.* 2002) Gibson's team, in particular, have successfully incorporated silicate ions into the HA lattice, as a single phase material with a similar *Ca/(P+Si)* ratio of 1.67 and minimal changes in the crystallographic parameters. Since the introduction of silicon in the HA lattice (Gibson, Best*, et al.* 1999), silicate-substituted hydroxyapatite (SA) has been shown to have a stronger affinity for BSA compared to stoichiometric HA (Balas, Perez-Pariente*, et al.* 2003; Patel, Best*, et al.* 2002), which has been quantified in this study also. This was especially true when porosity of the samples was introduced, shown in the works of Hing and Patel (Hing, Best*, et al.* 2004; Patel, Brooks*, et al.* 2005) where SA adsorbed more and thus enhanced the possibilities of improved bone repair and remodelling. However, there are still uncertainties regarding the mechanism by which the silicon, as a silicate ion, increases the bioactivity.

Fluorescence Images Interpretation

Having labelled the BSA directly, the qualitative data was also collected; see Figure 4.15 and Figure 4.16. These studies were set up into two experiments.

Amount of protein observed on the surface in MEM and PBS matched the Quant-IT kit analysis, especially the isotherm experiments in terms of demonstrating the fluctuations observed in the adsorption behaviour quantified previously and shown in Figure 4.9. They clearly show that protein was not uniform on the surfaces; this could also suggest that using equilibrium concentrations and shapes of isotherms to confirm monolayer formation (adsorption isotherms) on a biomaterial surface has its limitations. In the work of Zeng and Mavropoulos (Mavropoulos, Costa, *et al.* 2011; Zeng, Chittur, *et al.* 1999), the isotherms were analysed through non-fluorometric methods on thin films and powders, respectively, and did not include images to confirm protein morphology or homogeneity on the surface of the biomaterials. In the work in this study, FTCA-BSA in PBS adsorption at RT at all time points was clearly adsorbing differently on the silicate-substituted hydroxyapatite (SAD) compared to the stoichiometric hydroxyapatite (HAD). The morphology of the protein was also totally different, more globular on the SAD and elongated on the HAD samples. Also, BSA seems to adsorb more evenly (homogeneously) on SAD surfaces than on HAD, but no monolayer was observed. This difference could be explained by the differences in the biomaterial's surface charge, packing and composition of the ions. The work of Porter *et al.* tried to answer this question using high-resolution transmission electron microscopy to observe and characterise defect structures in SA. They found that SA formed an increased number of triple junctions compared to HA, which may have a role in the increased bioactivity of the material. (Porter, Best et al. 2004; Porter, Buckland et al. 2005) Thus, it could also explain why more protein was adsorbed, when taking into account the SEM images obtained in Chapter 2 for both dense discs and the porous samples of SA. Moreover, often protein morphology on HA is modelled *via* computational methods like in the work of Chen *et al.* (Chen, Wu, *et al.* 2008) where the images produced were simulated to show SA has stronger interaction to the carboxylic group from the protein compared to HA, but over 25 % silicate group content was used, that may not be representative to actual phenomena observed *in vitro* or *in vivo*, as silicate contents are usually lower than 16 %. However, their findings agreed to findings in this chapter that SA has stronger affinity than HA.

4.5   Summary & Conclusions

Quant-IT kit was only useful at physiological levels, compared to the FTCA-BSA tool that covered the complete concentration range. This was further confirmed when looking at the calibrations generated from both set ups. The Quant-IT kit detection pattern may suggest that a form of dynamic adsorption occurs on the biomaterials as time elapses, whereas using the FTCA-BSA fluorophore approach, the pattern suggests protein adsorption occurs cumulatively as time elapsed.

Endpoint data from both set ups were very similar when looking at the validation at RT. FTCA-BSA allowed for several concentrations to be determined, and using the fluorescence, the protein was successfully imaged on the HA and SA surfaces in two different media.

FTCA-BSA studies showed that more FTCA-BSA was adsorbed and desorbed at RT compared to 37 ^{o}C on the dense discs biomaterials with SAD adsorbing more and desorbing less than HAD.

More FTCA-BSA was adsorbed in PBS compared to MEM on SAG, SAD and HAD, except on HAG, where more was adsorbed in MEM. It was suggested that the components present in solution were influences on the interactions between protein and components before and during the adsorption process of the protein on the biomaterials. Introducing porosity increased the amount of FTCA-BSA adsorbed and desorbed in both media, with more affinity with the silicate-substituted hydroxyapatite over the stoichiometric one.

The use of FTCA covalently attached to BSA allowed for protein solutions to be measured at various concentrations in PBS and MEM with little limitation to the quantifiable aspect of the analysis.

Chapter 5. RECOMBINANT HUMAN BONE MORPHOGENETIC PROTEIN-2 (RHBMP-2) ADSORPTION & DESORPTION STUDY

5.1 Background

Recombinant human Bone morphogenetic protein-2 (rhBMP-2) is one of the most important growth factors in bone repair and remodelling. It was discovered in 1965 by Urist to induce bone formation from decalcified bone *in vivo* (Urist 1965; Urist and Strates 1971) and then further investigated as a member of the transforming growth factor-β (TGF-β) superfamily (Sampath, J.E.*, et al.* 1990) , which regulate new bone formation, showing BMP-2 to be an osteoinductive and osteogenic protein (Nickel, Dreyer*, et al.* 2001; Sampath, J.E.*, et al.* 1990; Wang, Rosen*, et al.* 1990) when adsorbed on carriers and implanted in animal models.

The clinical relevance of BMPs has been reviewed in the work of Schmitt *et al.* (Schmitt, Hwang*, et al.* 1999) and found to be a formidable tool to promote bone regeneration, which also plays a critical role in osteoblast function, (Zhao, Qiao*, et al.* 2006) that lead to BMP-2 being recognised as an osteoconductive and both morphogenic and mitogenic growth factor. (Hirata, Nomura*, et al.* 2007; Hoshino, Egi*, et al.* 2006; Schliephake, Aref*, et al.* 2005) It is often studied with carriers such as collagen (Col) (Matsumoto, Yamaji*, et al.* 2001), or polymer or ceramic materials (Groeneveld and Burger 2000), both *in vitro* and *in vivo* studies, at a particularly high concentration of 1.4 μg to 11 μg per mg of collagen compared to its physiological concentration of 300 ng/ml (Urist, DeLange*, et al.* 1983; Urist and Strates 1971). The high concentration is usually associated with the differences in species between rats (Yasko, Lane*, et al.* 1992), rabbit or baboon that required different concentration to result in a similar amount of bone formation *via* cell differentiation (Yamaguchi, Katagiri*, et al.* 1991). Thus differences in concentration were also seen in human clinical studies, especially in the area of bone defects. (Groeneveld and Burger 2000) Therefore, investigating the growth factor may aid in explaining these differences.

Although, rhBMP-2 is assessed *in vivo* in terms of bone regeneration applications *via* implantation in animal models (Ripamonti 1996) through histomorphometry and histology to measure and visualise both new bone growth within carriers, actual work on the growth factor's morphology and behaviour itself is limited. The work mostly

centred on the growth factor influences and not on a better mechanistic view into the adsorption process of rhBMP-2 on hydroxyapatite or its morphology on the surface prior to implantation.

In this chapter, the adsorption/desorption behaviour of the growth factor, bone morphogenetic protein-2 (rhBMP-2; Sera Laboratories, UK) was investigated on porous granules (PG) at 37 °C to assess any variation in BMP-2 affinity to apatite scaffolds with silicate substitution at both physiological and pharmacological doses, and to validate the use of direct labelling towards producing quantitative and qualitative results compared to using the rhBMP-2 specific kit.

5.2 Experimental Methodology

Studies were performed at both physiological (300 ng/mL) and pharmacological (4 µg/mL) concentrations to assess graft performance under wound healing conditions and as a BMP-2 carrier respectively. Two methods of analysis were employed to quantify BMP-2 adsorption and release, a commercially available sandwich ELISA and the in-house fluorophore labelling protocol previously described in Chapter 3 section 3.3.1.

All glassware and containers were used as received sterile from the manufacturer (VWR). All reagents were brought to 37 ^{o}C in an incubator before use. All chemicals were supplied by Sigma-Aldrich unless otherwise specified. The rhBMP-2 (RCYT-261) was purchased from Sera Laboratories, UK and the Human BMP-2 Quantikine ELISA kit (SBP200) purchased from R&D systems, UK.

5.2.1 Specimens and Test solutions

Tabulated below are the type of specimens in Table 5.1 and test solutions in Table 5.2 used for the experiments undertaken in Table 5.3 and Table 5.4.

Table 5.1 – Specimen description and acronyms used throughout study

Specimen description	Acronyms
Silicate-substituted apatite porous granules	SAG
Hydroxyapatite porous granules	HAG

Test solutions of unlabelled BMP-2 (rhBMP-2) were generated from a stock solution of 100 µg/mL in acetic acid and then diluted to the design concentration levels with either PBS or MEM as required. Labelled BMP-2 (FTCA-rhBMP-2) was prepared using the rhBMP-2 at a concentration of 12 µg/mL in PBS or MEM, and then diluted to generate a stock solution of 4 µg/mL, which was stored at -70 ^{o}C in 1 mL aliquots.

Table 5.2 – Test solutions: buffer, medium and protein solutions

Test solutions	Details	Concentrations
Phosphate Buffered Saline	PBS: dissolve one tablet in 200mL deionised water pH 7.4 (product code: P4417)	0.01 M
Minimum essential Eagles' medium	MEM: containing inorganic components, amino acids and vitamins (product code: M3024)	9.3 g/L
Recombinant Human Bone Morphogenetic protein-2	rhBMP-2: lyophilised powder reconstituted in acetic acid to make 100 µg/mL stock solution (product code: RCYT-261)	4, 12 µg/mL and 300 ng/mL

Table 5.3 – Specimen and experiments undertaken in PBS (at 37 ^{o}C)

Specimen	SAG	HAG
4 µg/mL rhBMP-2	√	√
300 ng/mL rhBMP-2	√	√
4 µg/mL FTCA-rhBMP-2	√	√
300 ng/mL FTCA-rhBMP-2	√	√

Table 5.4 – Specimen and experiments undertaken in MEM (at 37 ^{o}C)

Specimen	SAG	HAG
4 µg/mL rhBMP-2	√	√
300 ng/mL rhBMP-2	√	√
4 µg/mL FTCA-rhBMP-2	√	√
300 ng/mL FTCA-rhBMP-2	√	√

The concentration at 4 µg/mL is the pharmacological concentration, while the 300 ng/mL concentration represents the physiological BMP-2 amount; and 12 µg/mL is the stock solution that was prepared for the growth factor dilutions.

5.2.2   Protocol for Growth Factor Adsorption/ Desorption Study

rhBMP-2 or FTCA-rhBMP-2 solutions at physiological (300 ng/mL) and pharmacological (4 µg/mL) concentrations were prepared, and each of the protein solutions (1.5 mL) was then placed in a clean glass vial. Test biomaterial samples, porous granules of HA or SA (approx 0.50 g) were added to analyse **adsorption**, where 100 µL of protein solution was removed at the following intervals (1, 5, 10 and 15 minutes). After 15 minutes, the test sample was removed and the original soaking solution stored. The test sample was placed in PBS or MEM (1.5 mL), shaken for 5 minutes, then removed and the washing solution stored.

The biomaterial was then placed in fresh PBS or MEM (1.5 mL) to analyse **desorption** (or **release**), where 100 µL of the solution was removed at the following intervals (5, 60, 240, 1440, 2880 minutes). The biomaterial was then removed to a further lidded vial. All experiments were performed in an incubator at 37 ^{o}C, and a water-bath at 37 ^{o}C used for storage of the aliquots.

Figure 5.1 – Porous Granules of SA and HA submerged in physiological (300 ng/mL) and pharmacological (4 µg/mL) concentrations of FTCA-rhBMP-2

For the qualitative data, adsorption of FTCA-rhBMP-2 in PBS and MEM at 37 ^{o}C was imaged using a Zeiss Axioscope microscope as described in Chapter 4 on dense discs (prepared as described in Chapter 2) after discs were incubated for periods of 1, 5, 10, 15, 30 and 60 minutes.

5.2.3 Analysis using the Quantikine ELISA kit

The manufactures' standard protocol was followed, according to the leaflet provided. The wash buffer concentrate (20 mL) was diluted into deionised water (DIW) to prepare the wash buffer (500 mL). If crystals formed in the concentrate, the buffer was warmed to room temperature and mixed gently until the crystals completely dissolved.

Calibrator diluent RD5P concentrate (20 mL) was added into DIW to yield calibrator diluent RD5P (1X) (200 mL), and allowed to mix for 15 minutes prior to use.
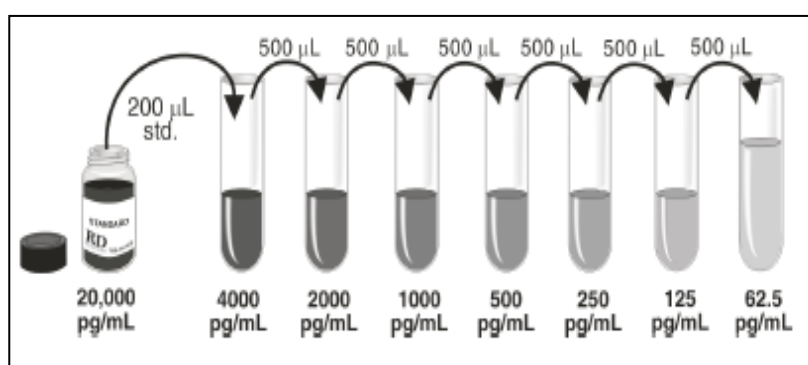
Figure 5.2 – Schematic of the Serial Dilution made of the rhBMP-2 Standards copied from the manufacturer procedure manual

The rhBMP-2 standard was reconstituted with DIW (1 mL). This produced a stock solution of a concentration of 20, 000 pg/mL. Using the stock, dilution series were made (see Figure 5.2). Each tube was thoroughly mixed before the next transfer, where the 4,000 pg/mL standard served as the high standard and the calibrator diluent RD5P (1X) served as the zero standard (0 pg/mL).

The substrate solution; colour reagent A and colour reagent B were mixed together in equal volumes within 15 minutes of use and protected from light. The resultant mixture was then transferred to each well in 200 μL aliquots.

All samples and standards were assayed in duplicates, following a plate layout (see Figure 5.3). The manufactures' protocol was followed, according to the booklet provided.

For the first step, all reagents were prepared as described in the previous section. The microplate strips were removed from the plate frame returned them to the foil pouch

containing the desiccant pack and resealed. To each well Assay Diluent RD1-19 was added (100 µL). The standard, control and samples were added 50 µl per well, covered with the adhesive strip provided, then felt to incubate for 2 hours at room temperature on a horizontal orbital microplate.
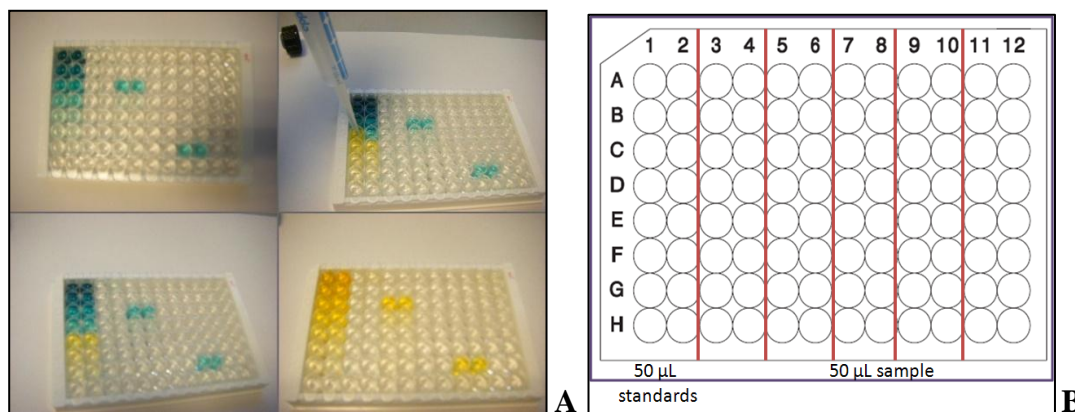
Figure 5.3 – (a) Plate and (b) layout for the unlabelled rhBMP-2 analysis

Each well was aspirated and washed, the process was repeated three times for a total 4 washes. Each well was washed by filling them with wash buffer (400 µl) using a multi-stream pipette. Complete removal of liquid at each step was essential for accurate data. After the last wash, any remaining wash buffer was removed by aspirating or inverting the plate and blotting it against clean paper towels. BMP-2 conjugate (200 µl) was added to each well, covered with a new adhesive strip and incubated for 2 hours at room temperature on the shaker. The aspiration/wash was repeated, before the next step, the substrate solution addition. Substrate Solution (200 µl) was added to each well and incubated for 30 minutes at room temperature on the benchtop, protected from light. Stop Solution (50 µl) was added to each well. The colour in the wells should change from blue to yellow. If the colour in the wells was green or did not appear uniform, the plate was gently tapped to ensure thorough mixing.

In order to generate the calibrations and use the optical density values, the data was initially corrected by subtracting the 544 nm values from the 450 nm values obtained from the GalaxyStar instrument. For the standards, only, a further subtraction of the 0 pg/mL value from all other standards was undertaken to correct for the calibration curve.

Using the FluoStar Galaxy Microplate Reader, 96 –well plate reader (BMG laboratories, UK) the absorbance, also known as optical density, was measured and set at 450 nm, and the correction at 544 nm with cycle time of 60 seconds.

5.2.4   Analysis using direct Fluorophore coupling

RhBMP-2 was labelled as described in Chapter 3 section 3.3.1 with a fluorophore concentration of 8.84 x 10^{-5} M. The final concentration of FTCA-rhBMP-2 was verified by freeze drying of a 3 mL sample, and the remainder diluted with PBS or MEM to a stock solution of 4 µg/mL.

Using the 4 µg/mL FTCA-rhBMP-2 stock solution, standards of known concentrations were made in fresh PBS or MEM, aliquots of 1 mL solutions, in order to determine protein amounts in unknown samples. Serial dilutions were produced including the 4 µg/mL (4000 ng/mL) as the highest concentration and PBS or MEM only to generate the 0 ng/mL concentration.

Table 5.5 – Concentrations of the rhBMP-2 in the FTCA-rhBMP-2 serial dilutions used for the Calibration curves

rhBMP-2 Concentrations (ng/mL)		
Original	10 µL	2 µL
4000	40.0	8.0
2000	20.0	4.0
1000	10.0	2.0
500	5.0	1.0
250	2.5	0.5
125	1.25	0.25
62.5	0.625	0.125
0	0	0

Calibration curves were thus generated, where for the high calibration 10 µL was used and 2 µL was used for the low calibration. Table 5.5 shows the standards used when constructing the calibration curves. All FTCA-rhBMP-2A and PBS or MEM solutions were equilibrated at 37 °C, where 200µL of the freshly made PBS or MEM was then

loaded into each microplate well. 5 µL of original and adsorbed samples were placed in the wells according to the layout made (see Figure 5.4), followed by 20 µL of the wash and desorbed samples. Standards were added as previous section described.
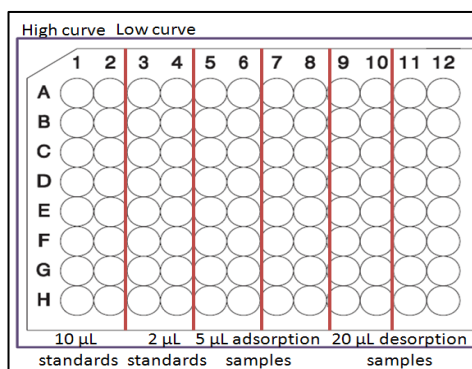
Figure 5.4 - Plate layout for the FTCA-rhBMP2 analysis

Fluorescence intensity and time resolved settings with excitation and emission were set at 485 and 520 nm, respectively. A cycle time of 120 seconds with 10 flashes, 0.5 seconds delay with orbital shaking set for 10 seconds before each cycle was used.

5.2.5 Fluorescence Microscopy

1 mL aliquots of FTCA-rhBMP-2 at 300 ng/mL in PBS and MEM at 37 ^{o}C was transferred in to 24-well plate containing dense disc of the biomaterials, and left submerged for 1, 5, 10, 15, 30 and 60 minutes. After immersion time, the discs were rinsed in PBS or MEM then imaged, and transferred into a clean 24-well plate containing formaldehyde.

Fluorescence microscopy was performed using a Zeiss Axioscope microscope, employing a mercury lamp UV source, and three filters with excitation/emission wavelengths of 450-490/515 nm, 365/395 nm and 546-512/598 nm which enable imaging of dyes that fluoresce in the green, blue or red, respectively. The images (micrographs) were taken at magnifications of 50, 100 or 200 and used for qualitative analysis of the protein adsorption on dense discs of the biomaterials with a working fixed exposure of 695 ms.

5.3   Results

5.3.1   Quantikine analysis

Calibration plots using the BMP-2 Quantikine kit were linear across the concentration range in both PBS and MEM, respectively (see Appendix 25, Figure 135), and showed good correlation, tabulated below.

Table 5.6 – R^2 values of the rhBMP-2 calibration curves in the various medium at 37 ^{o}C

Media	Curves generated / pg/mL	R^2 values obtained
PBS	0 - 4000	0.990
MEM	0 - 4000	0.996

The adsorption and desorption profiles of rhBMP-2 were determined for both physiological (300 ng/mL) and pharmacological (4 µg/mL) concentrations at 37 ^{o}C for silicon-substituted porous granules (SAG) and hydroxyapatite (HAG) in PBS and MEM.

The adsorption profiles at physiological concentration (300 ng/mL) for both biomaterials in PBS and MEM are depicted here in Figure 5.5A and B, along with the total adsorbed amount as a percentage (%) of the initial rhBMP-2 concentration used in this study. More rhBMP-2 was adsorbed in MEM compared to PBS. The behaviour in PBS was very similar to that of MEM, and approximately 7.5-fold lower with less than 2.0 ng/mL of rhBMP-2 being adsorbed onto the porous biomaterials in PBS.

The adsorption trend was similar to that observed for BSA and FTCA-BSA in Chapter 4 where SAG adsorbs more than HAG in the porous form in PBS and MEM.

The adsorption profile at the pharmacological concentration in PBS is shown in Figure 5.5C, where SAG was found to adsorb more than HAG. The patterns were similar in shape to that observed for the physiological concentration experiment, but with more rhBMP-2 overall detected from the SAG samples at all time points compared to HAG.

In MEM (Figure 5.5D), adsorption values were found to be greater that those obtained from the physiological concentration in MEM (300 ng/mL), but looked similar to those obtained from PBS (4 µg/mL). However, a faster rate of rhBMP-2 adsorption was seen in MEM compared to PBS for HAG, with little or no change for the SAG specimen.

PHYS   **PHARMA**
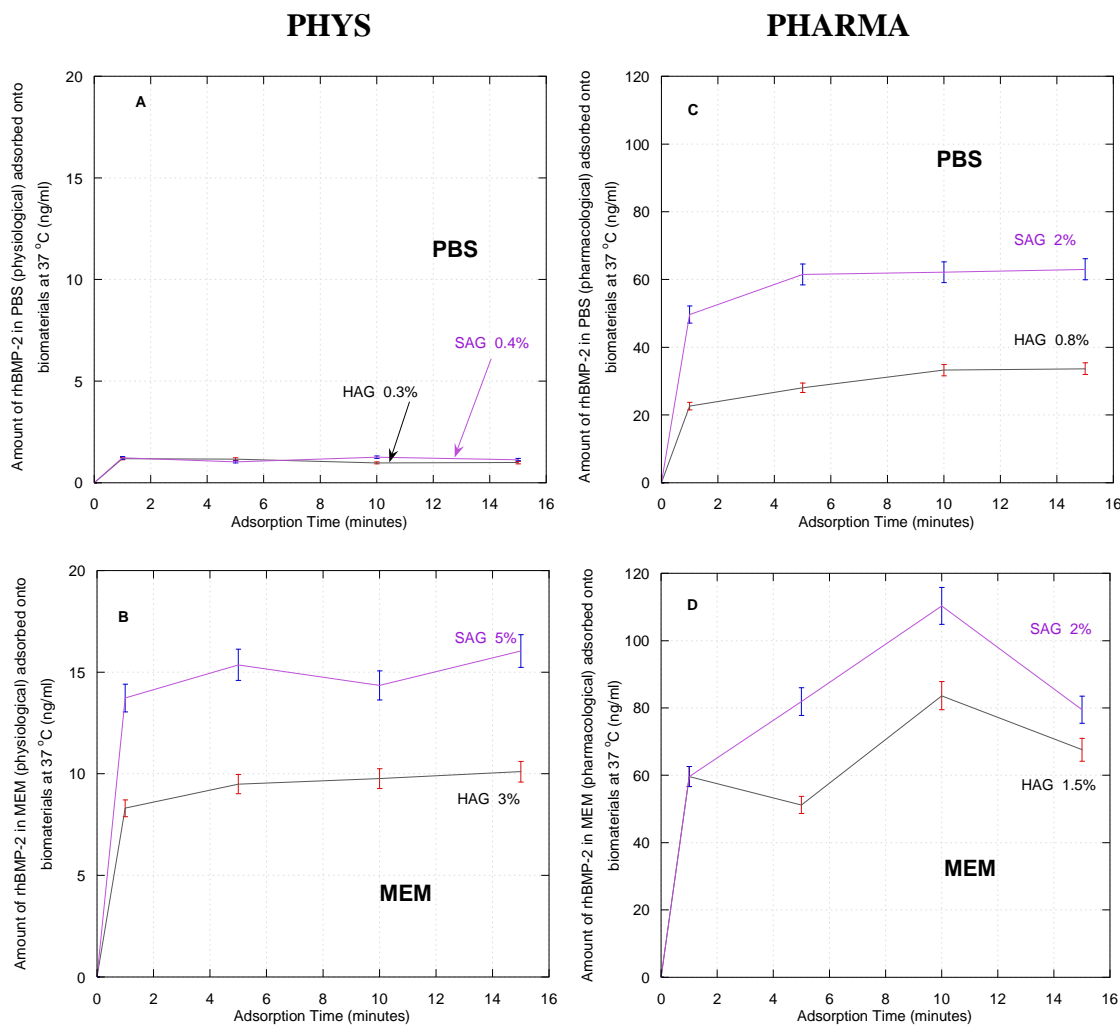
Figure 5.5 – Adsorption profiles of rhBMP-2 in (a) PBS and (b) MEM at physiological and in (c) PBS and (d) MEM at pharmacological concentrations at 37 ^{o}C biomaterials (n= 2 ±s.d.)

The rate of rhBMP-2 release from the physiological level study in PBS, as shown in Figure 5.6A, seemed rapid to release either all the adsorbed amounts or more with no clear trend in the magnitude of rhBMP-2 released in PBS with regard to materials chemistry. On the graphs, release is also shown as a percentage (%) from the total adsorbed at the end of the adsorption period. This may suggest that in PBS, the ionic composition of the medium influenced the rhBMP-2 release towards a complete

desorption of the growth factor from the biomaterial's surface, or due to its influence during the rhBMP-2 adsorption process, the growth factor was only loosely binding to the surface, as shown in Figure 5.5A, low adsorption and rapid release was obtained. Another suggestion would be that in PBS and at the physiological concentration, rhBMP-2 may be subject to large conformational changes, which the antibodies in the kit would be sensitive to, and allow only for a particular conformation to be detected during the adsorption and release, which would also explain the low adsorbed amounts previously obtained in Figure 5.5A.

In MEM, higher adsorbed (see Figure 5.5B) and released (see Figure 5.6B) amounts were obtained from HAG and SAG, with SAG adsorbing and releasing more at the physiological concentration. MEM is a medium with both inorganic and organic components, these components may have influenced both the interactions between the growth factor and the medium, but also the interactions between the growth factor and the biomaterial's surface, and thus enhanced the amount of rhBMP-2 adsorbed and released in solution.

At the pharmacological concentration, the rate of release was fast but minimal in both PBS and MEM (see Figure 5.6C and D) compared to the physiological level. Moreover, the amounts released from HAG were larger than those obtained at physiological, yet comparable to those obtained in MEM. While the release from SAG also showed a larger amount compared to the physiological, but in MEM less was released compared to values obtained from the physiological environment. It may also suggest that a change in test environment has affected the release pattern from SAG, compared to HAG. This may further confirm the observation clearly shown at the physiological level that a stronger affinity occurs with the growth factor to the biomaterials' surfaces due to the interaction with MEM and its components to either the protein or biomaterials' surfaces.

PHYS   PHARMA
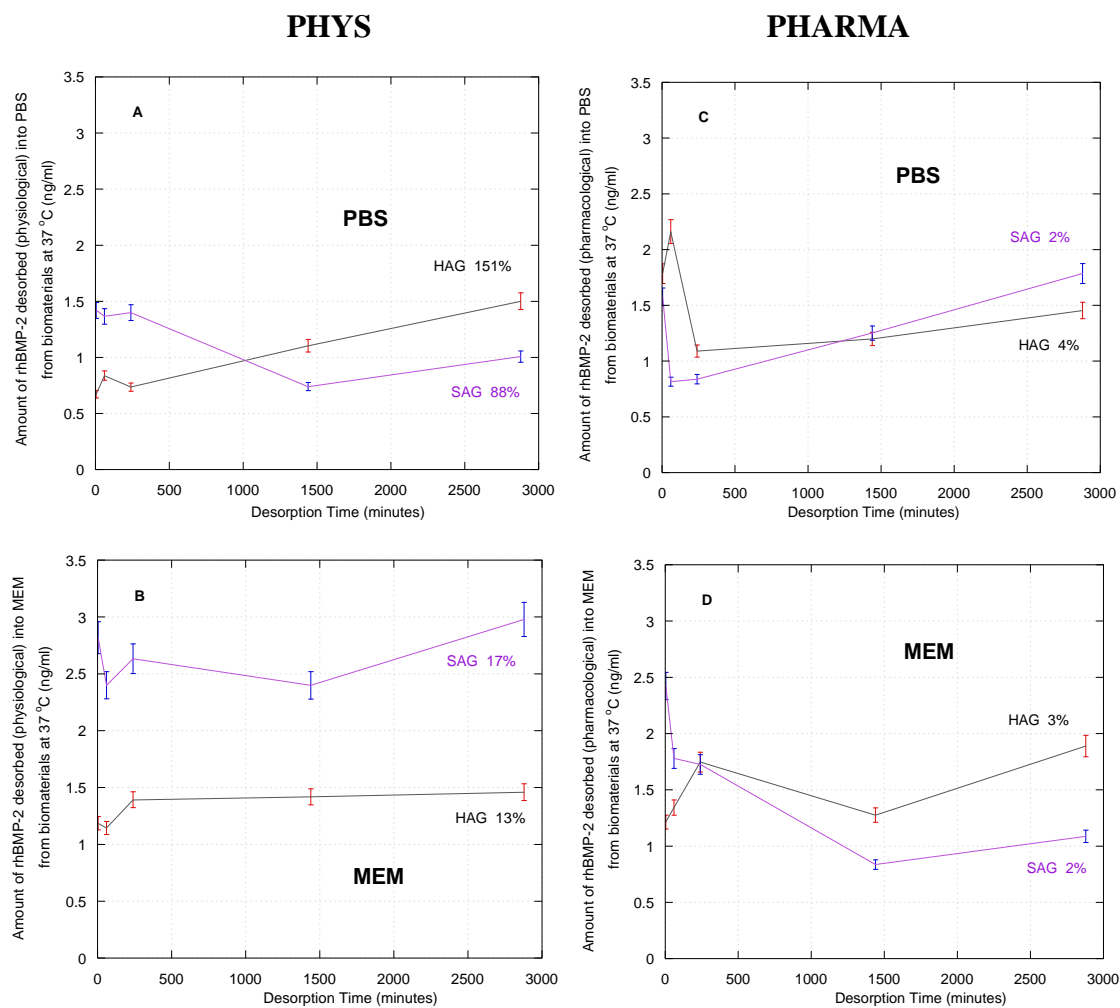
Figure 5.6 – Desorption profiles of rhBMP-2 in (a) PBS and (b) MEM at physiological and in (c) PBS and (d) MEM at pharmacological concentrations at 37 °C biomaterials (n=2±s.d.)

5.3.2 Analysis using the Fluorophore

Calibration curves were generated using the FTCA-rhBMP-2 in PBS and MEM show a linear relationship over high (0-40 ng/mL) and low (0-8 ng/mL) rhBMP-2 ranges per well (see Appendix 26 and Appendix 27, in Figure 55 and Figure 56, respectively). The calibration curves R^2 values are shown in Table 5.7 for the PBS solutions and in Table 5.8 for the MEM solutions.

Table 5.7 – R^2 values of the rhBMP-2 calibration curves in PBS at 37 ^{o}C

Concentration	Curves generated / ng/mL	R^2 values obtained
Low	0-8	0.993
High	0-40	0.942

Table 5.8 – R^2 values of the rhBMP-2 calibration curves in MEM at 37 ^{o}C

Concentration	Curves generated / ng/mL	R^2 values obtained
Low	0-8	0.985
High	0-40	0.982

Using the fluorophore covalently labelled to rhBMP-2, the adsorption (as shown in Figure 5.7) and desorption profiles of FTCA-rhBMP-2 were determined for both physiological and pharmacological concentrations at 37 ^{o}C in PBS and in MEM, also depicted in terms of percentage adsorbed from initial concentration and percentage desorbed from total adsorbed amount.
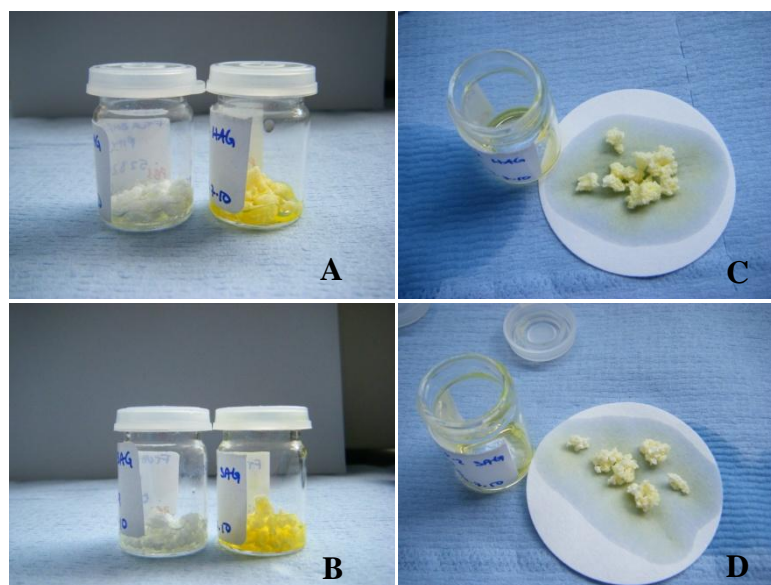
Figure 5.7 – Pictures of FTCA-rhBMP-2 adsorption onto HAG (a) and (c), and SAG (b) and (d)

PHYS   PHARMA
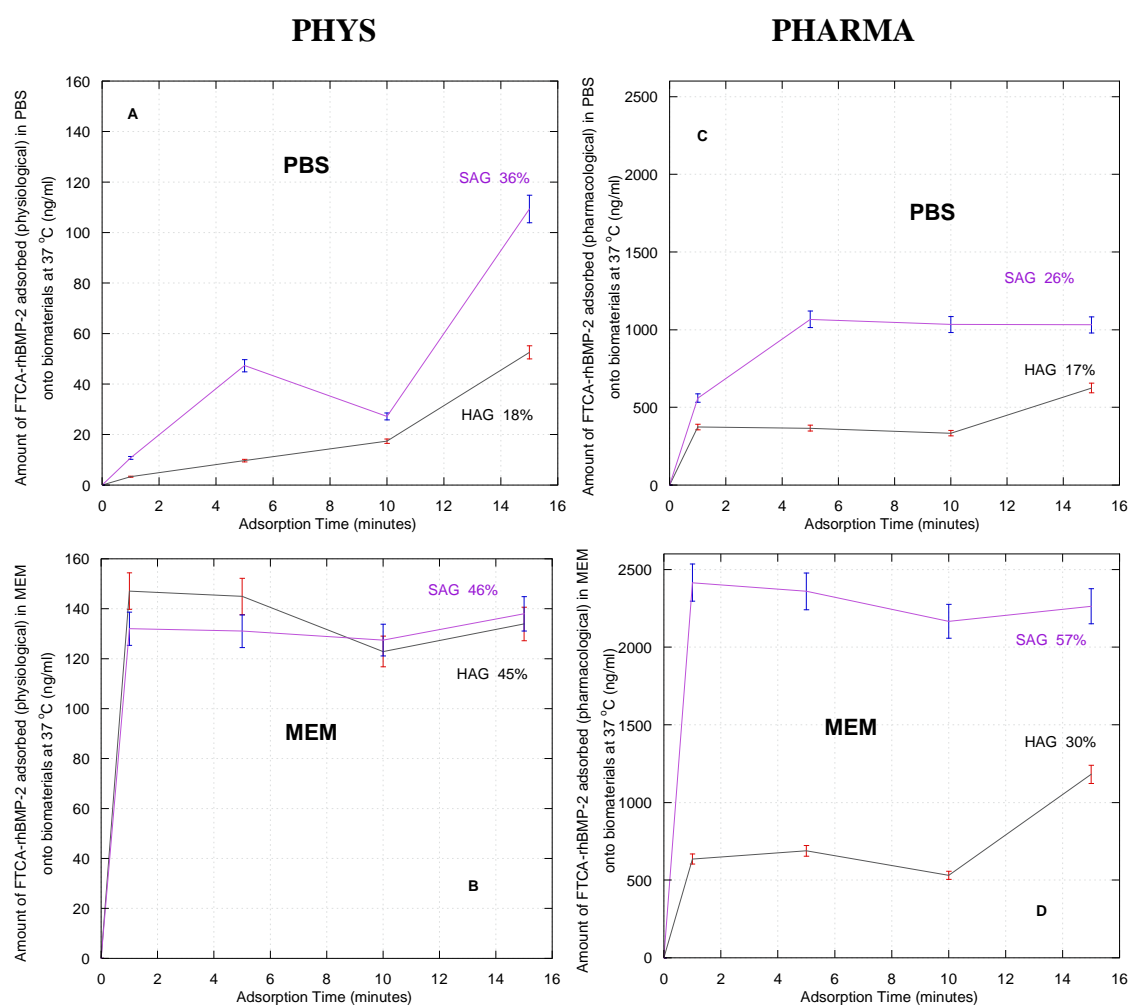
Figure 5.8 – Adsorption profiles of FTCA-rhBMP-2 in (a) PBS and (b) MEM at physiological (300 ng/mL) and in (c) PBS and (d) MEM at pharmacological (4 μg/mL) concentrations at 37 ^{o}C biomaterials (n= 3 ±s.d.)

The adsorption profiles at physiological concentration in PBS as shown in Figure 5.8A confirmed that SAG has a higher affinity for FTCA-rhBMP-2 than HAG, similarly observed when using the Quantikine kit, but only in pattern, values obtained here were hugely different. In MEM (see Figure 5.8B) the adsorption pattern for both SAG and HAG were higher than those obtained in PBS, with FTCA-rhBMP-2 having more affinity for the HAG for the first two time points, but at the end of the adsorption period SAG adsorbed slightly more than HAG.

At the pharmacological concentration, the adsorption profiles observed shown in Figure 5.8C and D, showed more FTCA-rhBMP-2 adsorbed by SAG compared to HAG with a relatively fast rate of adsorption in PBS compared to MEM. As seen previously, more FTCA-rhBMP-2 was adsorbed in MEM with an even faster rate of adsorption compared to the one seen in the PBS experiment. In both media, SAG adsorbed more FTCA-rhBMP-2 than HAG. However, the detected level of adsorbed growth factor was again much higher as compared to using the ELISA, and the greater affinity shown for SAG was not observed with FTCA-rhBMP-2 in MEM at physiological concentration.

PHYS   **PHARMA**
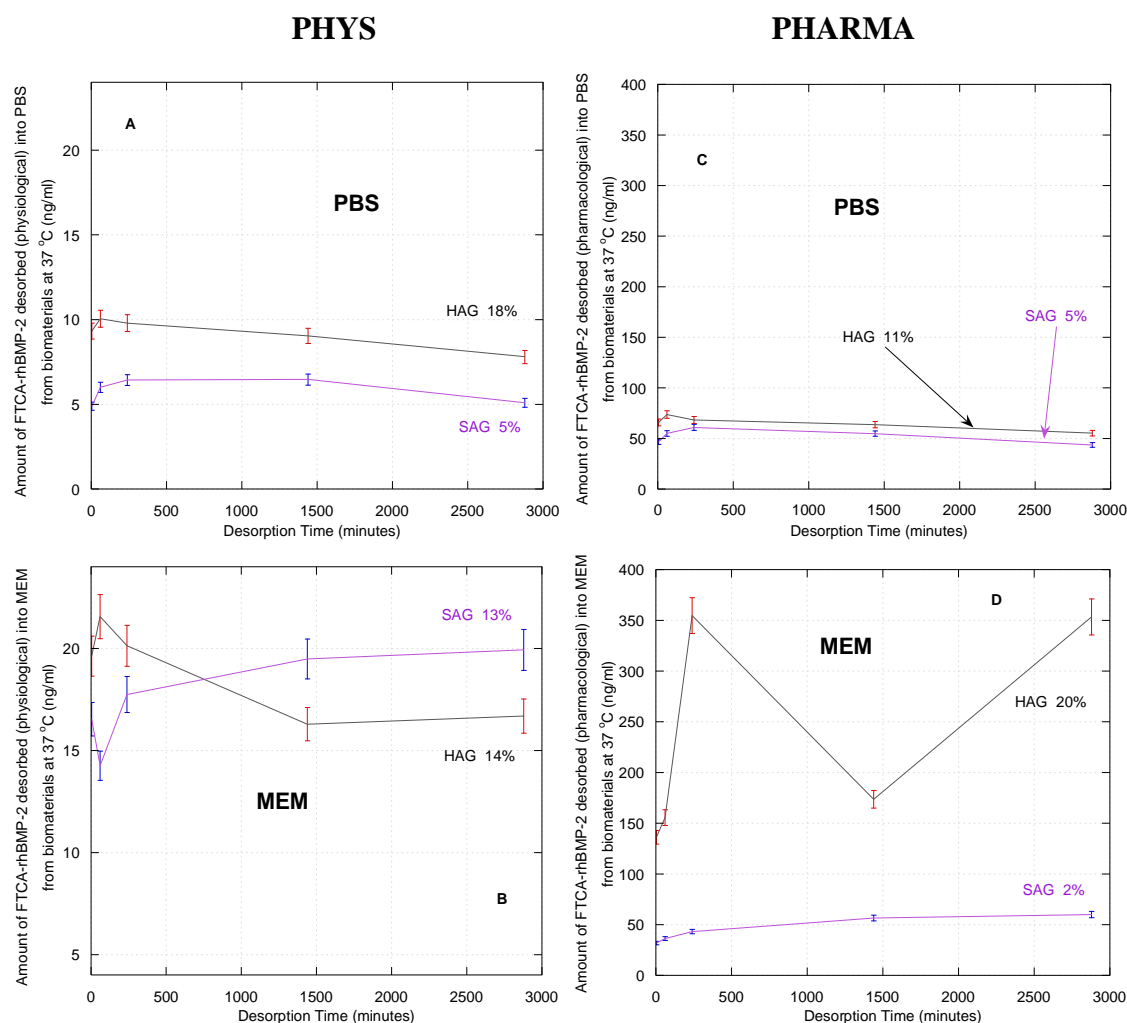
Figure 5.9 – Desorption profiles of FTCA-rhBMP-2 in (a) PBS and (b) MEM at physiological (300 ng/mL) and in (c) PBS and (d) MEM at pharmacological (4 µg/mL) concentrations at 37 ^{o}C biomaterials (n= 3 ±s.d.)

The release in PBS showed HAG releasing more than SAG at all time points at the physiological level as shown in Figure 5.9A, whereas in MEM, SAG released more than HAG (see Figure 5.9B). More FTCA-rhBMP-2 was released in MEM compared to PBS from both biomaterials with a strong affinity for the SAG in PBS, and a different behaviour in MEM with HAG showing a stronger affinity to FTCA-rhBMP-2.

At the pharmacological concentration, HAG and SAG released FTCA-rhBMP-2 in PBS at the same rate and pattern with little difference, other than HAG released slightly more. In MEM, however, HAG randomly released more FTCA-rhBMP-2 than SAG. HAG showed more desorption in MEM compared to in PBS, whereas SAG had a similar rate and pattern in both media.

5.3.3 Fluorescence Microscopy

Using FTCA-rhBMP-2 allowed for qualitative data to be collected in the form of fluorescence images on the dense discs form of the biomaterials as depicted at all time points in Figure 5.10 and Figure 5.11 in PBS and MEM on HAD and SAD, respectively. There was no protein auto fluorescence detected in the red or blue so only images with fluorescence in the green associated with the FTCA probe are presented.

Figure 5.10, Column A shows the FM images obtained when HAD was immersed in FTCA-rhBMP-2 in PBS solutions at particular time intervals. After 1 minute protein was adsorbed to the surface in distinct clusters with a globular morphology, the clusters being heterogeneously distributed over the disc surfaces. The number of clusters present on the surface increased with time up to 10 minutes, however from 15 minutes further protein adsorption was accommodated through growth on the globule clusters.

Figure 5.10, Column B shows the FM images from SAD samples of FTCA-rhBMP-2 in PBS. As on HAD samples, the adsorbed protein was observed to have a globular morphology; however these globules were initially adsorbed to the surface individually and homogeneously over the SAD surfaces. The formation of clusters was observed from 30 minutes.

The change from PBS to MEM showed a change in the protein morphology on HAD surfaces, as shown in Figure 5.11, Column A, where little protein was adsorbed in smaller globules compared to PBS, and as time elapsed the globules became more flat. Beyond the 15 minutes, the morphology of the protein changed to more sheet-like, and spread out, followed by the formation of clusters with increasing fluorescent intensity and time of immersion (30 and 60 minutes). While, protein morphology on the SAD samples did not changed, as shown in Figure 5.11, Column B, where the rhBMP-2 was still globular in shape, small; and increasing in intensity and amount with time. Only after the sixty minute immersion did the protein slightly change shape to a rather flatter cluster of small globules.

Columns: A. **HAD**   B. **SAD**
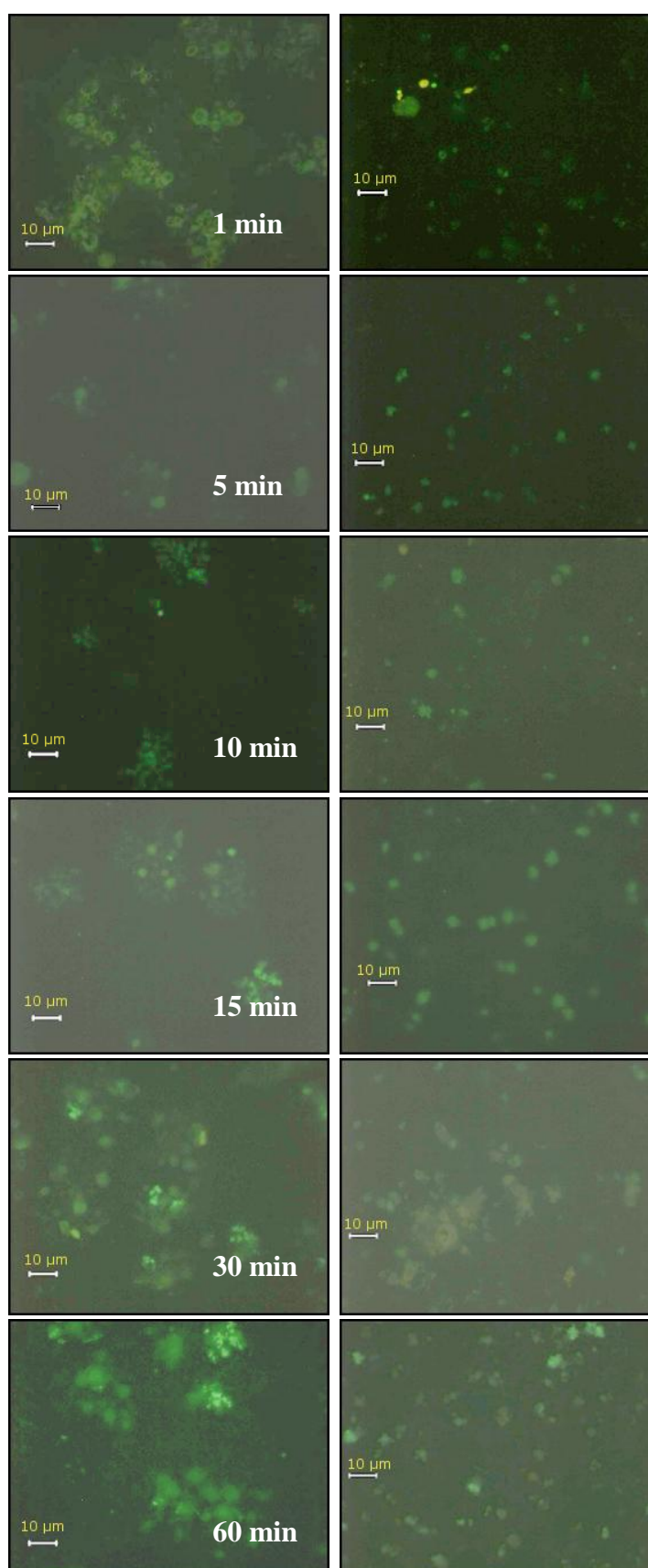
Figure 5.10 – FM images of FTCA-rhBMP-2 on (a) HAD and (b) SAD at all time intervals in PBS at 37 ºC

Columns: A. **HAD**   B. **SAD**
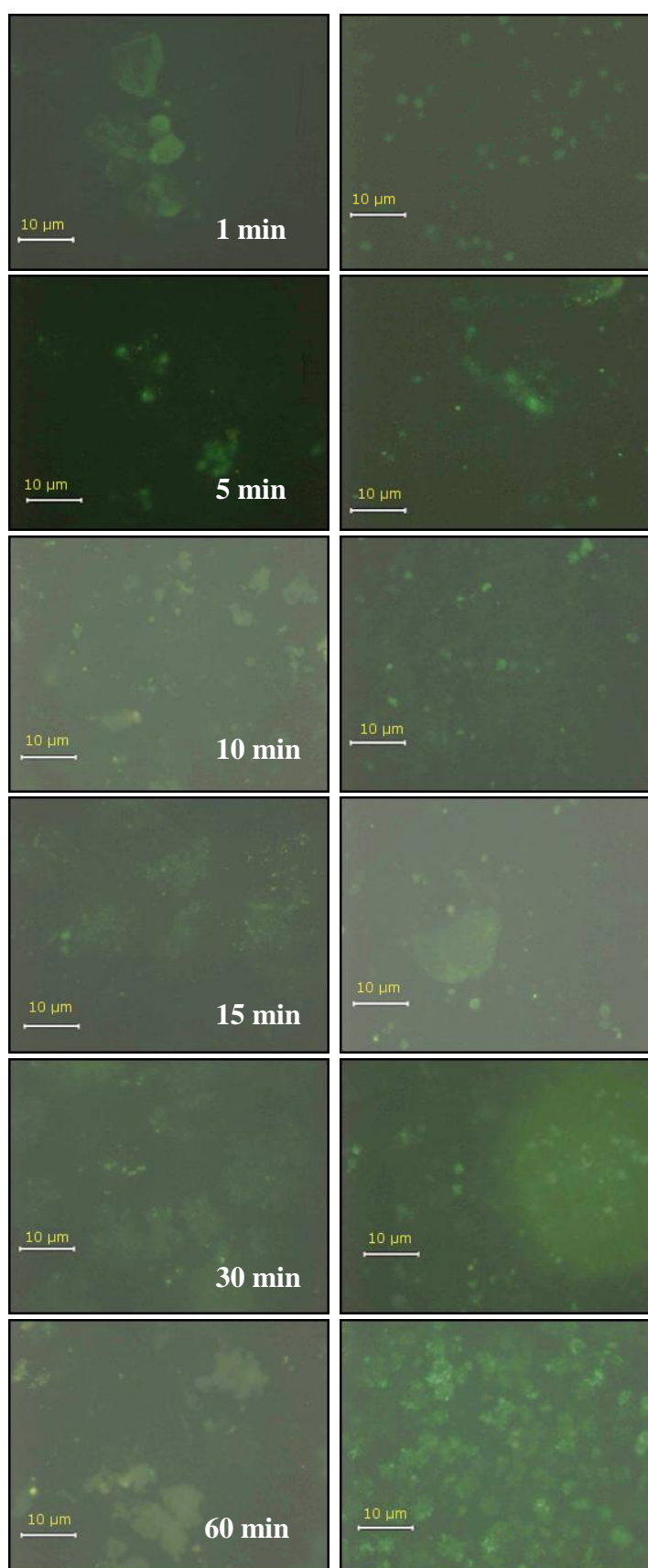
Figure 5.11 – FM images of FTCA-rhBMP-2 on (a) HAD and (b) SAD at all time intervals in MEM at 37°C

5.4   Discussions

Calibrations from both methods generated good linear relationships both in PBS and MEM, with R^2 values ranging from 0.900 to 0.990, as shown in Appendices 25 to 27 in Figures 135 to 137.

One of the striking observations in this study was the discrepancy in the level of rhBMP-2 adsorption identified using the ELISA and FTCA labelling methodologies. FTCA-rhBMP-2 indicated higher adsorption than indicated by the ELISA both in PBS and MEM, but also at the physiological and pharmacological concentrations.

This discrepancy could be due to the antibody sensitivity to protein conformation as the protein species was affected by the chemistry of the biomaterial. Also, the low or high BMP-2 concentration could be out of the calibration range.

rhBMP-2 Adsorption at Physiological and Pharmacological concentrations

Values generated from the ELISA were in the region of 0 to 60 ng/mL, while using FTCA-rhBMP-2 0 to 2000 ng/mL of growth factor was detected. This, thus, gave rise to a lower percentage of adsorbed amounts from the Quantikine kit, where at physiological concentration, SAG adsorbed 0.4 % of the growth factor and HAG 0.3 %, compared (see Figure 5.5A) to 36 % and 18 % (see Figure 5.8A) on SAG and HAG, respectively, using FTCA-rhBMP-2 in PBS. In MEM, a similar observation was seen from both methods with higher adsorbed amounts detected, just as previously seen in Chapter 4. An adsorbed percentage of 5 % and 3 % of rhBMP-2 were detected on SAG and HAG, respectively, as shown in Figure 5.5B, using the Quantikine kit compared to 46 % and 44 % using FTCA-rhBMP-2 at the physiological concentration in MEM (see Figure 5.8B).

More growth factor was adsorbed at pharmacological concentration, which was as expected as the concentration was 1000-fold larger (4000 ng/mL to 300 ng/mL concentration); see Figure 5.5C and D for the Quantikine kit and Figure 5.8C and D for FTCA-rhBMP-2. The percentage of adsorbed rhBMP-2 was also very different between the ELISA kit and FTCA-rhBMP-2 at this level, where using the Quantikine kit only 2 % and 0.8 % was adsorbed on SAG and HAG, respectively, compared to 26 % and 17%

using FTCA-rhBMP-2 in PBS. While in MEM, the percentages adsorbed were 2 % and 1.5 %, SAG and HAG using the Quantikine kit compared to 57 % and 30 % using FTCA-rhBMP-2. This may suggest the influence of two factors affecting the adsorption and release process. The first would be that the Quantikine kit is too sensitive to the rhBMP-2 conformational changes when in contact with the biomaterials. Thus, only minimal amounts of rhBMP-2 were detectable, while the rest was ignored by the antibodies within the sandwich analysis, as the inappropriate conformation was adapted by the growth factor. This observation was further confirmed when looking at the rate of release of rhBMP-2 in PBS, especially during the physiological concentration experiment, where the percentage of desorbed amounts was apparently higher, at particular time points, compared to the percentage adsorbed for both SAG and HAG. For example, up to 151 % of rhBMP-2 was released from HAG at the end of the release period compared to 88% for SAG, while at the beginning of the release period 123 % was released from SAG, as shown in Figure 5.6A. This suggests that during the desorption period, the rhBMP-2's conformation changed to the preferred one for the Quantikine kit, and thus was detected by the antibodies and may indicate that the specificity of the antibodies has affected the recorded rhBMP-2 pattern of release, and that the data collected may not be truly representative.

The second factor that may have an influence on the adsorbed and released amounts of rhBMP-2, especially at the physiological concentration, may be the presence of the different component of the media present in solution. In PBS, the medium has a more ionic character consisting of potassium chloride (KCl) and sodium chloride (NaCl) in contrast; MEM has a mixture of both inorganic and organic components such as amino acids, vitamins and salts. Clearly in MEM, higher adsorbed and desorbed amounts were detected by the Quantikine kit and FTCA-rhBMP-2. This may be due to the presence of the extra amino acids as demonstrated in the work of Dong *et al* (Dong, Wang, *et al.* 2007) where *via* the use of computational study showed that rhBMP-2 adsorption to HA can be influenced by the presence of amino acids. The group showed that *via* a displacement study that non-adsorption residues like lysine (Lys) or proline (Pro) have no effect on the adsorption process, but fulcrum-adsorption residues such as asparagine (Asn) or glutamic acid (Glu) have. These fulcrum-adsorption residues are all present in the MEM at an average concentration of 0.0134 g/L, and therefore could have been responsible for the enhanced rhBMP-2 adsorption and release on the biomaterial's surface in MEM in this study also.

rhBMP-2 Desorption (release) at Physiological and Pharmacological concentrations

The release of rhBMP-2 from the biomaterials into fresh PBS or MEM using both methods, ELISA and FTCA-rhBMP-2, are shown in Figure 5.6 and Figure 5.9, respectively. Depletion of the FTCA-rhBMP-2 was clearly evident from the solution by eye observation, as the labelled growth factor (light yellow in colour) diffused from the biomaterials into PBS and MEM to then be quantified. These observations confirmed the growth factor release at physiological and pharmacological concentrations, with both observed and quantified larger amounts at the pharmacological concentration as expected, as shown in Figure 5.7.

At the physiological concentration in PBS, as a percentage of the growth factor adsorbed by a greater percentage of rhBMP-2 was released from the biomaterials as measured by the Quantikine kit (see Figure 5.6A) compared to FTCA-rhBMP-2 (see Figure 5.9A) with release percentages ranging from 68 % to 151% for HAG, and 123 % to 88% for SAG using the Quantikine kit, compared to an average of 18 % for HAG and 5 % for SAG from FTCA-rhBMP-2. The release trend in PBS showed HAG desorbing more than SAG. While in MEM, an average of 13 % rhBMP-2 was released from HAG compared to 17 % from SAG using the Quantikine kit (see Figure 5.6B), compared to 14 % from HAG and 13 % from SAG using FTCA-rhBMP-2 (see Figure 5.9B). This showed that in MEM when using the Quantikine kit SAG desorbed more than HAG, while the opposite trend was observed when using FTCA-rhBMP-2. However considering that release values of over 100 % were obtained when using the kit, it is likely that data so obtained is unreliable as compared to the data obtained from FTCA-rhBMP-2. These observations suggest that the Quantikine kit's detection behaviour has been influenced by a change in protein conformation which may be sensitive to the change in chemistry of the biomaterials. Thus, the data may not be representative of the actual adsorption and desorption behaviour, which further validates the use of FTCA-rhBMP-2 as a more reliable method of monitoring the adsorption and release behaviour of the growth factor.

Previous investigations into the nature of BMP-2 confirmation reported that BMP-2 carries two negative charges that would be available for adsorption on biomaterials

surfaces. In the work of Dong *et al.*, these charges were neutralised with sodium ions that limited the BMP-2 interactions with the HA surface due to the water-bridged H-bonds that kept on forming and breaking changing the conformation. In this work, the charges were not neutralised, suggesting they may have been free to interact with ions present in solution, for example the amino acids, before interacting with the biomaterial's surfaces, and thus affected the growth factor's conformation, which would agree with Dong *et al.* (Dong, Wang*, et al.* 2007) This change in protein/cell conformation/morphology was also observed in the work of Guth *et al.* where the cytoskeletal arrangement of cells grown on the rough biomaterial surfaces against the control were different as judged by the actin filament labelled with FITC. (Guth, Campion*, et al.* "Effect of Silicate-Substitution on Attachment and Early Development of Human Osteoblast-Like Cells Seeded on Microporous Hydroxyapatite Discs" 2010) This suggests that morphology was affected by the surface roughness, but also the physiochemical properties of the biomaterials.

At the pharmacological concentration, the release of rhBMP-2 was higher from FTCA-rhBMP-2 compared to the Quantikine kit, and higher in MEM compared to PBS from both methods. HAG desorbed more in PBS and MEM compared to SAG. Again value discrepancies were observed at this level where an average of 5 % rhBMP-2 was released from HAG compared to 2 % from SAG into PBS and MEM using the kit. While when using FTCA-rhBMP-2, an average of 11 % of rhBMP-2 was released from HAG and 5 % from SAG in PBS, compared to 20 % from HAG and 2.0 % from SAG in MEM, showing HAG desorbed more than SAG.

This study, therefore, suggests that the use of the FTCA-rhBMP-2 labelling methodologies gave rise to more reliable data than when the ELISA was used with an adsorption and release trend clearly showing SAG to have stronger affinity to the growth factor compared to HAG in both PBS and MEM at 37 $^{\circ}$C.

Interpretations of the Fluorescent Images

Slightly more FTCA-rhBMP-2 was observed on the SA samples (see Figure 5.10 B and Figure 5.11B) compared to HA (see Figure 5.10A and Figure 5.11A). In PBS, the morphology of rhBMP-2 on HAD showed large globule, which clustered as immersion time elapsed heterogeneously (see Figure 5.10A). While on the SAD, FTCA-rhBMP-2 observed showed to have smaller globules across the surface, evenly spread (see Figure

5.10B). In MEM, there was an evident change in the protein morphology on HAD, as shown in Figure 5.11A from globular to sheet-like, heterogeneously spread across the surface. However, on the SA surface, as shown in Figure 5.11B, showed little morphological changes, where the globules seem smaller than on HAD in PBS and MEM, but not so compared to on the SAD surface in PBS.

The images and changes in the growth factor's morphology further confirmed the dynamic behaviour of the rhBMP-2 adsorption process, which was also shown in Chapter 4 for BSA and Chapter 6 when in a competitive environment, but also the changes in protein conformation. This would agree with the work of Dong *et al.* but also Guth *et al.* (Dong, Wang*, et al.* 2007; Guth, Campion*, et al.* "Surface Physiochemistry Affects Protein Adsorption to Stoichiometric and Silicate-Substituted Microporous Hydroxyapatites" 2010) previously described in adsorption and release of rhBMP-2 sub-section in this discussion.

It is important to have a good understanding of the rhBMP-2 adsorption and desorption processes, in terms of the drug delivery system in which BMPs are expected to be kept in place at the site of delivery, so that the molecules can exert their biological action and then provide an initial substratum for growth and differentiation of bone forming cells. (Saito and Takaoka 2003) Also the use of the appropriate carrier for such system, and the ability to induce controlled bone growth, is essential (Luginbuehl, Meinel*, et al.* 2004), thus this study showed that the porous granular form of the silicate-substituted hydroxyapatite (SAG) to be ideal, as it adsorbed more and released less in time, especially in MEM.

Previous studies have shown that the most common carrier for BMP is collagen , others have used demineralised bone matrix (DBM) carrier (Wang, Rosen*, et al.* 1990), polymers (Lutolf, Weber*, et al.* 2003), ceramics (Ripamonti 1996) or a form of composite consisting of polymer/ceramics (Saito, Okada*, et al.* 2003) or collagen/ceramics (Hirata, Nomura*, et al.* 2007). The importance of the studies was to achieve reproducibility of the pharmacokinetics that would allow BMP to be retained and released effectively, for a more control bone formation. The work of Kaito *et al.* found that as little as 5 or 20 µg of BMP was required to have a complete repair of the bone defect with sufficient strength using a carrier which contain biodegradable polymer and interconnected-porous in calcium hydroxyapatite ceramics, compared to often suggested milligram amounts in other studies (Kaito, Myoui*, et al.* 2005).

(Nilsson, Urist, *et al.* 1986; Urist 1965; Urist and Strates 1971; Yasko, Lane, *et al.* 1992). Although in the present study, the bone repair effect has not yet been determined, the study still showed that an even lower BMP concentration can be used for controlled adsorption and release of the growth factor on a one phase porous carrier at 37 ^{o}C. This could be advantageous if it shows to generate complete bone repair with sufficient strength, as it would lower the cost on BMP concentration required in relation to the carrier used.

5.5   Summary & Conclusions

In this chapter, two methods, the ELISA using a rhBMP-2 specific kit (Quantikine) and the FTCA labelling methodologies were used.

Quantikine data obtained clearly showed that the sensitivity of the antibodies to a specific rhBMP-2 conformation was a disadvantage. Adsorbed amounts were lower (see Figure 5.5) than desorbed amounts (see Figure 5.6), especially at the physiological (300 ng/mL) level in PBS as shown in Figure 5.5A and Figure 5.6A. Although, the patterns still suggested that SAG adsorbed more than HAG; the data was found to be unreliable.

FTCA-rhBMP-2 appeared to give more reliable data, than when using the ELISA with respect to quantification of the rhBMP-2 growth factor adsorbed (see Figure 5.8) and released (see Figure 5.9) of rhBMP-2 from the biomaterials.

Changing medium from an ionic solution (PBS) to a more mixed inorganic and organic solution (MEM) showed an increase in rhBMP-2 adsorption on both biomaterials compared to PBS at both physiological (300 ng/mL) and pharmacological (4 µg/mL) concentrations, suggesting that MEM may have induced a stronger affinity to the biomaterials *via* its component interactions with rhBMP-2 during the adsorption process. The interactions between growth factor and medium (i.e. the amino acid or vitamin component) or those between growth factor and biomaterial (i.e. porosity, surface area and surface chemistry) may have been enhanced to create a stronger affinity. The study did not provide evidence to distinguish among the possibilities, but did look at the protein unfolding in Chapter 6 to show the change in protein conformation that may affect the interactions between biomaterials, component of solution and protein. Overall, the adsorption pattern showed that SAG adsorbed more than HAG, and desorbed less, suggesting that a greater affinity for the growth factor to adhere on SAG surfaces was revealed.

Using the fluorometric analysis, also allowed for qualitative data to be collected where for the most part, more rhBMP-2 was evenly adsorbed on the SA surface compared to the HA surface, with little change in protein morphology on the biomaterial's surface in the two media .

Chapter 6. COMPETITIVE PROTEIN BINDING STUDIES

6.1   Background

The competitive nature of protein adsorption has been of interest within the biomaterials community and the orthobiologics industries, as understanding or control of protein adsorption is key to the performance of many classes of implant while more recently the kinetics of protein adsorption and desorption have proved critical to the design of suitable drug delivery vehicles.

Previous competitive studies analysed *via* different techniques and on various biomaterials, all showed that the competitive nature of proteins was strongly influenced by the protein concentration (Fabrizius-Homan and Cooper "Competitive adsorption of vitronectin with albumin, fibrinogen, and fibronectin on polymeric biomaterials" 1991), affinity to the biomaterial surface (Fabrizius-Homan and Cooper "A comparison of the adsorption of three adhesive proteins to biomaterial sufaces" 1991), and time (Green, Davies*, et al.* 1999), where the temporal dependence is usually known as the "Vroman" effect. The presence of secondary protein species has also been shown to affect adsorption of a primary protein through influence on conformational change of the primary species (Arai and Norde 1990).

In this chapter, the aim was to quantitatively determining protein adsorption and desorption in a competitive environment using proteins directly coupled to fluorescent probes. The use of 2 fluorescent probes was initially undertaken to determine whether simultaneous quantification of two different protein species could be performed within the same experiment. However, the work revealed the phenomenon of auto-fluorescence plasticity in proteins, i.e. changes in protein auto-fluorescence on interaction with biomaterials.

This chapter includes three sets of experiments;

<u>Study A</u>: the initial trial with two species of protein coupled to different fluorescent probes;

<u>Study B:</u> the investigation of auto-fluorescence and finally,

<u>Study C</u>: the revised work using a single species of coupled protein in MEM containing 10 % FBS as the competitive environment.

6.2 Experimental Methodology

All glassware and containers were used as received sterile from the manufacturer (VWR). All reagents, protein solutions were brought to 37 ^{o}C before use.

6.2.1 **Study A**: Investigation of the competitive binding using two independently labelled protein species

The aim of this study was to analyse the binding of fibronectin (FN) in competition with BSA by independently labelling both proteins with two distinct fluorophores. The labelling of the proteins was prepared as described in Chapter 3, section 3.3.1.

Test solutions & Experiments

Fibronectin, FN (341631, Calbiochem, UK) was thawed to yield a protein concentration of 3000 µg/mL. FN was then further diluted using water or PBS for the analysis. Bovine serum albumin, BSA (A9647, Sigma-Aldrich), lyophylised, was reconstituted in water or PBS when required to make a stock solution of 50 mg/mL concentration.

Table 6.1 – Test solutions: buffer, medium and protein solution concentrations

Test solutions	Details	Concentrations
Phosphate Buffered Saline (PBS)	PBS: dissolve one tablet in 200mL deionised water pH 7.4 (P4417)	0.01 M
Fibronectin (FN)	FN, bovine plasma, liquid in NaCl and NaHPO$_4$ buffer (341631)	300 µg/mL stock solution
Bovine serum albumin (BSA)	BSA: Lyophilized bovine serum albumin (A9647)	16.1 mg/mL stock solution

Table 6.2 – Specimen and preliminary experiments undertaken in PBS (at 37 ^{o}C only)

Specimen	SAD	HAD
SR101-BSA	√	√
FTCA-FN	√	√

Adsorption Protocol

Using the 24-well plate with a plate layout illustrated in Figure 6.1 and dense discs (DD) form of the biomaterials, the competitive binding of FTCA-FN and SR101-BSA was determined.

Figure 6.1 – Competitive binding layout in 24-well plates

Experiments were conducted with the final dual labelled test solutions in 1.5 mL protein solution at two ratios, (1) the 50/50 ratio containing FTCA-FN at a concentration of 150 µg/mL and SR101-BSA at a concentration of 4 mg/mL in PBS, near physiological levels, and (2) the 40/60 ratio with 120 µg/mL of FTCA-FN and 8 mg/mL SR101-BSA in PBS. Adsorption was then analysed by transfer of 1.5 mL of the dual labelled solution into clean glass vials and left to adsorb for 15 and 60 minutes. The serial dilutions of the stock solutions were made in PBS so as to generate high and low calibration curves for both the individually labelled protein solutions. Figure 6.2 shows the schematic of the 24-well plate layout.
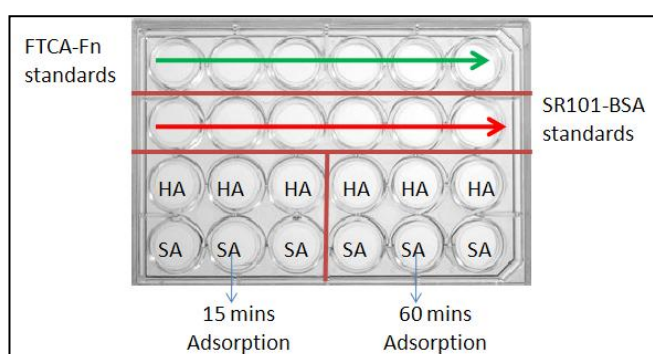
Figure 6.2 – 24-well plate layout for the dual label experiments

Table 6.3 shows the actual protein amount used in the fibronectin calibrations. Calibrations generated for FN and BSA illustrated in Appendices 28 and 29 in Figures

138 and 139, respectively, showed good calibrations with high R^2 values obtained, see Table 6.4.

Table 6.3 – Amount of Protein per well used the calibration curves: high and low ranges

FTCA-FN (High) μg	FTCA-FN (Low) μg	SR101-BSA (High) mg	SR101-BSA (Low) mg
22.2	1.1	7	1
16.7	0.88	6	0.8
11.1	0.66	5	0.6
5.5	0.44	4	0.4
2.2	0.22	2	0.2
1.1	0.11	1	0.1

Table 6.4 – R^2 values obtained from the Calibrations in PBS at 37 ^{o}C

Protein Solutions	High	Low
FTCA-FN	0.942	0.979
SR101-BSA	0.924	0.990

Although, the R^2 values were higher than 0.900, the trend was clearly giving a negative correlation for BSA compared to FN, when labelled with SR101 showing that this labelling may not be suitable.

6.2.2   **Study B**: Investigation of the Autofluorescence

The data for this study were represented in terms of fluorescence intensity against time adsorbed, using dense discs of the biomaterials following a layout in 24-well plates as shown in Figure 6.3. Data obtained from the dual label study suggested that the fluorescence of SR101-BSA was influenced by external confounding factors. Therefore a series of experiments were devised to assess whether BSA auto-fluorescence was sensitive to experimental conditions which may confound the quantitative data obtained. Fluorescence intensity was measured using a plate reader (GalaxyStar) at excitation/emission conditions of 576/606 and 494/520 nm.
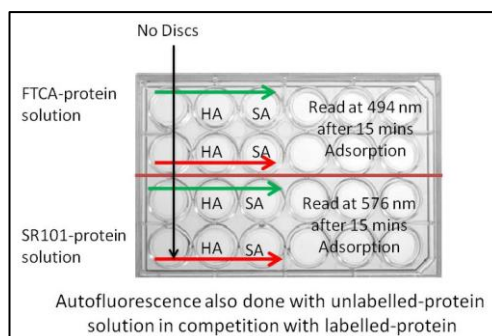
Figure 6.3 – Layout for the Autofluorescence Study

Experiments were first performed on both unlabeled BSA and FN solutions in PBS, at concentrations of 4 mg/mL and 300 µg/mL, respectively, to determine whether or not BSA exhibited auto-fluorescence under the conditions of excitation/emission relevant to the FTCA and SR101 labels. These experiments were then repeated on protein solutions that had been exposed to HA and SA discs for a 15 minute adsorption period at 37 ^{o}C. Further experiments were then performed to assess whether auto-fluorescence was also sensitive to the presence of other proteins in solution. FTCA-BSA and SR101-BSA were combined with unlabelled FN at the physiological level for a 15 minute adsorption period at 37 ^{o}C, followed by the analysis of FTCA-FN and SR101-FN with unlabeled BSA at similar conditions denoted in the previous sentence.

Fluorescence intensity and time resolved settings with excitation set at 494/576 nm and emission at 520/620 nm, respectively, was employed. 16 cycles time of 60 seconds with 10 flashes, 0.5 seconds delay with orbital shaking set for 10 seconds before each cycle was used.

Circular Dichroism (CD) Spectroscopy

The folding or unfolding of the proteins was determined after contact with the dense discs. The CD spectra were obtained in the wavelength range from 190 to 260 nm, at 1 nm bandwidth, 3 seconds per point, through a pathlength of 0.1 cm in triplicates, using Chirascan (Applied Photophysics, UK) and Prodata viewer software.
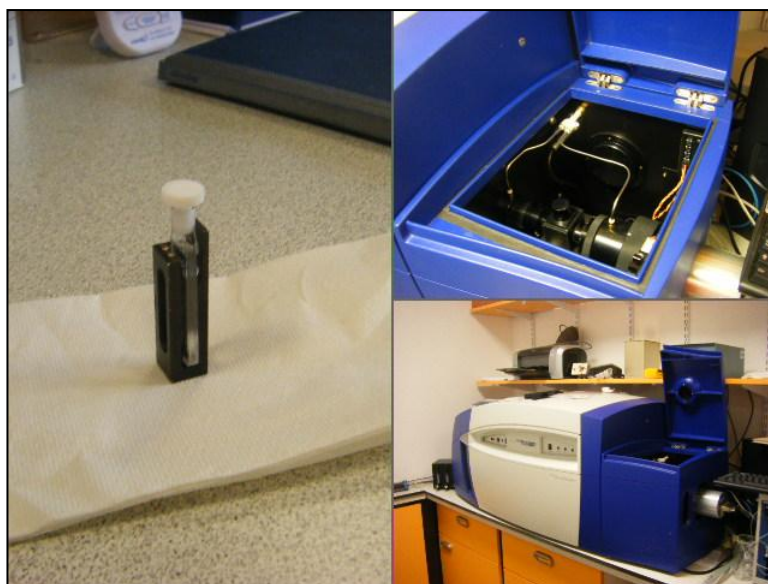
Figure 6.4 – CD 300 µL holder and Chirascan Instrument

Using the CD spectra, the secondary protein structure for each protein was determined using DICHROWEB (Whitemore and Wallace 2004), an online server. The data was converted from ellipticity (θ in degree.cm^2/mol), the unit given from the instrument, to epsilon ($\Delta\varepsilon$ in M^{-1} cm^{-1}), the unit required to do the online analysis using Equation 6.1.

$$\Delta\varepsilon = \frac{\theta \; value \; of \; CD \; spectra}{33000 \; x \; Concentration \; in \; M \; x \; l}$$

Equation 6.1

$$Mean \; Residue \; Weight \; Daltons = \frac{RMM}{Number \; of \; Residues - 1}$$

Equation 6.2

Protein concentration was also converted from mass per volume to molar (M) concentration, using the relative molecular mass (RMM) of the proteins, and the number of residue, further information (mean residue weight in Equation 6.2) allowed for the secondary analysis to be undertaken.

6.2.3 **Study C**: Investigation of the competitive binding in MEM containing 10 % FBS

Labelling of the BSA and rhBMP-2 with FTCA has been described previously in Chapter 3 section 3.3.1, and similarly for the labelling with SR101 to FN and OPN.

The preparation of FTCA-BSA standards were as described in Chapter 4 and used to determine the unknown in MEM + 10 % FBS. Similarly for the preparation of FTCA-rhBMP-2 standards in Chapter 5, the calibrations were prepared.

The preparation of SR101-rmOPN standards were undertaken using the 50 ng/mL SR101-rmOPN stock solution, standards of known concentrations were made in fresh MEM + 10 % FBS, aliquots of 1 mL solutions, in order to determine protein amounts in unknown samples.

Table 6.5 – Concentrations of the rmOPN in the SR101-rmOPN serial dilutions

OPN Concentrations (pg)		
Original	10 µL	2 µL
50000	500.0	100.0
25000	250.0	50.0
12500	125.0	25.0
6250	62.5	12.5
3125	31.25	6.25
1562.5	15.625	3.125
781.25	7.8125	1.5625
0	0	0

Serial dilutions were produced including the 50 ng/mL (50000 pg/mL) as the highest concentration and MEM + 10 % FBS only to generate the 0 pg/mL concentration, summarised in Table 6.5.

Test solutions & Experiments

Bovine serum albumin, BSA (A9647, Sigma-Aldrich), lyophilised, was reconstituted in water the appropriate solvent when required to make a stock solution of 50 mg/mL concentration in MEM.

The lyophilised recombinant human bone morphogenetic protein-2, rhBMP-2 (10 µg, RCYT-261, Sera Laboratories, UK) was reconstituted in acetic acid (AcOH, 20 mM, 100 µL) at a concentration of 100 µg/mL, which was then stored below -18 $^{\circ}$C for future use or further diluted in phosphate buffered saline, PBS (P4417; Sigma-Aldrich; pH7.4; 0.01 M), minimum essential medium, MEM (M3024, Sigma-Aldrich) and MEM + 10 % fetal bovine serum, FBS (F9665, Sigma-Aldrich). rhBMP-2 was further diluted and incubated at 37 $^{\circ}$C to make a concentration 3 times higher than that of the super physiological concentration at 4 µg/mL. The rhBMP-2A (12 µg/mL in 1 mL aliquot) was then used for the coupling (labelling) reaction.

The lyophilised recombinant mouse osteopontin, rmOPN (50 µg, 499260, Calbiochem, UK) was reconstituted in PBS and MEM to yield 50 µg/mL concentration stock solutions (1 mL aliquots of each), from which lower stock solutions of 5 µg/mL in PBS, MEM and MEM + 10 % FBS were made. These stock solutions were then used to make 150 ng/mL aliquots (1 mL) for the coupling reaction. All test solutions and concentrations are tabulated below (see Table 6.6).

Tabulated below are the type of specimens (Table 6.7) used for the experiments undertaken within this chapter. All were prepared and characterised as previously described in Chapter 2.

Table 6.8 shows the experiments undertaken for each protein solution in order to determine the competitive binding affinity with the specimen.

Table 6.6 – Test solutions: buffer, medium and protein solution concentrations

Test solutions	Details	Concentrations
Minimum essential Eagles' medium (MEM)	MEM: containing inorganic components, amino acids and vitamins (product code: M3024)	9.3 mg/mL
Fetal Bovine Serum (FBS)	FBS: Heat inactivated liquid (F9665)	≤ 20mg/dL Hemoglobin
Bovine serum albumin (BSA)	BSA: Lyophilised bovine serum albumin (A9647)	4 mg/mL
Bone Morphogenetic protein-2 (rhBMP-2)	rhBMP-2: lyophilised powder reconstituted in acetic acid to make 100 µg/mL stock solution (RCYT-261)	300 ng/mL
Recombinant mouse Osteopontin (rmOPN)	rmOPN lyophilised powder reconstituted in MEM or PBS to make a 50 µg/mL stock solution (499260)	50 ng/mL

Table 6.7 – Specimen description and acronyms used throughout study

Specimen description	Acronyms
Silicate-substituted apatite porous granules	SAG
Silicate-substituted apatite dense discs	SAD
Hydroxyapatite porous granules	HAG
Hydroxyapatite dense discs	HAD

Table 6.8 – Specimen and revised experiments undertaken in MEM with 10 % FBS at 37 ^{o}C

Specimen	SAD	SAG	HAD	HAG
4 mg/mL FTCA-BSA	√	√	√	√
300 ng/mL FTCA-rhBMP-2	√	√	√	√
50 ng/mL SR101-rmOPN	√	√	√	√

The concentrations in Table 6.8 are the respective physiological concentrations for each of the protein solution used in this investigation.

Adsorption Protocol

The work was then set up as described in previous chapters, where specimens and test solution were placed in vials, then the aliquots (1.5 mL) were analysed in 96-well plates with 200 µL of the MEM + 10 % FBS, standards and samples transferred into the each well, according to the plate layout as shown in Figure 6.5.
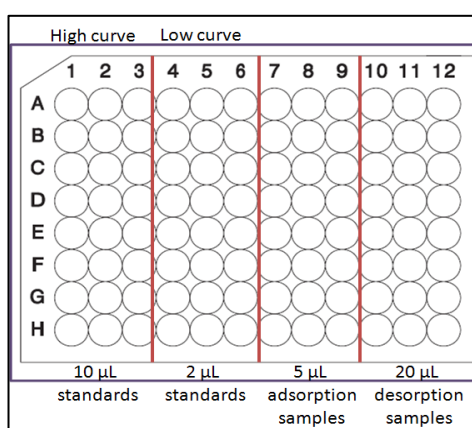
Figure 6.5 – Adsorption and desorption plate layout for the revised work

The competitive study was undertaken at physiological concentrations for all protein under investigation, previously stated in Table 4.2. 5 µL of original and adsorbed samples were placed in the wells according to the layout, followed by 20 µL of the wash and desorbed samples, and the standards for each method where 10 and 2 µL were added to each well, for the high and low calibrations, respectively.

Fluorescence intensity and time resolved settings with excitation and emission were set at 494/576 and 520/620 nm, respectively. A cycle time of 60 seconds with 10 flashes, 0.5 seconds delay with orbital shaking set for 10 seconds.

6.2.4   Fluorescence Microscopy

This part of the study was done at physiological level of the protein solutions at 4 mg/mL for the FTCA-BSA, 300 ng/mL for the FTCA-rhBMP-2 and 50 ng/mL for the SR101-rmOPN on dense discs of the biomaterials at 37 ^{o}C.

The adsorption behaviour only was observed after samples were submerged in the labelled protein solution for particular time intervals (1, 5, 10, 15, 30 and 60 minutes).

FM images here will be illustrated through all three filters of the fluorescence microscope, green, blue, and red as the FBS will have other proteins, amino acids, which may auto-fluoresce in all the three wavelengths. All images will be represented at a 200X magnification, unless stated otherwise, where the scale bar on the image represent a 10 μm size.

Fluorescence microscopy was performed using a Zeiss Axioskop microscope, employing a mercury lamp UV source, and three filters with excitation/emission wavelengths of 450-490/515nm, 365/395nm and 546-512/598 which enable imaging of dyes that fluoresce in the green, blue or red, respectively. The images (micrographs) were taken at magnifications of 50, 100 or 200 and used for qualitative analysis of the protein adsorption on dense discs of the biomaterials with a working fixed exposure of 695 ms.

6.3   Results

6.3.1   Competitive Binding with two individually labelled proteins (Study A)

The following two graphs showed the amount of independently labelled FTCA-FN and SR101-BSA adsorbed after 15 and 60 minutes on the biomaterials in the presence of each other in competition.

There was an increase in intensity of the colour observed from the two labelled proteins, which was as expected with increasing protein concentration. For both labelled protein solutions, high and low calibrations concentrations were generated in order to determine the unknown adsorption behaviour (see Appendix 28 and Appendix 29, in Figure 138 and 139).
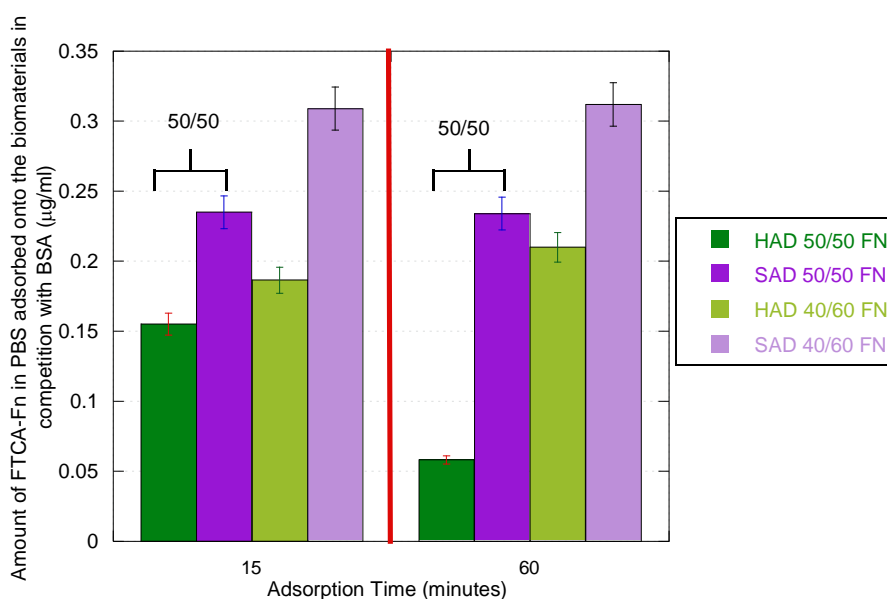
Figure 6.6 – Amount of FTCA-FN adsorbed onto biomaterials in the presence of SR101-BSA biomaterials (n= 3 ±s.d.)

At the two protein ratios in solution, FN adsorbed more with increasing amount of BSA especially on the SAD surfaces, as shown here in Figure 6.6, whereas increasing the amount of BSA proved to have little effect on the amount of BSA adsorbed on the biomaterials' surfaces, as seen here in Figure 6.7.
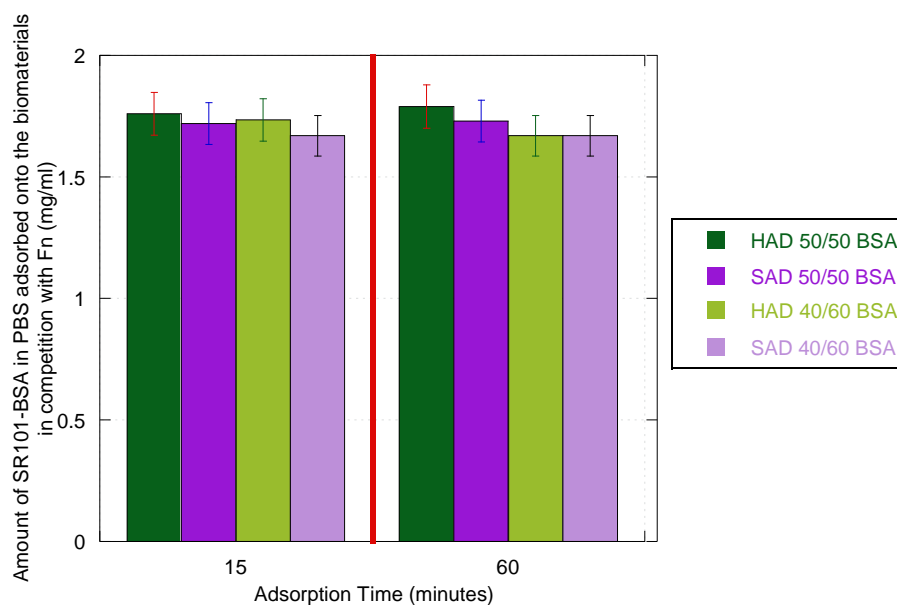
Figure 6.7 – Amount of SR101-BSA adsorbed onto the biomaterials in the presence of FTCA-FN biomaterials (n= 3 ±s.d.)

However, the strange phenomena of decreasing fluorescence intensity with increasing SR101-BSA concentration suggested that further investigation of these confounding factors were necessary to ensure that the data collected for the BSA was in fact reliable, refering back to Appendix 29, Figure 139.

6.3.2 Autofluorescence Investigation (Study B)

Figure 6.8 and Figure 6.9 show the autofluorescence data of bovine serum albumin (BSA) and fibronectin (FN), respectively at physiological concentration, unlabelled in PBS excited at 494 and 576 nm at 37 ^{o}C.

In both Figure 6.8 and Figure 6.9, the contact of the protein with the biomaterial surfaces induced autofluorescence, increased fluorescence intensity was observed from the unlabelled proteins excited at 494 nm compared to the unlabelled protein solution that had no contact with the biomaterials. There were no significant differences between the biomaterials from both solutions with FN having slightly more autofluorescence than BSA.

At 576 nm, the autofluorescence between the free protein solutions and the two contact solutions showed little differences.
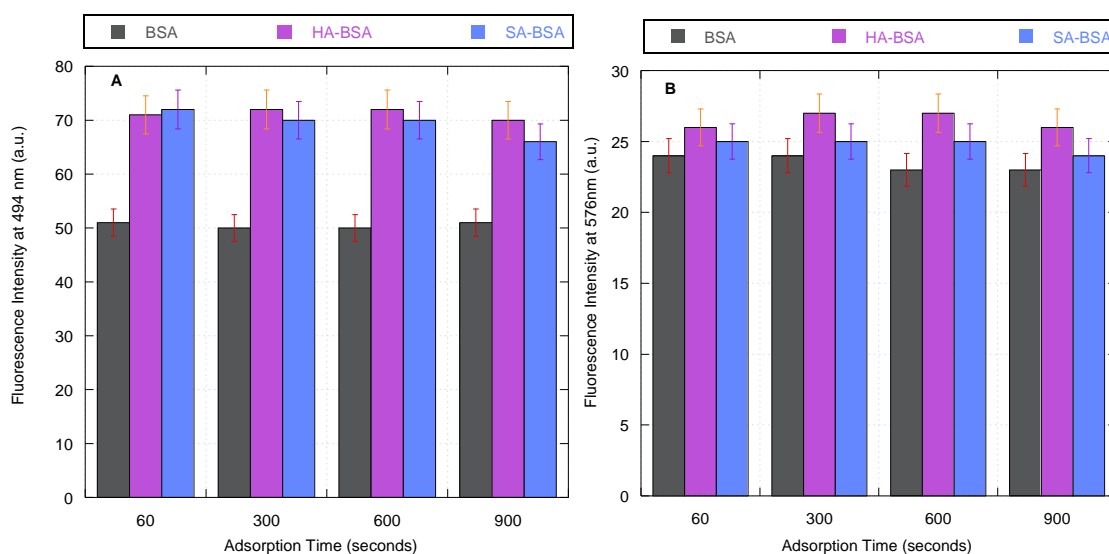
Figure 6.8 – Autofluorescence Observed from unlabelled BSA excited at (a) 494 and (b) 576 nm in PBS biomaterials (n= 3 ±s.d.)
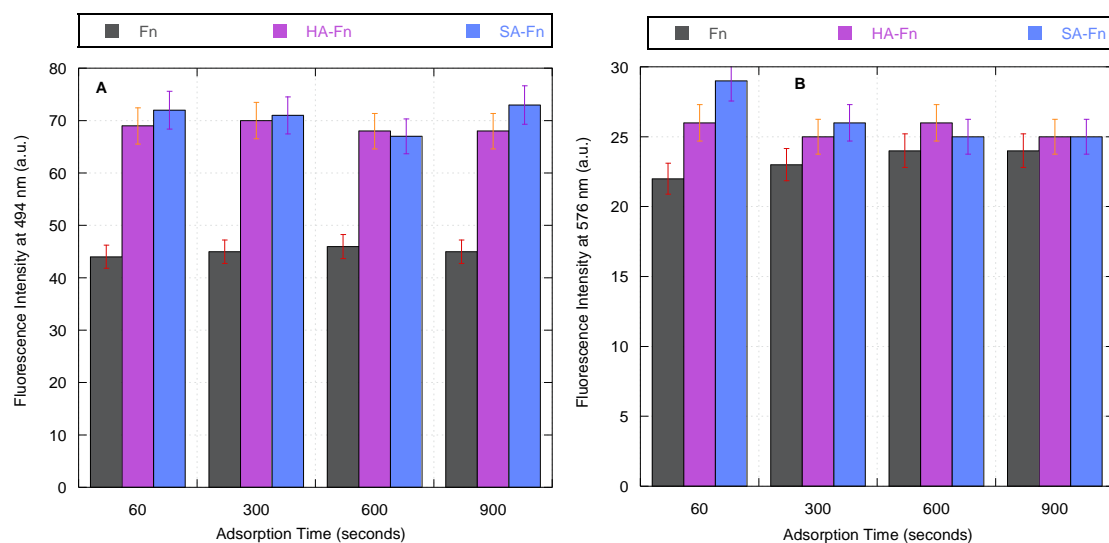
Figure 6.9 – Autofluorescence Observed from unlabelled FN excited at (a) 494 and (b) 576 nm in PBS biomaterials (n= 3 ±s.d.)

The following graphs show the autofluorescence effect observed when BSA (see Figure 6.10) and FN (see Figure 6.11) were labelled green in the presence of unlabelled FN and BSA, respectively.
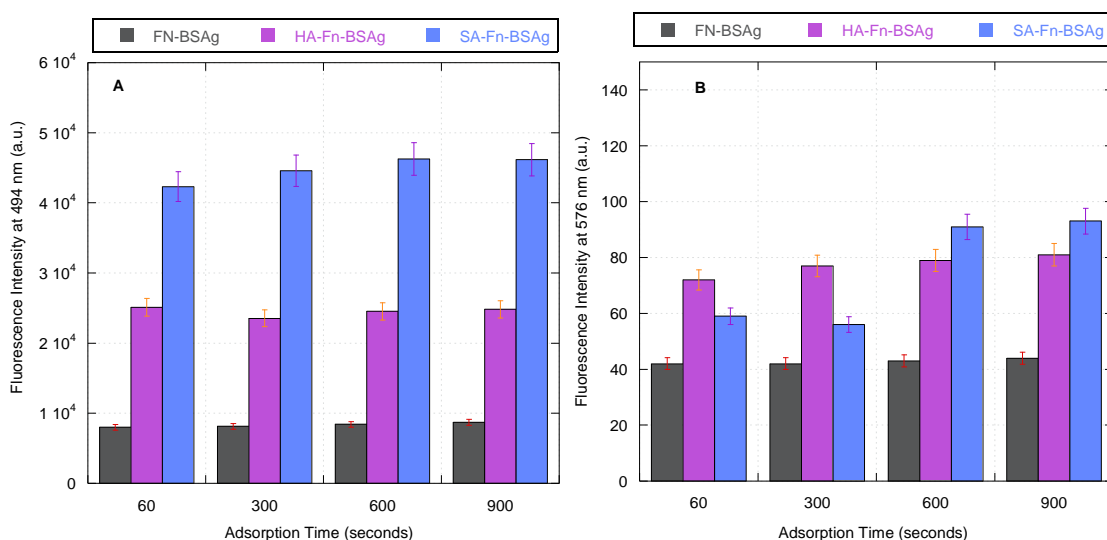
Figure 6.10 – Autofluorescence of FTCA-BSA in the presence of unlabelled-FN excited at (a) 494 and (b) 576 nm biomaterials (n= 3 ±s.d.)

Figure 6.10 showed that the presence of unlabelled FN may not have influenced the measuring of the FTCA-BSA intensity as high values were detected when excited at 494 nm with more effect observed on contact with the SAD surface at all time points. At 576 nm (red emitting region) low fluorescence intensity was seen, still higher than those observed from the free protein solutions (BSA or FN), but with a large increase in fluorescence between the control and contact on the biomaterials.
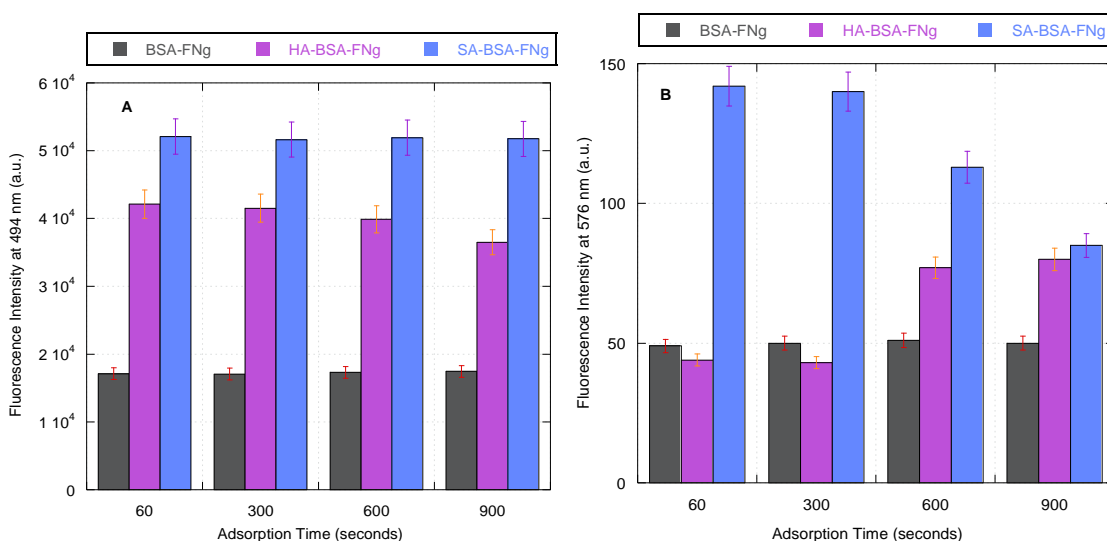
Figure 6.11 – Autofluorescence of FTCA-FN in the presence of unlabelled-BSA excited at (a) 494 and (b) 576 nm biomaterials (n= 3 ±s.d.)

Figure 6.11 showed the autofluorescence on FN labelled green in the presence of the unlabelled BSA. Just like for the BSA a very high green fluorescence was observed for the FTCA-FN, especially once in contact with the biomaterials compared to the protein solution only when excited at 494 nm, with more seen from the SAD surface at all time points. At 576 nm, SAD surfaces showed higher red autofluorescence compared to HAD and control samples; as time elapsed increased autofluorescence was observed from HAD.

Figure 6.12 showed the effect of labelling BSA red with SR101 in the presence of unlabelled FN, and when excited at 576 nm. Lower fluorescence intensity was observed compared to when BSA was labelled green. This may suggest that the red fluorophore with BSA was not compatible as seen from the negative correlation on the calibration in Appendix 29, Figure 139.

While Figure 6.13 showed the effect of labelling FN red with SR101 in the presence of unlabelled BSA. A higher red intensity was observed at 576 nm compared to BSA labelled red, and more autofluorescence was seen in the green region (494 nm).
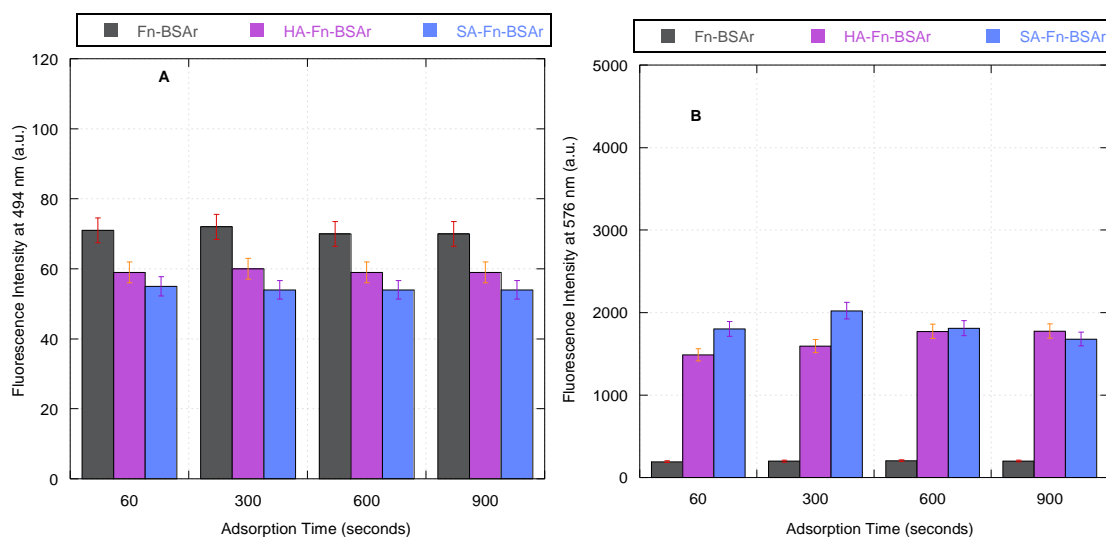
Figure 6.12 – Autofluorescence of SR101-BSA in the presence of unlabelled-FN excited at (a) 494 and (b) 576 nm biomaterials (n= 3 ±s.d.)
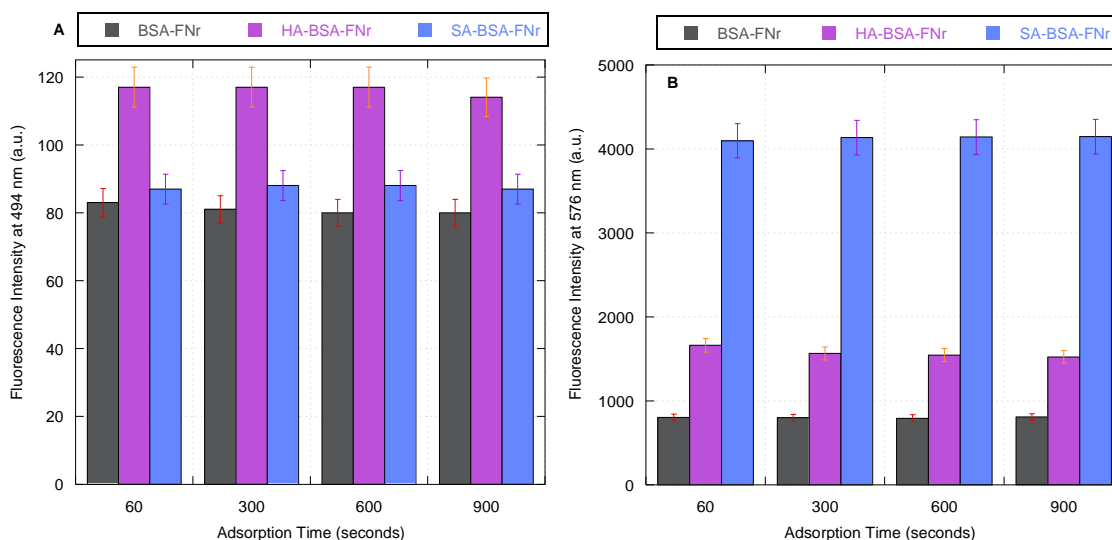
Figure 6.13 – Autofluorescence of SR101-FN in the presence of unlabelled-BSA excited at (a) 494 and (b) 576 nm biomaterials (n= 3 ±s.d.)

6.3.2.1   The Circular Dichroism (CD) Analysis

Due to the observations seen by the data from the autofluorescence, the CD work was used to show that the differences in fluorescence intensity are due to changes in protein conformation, from the measurements of proteins in solution. CD allowed for the illustration and quantification of this phenomenon in wavelength ranges of 190 to 250 nm. Unfortunately, the analysis could not be done at physiological level due to the limitations of the instrumentation, where the sensitivity ranged from 0.1 to 0.02 mg/mL. However it clearly showed the changes in conformation from the free proteins or growth factor to when they were in contact with biomaterials in the two different media (PBS or MEM). The red line (⎯⎯) represents the line of no change in protein conformation in all spectra. In all following spectra **Figure XA** represents the CD values as the raw data, while **Figure XB** represents the effect of contact with the biomaterials on the protein conformation.

There was definitely a conformational change on BSA in PBS and MEM, as shown in Figure 6.14 and Figure 6.15, respectively.

The curves in MEM were much broader to those observed in PBS; however the effect was much larger in PBS than MEM. The larger effect was seen on the SA samples compared to HA, which was closer to zero (the red line). In PBS, the difference between

the biomaterials was larger than in MEM, the presence of the amino acids, vitamins and inorganic components in MEM may have influenced the BSA conformation once in contact with the biomaterials.
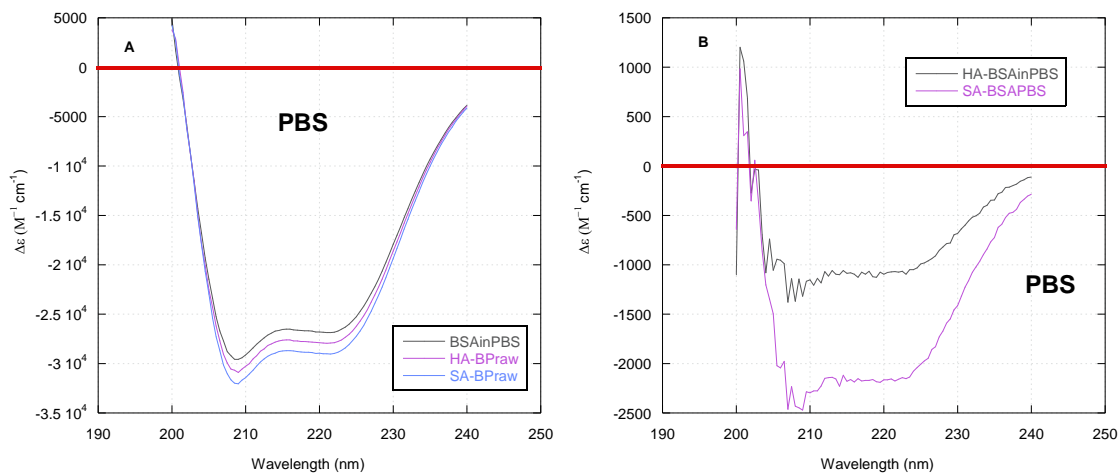
Figure 6.14 – BSA in PBS CD analysis (a) raw data and (b) effect of the biomaterials
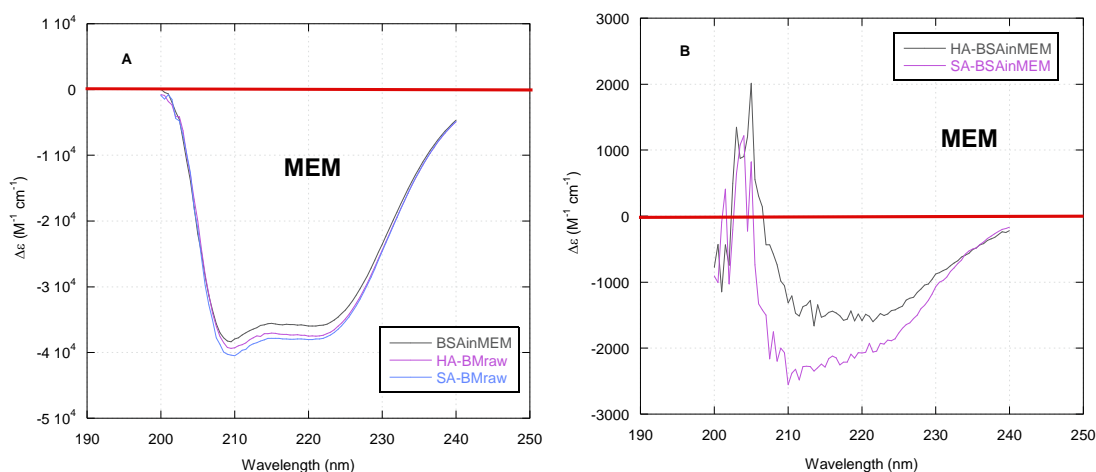
Figure 6.15 – BSA in MEM CD analysis (a) raw data and (b) effect of the biomaterials

When looking at the CD spectra for FN in PBS and MEM in Figure 6.16 and Figure 6.17, respectively, clearly a different pattern was observed compared to that observed for BSA.

More towards the positive side of the delta epsilon similarly in both medium, but a larger difference was observed between SAD and HAD in MEM.
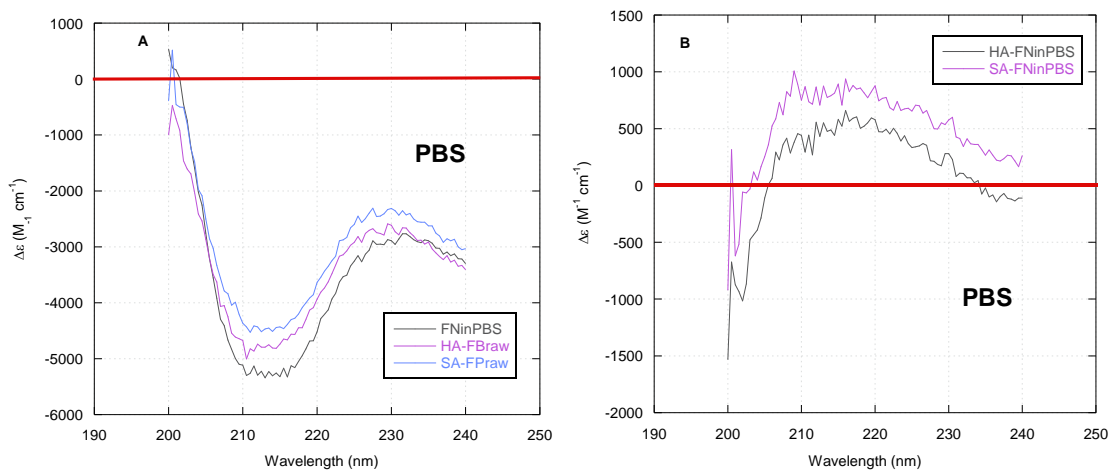
Figure 6.16 – FN in PBS CD analysis (a) raw data and (b) effect of the biomaterials
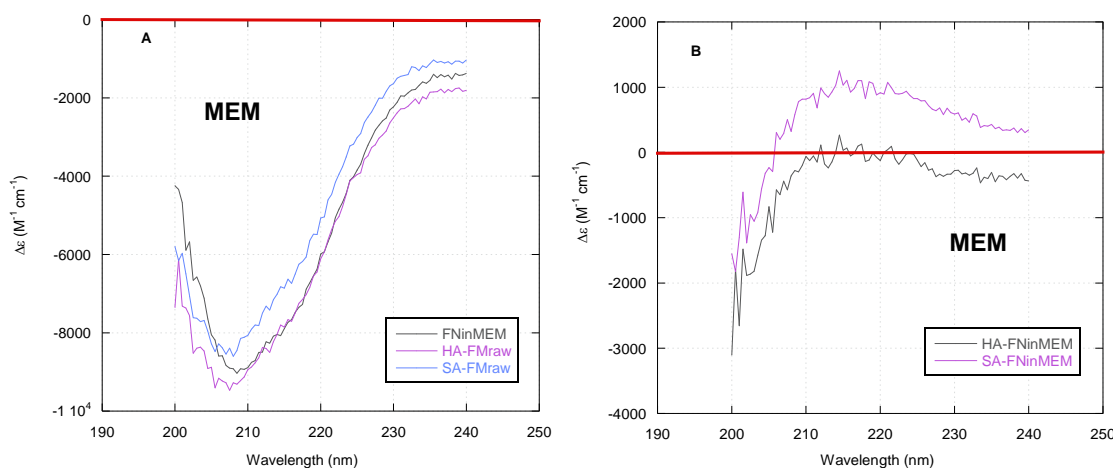
Figure 6.17 – FN in MEM CD analysis (a) raw data and (b) effect of the biomaterials

Figure 6.18 and Figure 6.19 show the CD spectra of rhBMP-2 in PBS and MEM, respectively. The pattern here in both media was different from previously seen with BSA and FN observations. In PBS, the change started positive for both biomaterials and with time become more negative with SAD having a larger effect on the conformation of rhBMP-2 compared to HAD. In contrast, the opposite effect was observed in MEM, but the conformational differences observed on both biomaterials were small yet similar; however, contact with SAD induced a greater response.
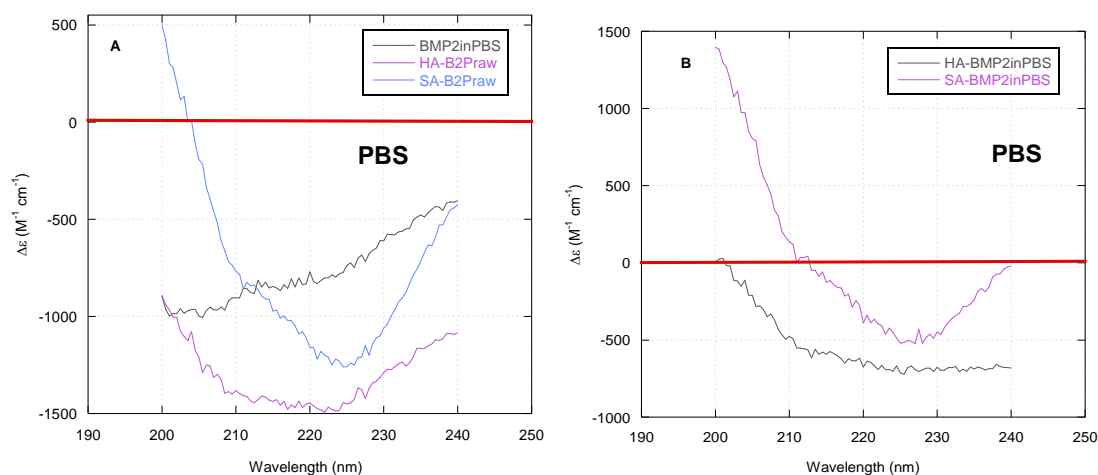
Figure 6.18 – rhBMP-2 in PBS CD analysis (a) raw data and (b) effect of the biomaterials
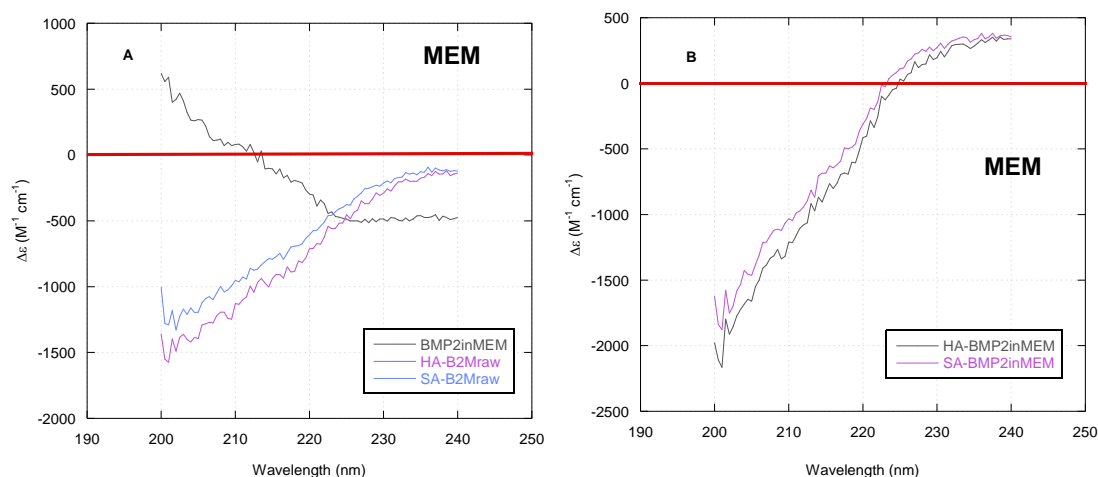
Figure 6.19 – rhBMP-2 in MEM CD analysis (a) raw data and (b) effect of the biomaterials

For the OPN protein solution, the raw CD data both in PBS and MEM seemed similar in pattern, as shown in Figure 6.20 and Figure 6.21, respectively, but there was a larger difference between samples in MEM. In PBS, the presence of HAD had a very low influence on the OPN conformation as the curve was close to zero compared to SAD. However, in MEM, the OPN was affected by both biomaterials on either side of the circular dichroism, positive for HAD and negative for SAD.
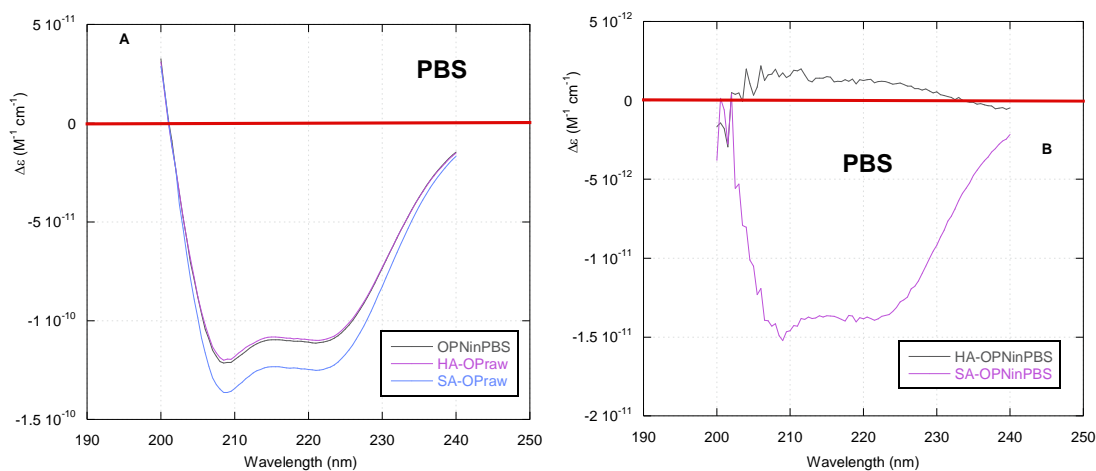
Figure 6.20 – OPN in PBS CD analysis (A) raw data and (B) effect of the biomaterials
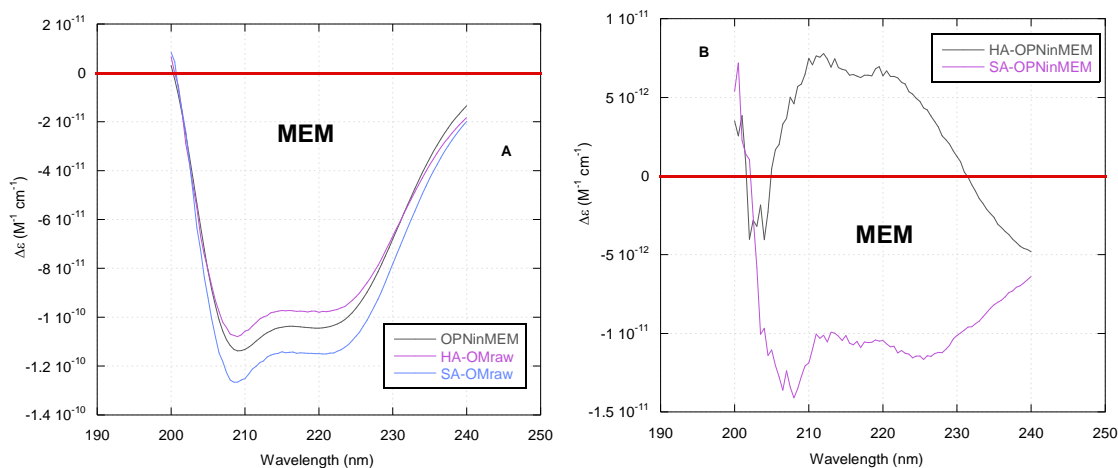
Figure 6.21 – OPN in MEM CD analysis (A) raw data and (B) effect of the biomaterials

Using the CD spectroscopic data and DICHROWEB online server (Whitemore and Wallace 2004; Whitemore and Wallace 2007), the protein secondary structure analyses were further confirmed in terms of average length of helices and strands observed by the protein solutions on HAD and SAD compared to contact-free in the two media, shown in Table 6.9 and Table 6.10, respectively.

All the remaining data for the dichroweb are illustrated in Appendices 30 to 47 in Figures 140 to 157. Table 6.9 and Table 6.10 confirmed the observations seen from the CD spectra for all proteins, where overall more changing in conformation was observed in MEM compared to PBS.

Table 6.9 – Average lengths of Helices and Strands of protein in PBS

Proteins	Helices	Strands	ΔHelix / %	ΔStrand / %
FN	6.51	4.89	-	-
rhBMP-2	8.41	0.438	-	-
rmOPN	10.2	3.36	-	-
HA-FN	6.30	5.08	↓ 3.2	↑ 3.9
HA-rhBMP-2	10.21	4.92	↑ 21.4	↑ 930
HA-rmOPN	10.22	3.37	-	↑0.09
SA-FN	6.24	5.38	↓ 4.1	↑ 10.1
SA-rhBMP-2	7.87	1.36	↓ 6.5	↑ 210
SA-rmOPN	10.2	3.52	↓ 0.05	↓ 4.8

Table 6.10 – Average lengths of Helices and Strands of protein in MEM

Proteins	Helices	Strands	ΔHelix / %	ΔStrand / %
FN	6.97	5.45	↑ 6.4 c.f. PBS	↑ 11.6 c.f. PBS
rhBMP-2	7.42	4.84	↓ 11.8	↑ 1004
rmOPN	10.2	3.55	↓ 0.16	↓ 5.6
HA-FN	7.26	5.27	↑ 4.3	↓ 3.4
HA-rhBMP-2	8.47	4.49	↑ 14.0	↓ 7.2
HA-rmOPN	5.99	6.95	↓ 41.2	↑ 95.7
SA-FN	5.76	5.69	↓ 17.3	↑ 4.4
SA-rhBMP-2	9.09	5.74	↑ 22.4	↑ 18.7
SA-rmOPN	6.01	6.95	↓ 41.1	↑ 95.7

6.3.3   Competitive binding with a labelled protein with 10 % FBS in MEM (Study C)

These different competitive studies were performed in MEM with 10 % FBS, where the probes were selected to avoid issues with autofluorescence.

The following study was illustrated as protein amounts actually determined; and as both percentage adsorbed from initial physiological concentration of each protein species, and percentage desorbed from the total actual adsorbed amounts.

6.3.3.1   FTCA-BSA in MEM with 10 % FBS Analysis

Calibrations for the FTCA-BSA protein solution in MEM + 10% FBS were illustrated, in Appendices 23 and 24, Figures 133 and 134, where the R^2 values generated from these showed a good linear relationship, tabulated below.

Table 6.11 – R^2 values of the FTCA-BSA calibration curves in MEM + 10 % FBS at 37 $^{\circ}$C

Range	Curves generated / µg/mL	R^2 values obtained
High	0-158	0.955
Low	0-31	0.940

Results of the analysis of FTCA-BSA adsorption and desorption on dense discs and porous granules in competition with FBS are shown in Figure 6.22, with an initial FTCA-BSA concentration of 4 mg/mL.

In competition with MEM + 10 % FBS, more FTCA-BSA was adsorbed on SAD compared to HAD, as shown in Figure 6.22A. On HAD the adsorption rate was slow, while fast and dynamic on SAD. HAD desorbed more FTCA-BSA compared to SAD, as shown in Figure 6.22B, suggesting that SAD had more binding affinity with BSA.

Dense Discs   **Porous Granules**
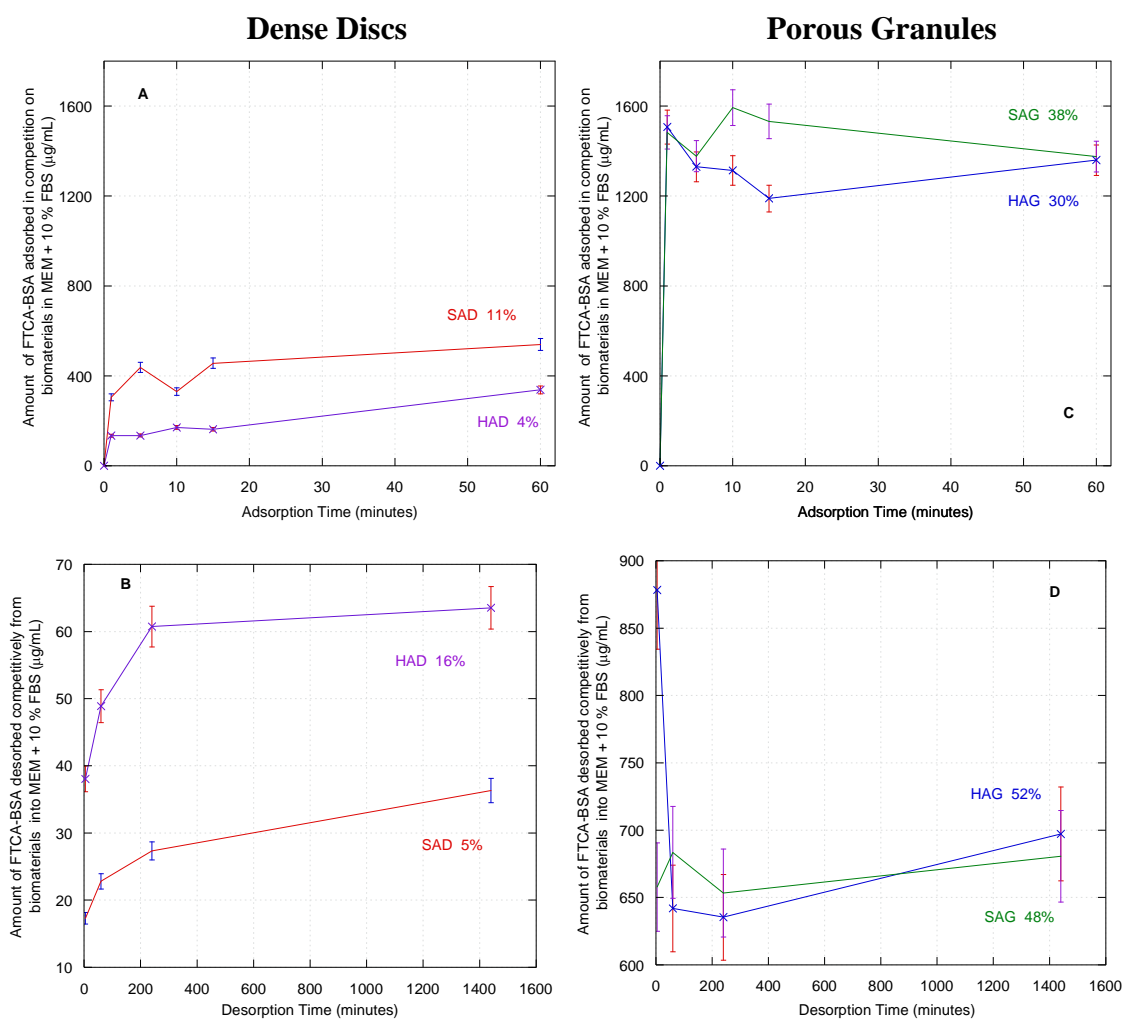
Figure 6.22 – FTCA-BSA in MEM with 10% FBS (a) adsorption and (b) desorption profiles from dense and (c) adsorption and (d) desorption profiles from porous biomaterial at 37 °C biomaterials (n= 3 ±s.d.)

In the porous morphological form, SAG adsorbed more protein than HAG especially at the 15 minutes time point, as shown in Figure 6.22C, and compared to DD, as shown in Figure 6.22D, the desorption from both biomaterial was very similar. SA still had the higher binding affinity to BSA compared to HA in both morphological forms.

The rate of adsorption of FTCA-BSA on both morphological forms of the biomaterials in competition was comparable to the rate found in the MEM only study in Chapter 4, Figure 4.13 and Figure 4.14 on page139 and 140, respectively. Higher adsorption on DD was found in MEM compared to MEM +10% FBS, while for PG, higher adsorption was found in competition compared to MEM. Very similar desorption pattern were obtained from both environment.

6.3.3.2   FTCA-BMP-2 in MEM with 10 % FBS Analysis

Calibrations for the FTCA-rhBMP-2 protein solution in MEM + 10% FBS were illustrated in Appendices 26 and 27, Figures 136 and 137, where the R^2 values generated from these showed a good linear relationship, tabulated below.

Table 6.12 – R^2 values of the FTCA-rhBMP-2 calibration curves in MEM + 10 % FBS at 37 °C

Range	Curves generated / ng/mL	R^2 values obtained
High	0-40	0.931
Low	0-8	0.986

Results of the analysis of FTCA-rhBMP-2 adsorption and desorption on dense discs and porous granules in competition with FBS are shown in Figure 6.23 with an initial FTCA-rhBMP-2 concentration of 300 ng/mL.

In competition with MEM + 10 % FBS, FTCA-rhBMP-2 was adsorbed on both morphological forms at a relatively close range compared to differences observed for the FTCA-BSA.

SAD adsorbed more than HAD at the 15 minutes time point and end of the adsorption period, only, as shown in Figure 6.23A, which was the expected trend because of the morphological form of the biomaterial and further confirmed in previous study with the FTCA-BSA and FTCA-rhBMP-2 analyses observed in Chapter 4 and 5, respectively. Less rhBMP-2 was adsorbed overall in competition compared to in PBS or MEM.

The rate of desorption on DD was fast then plateaued for both SAD and HAD (Figure 6.23B) throughout the desorption period with very little difference in release between the biomaterials.

Dense Discs   **Porous Granules**
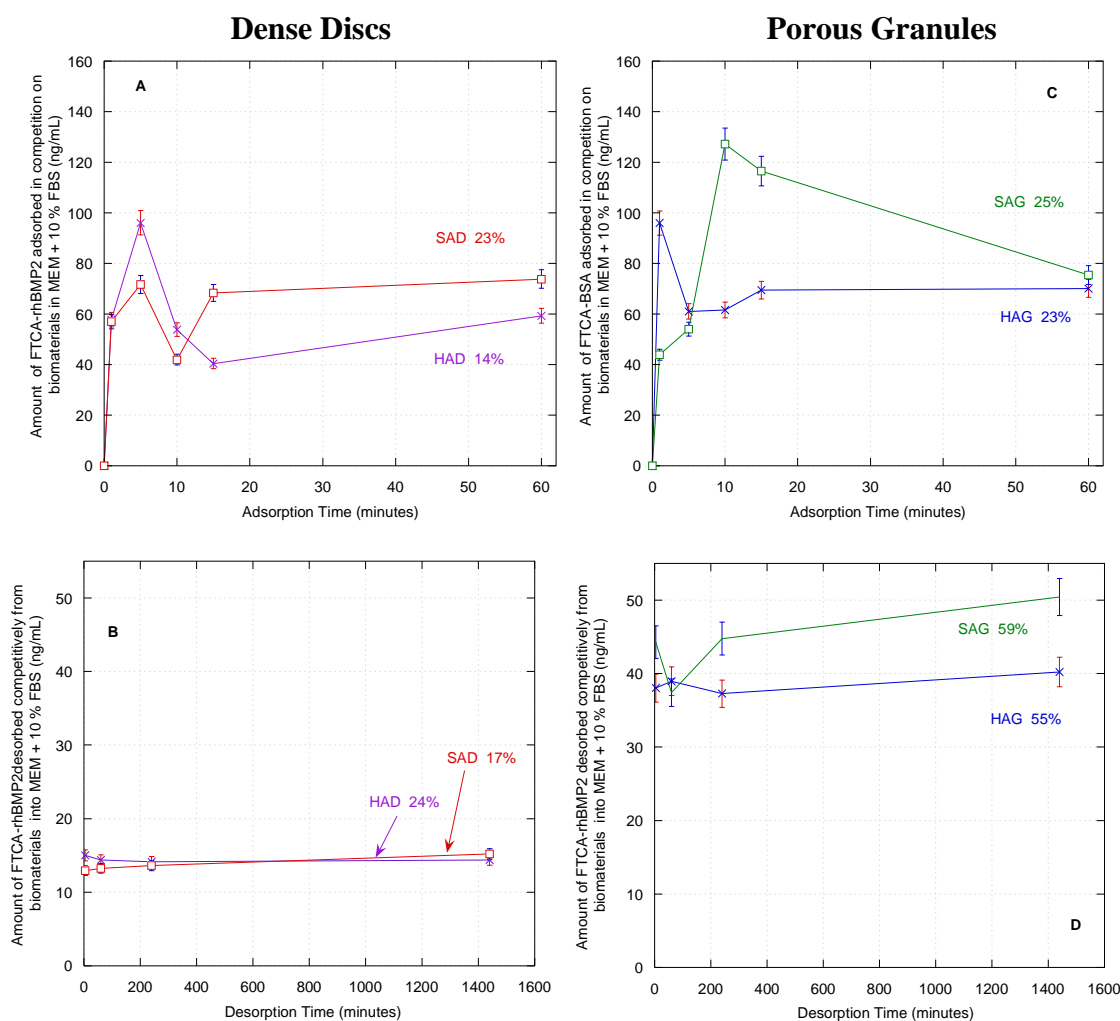
Figure 6.23 - The FTCA-BMP-2 in MEM with 10% FBS (a) adsorption and (b) desorption profiles from dense and (c) adsorption and (d) desorption profiles from the porous biomaterial at 37 °C biomaterials (n= 3 ±s.d.)

In the porous morphological form (Figure 6.23C and D), SAG adsorbed and desorbed more than HAG with a rapid rate of adsorption for the first three time points, followed by a slow decline. More desorption was observed from the porous samples compared to the dense samples, as shown in Figure 6.23C.

Only the porous granules were investigated in the MEM only study as seen in Chapter 5, Figure 5.8 and Figure 5.9 on pages 171 and 173. Less FTCA-rhBMP-2 was adsorbed in competition compared to MEM with very different rate and pattern of adsorption. While for the desorption, both the rate and pattern were similar in both environment, the only difference observed was the amounts; where more was released in competition.

6.3.3.3   SR101-rmOPN in MEM with 10 % FBS

Calibrations for the SR101-rmOPN protein solution in MEM + 10% FBS were illustrated in Appendix 48, Figure 158, where the R^2 values generated from these showed a good linear relationship, tabulated below.

Table 6.13 – R^2 values of the SR101-OPN calibration curves in MEM + 10 % FBS at 37 $^{\circ}$C

Range	Curves generated / pg/mL	R^2 values obtained
High	0-500	0.964
Low	0-100	0.997

Results of the analysis of SR101-rmOPN adsorption and desorption on dense discs and porous granules in competition with FBS are shown in Figure 6.24 with an initial SR101-OPN concentration of 50 ng/mL.

In competition with MEM + 10 % FBS, SR101-rmOPN was adsorbed more on HAD compared to SAD in Figure 6.24A. On HAD the adsorption rate was fast while showing a dynamic behaviour, compared to SAD, which had a fast rate that then plateau.
Contrary to previous observations, in this instance SAD desorbed more SR101-rmOPN than HAD. RmOPN seemed to have more affinity to the stoichiometric HA than SA.

Dense Discs   **Porous Granules**
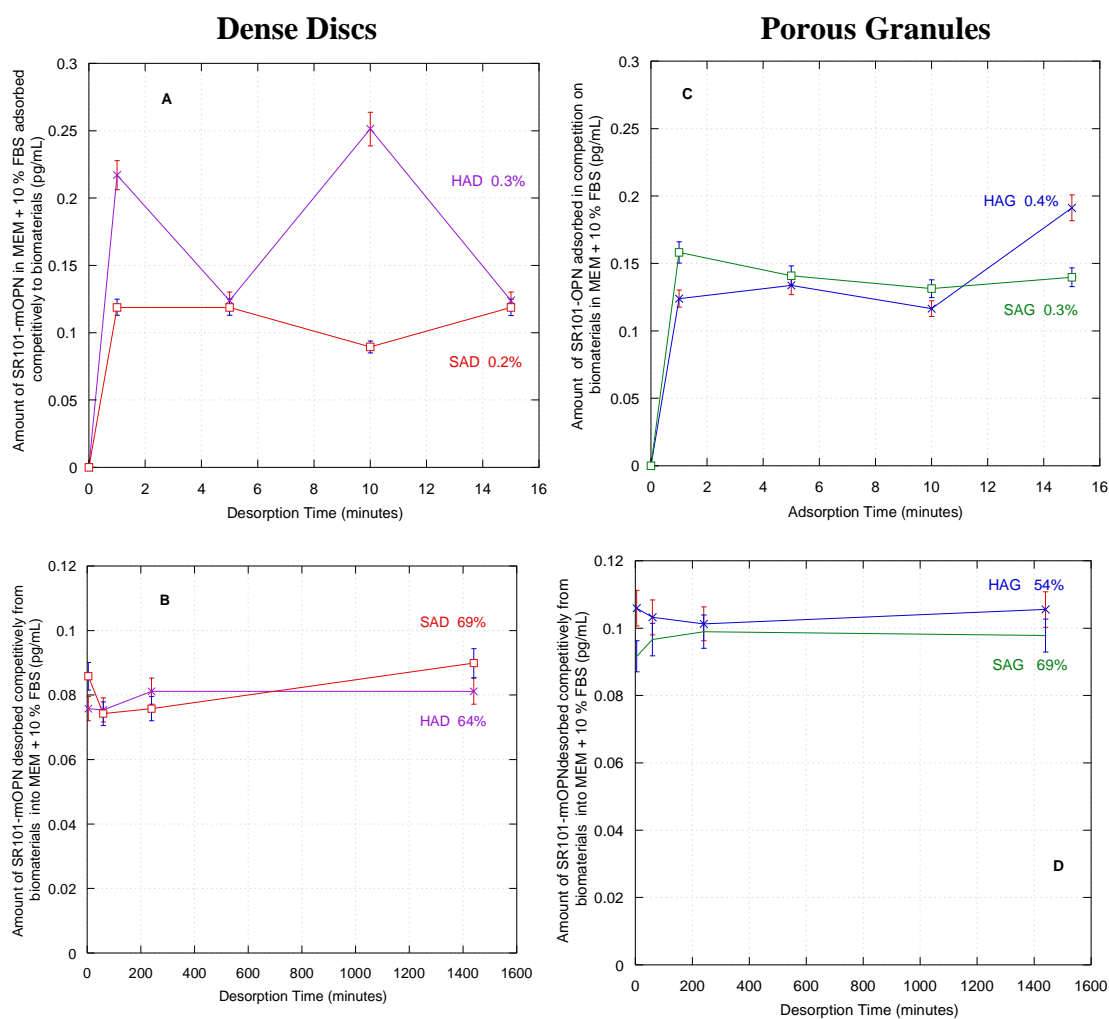
Figure 6.24 - The SR101-rmOPN in MEM with 10 % FBS (a) adsorption and (b) desorption profiles from dense , and (c) adsorption and (d) desorption profiles from porous biomaterials at 37 ^{o}C biomaterials (n= 3 ±s.d.)

In the porous morphological form, SAG and HAG adsorption capacities were quite similar, see Figure 6.24C. However, SAG seemed to adsorb more at the early time points, but after the 15 minutes, HAG adsorbed more.

The desorption pattern in Figure 6.24D showed HAG desorbed more than SAG, which was as expected, suggesting SR101-rmOPN has more affinity to the porous SA compared to the dense form.

6.3.4   Fluorescence Microscopy (FM)

The following fluorescence microscope (FM) images have been visualised using 3 filters, resulting in green, blue and red emitting images of the protein species on the biomaterial's surface. For the BSA, the green images are the most important while; the blue could represent the presence of the amino acids within the medium on the surface: and the red ones may suggest autofluorescence.

FTCA-BSA in MEM + 10 % FBS FM Images

The following two pages represent the fluorescence images obtained from the competitive binding of FTCA-BSA in MEM + 10 % FBS on the morphologically dense disc form of the biomaterials HAD and SAD, in Figure 6.25 and Figure 6.26.

Overall, larger clusters of FTCA-BSA were observed on the HAD surface compared to that on the SAD. For both specimen protein amounts adsorbed on the surfaces increased with increased immersion time. Protein was more heterogeneously spread on HAD compared to more homogeneously on the SAD surface with similar fluorescence intensity.

Figure 6.25 – FM images of FTCA-BSA with 10 % FBS on HAD at 37 ^{o}C in competition, scale bar representing 10 µm
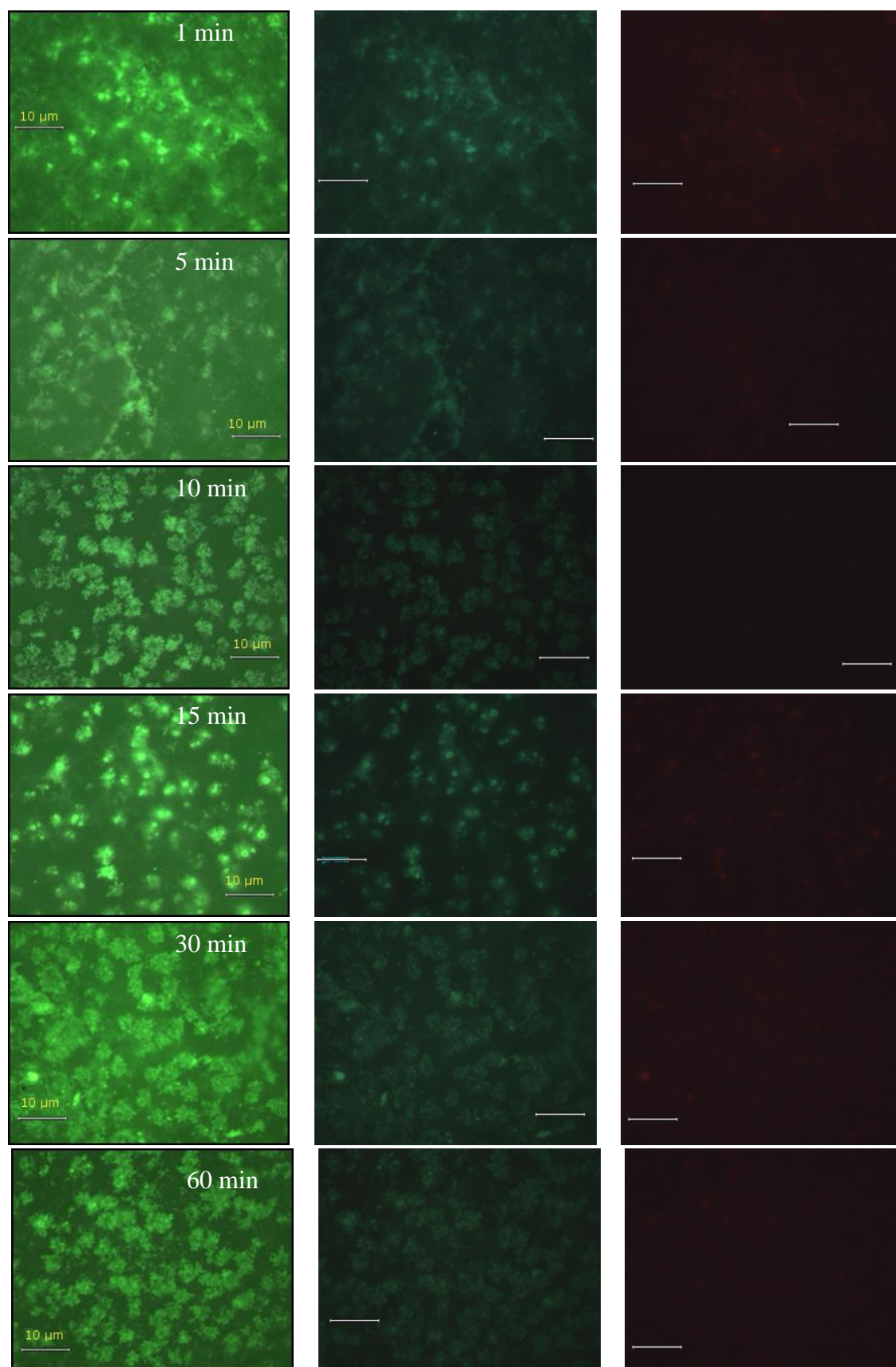
Figure 6.26 - FM images of FTCA-BSA with 10 % FBS on SAD at 37 ^{o}C in competition, scale bar representing 10 μm

The following fluorescence microscope (FM) images have been visualised using 3 filters, resulting in green, blue and red emitting images of the protein species on the biomaterial's surface. For the rhBMP-2 the green images are the most important while, the blue could represent the presence of the amino acids within the medium on the surface: and the red ones may suggest autofluorescence.

FTCA-rhBMP-2 in MEM + 10 % FBS FM Images

The next set of images represent the labelled growth factor, FTCA-rhBMP-2 adsorbed on the biomaterials, competitively, in the presence of 10 % FBS, in Figure 6.27 and Figure 6.28 on HAD and SAD, respectively.

Overall, larger clusters of FTCA-rhBMP-2 were observed on the HAD surface compared to that on the SAD. For both specimen protein amounts adsorbed on the surfaces increased with increased immersion time. Protein was more heterogeneously spread on HAD compared to more homogeneously on the SAD surface with some similarity to fluorescence intensity pattern.
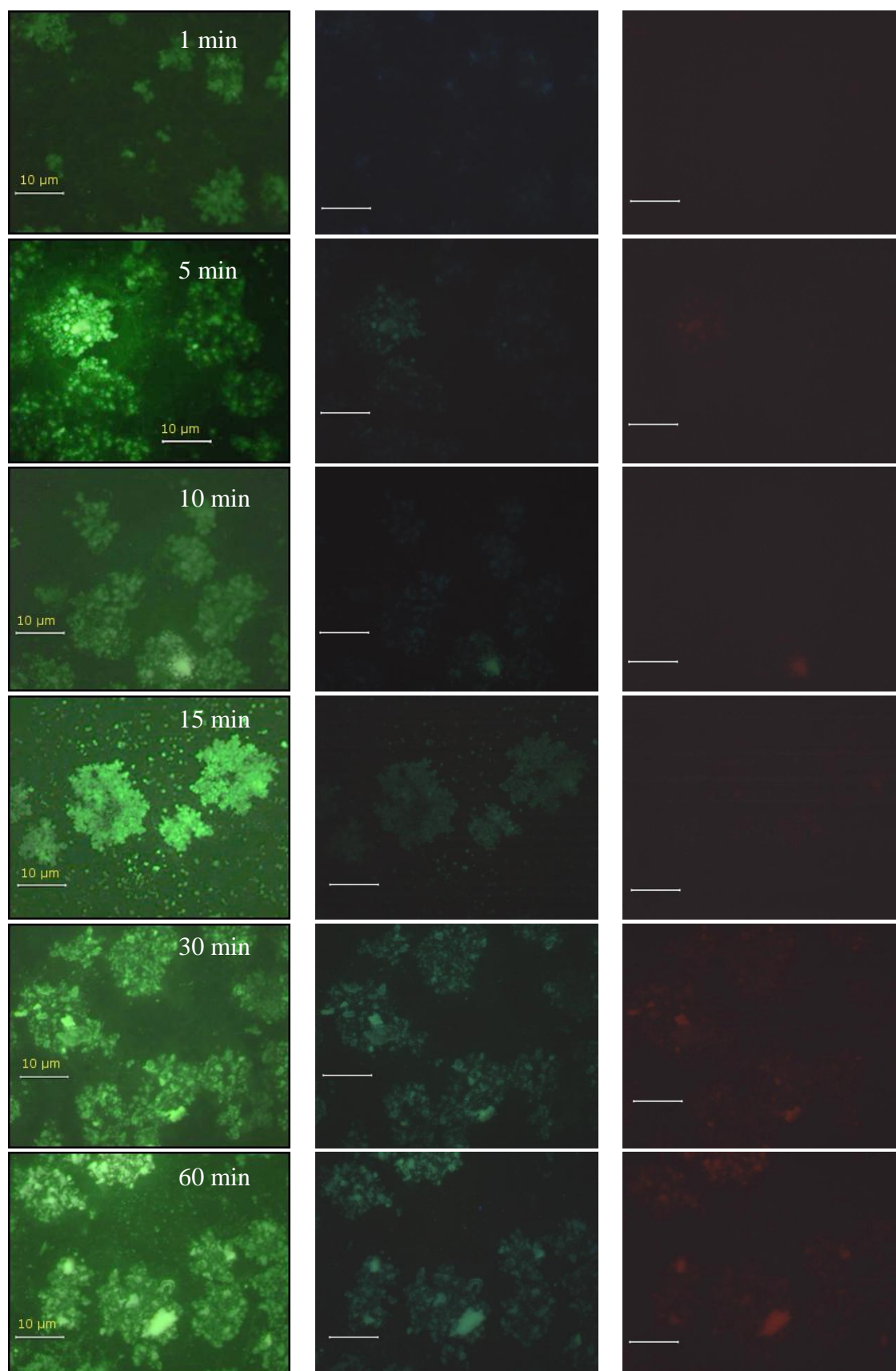
Figure 6.27 - FM images of FTCA-rhBMP2 with 10 % FBS on HAD at 37 ^{o}C in competition, scale bar representing 10 μm

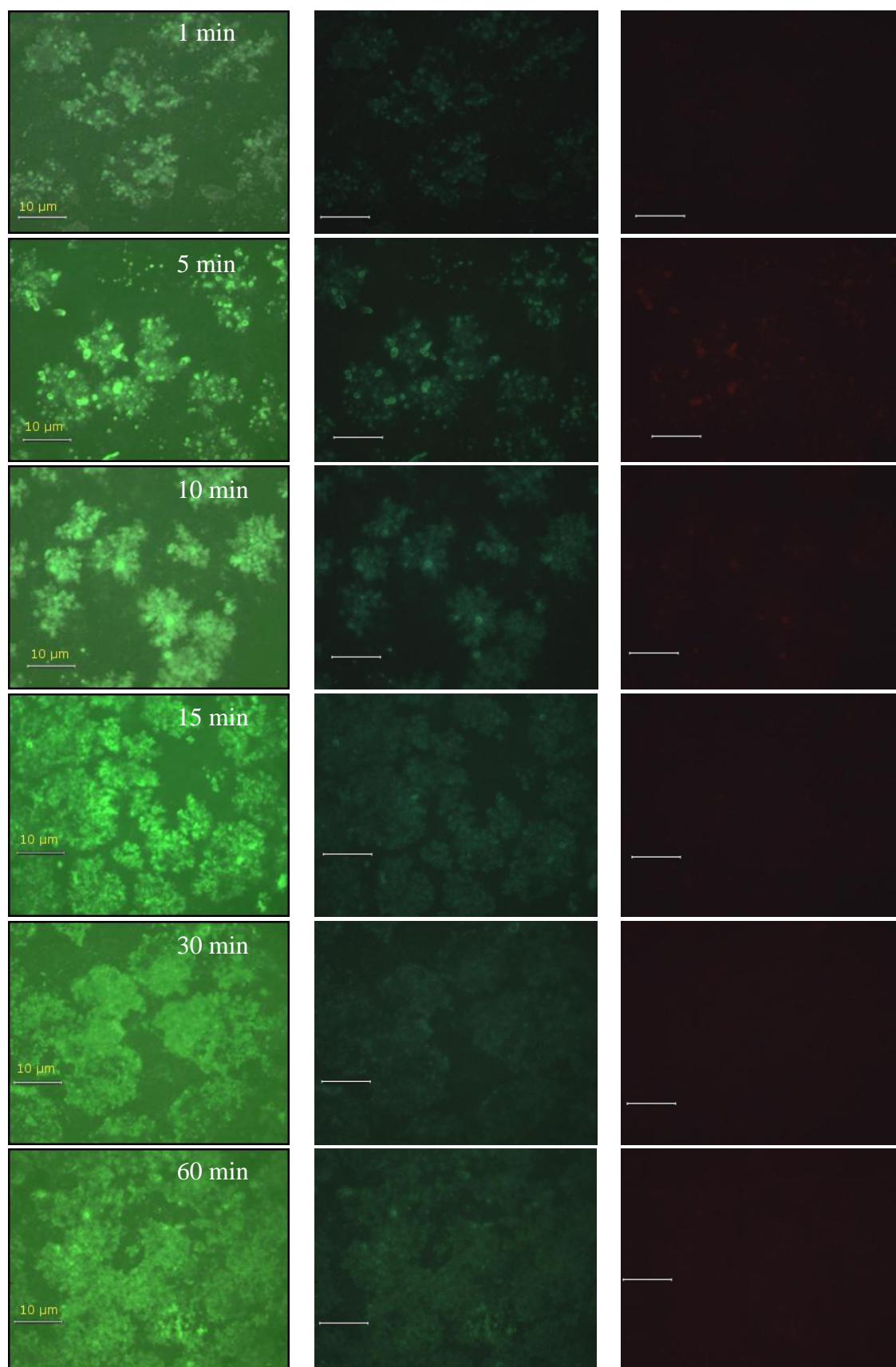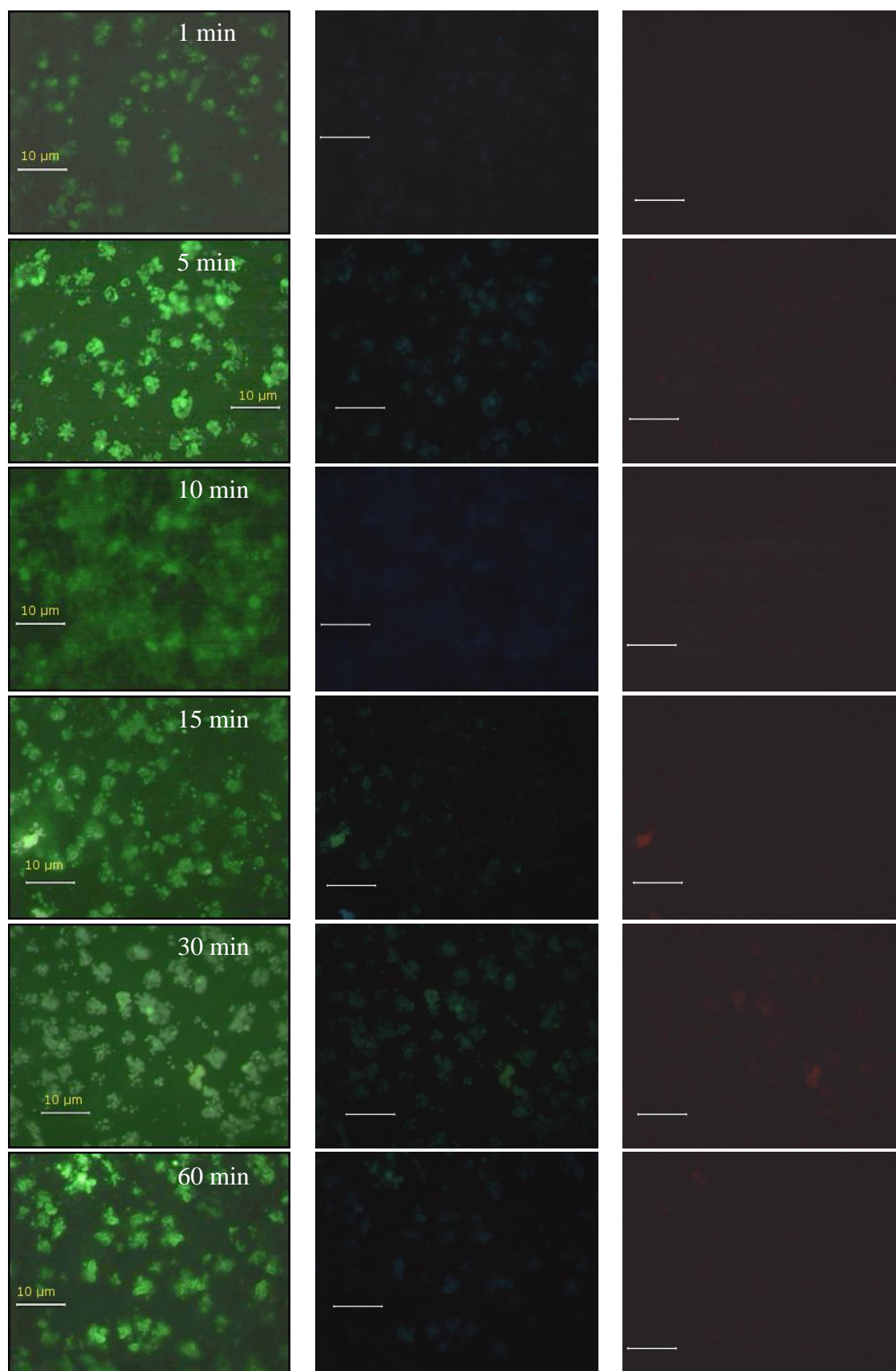**Figure 6.28 - FM images of FTCA-rhBMP2 with 10 % FBS on SAD at 37 ^{o}C in competition, scale bar representing 10 μm**

The following fluorescence microscope (FM) images have been visualised using 3 filters, resulting in green, blue and red emitting images of the protein species on the biomaterial's surface. For the OPN, the red images are the most important while, the blue could represent the presence of the amino acids within the medium on the surface: and the green ones may suggest autofluorescence of other protein within competitive environment.

SR101-rmOPn in MEM + 10 % FBS FM Images

Figure 6.29 and Figure 6.30 show the FM images of SR101-rmOPN adsorbed onto the biomaterials competitively with 10 % FBS.

Overall, it was slightly more difficult to qualitatively image the protein morphology of SR101-rmOPN on HAD compared to SAD. For both specimen protein amounts adsorbed on the surfaces increased with increased immersion time, more significantly on SAD than HAD. Protein was heterogeneously spread on both HAD and SAD, but centered in the middle of the biomaterial' surface. A lot more was seen through the green and blue emission, however, this could also be due to the fact that the physiology amount of rmOPN was quite small relative to BSA and rhBMP-2. Hence, the fluorescence on the competitive proteins in solution was more easily observed compared to rmOPN. However, some red emitting was seen and enough to construct an adsorption observation pattern.
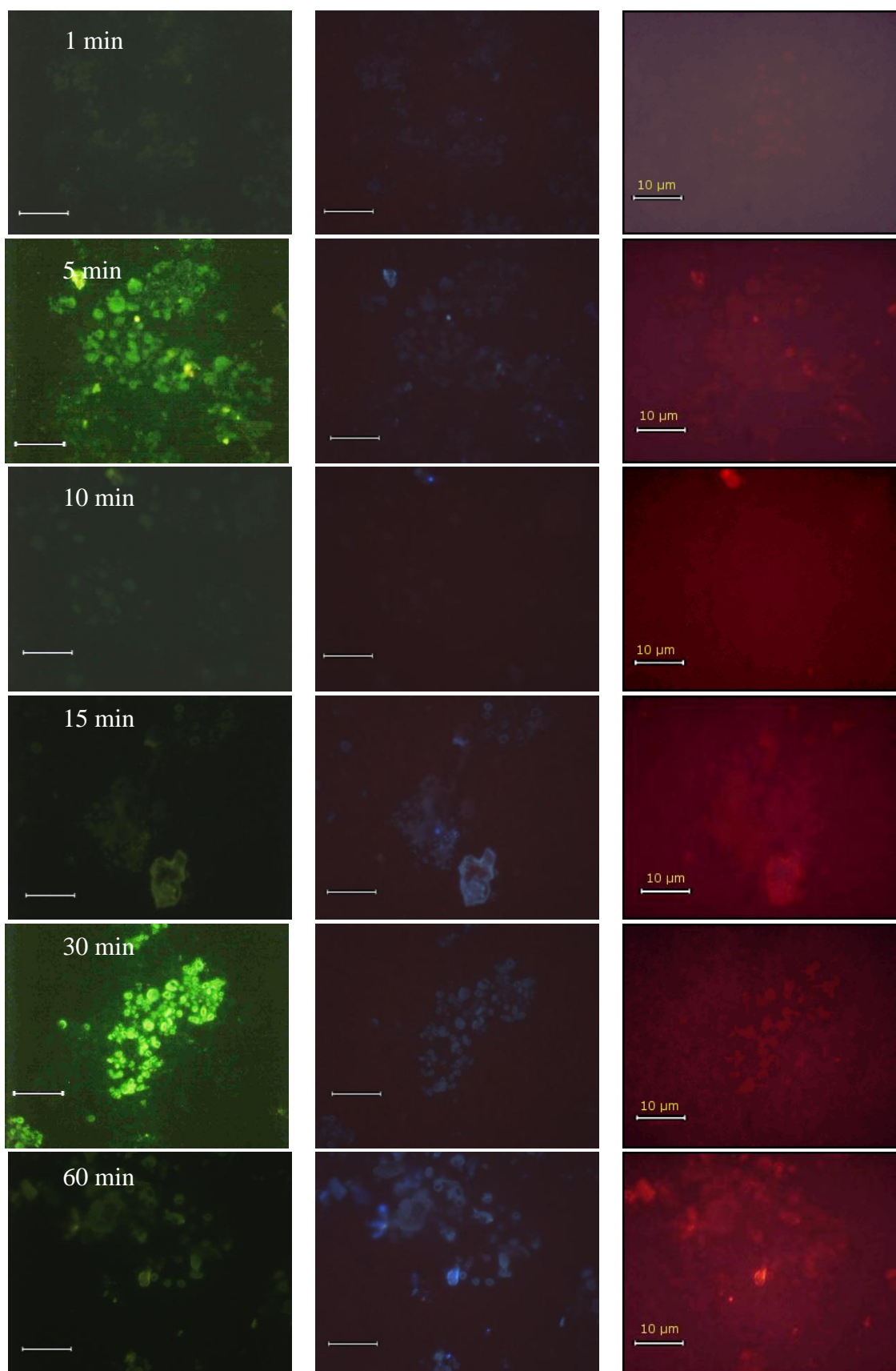
Figure 6.29 - FM images of SR101-rmOPN with 10 % FBS on HAD at 37 ^{o}C in competition, scale bar representing 10 µm
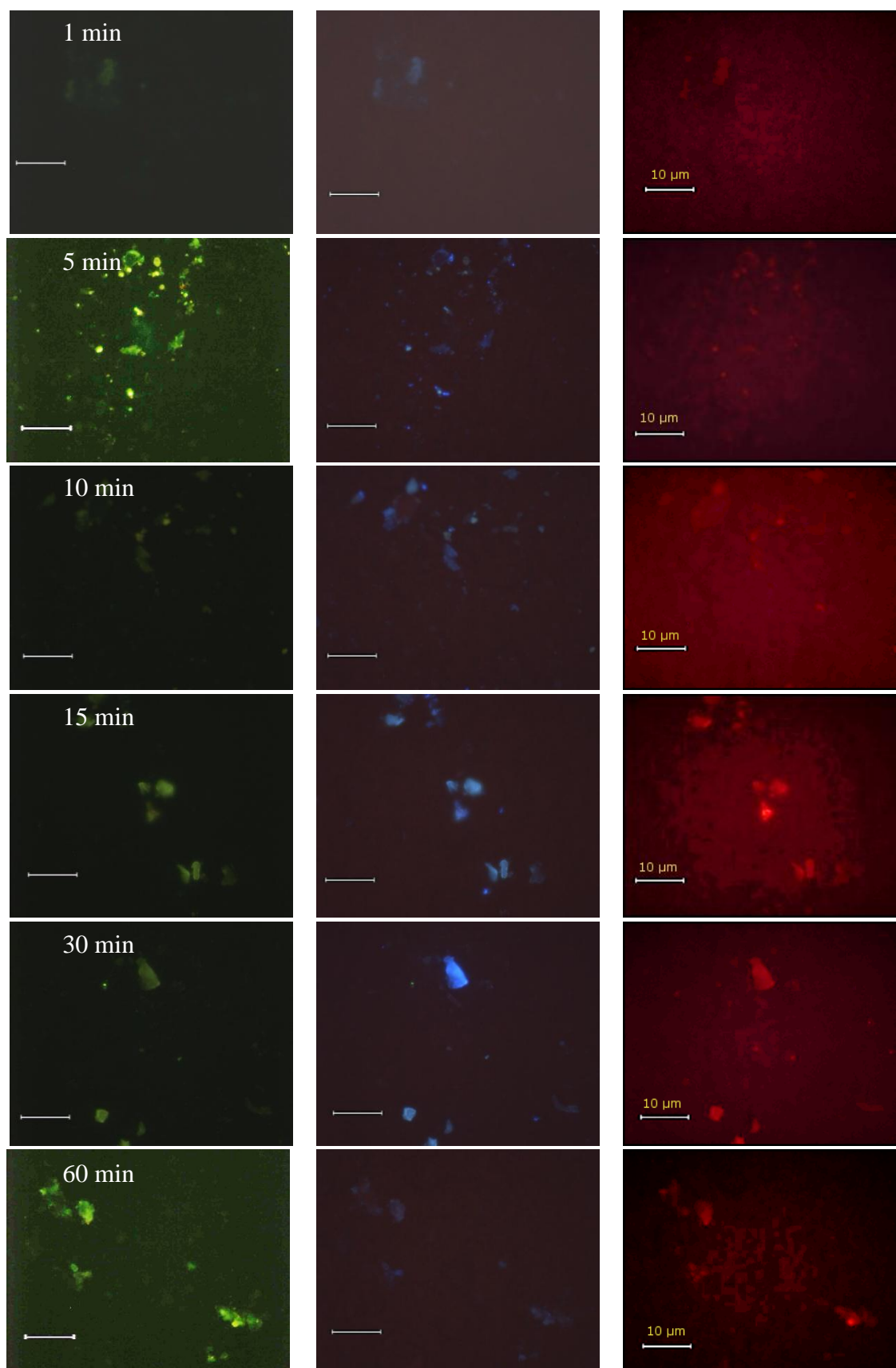
Figure 6.30 - FM images of SR101-rmOPN with 10 % FBS on SAD at 37 ^{o}C in competition, scale bar representing 10 μm

6.4   Discussions

6.4.1   Competitive Binding with two individually labelled proteins (Study A)

Previous studies using FTCA-BSA worked well, as shown in Chapter 4. This showed that the fluorophore labelling technique was reliable, it generated good calibrations and good data were collected, analysed and interpreted.

This lead to the labelling of both fibronectin (FN) and bovine serum albumin (BSA) to be undertaken with FTCA and SR101, respectively. The labelling methodologies were further confirmed as the protein solutions were isolated, FTCA-FN and SR101-BSA, calibrations generated and data collected.

The calibration curves generated by FTCA-FN were linear and positive, i.e. fluorescence intensity increased with protein concentration, as observed with FTCA-BSA and FTCA-rhBMP-2 in Chapters 4 and 5, respectively. However, the calibrations generated by SR101-BSA were linear and negative, i.e. fluorescence intensity decreased with protein concentration. This observation was unexpected as it may suggest that quenching of the fluorophore may be occurring with increasing protein concentration, which may further suggest a change in the protein conformation dependency in solution.

FTCA-FN analysis in the presence of SR101-BSA

The data collected from FTCA-FN showed that increasing BSA promoted FN adsorption on HAD and SAD, as shown in Figure 6.6. The main interest in this study was in the analysis of FN adsorption under near physiological conditions to evaluate whether or not enhanced FN affinity may contribute to a biomaterial's relative osteogenic potential *in vivo*. FTCA-FN was stabilised on HAD in the presence of 8 mg/mL SR101-BSA, whereas on SAD the FTCA-FN adsorption was stable indifferently to the presence of 4 or 8 mg/mL SR101-BSA. In the presence of this adhesive protein, it seemed that FN had maximised its interactions with the HA surface, which agreed with the work of Fabrizius-Homan *et al.* (Fabrizius-Homan and Cooper "Competitive adsorption of vitronectin with albumin, fibrinogen, and fibronectin on polymeric biomaterials" 1991) FN was often shown to adsorb better individually than BSA on biomaterials, especially on titanium surfaces as shown in the work of Yang *et*

al. (Yang, Cavin*, et al.* 2003), thus in competition a similar behaviour could be expected, and this was true in the present study.

Most studies have reported the use of low concentration of FN to demonstrate the "Vroman Effect", which is based on the desire to optimise FN adsorption to biomaterials' surfaces to facilitate cell adhesion. (Kowalczynska, Nowak-Wyrzykowska*, et al.* 2005; McFarland, Thomas*, et al.* 2000) Others have started to investigate the competitive behaviour of FN, still at low concentration, as in the work of Guth *et al.*(Guth, Campion*, et al.* "Surface Physiochemistry Affects Protein Adsorption to Stoichiometric and Silicate-Substituted Microporous Hydroxyapatites" 2010) in the presence of 10 % FCS; FN showed a dynamic adsorption behaviour over a 24 hour period at 37 ^{o}C with SA adsorbing more than HA. The worked also showed that in the presence of more adhesive proteins, FN adsorption was increased, which agreed with the finding in this study.

SR101-BSA analysis in the presence of FTCA-FN

The data collected from the SR101-BSA was inconsistent. When protein solutions were isolated as shown in Figure 6.7, the presence of FTCA-FN at 150 or 120 µg/mL did not affect the amount of SR101-BSA adsorbed onto the biomaterials. Amounts of SR101-BSA adsorbed on HAD and SAD were similar, there seemed to be little influence of chemistry on the adsorption behaviour, this could possibly be due to the inconsistency and the possible influence of quenching. Therefore the data was deemed unreliable.

Study A showed that the analysis of FTCA-FN in the presence of SR 101-BSA has worked, but not for the quantification of SR101-BSA. This may be due to the influence of protein conformational changes observed by the BSA in contact with the biomaterials, therefore the selection of the probe may be dependent on the autofluorescence potential of each protein.

6.4.2   Autofluorescence Investigation (Study B)

Thus, the phenomenon seen in Study A has led to the investigation of the autofluorescence of the proteins in solution, as shown in Figure 6.8 and Figure 6.9 for the unlabelled BSA and FN studies, respectively.

This was then followed by the analysis of the FTCA labelled BSA and FN in the presence of unlabelled FN and BSA, as shown in Figure 6.10 and Figure 6.11, respectively. And finally, the analysis of SR101 labelled BSA and FN in the presence of unlabelled FN and BSA, respectively, as shown in Figure 6.12 and Figure 6.13.

Initially, the study was undertaken in PBS, an ionic solution with no organic component. Figure 6.8 and Figure 6.9 clearly demonstrated that autofluorescence did occur in both proteins, BSA and FN. In contact with the biomaterials, higher levels of autofluorescence were observed from both proteins, especially when the protein solutions were excited at 494nm, the green emitting region compared to when excited at 576 nm, the red region. This occurred in the absence of the fluorophore, clearly indicating an effect has taken place, and using CD work supported this possibility and allowed it to be quantified as a change in the protein conformation in solution, as shown in Figure 6.14 and Figure 6.16 for BSA and FN in PBS, respectively. Evidently, there must be interactions between the components of the PBS and proteins, in which the resulting effect is a change in conformation after the protein solution comes in contact with the biomaterials.

A similar observation was seen when BSA and FN in MEM solution were investigated (see Figure 6.15 and Figure 6.17). The influences of the extra components in the medium such as amino acids and vitamins in MEM may have also induced changes in the protein conformation. In BSA little change occurred in the presence of MEM, the HA CD pattern seemed to match the SA one more so compared to PBS, whereas for FN in MEM solutions, reduced CD patterns were seen in contact with both biomaterials, suggesting a change in conformation. The influences on media on the CD spectra on different proteins were further investigated, as shown from Figure 6.18 to Figure 6.21, clearly showing that a change in medium did affect the protein conformation of both rhBMP-2 and rmOPN, and thus would show to exhibit the autofluorescence phenomenon.

The autofluorescence phenomenon was also investigated on the labelled BSA and FN solutions in PBS, as shown from Figure 6.10 to Figure 6.13, FTCA and SR101, respectively. For both proteins, large green fluorescence was observed from FN (see Figure 6.11) more than BSA (see Figure 6.10) when labelled with FTCA, but a larger red fluorescence was observed from the FTCA-FN solution, higher than both BSA and FN only spectra. Interestingly, when the proteins were labelled with SR10, as shown in Figure 6.12 and Figure 6.13, for BSA and FN, respectively, FN showed a larger red fluorescence than BSA with little effect upon contact with the biomaterials when excited at 494 nm (green region). However, on BSA the effect upon the excitation at 494 nm was lower upon contact with biomaterials compared to the control, clearly showing a loss of fluorescence, which would account for the loss of fluorescence observed in the calibrations undertaken in Study A (see Appendix 29, Figure 139) that resulted in a negative correlation.

The CD work that followed was used to further understand the nature of the change in the auto-fluorescence of proteins when in contact with the biomaterials surface. The CD analysis, further confirmed the change in conformation of the proteins upon contact with the biomaterials compared to the free protein solutions in the various media.

The overall effect on BSA in PBS and MEM (Figure 6.14 and Figure 6.15) was clearly negative for both biomaterials, where according to Drake (Drake 1994) this suggested that a low energy electronic configuration was observed, which is preferred by the right circularly polarized light (RCPL). Thus, the conformation of BSA can be expected to be α-helix, H-bonded, which may be (Drake 1994).

The effect of the biomaterials on the FN in PBS and MEM (Figure 6.16 and Figure 6.17) was also different indicating a more positive circular dichroism, which is usually associated with the left circularly polarized light (LCPL), suggesting a high energy electronic configuration. This type of pattern, according to Drake, is usually associated with a helix configuration, but not H-bonded.

The CD spectra of rhBMP-2 were strongly affected by the different media as shown in Figure 6.18 and Figure 6.19. In PBS, the effect of the biomaterials resulted in a more positive circular dichroism similarly to FN, compared to that in MEM, which was more negative similar to BSA. This suggests that the conformation of the growth factor would also be different and BMP-2 would be expected to behave differently in PBS and MEM, and even more likely in a competitive environment with 10 % FBS.

And finally, for OPN in PBS and MEM (see Figure 6.20 and Figure 6.21) the greater conformational change was observed on SAD more than HAD, more positive but close to zero on HAD and negative on SAD in both media. This suggests a large proportion of the protein on SAD to be helical compared to its conformation on HAD. (Drake 1994)

Overall, the CD analysis suggested that the larger proteins showed conformational changes in both media in a very similar manner, whereas the smaller proteins showed different conformational changes in the two media with distinct behaviour seen.

Table 6.9 and Table 6.10 depicted the differences in protein conformation observed in term of percentages in relation to the control (contact-free protein solutions), and thus confirming that the proteins, both free and in contact, were mainly in a helical conformation, and that contact either reduced or increased the average lengths observed by the helices or strands of the proteins in solutions. Therefore a loss of secondary structure was observed, this apparent transformation of the α helix into a more random coil is known to increase the bond mobility within the proteins (Wilson, Clegg, *et al.* 2005), which could explain the change in fluorescence intensity but also the different protein morphologies observed later in this study through the fluorescent images on the biomaterials. Therefore, as a result, this change in conformation could also affect the adsorption and desorption processes of the proteins in different ways in a competitive environment. This would be further quantified and explained in the following sub-section that depicts the findings and interpretation found in Study C.

6.4.3 Competitive binding with a labelled protein with 10 % FBS (Study C)

FTCA-BSA Competitive Study

The study of FTCA-BSA with 10 % FBS showed SA to adsorb more than HA, as shown in Figure 6.22A and C for the two morphological forms, which was similarly observed in the MEM only study, as shown in Figure 4.13B and Figure 4.14B pages 139 and 140 in Chapter 4. However, the amount adsorbed in competition was lower than that found in MEM only study, and the patterns of adsorption were similar with a slower rate of adsorption observed. This was expected as the introduction of 10 % FBS, would introduce to the system various sized proteins that would be able to compete for both the surface, but also the protein-protein and protein-medium interactions.

Dense discs (DD) of the biomaterials showed SAD adsorbing more than HAD in MEM (see Figure 4.13B), and a similar observation was seen with the 10 % FBS study (see Figure 6.22A) and further showed more inhibition of the FTCA-BSA to adsorb on HAD, 4 % compared to 11 % in competition and MEM, respectively. In this instance, the change in chemistry between SAD and HAD showed silicate-substituted hydroxyapatite to have a stronger affinity with FTCA-BSA both in MEM and in competition with 10 % FBS with an obvious gap between the pattern of adsorption and a slower rate observed in competition due to the dynamic nature of the environment.

The differences in adsorption were also evident when looking at the FM images in Figure 6.25 and Figure 6.26 in competition with 10 % FBS, compared to those observed in Figure 4.16A and C in MEM only study in Chapter 4 page 145, for HAD and SAD, respectively. Although, images observed in competition were more fluorescent compared to MEM only, some fluorescence could be due to a little autofluorescence from the 10 % FBS, as proteins more naturally fluoresce in the green emitting region. The amino acids were expected to emit within the blue region, which agreed with Herman (Herman 1998). The addition of 10 % FBS enlarged the protein morphology on both HAD and SAD with larger clusters formed across the surface of the HAD compared to SAD, more intense on the SAD surfaces as time elapsed. These observations confirmed the influence of chemistry of the FTCA-BSA adsorption observed in the dynamic behaviour of the quantitative data.

The introduction of porosity (PG), increased the amount of FTCA-BSA adsorbed both in the MEM only (see Figure 4.14B), but also in competition with 10 % FBS compared to the DD study. This was expected as the surface area of the biomaterials was increased. On DD SA and HA adsorbed 15 % and 11 % of the protein from the initial 4 mg/mL FTCA-BSA solution, respectively, whereas on PG SA and HA adsorbed 26 % and 25 %, respectively. Thus the influence of chemistry has been overcome by porosity, and even more so in competition with the presence of 10 % FBS, where on DD SA and HA adsorbed 11 % and 4 % of FTCA-BSA in solution, while on PG both SA and HA adsorbed an average of 35 % of the FTCA-BSA in solution. The introduction of the pore structure has clearly facilitated protein adsorption, also due to the change in fluid shear experienced by PG instead of DD within a static with flow experiments. The possibilities of adsorbing on PG depending on the protein conformation and size, but also the availability of pores and their size where for example:

(1) large labelled BSA (FTCA-BSA) could adsorb on the surface of a pore, as if attached to a wall in a cavern, or adsorb across a pore, like a web across a door

(2) the smaller proteins could do the same as above

(3) both FTCA-BSA and small protein could adsorb on the wall of a pore and anchor to the surface by a process of exchange, then slowly layer across the surface to then finally accommodate for the

(4) loosely anchored proteins either small or FTCA-BSA within the pore, that may have weaker interactions (protein-protein)

(5) or any combination of the above possibilities that would result in a dynamic behaviour.

This would thus lead to an enrichment of proteins to be observed, and as a result the rate of adsorption behaviour was slow, and the dynamic behaviour not as defined compared to MEM only study.

For the desorption, FTCA-BSA in MEM with 10 % FBS HA desorbed more than SA, as shown in Figure 6.22B and D for the two morphological forms, which was similar to values found for the MEM only study, as shown in Figure 4.13D and Figure 4.14D in Chapter 4, pages 139 and 140. Differences between amounts desorbed from the dense discs (DD) biomaterials were large in the competitive environment compared to in the MEM only study, where 5 % and 16 % of adsorbed FTCA-BSA was desorbed from SA and HA DD in MEM with 10 % FBS, compared to 9% desorbed from both biomaterials

in MEM. This suggests that BSA affinity to HA was lower than SA in MEM. This was further confirmed when in competitive environment due to the presence of other protein species.

The introduction of porosity resulted also in an increased amount of FTCA-BSA desorbed from the biomaterials (see Figure 6.22D) with HAG desorbing more than SAG. This implied that a similar dynamic behaviour may also be observed during the desorption process in a fresh solution of MEM with 10 % FBS, the balance of labelled (FTCA-BSA) to unlabelled now was slightly biased towards the FBS, so protein-protein interactions may be increased that may lead to the increase release of the FTCA-BSA in solution. Significantly higher percentage of adsorbed BSA was desorbed from PG as compared to DD, which further supports the hypothesis that the presence of porosity facilitated BSA enrichment at the surface as loosely bound protein within the pores can now be quantified through the desorption analysis.

In summary, these studies show that BSA adsorption was sensitive to chemistry but more greatly influenced by porosity.

FTCA-rhBMP-2 Competitive Study

The growth factor (FTCA-rhBMP-2) adsorption process showed a similar pattern to that observed for the FTCA-BSA where SA adsorbed more than HA in the porous granule (PG) form with more observed in MEM (see Figure 5.8B in Chapter 5, page 171) compared to in MEM with 10 % FBS (see Figure 6.23C). As seen for FTCA-BSA in competition, it seemed the influence of porosity with FTCA-rhBMP-2, also overcame the influence of chemistry, as the percentage adsorbed on HAG and SAG were similar, 45 and 46 %, respectively, in MEM. Likewise observed in MEM with 10 % FBS but at lower adsorbed amounts of 23 and 25 % on HAG and SAG, respectively. Here FBS has strongly influenced the adsorption behaviour of FTCA-rhBMP-2 on the biomaterials.

The differences in adsorption were also evident when looking at the FM images in Figure 6.27 and Figure 6.28 in competition with 10 % FBS, compared to those observed in Figure 5.11A and B in MEM only study in Chapter 5, for HAD and SAD, respectively. Although quantitatively half the amount was detected in competition, the images were more fluorescent; this could be due to the microscope picking up a wide

range of bands. The FTCA-rhBMP-2 protein morphology did not alter, large clusters were observed on HAD compared to smaller ones on SAD, as previously seen in the MEM only study in Chapter 5, with some autofluorescence in the blue emitting region and very little in the red. This further suggests that the addition of FBS had a strong influence on the adsorption interactions of the growth factor to the biomaterial surfaces.

In competition (MEM with 10 % FBS) SA adsorbed more than HA in both morphological forms. Dense discs (DD) adsorption was marginally lower than PG. There was an apparent influence of chemistry on DD where less FTCA-rhBMP-2 was adsorbed on HAD (14 %) compared to SAD (23 %), which was overcome by the introduction of porosity in the PG study, especially for HA samples, where only 23 and 25 % was adsorbed on HAG and SAG, respectively.

It has been previously discussed in Chapter 5 that the amino acid component of the MEM had strong affinity with rhBMP-2 to enhance adsorption, which was also observed for BSA. However, here with rhBMP-2, the extra proteins in solution inhibited the effect of MEM adsorption enhancement.

This implies that the dynamic behaviour with the growth factor is more related to protein-protein interaction influence over the protein-surface one in its porous form, compared to BSA where it could be combinations of either. Another explanation could be that an increase in the protein isoelectric point (pI) in solution due to the extra smaller proteins resulted in higher retention of the growth factor in solution (Uludag, Gao, *et al.* 2008).

FTCA-rhBMP-2 release showed similar levels of desorption between biomaterials, where in MEM 14 % and 13 % of FTCA-rhBMP2 was desorbed from HAG and SAG, while in competition 55 % and 59 % was desorbed from HAG and SAG, respectively, as shown in Figure 5.9B and Figure 6.23D. A higher percentage release was observed from MEM with 10 % FBS solution, which would support the previous hypothesis that the presence of 10 % FBS inhibits the effect of MEM on the FTCA-rhBMP-2 adsorption enhancement observed in Chapter 5.

In summary, this study clearly showed the importance of porosity in adsorbing more FTCA-rhBMP-2 with SA as the bone graft substitute, but also that the influence of MEM on its adsorption was a factor that inhibited by half the amounts of FTCA-rhBMP-2 adsorbed in a competitive environment.

SR101-rmOPN Competitive Study

Osteopontin is a protein known to inhibit apatite nucleation and crystal growth. (George and Veis 2008) rmOPN is generally researched for the purpose of showing that it has various functions as detailed in the review by Denhardt *et al.* (Denhardt and Guo 1993) such as binding to cells, regulating formation and remodelling of mineralised tissue; interacting with Ca^{2+} and inhibiting HA formation (Hunter, Hauschka*, et al.* 1996). The aim was to investigate this protein to show that, as an inhibitor of osteogenesis, whether it may have a different affinity with HA and SA.

Labelling rmOPN with the red emitting fluorophore, SR101, gave rise to good calibrations, as shown in Appendix 48, Figure 36, and tabulated in Table 6.13.

More SR10-rmOPN was adsorbed on porous granule (PG) specimen compared to the dense disc (DD) specimen. However, contrary to what was observed for both FTCA-BSA and FTCA-rhBMP-2, HA adsorbed more than SA in both morphological forms, as shown in Figure 6.24.

In this instance, OPN adsorption was indifferent to chemistry and porosity, the differences in the adsorbed percentages were quantitatively low and relatively similar on the biomaterials, i.e. 0.3 and 0.2 % from HAD and SAD, respectively, compared to 0.4 and 0.3 % for HAG and SAG in MEM with 10 % FBS.

This was further confirmed by the FM images, as shown in Figure 6.29 and Figure 6.30 for HAD and SAD, respectively.

As no significant difference was found, this suggests that OPN interactions with HA and SA does not affect bioactivity, but BSA and BMP-2 may be involved.

6.5 Summary & Conclusions

The two independently labelled protein studies showed FTCA-FN to adsorb more on SAD than HAD with increasing amount of SR101-BSA present, which often was the observed behaviour in previous studies. However due to the phenomenon of autofluorescence of BSA when labelled with the red emitting fluorophore (SR101), this study required changes.

The autofluorescence distinctively showed that an increase of fluorescence was observed for all proteins upon contact with the biomaterial surface when excited at both 494 and 576 nm, green and red regions, respectively. In conjunction with the CD work, changes of protein conformation were showed to be the cause of this phenomenon, thus the importance of selecting the fluorophore that showed the least effect was very important. Direct labelling with FTCA or SR101 allowed monitoring and imaging of the adsorption and desorption processes, to reveal the importance of selecting a fluorophore and that proteins were subject to conformational changes upon contact with the biomaterials. The changes thus influenced the interactions between components of the media with the protein, which then influenced the interactions with the biomaterials.

The competitive binding of dense discs and porous granules was determined and showed different patterns of behaviour to amounts of protein adsorbed on the surface in the presence of 10 % FBS. The presence of the serum affected the adsorption and release, lowering adsorption of FTCA- BSA and FTCA-BMP-2, but no effect on SR101-OPN, however, even under competitive conditions higher affinity to SA was still observed with FTCA-FN, FTCA-BSA and FTCA-rhBMP-2.

The introduction of porosity increased adsorption affinity for both HA and SA in some cases it was more influential than the material chemistry.

Chapter 7. SUMMARY OF FINDINGS, FUTURE WORK AND PERSONAL TRAINING

7.1   Protein Adsorption and Desorption Behaviour (BSA only)

Using the Quant-IT kit for determining the adsorption and desorption behaviour of BSA showed to be unreliable for very low or high BSA concentrations. At physiological levels, the work was comparable to values found when using the fluorophore labelling methodologies. Calibrations generated from the kit and FTCA-BSA both in PBS and MEM showed good linearity. Overall more FTCA-BSA was adsorbed on SA compared to HA in both morphological forms at RT and 37 ^{o}C in PBS and MEM. Differences observed were usually seen through the pattern of adsorption, when using FTCA-BSA a more dynamic pattern was observed compared to a static behaviour from the kit.

The findings for this study showed to be relevant to the pre-clinical studies towards osteoinduction, as real samples were used. This was the novelty of this study as samples were not manipulated to maximise surface chemistry, area or binding contact through grinding, polishing or etching.   The samples were synthesised, heat-treated and used similarly to specimen used in clinical trials (i.e. Apatech procedures); thus the behaviour observed and quantified can be directly related to possible effects seen during real pre-clinical studies.

7.2   Growth Factor (rhBMP-2) Study

One of the striking observations in this study was the discrepancy in the level of rhBMP-2 adsorption identified using the ELISA and FTCA labelling methodologies. FTCA-rhBMP-2 adsorbed more than with the ELISA both in PBS and MEM, but also at the physiological and pharmacological concentrations with respect to the original amounts used to be detected.

Quantikine data obtained clearly showed that the sensitivity of the antibodies to a specific rhBMP-2 conformation was a disadvantage, as values generated were too low and inconsistent.

FTCA-rhBMP-2 showed more reliable data, which could be used to distinctively comment on the pattern and amounts adsorbed and released of rhBMP-2 from the biomaterials. The adsorption behaviour of FTCA-rhBMP-2 on the biomaterials was not affected whether physiological or pharmacological levels were used. The influence of concentration was more significant on the desorption process where less was desorbed from pharmacological level. In addition, the influence of chemistry was more obvious in the pharmacological compared to the physiological levels. Overall, more FTCA-rhBMP-2 was adsorbed onto porous SA than HA both in PBS and MEM, thus clearly showing a stronger affinity with SA.

Due to the presence of the amino acid component of the MEM more adsorption and less release was observed, especially at pharmacological levels.

The findings for this study also showed to be relevant to the pre-clinical studies towards osteoinduction, as real samples were used, which further emphasises the research potential of this study, as shown in Chapter 4; and also throughout this thesis. This study was aimed to show the importance of the influence of rhBMP-2 adsorption and desorption processes from the porous granular biomaterials, not its mechanistic view. This *in vitro* study showed selection of appropriate test conditions are critical to adsorption and desorption behaviour of rhBMP-2.This could further translate to behaviour seen *in vivo* and allow for better understanding of the osteoinduction phenomenon. Furthermore, silicate substitution (**SA**) increased affinity between rhBMP-2 and HA.

7.3   Competitive Binding Studies

The autofluorescence distinctively showed that an increase of fluorescence was observed for all proteins upon contact with the biomaterials. In conjunction with the CD work, changes of protein conformation were shown to be the cause of this phenomenon, and thus selecting the fluorophore that showed the least effect was very important.

In the competitive environment (MEM with 10 % foetal bovine serum (FBS)), the target protein affinity was lower than in MEM, especially for FTCA-BSA and FTCA-rhBMP-2, but not for SR101-rmOPN, with more of the protein species adsorbed on SA compared to HA.

The introduction of porosity in the competitive environment reduced the influence of chemistry. This suggests that porosity and conformational effects may have a big impact on bioactivity.

The findings for this study showed to be relevant to the pre-clinical studies towards osteoinduction, as real samples were used. Further emphasis on test environment conditions suggest that this factor was more pronounced throughout this study, as seen in Chapters 4 and 5. The research potential of this study suggests that pre-clinical procedures for more effective protein species adsorption on the biomaterials should be done in cell culture medium, not ionic as often required, at 37 ^{o}C. Silicate-substituted hydroxyapatite specimens should be favoured over stoichiometric hydroxyapatite, as they would adsorbed similar amounts, but retain more with a slower rate of release, which could possibly be more controlled with the addition of other adhesive protein species.

Overall, this in vitro study showed the importance of test conditions that are critical to adsorption and release behaviour of the protein species in competition. This could further translate to behaviour seen in vivo; and allow for better understanding of the osteoinduction phenomenon.

7.4   Future Work

Silicate substitution increases affinity between FN, BSA and BMP-2 and HA. Selection of an appropriate media can raise protein loading efficiency and effects protein delivery kinetics, which should be considered when translating laboratory data to the *in vivo* situation.

Initially, further work would be to expand on Chapter 4's fluorescence images study where the protein conformation of the labelled bovine serum albumin, BSA, (FTCA-

BSA) could be visualied over time on the same area on the surface of the biomaterials. Will the protein surface resemble the previous one obtained when using different samples for the different time points? Will accumulation or displacement of thr protein species on the surface be observed?

Similarly experiments could then be set up for recombinant human bone morphogenetic protein-2 (rhBMP-2) in Chapter 5, fibronectin (FN) and osteopontin (OPN).

Futher work would be required to determine whether these differences translate to a significant variation in cell response to HA and SA grafts after treatment with FN, BSA or rhBMP-2, specifically to look at the impact of the conformational changes on protein activity at their respective physiological amounts.

Autofluorescence of the protein species may need more investigating and be better defined per protein, to further understand the interactions between protein and biomaterials, possibly at physiological levels, as the CD work was limited to the sensitivity of the instrument. The influences of temperatures could be included in this work would also be advantageous in collecting representative data comparable to the studies experimental set ups undertaken in cell culture medium and in competition with 10 % fetal bovine serum (FBS).

The influence of porosity should be further investigated with rhBMP-2 in competition at the pharmacological levels to look at the impact of the stronger affinity observed from SA due to observed low release, which could then also translate to significant variation in cell response.

7.5   Notes

Publications and awards are included in Appendix 49, and courses, conferences, visits and training attended during the course of this study are tabulated in Tables 74 and 75 (see Appendices 50 and 51).

REFERENCES

Abuelyaman, A.S., Hudig, D*., et al.* (1994). "Fluorescent Derivatives of Diphenyl [1-(N-Peptidylaminoalkyl]phosphonate Esters: Synthesis and Use in the Inhibition and Cellular Localisation of Serine Proteases." *Bioconjugate Chemistry* **5**: 400-405.

Akao, M., Aoki, H*., et al.* (1981). "Mechanical properties of sintered hydroxyapatite for prosthetic applications." *J Mater Sci* **16**: 809-812.

Alberts, B., Bray, D*., et al.* (1994). "Molecular Biology of The Cell". USA, Garland Publishing.

Allen, L.T., Tosetto, M*., et al.* (2006). "Surface-induced changes in protein adsorption and implications for cellular phenotypic responses to surface interaction." *Biomaterials* **27**(16): 3096-3108.

Anselme, K. (2000). "Osteoblast adhesion on biomaterials." *Biomaterials* **21**(12): 667-681.

Anselme, K., Noel, B*., et al.* (1999). "Human Osteoblast Adhesion on Titanium alloy, Stainless steel, Glass and Plastic substrates with same Surface Topography." *Journal of Materials Science: Materials in Medicine* **10**: 815-819.

Arai, T. and Norde, W. (1990). "The behavior of some model proteins at solid liquid interfaces .2. Sequential and competitive adsorption." *Colloids and Surfaces* **51**: 17-28.

Balas, F., Perez-Pariente, J*., et al.* (2003). "In vitro bioactivity of silicon-substituted hydroxyapatites." *J. Biomed Mater Res* **66 A**: 364-375.

Barralet, J.E., Best, S.M*., et al.* (2000). "Effect of sintering parameters on the density and microstructure of carbonate hydroxyapatite." *Jourmal of Material Science: Material Medicine* **11**: 719-724.

Baxter, L.C., Frauchiger, V*., et al.* (2002). "Fibroblast and osteoblast adhesion and morphology on calcium phosphate surfaces." *Eur. Cell Mater.* **4**: 1-17.

Belous, A.M. and Skoblin, A.P. (1962). "Silicon content of Bone Callus in experimental fractures." *Byulleten' Eksperimental'noi Biologii i Meditsiny (translated from Russian)* **53**(5): 72-75.

Best, S.M., Sim, B*., et al.* (1997). "The dependence of osteoblastic response on variations in the chemical composition and physical properties of hydroxyapatite." *J Mater Sci Mater Med* **8**: 97-103.

Bolton, A.E. and Hunter, W.M. (1973). "The Labelling of Proteins to High Specific Radioactivities by Conjugation to a ^{125}I-Containing Acylating agent." *Biochem J* **133**: 529-539.

Botelho, C.M., Lopes, M.A.*, et al.* (2002). "Structural analysis of Si-substituted hydroxyapatite: zeta potential and X-ray photoelectron spectroscopy." *J Mater Sci Mater Med* **13**: 1123-1127.

Bumgardner, J.D., Wiser, R.*, et al.* (2003). "Contact angle, protein adsorption and osteoblast precursor cell attachment to chitosan coatings bonded to titanium." *J Biomater. Sci. Polym. Ed.* **14**: 1401-1409.

Caddick, S., Wilden, J.D.*, et al.* (2004). "Direct Synthesis of Sulfonamides and Activated Sulfonate Esters from Sulfonic Acids." *JACS* **126**(4): 1024-1025.

Callister, W.D. and Rethwisch, D.G. (2007). "Materials Science and Engineering". USA, John Wiley &Sons.

Cantor, C.R. and Schimmel, P.R. (1980). "Biophysical Chemistry Part II: Techniques for the study of Biological Strucutre and Function". USA, W.H.Freeman and Company.

Cantor, C.R. and Schimmel, P.R. (1980). "Part II: Techniques for the study of biological structure and function". *Biophysical Chemistry*. Vapnek, P.C. San Francisco, W.H. Freeman and Company**:** 409-480.

Carlisle, E.M. (1970). "Silicon: A Possible Factor in Bone Formation." *Science* **167**: 279-280.

Carlisle, E.M. (1972). "Silicon-Essential Element for Chick." *Science* **178**(4061): 619-621.

Carlisle, E.M. (1976). "In Vivo Requirement for Silicon in Articular-Cartillage and Connective-Tissue Formation in Chick." *Journal of Nutrition* **106**(4): 478-484.

Carlisle, E.M. (1980). "Biochemical and Morphological-changes associated with Long-bone Abnormalities in Silicon Deficiency." *Journal of Nutrition* **110**(5): 1046-1056.

Carlisle, E.M. (1980). "Silicon requirement for Normal Skul Formation in Chicks." *Journal of Nutrition* **110**(2): 352-359.

Carlisle, E.M. (1981). "Silicon- A Requirement in Bone-formation Independent of Vitamin-D1." *Calcified Tissue International* **33**(1): 27-34.

Carlisle, E.M. (1988). "Silicon as a trace nutrient." *Science of the Total Environment* **73**(1-2): 95-106.

Carlisle, E.M. and Everly, J.A. (1991). "Interactions between Silicon and Fluoride on Growth and Other Parameters." *Faseb Journal* **5**(6): A1646-A1646.

Cazalbou, S., Combes, C.*, et al.* (2004). "Adaptive physico-chemistry of bio-related calcium phosphates." *Journal of Materials Chemsitry* **14**: 2148-2153.

Chen, P., Carrington, J.L.*, et al.* (1991). "Stimulation of chondrogenesis in limb bud mesoderm cells by recombinant human bone morphogenetic protein 2B (BMP-2B) and modulation by transforming growth factor beta 1 and beta 2." *Exp. Cell Res* **195**(2): 509-515.

Chen, X., Wu, T.*, et al.* (2008). "Shield effect of silicate on adsorption of proteins onto silicon-doped hydroxyapatite (100) surface." *Biomaterials* **29**: 2423-2432.

Chen, Z.W., Gibson, W.M.*, et al.* (2008). "High Definition X-Rau Flourescence: Principles and Techniques." *X-ray optics and Instrumentation*: 1-10.

Colopy, S.A., Benz-Dean, J.*, et al.* (2004). "Response of the osteocyte syncytium adjacent to and distant from linear microcracks during adaptation to cyclic fatigue loading." *Bone* **35**: 881-891.

Coons, A.H. and Kaplan, M.H. (1950). "Localization of Antigen in Tissue Cells." *J. Exp. Med.* **91**: 1-13.

Currey, J.D. (2002). "Bones: Structure and Mechanics", Princeton University Press.

D'Andrea, S.C. and Fadeev, A.Y. (2003). "Covalent Surface Modification of Calcium Hydroxyapatite Using n-Alkyl- and n-Fluoroalkylphosphonic Acids." *Langmuir* **19**(19): 7904-7910.

Denhardt, D.T. and Guo, X. (1993). "Osteopontin: a protein with diverse functions." *The FASEB Journal* **7**: 1475-1482.

Dong, X., Wang, Q.*, et al.* (2007). "Understanding Adsorption-Desorption Dynamics of BMP-2 on Hydroxyapatite (001) surface." *Biophys. J.* **93**: 750-759.

dos Remedios, C.G. and Moens, P.D.J. (1999). "Resonance Energy Transfer in Proteins". *Resonance Energy Transfer*. D.L. Andrews, A.A.D., John Wiley & Sons Ltd**:** 1-64.

Dowd, T.L., Rosen, J.F.*, et al.* (2003). "The Three-Dimensional structure of bovine Calcium ion-bound Osteocalcin using ^{1}H NMR Spectroscopy." *Biochemistry* **42**: 7769-7779.

Drake, A.F. (1994). "Circular Dichroism". *Methods in Molecular Biology: Microscopy, Optical Spectroscopy and Macroscopic techniques*. Jones, C., Mulloy, B. and Thomas, A.H. Totowa NJ, Humana Press Inc. **22:** 219-243.

Ducheyne, P. and Qui, Q. (1999). "Bioactive ceramics: the effect of surface reactivity on bone formation and bone cell function." *Biomaterials* **20**: 2287-2303.

Ellingsen, J.E. (1991). "A Study on the Mechanism of Protein Adsorption to TiO$_2$." *Biomaterials* **12**(6): 593-596.

Elwing, H. (1998). "Protein absorption and ellipsometry in biomaterial research." *Biomaterials* **19**(4-5): 394-406.

Fabrizius-Homan, D.J. and Cooper, S.L. (1991). "A comparison of the adsorption of three adhesive proteins to biomaterial sufaces." *J Biomater Sci Polymer Edn* **3**(1): 27-47.

Fabrizius-Homan, D.J. and Cooper, S.L. (1991). "Competitive adsorption of vitronectin with albumin, fibrinogen, and fibronectin on polymeric biomaterials." *Journal of Biomedical Material Research* **25**(8): 953-971.

Fisher, L.W., Hawkins, G.R.*, et al.* (1987). "Purification and partial characterisation of Small Proteoglycans I & II, Bone Sialoprotein I & II and Osteonectin from Mineral Compartment of Developing Human bone." *J Biol Chem* **262**: 9702-9708.

George, A. and Veis, A. (2008). "Phosphorylated Proteins and Control Over Apatite Nulcleation, Crystal Growth and Inhibition." *Chem Rev* **108**(11): 4670-4693.

Gibson, I.R., Best, S.M.*, et al.* (1999). "Chemical Characterisation of Silicon-substituted Hydroxyapatite." *J. Biomed Mater Res* **44**: 422-428.

Gibson, I.R., Best, S.M.*, et al.* (2002). "Effect of Silicon Substitution on the Sintering and Microstructure of Hydroxyapatite." *J. Am. Ceram. Soc.* **85**(11): 2771-2777.

Gibson, I.R., Ke, S.*, et al.* (2001). "Effect of powder characteristics on the sinterability of hydroxyapatite powders." *J. Mater Sci Mater Med* **12**: 163-171.

Gibson, I.R., Rehman, I.*, et al.* (2000). "Characterization of the transformation from calcium-deficient apatite to beta-tricalcium phosphate." *Journal of Materials Science-Materials in Medicine* **11**(9): 533-539.

Goldstein, J., Newbury, D.*, et al.* (2003). "Scanning Electron Microscopy and X-Ray Microanalysis", Springer.

Gordon, D.B. (2000). "Spectroscopic techniques: I Atomic and molecular electronic spectroscopy". *Principles and techniques of Practical Biochemistry*. Wilson, K. and Walker, J. Cambridge, Cambridge University Press**:** 453-497.

Green, R.J., Davies, M.C.*, et al.* (1999). "Competitive protein adsorption as observed by surface plasmon resonance." *Biomaterials* **20**(4): 385-391.

Gregori, G., Kleebe, H.J.*, et al.* (2006). "EELS characterisation of β-tricalcium phosphate and hydroxyapatite." *Journal of the European Ceramic Society* **26**(8): 1473-1479.

Griessera, H.J., Kingshottb, P.*, et al.* (2004). "Surface-MALDI mass spectrometry in biomaterials research." *Biomaterials* **25**(20): 4861-4875.

Griessera, H.J., Kingshottb, P.*, et al.* (2004). "Surface-MALDI mass spectrometry in biomaterials research." *Biomaterials* **25**(20): 4861-4875.

Grinnell, F. and Feld, M.K. (1982). "Fibronectin ddsorption on hydrophilic and hydrophobic surfaces detected by antibody binding and analysed during cell adhesion in serum-containing medium." *Journal of Bioligical Chemistry* **257**(9): 4888-4893.

Groeneveld, E.H.J. and Burger, E.H. (2000). "Bone morphogenetic proteins in human bone regeneration." *European Journal of Endocrinology* **142**: 9-21.

Gugala, Z. and Gogolewski, S. (2004). "Protein adsorption, attachment, growth and activity of primary rat osteoblasts on polyactide membranes with defined surface characteristics." *Biomaterials* **25**(12): 2341-2351.

Guth, K., Campion, C.*, et al.* (2010). "Effect of Silicate-Substitution on Attachment and Early Development of Human Osteoblast-Like Cells Seeded on Microporous Hydroxyapatite Discs." *Advanced Engineering Materials* **12**(1-2): B26-B36.

Guth, K., Campion, C.*, et al.* (2010). "Surface Physiochemistry Affects Protein Adsorption to Stoichiometric and Silicate-Substituted Microporous Hydroxyapatites." *Advanced Engineering Materials* **12**(4): B113-121.

Hamilton, V., Yuan, Y.*, et al.* (2007). "Bone cell attachment and growth on the well-characterised chitosan films." *Polym Int* **56**: 641-647.

Harding, I.S., Rashid, N.*, et al.* (2005). "Surface charge and the effect of excess calcium ions on the hydroxyapatite surface." *Biomaterials* **26**: 6818-6826.

Harlow, E. and Lane, D. (1988). "Antibodies: A Laboratory Manual", CSHL Press.

Hauschka, P.V., Lian, J.B.*, et al.* (1989). "Osteocalcin and Matrix Gla protein: Vitamin K-dependent proteins in bone." *Physiol Rev* **69**(3): 990-1047.

Hauschka, P.V., Lian, J.B.*, et al.* (1975). "Direct identification of the calcium-binding amino acid, γ–carboxyglutamate, in mineralsed tissue." *Proc. Nat. Acad. Sci.* **72**: 3925-3929.

Hench, L.L. (1991). "Bioceramics: From Concept to Clinic." *Journal of American Ceramic Society* **74**(7): 1487-1510.

Hench, L.L. and Andersson, O. (1993). "Bioactive Glasses". *An Intorduction to Bioceramics*. L.L. Hench, J.W. Singapore, World Scientific Publishing Co. Ltd.**:** 41-62.

Herman, B. (1998). "Fluorescence Microscopy".

Hijya, N., Setoguchi, M.*, et al.* (1994). "Cloning and characterisation of the human osteopontin gene & its promoter." *Biochem J* **303**: 255-262.

Hing, K.A. (2004). "Bone repair in the twenty-first century: biology, chemistry or engineering?" *Phil. Trans. R. Soc. Lond. A* **362**: 2821-2850.

Hing, K.A. (2005). "Bioceramic Bone Graft Substitutes: Influence of Porosity and Chemistry." *Int. J. Appl. Ceram. Technol.* **2**(3): 184-199.

Hing, K.A., Annaz, B.*, et al.* (2005). "Microporosity enhances bioactivity of synthetic bone graft substitutes." *Journal of Material Science: Material Medicine* **16**: 467-475.

Hing, K.A., Best, S.M.*, et al.* (1999). "Characterisation of porous hydroxyapatite." *J Mater Sci Mater Med* **10**: 135-145.

Hing, K.A., Best, S.M.*, et al.* (1997). "Biomechanical assessment of bone ingrowth in porous hydroxyapatite." *J Mater Sci Mater Med* **8**: 731-736.

Hing, K.A., Best, S.M.*, et al.* (2004). "Mediation of bone ingrowth in porous hydroxyapatite bone graft substitutes." *Inc. J Biomed Mater Res* **68A**: 187-200.

Hing, K.A., Gibson, I.R.*, et al.* (1998). "Effect of variation in Ca:P ratio on Cellular response of Primary Human Osteobalst-like cells to Hydroxyapatite-based ceramics." *Bioceramics* **11**: 293-296.

Hing, K.A., Revell, P.A.*, et al.* (2006). "Effect of silicon level on rate, quality and progression of bone healing within silicate-substituted porous hydroxyapatite scaffolds." *Biomaterials* **27**: 5014-5026.

Hing, K.A., Wilson, L.F.*, et al.* (2007). "Comparative Performance of Three Ceramic Bone Graft Substitutes." *Spine J* **07**(04): 475-490.

Hirata, I., Nomura, Y.*, et al.* (2007). "Acceleration of bone formation with BMP2 in frame-reinforced carbonate apatite-collagen sponge scaffolds." *Journal of Artificial Organs* **10**(4): 212-217.

Hirayama, K., Akashi, S.*, et al.* (1990). "Rapid confirmation and revision of the primary structure of bovine serum albumin by ESIMS and FRIT-FAB LC MS." *Biochemical and Biophysical Research Communications* **173**: 639-646.

Hoang, Q.Q., Sicheri, F.*, et al.* (2003). "Bone recognition mechanism of porcine osteocalcin from crystal structure." *Nature* **425**: 977-980.

Holland, T.J.B. and Redfern, S.A.T. (1997). "Unicell Refinement from Powder Diffraction data: The Use of Regression Diagnostics." *Mineralogical Magazine* **61**: 65-77.

Hollinger, J.O., Einhorn, T.A.*, et al.* (2005). "Bone Tissue Engineering", CRC press.

Hoshino, M., Egi, T.*, et al.* (2006). "Repair of long intercalated rib defects using porous beta-tricalcium phosphate cylinders containing recombinant human bone morphogenetic protein-2 in dogs." *Biomaterials* **27**: 4034-4940.

Hunter, G.K., Hauschka, P.V.*, et al.* (1996). "Nucleation and Inhibition of Hydroxyapatite formation by mineralised Tissue Proteins." *Biochem J* **317**: 59-64.

Ishizaka, S., Habuchi, S.*, et al.* (1999). "Excitation Energy Transfer from Sulforhodamine 101 to Acid Blue 1 at a Liquid/Liquid Interface: Experimental Approach To Estimate Interfacial Roughness." *Anal. Chem.* **71**: 3382-3389.

Itri, R., Caetano, W.*, et al.* (2004). "Effect of urea on Bovine Serum Albumin in aqueous and Reverse Micelle environments investigated by Small Anle X-ray scattering, Fluorescence and Circular Dichroism." *Brazilian Journal of Physics* **34**(1): 58-63.

Jallot, E., Nedelec, J.M.*, et al.* (2005). "STEM and EDXS characterisation of physico-chemical reactions at the periphery of sol-gel derived Zn-substituted hydroxyapatites during interactions with biological fluids." *Colloids and Surfaces B-Biointerfaces* **42**(3-4): 205-210.

Kaito, T., Myoui, A.*, et al.* (2005). "Potentiation of the activity of bone morphogenetic protein-2 in bone regeneration by a PLA–PEG/hydroxyapatite composite." *Biomaterials* **26**: 73-79.

Kamikubo, Y., De Guzman, R.*, et al.* (2004). "Dislufide Bonding Arrangements in Active Forms of the Somatomedin B Domain of Human Vitronectin." *Biochemistry* **43**: 6519-6534.

Kamikubo, Y., Okumura, Y.*, et al.* (2002). "Identification of the Disulfide Bonds in the Recombinant Somatomedin B Domain of Human Vitronectin." *J Biol Chem* **277**(30): 27109-27119.

Kao, W.J. (1999). "Evaluation of protein-modulated macrophage behavior on biomaterials: designing biomimetic materials for cellular engineering." *Biomaterials* **20**(23-24): 2213-2221.

Kao, W.J., Hubbell, J.A.*, et al.* (1999). "Protein-mediated macrophage adhesion and activation on biomaterials: a model for modulating cell behavior." *J Mater Sci. Mater Med* **10**(10-11): 601-605.

Kilpadi, K.L., Chang, P.-L.*, et al.* (2001). "Hydroxyapatite binds more serum proteins, purified integrins and osteobalst precursor cells than titanium or steel." *J Biomed Mater Res* **57**: 258-267.

Kilpadi, K.L., Sawyer, A.A.*, et al.* (2004). "Prmiary human marrow stromal cells and Saos-2 osteosarcoma cells use different mechanisms to adhere to hydroxyapatite." *J Biomed Mater Res* **68A**: 273-285.

Kim, S.R., Lee, J.H.*, et al.* (2003). "Synthesis of Si, Mg substituted hydroxyapatites and their sintering behaviours." *Biomaterials* **24**: 1389-1398.

Klages, J., Kotzsch, A.*, et al.* (2008). "The Solution Structure of BMPR-IA reveals a Local Disorder-to-Order Transition upon BMP-2 Binding." *Biochemistry* **47**: 11930-11939.

Klonis, N. and Sawyer, W.H. (2003). "The Thiourea Group Modulates the Fluorescence Emission Decay of Fluorescein-labeled Molecules." *Photochem. Photobio* **77**(5): 502-509.

Knowles, J.C. (2003). "Phosphate based Glasses for Biomedical Applications." *Journal of Materials Chemsirty* **13**: 2395-2401.

Kowalczynska, H.M., Nowak-Wyrzykowska, M.*, et al.* (2005). "Fibronectin adsorption and arrangement on copolymer surfaces and their significance in cell adhesion." *J Biomed Mater Res* **72A**: 228-236.

Kuhn, L.T., Fink, D.J.*, et al.* (1996). "Biomimetic Strategies and materials Processing", VCH Inc.

Lackie, J.M. and Dow, J.A.T. (1995). "The Dictionary of Cell Biology", Academic Press Ltd.

Lakowicz, J.R. (1999). "Principles of Fluorescence Spectroscopy". New York, Kulwer Academic/ Plenum Press**:** 63-94.

Landi, E., Tampieri, A.*, et al.* (2004). "Influence of synthesis and sintering parameters on the characteristics of carbonate apatite." *Biomaterials* **25**(10): 1763-1770.

Leahy, D.J., Aukhil, I., *et al.* (1996). "2.0 A Crystal Structure of a Four-Domain Segment of Human Fibronectin Encompassing the RGD Loop and Synergy Region." *Cell* **84**: 155-164.

Leahy, D.J., Hendrickson, W.A., *et al.* (1992). "Structure of a Fibronectin Type III Domain from Tenascin Phased by MAD Analysis of the Selenomethionyl Protein." *Science* **258**: 987-991.

Lebaron, R.G. and Athanasiou, K.A. (2000). "Extracellular Matrix Cell Adhesioon Peptides: Functional Applications in Orthopedic Materials." *Tissue Engineering* **6**(2): 85-103.

Lefevre, C., Kang, H.C., *et al.* (1996). "Texas Red-X and Rhodamine Red-X, New Derivatives of Sulforhodamine 101 and Lissamine Rhodamine B with Improved Labeling and Fluorescence Properties." *Bioconjugate Chem* **7**: 482-489.

LeGeros, R.Z. and LeGeros, J.P. (1993). "Dense Hydroxyapatite". *An Introduction to Bioceramics*. L.L. Hench, J.W. Singapore, World Scientific Publishing Co. Ltd.**:** 139-180.

Li, G., Xi, N., *et al.* (2006). "An AFM method for *in situ* Probing Membrane Proteins under Physiological condition." *IEEE*.

Little, M.J., Paquette, D.M., *et al.* (1997). "Single-label fluorescent derivatization of peptides." *Analytica Chimica Acta* **339**: 279-288.

Luginbuehl, V., Meinel, L., *et al.* (2004). "Localized delivery of growth factors for bone repair." *European Journal of Pharmaceutics and Biopharmaceutics* **58**: 197-208.

Lutolf, M.P., Weber, F.E., *et al.* (2003). "Repair of bone defects using synthetic mimetics of collagenous extracellular matrices." *Nature Biotechnology* **21**: 513-518.

Maddalo, S.L. and Zimmer, M. (2006). "The Role of the Protein Matrix in green Fluorescent Protein Fluorescence." *Photochem. Photobiol* **82**: 367-372.

Marques, P., Magalhaes, M.C.F., *et al.* (2000). "Synthesis and characterisation of silicon-substituted hydroxyapatite". *Bioceramics*. Zurich-Uetikon, Trans Tech Publications Ltd. **192-1:** 247-250.

Massip, C., Riollet, P., *et al.* (2002). "Choice of different dyes to label tyrosine and nitrotyrosine." *J. Chromatogr A* **979**: 209-215.

Matsumoto, A., Yamaji, K., *et al.* (2001). "Effect of aging on bone formation induced by recombinant human bone morphogenetic protein-2 combined with fibrous collagen membranes at subperiosteal sites." *J Periodont Res* **36**: 175-182.

Matsuura , T., Hosokawa, R., *et al.* (2000). "Diverse Mechanisms of Osteoblast Spreading on Hydroxyapatite and Titanium." *Biomaterials* **21**: 1121-1127.

Mavropoulos, E., Costa, A.M., *et al.* (2011). "Adsorption and bioactivity studies of albumin onto hydroxyapatite surface." *Colloids ans Surfaces B: Biointerfaces* **83**: 1-9.

Mayasundari, A., Whittemore, N.A., *et al.* (2004). "The Solution Structure of the N-terminal Domain of Human Vitronectin." *J Biol Chem* **279**(28): 29359-29366.

McFarland, C.D., Thomas, C.H., *et al.* (2000). "Protein adsorption and cell attachment to patterned surfaces." *J Biomed Mater Res* **49A**: 200-210.

McKinsey, R.M., Spillane, J.T., *et al.* (1962). "Amino- and Nitrofluorescien Derivatives." *J Org Chem* **27**: 3986-3988.

Megley, C.M., Dickson, L.A., *et al.* (2009). "Photophysics and Dihedral freedom of the chromophore in Yellow, Blue and Green fluorescent protein." *J Phys Chem* **113B**: 302-308.

Meyer, U. and Wiesmann, H.P. (2006). "Bone and Cartilage Engineering", Springer-Verlag Berlin Heidelberg.

Micic, M., Chen, A., *et al.* (1999). "Scanning Electron Microscopy Studies of Protein-Functionalized Atomic Force Microscopy Cantilever tips." *Scanning* **21**(6): 394-397.

Miller, S.C., St-George, L.d., *et al.* (1989). "Bone Lining Cells: Structure and Function." *Scanning Microscopy* **3**(3): 953-961.

Mosher, D.F. (1984). "Physiology of Fibronectin." *Ann. Rev. Med* **35**: 561-575.

Mostafa, N.Y. (2005). "Characterization, thermal stability and sintering of hydroxyapatite powders prepared by different routes." *Materials Chemistry and Physics* **94**(2-3): 333-341.

Myers, R.T. (1980). "Rhodamine B and rhodamine 101 as reference substance for fluorescence quantum yield measurements." *J Phys Chem* **84**: 1871.

Nickel, J., Dreyer, M.K., *et al.* (2001). "The Crystal Structure of the BMP-2:BMPR-IA complex and the Generation of BMP-2 Antagonists." *J Bone Joint Surg Am* **83-A**: 7-14.

Nilsson, O.S., Urist, M.R., *et al.* (1986). "Bone repair induced by bone morphogenetic protein in ulnar defects in dogs." *Joint Bone Joint Surg* **68 B**(4): 635-642.

Noh, H., Yohe, S.T.*, et al.* (2008). "Volumetric interpretation of protein adsorption: Ion-exchange adsorbent capacity, protein pI, and interaction energetics." *Biomaterials* **29**: 2033-2048.

Oldberg, A., Franzen, A.*, et al.* (1986). "Cloning and sequence analysis of rat bone sialoprotein (osteopontin) cDNA reveals an Arg-Gly-Asp cell-binding sequence." *Proc Natl Acad Sci U S A* **83**(23): 8819-8823.

Osaka, A., Miura, Y.*, et al.* (1991). "Calcium apatite prepared from calcium hydroxide and orthophosphoric acid." *Journal of Materials Science-Materials in Medicine* **2**(1): 51-55.

Park, J.B. and Lakes, R.S. (2007). "Biomaterials: An Introduction", Springer.

Patel, N., Best, S.M.*, et al.* (2002). "A comparative study on the *in vivo* behaviour of hydroxyapatite and silicon substituted hydroxyapatite granules." *J. Mater Sci Mater Med* **13**: 1199-1206.

Patel, N., Brooks, R.A.*, et al.* (2005). "In vivo assessment of hydroxyapatite and silicate-substituted hydroxyapatite granules using an ovine defect model." *Journal of Materials Science-Materials in Medicine* **16**(5): 429-440.

Patel, N., Gibson, I.R.*, et al.* (2001). "Calcining influence on the powder properties of hydroxyapatite." *J. Mater. Sci.: Mater. Med.* **12**: 181-188.

Pluhar, G.E., Turner, A.S.*, et al.* (2006). "A comparison of two biomaterial carriers for osteogenic protein-1 (BMP-7) in an ovine critical defect model." *J Bone Joint Surg Br* **88-B**: 960-966.

Plummer, D.T. (1987). "An Introduction to Practical Biochemistry". Maidenhead, McGraw-Hill Book Company ltd.

Puleo, D.A. and Nanci, A. (1999). "Understanding and controlling the bone-implant interface." *Biomaterials* **20**: 2311-2321.

Rashid, N., Harding, I.S.*, et al.* (2008). "Nano-scale manipulation of silicate-substituted apatite chemistry impacts surface charge, hydrophilicity, protein adsorption and cell attachment." *Int. J. Nano and Biomaterials* **1**(3): 299-319.

Ratner, B.D., Hoffman, A.S.*, et al.* (2004). "Biomaterials Science", Elsevier.

Raynaud, S., Champion, E.*, et al.* (2002). "Calicum phosphate apatites with variable Ca/P atomic ratio I. Synthesis, characterisation and thermal stability of powders." *Biomaterials* **23**: 1065-1072.

Raynaud, S., Champion, E.*, et al.* (2002). "Calcium phosphate apatites with variable Ca/P atomic ration III. Mechanical properties and degradation in solution of hot pressed ceramics." *Biomaterials* **23**: 1081-1089.

Reinhott, F.P., Hultenby, K.*, et al.* (1990). "Osteopontin-a possible anchor of osteoblasts to bone." *Proc Natl Acad Sci U S A* **87**: 4473-4475.

Ripamonti, U. (1996). "Osteoinduction in porous hydroxyapatite implanted in heterotopic sites of different animal models." *Biomaterials* **17**: 31-35.

Roach, P., Farrar, D.*, et al.* (2005). "Interpretation of Protein Adsorption: Surface-Induced Conformational Changes." *J Am Chem Soc* **127**: 8168-8173.

Rochow, T.G. and Tucker, P.A. (1994). "Introdution to Microscopy by means of Light, Electrons, X-rays, or Acoustic". New York, Plenum Press.

Rosengren, A., Pavlovic, E.*, et al.* (2002). "Plasma proteins adsorption pattern on characterised ceramic biomaterials." *Biomaterials* **23**: 1237-1247.

Rouahi, M., Champion, E.*, et al.* (2006). "Physio-chemical characteristics and protein adsorption potential of hydroxyapatite particles: Influence on *in vitro* biocompatibility of ceramics after sintering." *Colloids Surf. B Biointerfaces* **47**(1): 10-19.

Rouahi, M., Gallet, O.*, et al.* (2006). "Influence of hydroxyapatite microstructure on human bone cell response." *J Biomed Mater Res* **78A**: 222-235.

Ruoslahti, E. (1996). "RGD and Other Recognition Sequences for Integrins." *Annu. Rev. Cell Dev. Biol.* **12**: 697-715.

Saito, N., Okada, T.*, et al.* (2003). "Local bone formation by injection of recombinant human bone morphogenetic protein-2 contained in polymer carriers." *Bone* **32**: 381-386.

Saito, N. and Takaoka, K. (2003). "New synthetic biodegradable polymers as BMPcarriers for bone tissue engineering." *Biomaterials* **24**: 2287-2293.

Sampath, T.K., J.E., C.*, et al.* (1990). "Bovine Osteogenic protein is composed of dimers of OP-1 and BMP-2A, Two members of Transforming Growth factor-β Superfamily." *J Biol Chem* **265**(22): 13198-13205.

Sawyer, A.A., Hennessy, K.M.*, et al.* (2005). "Regulation of mesenchymal stem cell attachment and spreading on hydroxyapatite by RGD peptides and adsorbed serum proteins." *Biomaterials* **26**(13): 1467-1475.

Schaffner, P. and Dard, M.M. (2003). "Structure and function of RGD peptides involved in bone biology." *Cellular and Molecular LIfe Sciences* **60**: 119-132.

Schliephake, H., Aref, A*., et al.* (2005). "Effect of immobilized bone morphogenic protein 2 coating of titanium implants on peri-implant bone formation." *Clin. Oral Impl. Res.* **16**: 563-569.

Schmitt, J.M., Hwang, K*., et al.* (1999). "Bone Morphogenetic Proteins: An Update on Basic Biology and Clinical Relevance." *J Orthop Res* **17**(2): 269-278.

Schwartz, K. (1973). "A Bound Form of Silicon in Glycosaminoglycans & Polyuronides." *Proc. Nat. Acad. Sci.* **70**: 1608-1612.

Shors, E.C. and Holmes, R.E. (1993). "Porous Hydroxyapatite". *An Introduction to Bioceramics*. L.L. Hench, J.W. Singapore, World Scientific Publishing Co. Ltd.**:** 181-198.

Skinner, J.A., Kroon, P.O*., et al.* (2003). "A femoral component with proximal HA coating: An analysis of survival and fixation at up to ten years." *J Bone Joint Surg Br* **85**(3): 128-140.

Skorstengaard, K., Jensen, M.S*., et al.* (1986). "Complete primary structure of bovine plasma fibronectin." *Eur.J.Biochem* **161**: 441-453.

Smith, D.A., Connell, S.D*., et al.* (2003). "Chemical force microscopy: applications in surface characterisation of natural hydroxyapatite." *Analytica Chimica Acta* **479**(1): 39-57.

Sodek, J., Ganss, B*., et al.* (2000). "Osteopontin." *Crit Rev Oral Biol Med* **11**(3): 279-303.

Steele, J.G., Johnson, G*., et al.* (1992). "Role of serum vitronectin and fibronectin in adhesion of fibroblasts following seeding onto tissue-culture polystyrene." *J Biomed Mater Res* **26**(7): 861-884.

Takami, Y., Yamane, S*., et al.* (1998). "Protein Adsorption on Ceramic Surfaces." *Journal of Biomedical Material Research* **40**: 24-30.

Takemoto, S., Kusudo, Y*., et al.* (2004). "Selective protein adsorption and blood compatibility of hydroxy-carbonate apatites." *J Biomed. Mater. Res* **69A**: 544-551.

Taylor, D., Hazenberg, J.G*., et al.* (2007). "Living with cracks:Damage and repair in human bone." *Nature materials* **6**: 263-268.

Thian, E.S., Huang, J*., et al.* (2006). "Silicon-substituted hydroxyapatite (SiHA): A novel calcium phosphate coating for biomedical applications." *J Mater Sci* **41**: 709-717.

Thomas, C.H., McFarland, C.D*., et al.* (1997). "The role of vitronectin in the attachment and spatial distribution of bone-derived cells on materials with patterned surface chemistry." *J Biomed Mater Res* **37**: 81-93.

Thorpe, R. and Thorpe, S. (2000). "Immunochemical techniques". *Principles and techniques of Practical Biochemistry*. Wilson, C.J. and Walker, J. Cambridge, Cambridge University Press 206-262.

Titus, J.A., Haugland, R*., et al.* (1982). "Texas Red, a Hydrophilic, Red-emitting Fluoruophore for use with Fluorescein in Dual Parameter Flow Microfluorometric and Fluoreescence Microscopic Studies." *Journal of Immunological Methods* **50**: 193-204.

Tortora, G.J. and Derrickson, B. (2009). "Principles of Anatomy and Physiology". USA, John Wiley & Sons, inc.

Trowbridge, J.M. and Gallo, R.L. (2002). "Dermatan sulfate: new functions from an old glycosaminoglycan." *Glycobiology* **12**(9): 117R-125R.

Uludag, H., Gao, T*., et al.* (2008). "Delivery Systems for BMPs: Factors Contributing to Protein Retention at an Application Site." *Journal of Bone & Joint Surgery* **83-A**: S1-128-135.

Umberger, J.Q. and Lamber, V.K. (1945). "The kinetics of diffusion controlled molecular and ionic reactions in solution as determined by measurements of the quenching of fluorescence." *J Am Chem Soc* **67**: 1099.

Urist, M.R. (1965). "Bone: Formation by autoinduction." *Science* **150**: 893-899.

Urist, M.R., DeLange, R.J*., et al.* (1983). "Bone Cell Differentition and Growth factors." *Science* **220**(680-686).

Urist, M.R. and Strates, B.S. (1971). "Bone Morphogenetic Protein." *J Dent Res* **50**(6): 1392-1406.

Valentine, W.M., Amarnath, V*., et al.* (1992). "Covalent Cross-Linking of Proteins by Carbon Disulfide." *Chem. Res. Toxicol* **5**: 254-262.

van Wachem, P.B., Vreriks, C.M*., et al.* (2006). "The influence of protein adsorption on interactions of cultured human endothelial cells with polymers." *J Biomed Mater Res* **21A**: 701-718.

Vunjak-Novakovic, G. and Freshney, R.I. (2006). "Culture of Cells for Tissue Engineering", John Wiley & Sons.

Walker, J. (2000). "Protein structure, purification and characterisation". *Principles and techniques of Practical Biochemistry*. Wilson, C.J. and Walker, J. Cambridge, Cambridge University Press**:** 312-356.

Walker, J.M. (2000). "Electrophoresis techniques". *Principles and Techniques of Practical Biochemistry*. Wilson, K. and Walker, J. Cambridge, Cambridge University Press**:** 580-618.

Wang, E.A., Rosen, V.*, et al.* (1990). "Recombinant human bone morphogenetic protein induces bone formation." *Proc. Nati. Acad. Sci. USA* **87**: 2220-2224.

Weber, D., Kotzsch, A.*, et al.* (2007). "A silent H-bond can be mutationally activated for high affinity interaction of BMP-2 and activin type IIB receptor." *BMC Structural Biology* **7**: 6.

Webster, T.J., Ergun, C.*, et al.* (2002). "Hydroxylapatite with substituted magnesium, zinc, cadmium, and yittrium. II. Mechanisms of Osteoblast adhesion." *J Biomed Mater Res* **59**: 312-317.

Wei, A.-P., Blumenthal, D.K.*, et al.* (1994). "Antibody-Mediated Fluorescence Enhancement Based on Shifting the Intramolecular Dimer<=> Monomer Equilibrium of Fluorescent Dyes." *Anal. Chem.* **66**: 1500-1506.

Weiner, S. and Wagner, H.D. (1998). "The Material bone: Structural-Mechanical function relations." *Annu. Rev. Mater. Sci* **28**: 271-298.

Whitemore, L. and Wallace, B.A. (2004). "DICHROWEB, an online server for protein secondary structure analyses from circular dichroism spectroscopic data." *Nucleic Acids Research* **32**: W669-W673.

Whitemore, L. and Wallace, B.A. (2007). "Protein Secondary Structure Analyses from Circular Dichroism Spectroscpy: Methods and Reference Databases." *Biopolymers* **89**(5): 392-400.

Wilson, C.J., Clegg, R.E.*, et al.* (2005). "Mediation of Biomaterial-Cell Interactions by Absorbed Proteins: A Review." *Tissue Engineering* **11**(1/2): 1-18.

Xie, J., Riley, C.*, et al.* (2002). "FTIR/ATR study of protein adsorption and brushite transformation to hydroxyapatite." *Biomaterials* **23**(17): 3609-3616.

Xu, D., Baburaj, K.*, et al.* (2001). "Model for the Three-Dimensional Structure of Vitronectin: Predictions for the Multi-Domain Protein from threading and docking." *Proteins* **44**(3): 312-320.

Yamada, K.M. (1983). "Cell Surface Interactions with Extracellular Matrix." *Annu. Rev. Biochem* **52**: 761-799.

Yamaguchi, A., Katagiri, T.*, et al.* (1991). "Recombinant Human Bone Morphogenetic Protein-2 Stimulates Osteoblastic Maturation and Inhibits Myogenic Differentiation In Vitro." *The lournal of Cell Biology* **113**(3): 681-687.

Yang, X.B., Roach, H.I.*, et al.* (2001). "Human osteoprogenitor growth and differentiation on synthetic biodegradable structures after surface modification." *Bone* **29**(6): 523-531.

Yang, Y., Cavin, R.*, et al.* (2003). "Protein adsorption on titanium surfaces and their effect on osteoblast attachment." *J Biomed Mater Res* **67A**: 344-349.

Yasko, A.W., Lane, J.M.*, et al.* (1992). "The Healing of Segmental Bone Defects, Induced by Recombinant Human Bone Morphogenetic Protein (rhBMP-2)." *Journal of Bone & Joint Surgery* **74-A**(5): 659-670.

Yin, G., Liu, Z.*, et al.* (2002). "Impacts of the surface charge property on protein adsorption on hydroxyapatite." *Chemical Engineering Journal* **87**(2): 181-186.

Young, M.F., Kerr, J.M.*, et al.* (1992). "Structure, Expression, and Regulation of the Major Non-collagenous Matrix Proteins of Bone." *Clin Ortho Rel Res* **281**: 275-294.

Zeng, H.T., Chittur, K.K.*, et al.* (1999). "Analysis of bovine serum albumin adsorption on calcium phosphate and titanium surfaces." *Biomaterials* **20**(4): 377-384.

Zhang, Q., Domenicucci, C.*, et al.* (1990). "Characterization of Fetal Porcine Bone Sialoproteins, Secreted Phophoprotein I (SPPI, Osteopontin), Bone Sialoprotein and a 23-kDa Glycoprotein." *J Biol Chem* **265**(13): 7583-7589.

Zhao, M., Qiao, M.*, et al.* (2006). "The Zinc Finger Transcription Factor Gli2 Mediates Bone Morphogenetic Protein 2 Expression in Osteoblasts in Response to Hedgehog Signaling." *Mol. Cell. Biol.* **26**(16): 6197-6208.

Zhou, A., Huntington, J.A.*, et al.* (2003). "How vitronectin binds PAI-1 to modulate fibrinolysis and cell migration." *Nat. Struct. Biol.* **10**(7): 541-544.

Zunszain, P.A., Ghuman, J.*, et al.* (2003). "Crystal structural analysis of human serum albumin complexed with hemin and fatty acids." *BMC Structural Biology* **3**(1): 6.

APPENDICES

CHAPTER 2

Appendix 1

XRD spectra for the HA from CERAM - two PDF files (A) the first trial with 5% CaO impurity and (B) the second attempt with no impurities, respectively on the CD.

Appendix 2
Table 14 – SA-DD dimensions, weight and density at all sintering temperature
pressed at 75.8 MPa, using micrometer

Sintering Temperature / $^{\circ}$C	Diameter ($\pm\sigma$) / cm	Thickness ($\pm\sigma$) / cm	Weight ($\pm\sigma$) / g	Density ($\pm\sigma$) / gcm^{-3}
1200	11.70 ($\pm$0.06)	3.05 ($\pm$0.05)	0.9461 ($\pm$0.004)	2.887 ($\pm$0.06)
1225	11.71 ($\pm$0.09)	3.04 ($\pm$0.06)	0.9391 ($\pm$0.004)	2.865 ($\pm$0.06)
1250	11.63 ($\pm$0.05)	3.02 ($\pm$0.02)	0.9432 ($\pm$0.002)	2.944 ($\pm$0.09)
1275	11.82 ($\pm$0.04)	2.98 ($\pm$0.02)	0.9405 ($\pm$0.003)	2.876 ($\pm$0.04)
1300	11.77($\pm$0.03)	3.06 ($\pm$0.07)	0.9408 ($\pm$0.007)	2.831 ($\pm$0.06)
1325	11.82 ($\pm$0.05)	3.00 ($\pm$0.04)	0.9362 ($\pm$0.001)	2.843 ($\pm$0.05)
1350	11.74 ($\pm$0.06)	3.06 ($\pm$0.07)	0.9393 ($\pm$0.005)	2.844 ($\pm$0.07)
1375	11.75 ($\pm$0.05)	3.04 ($\pm$0.04)	0.9419 ($\pm$0.001)	2.863 ($\pm$0.05)

Appendix 3
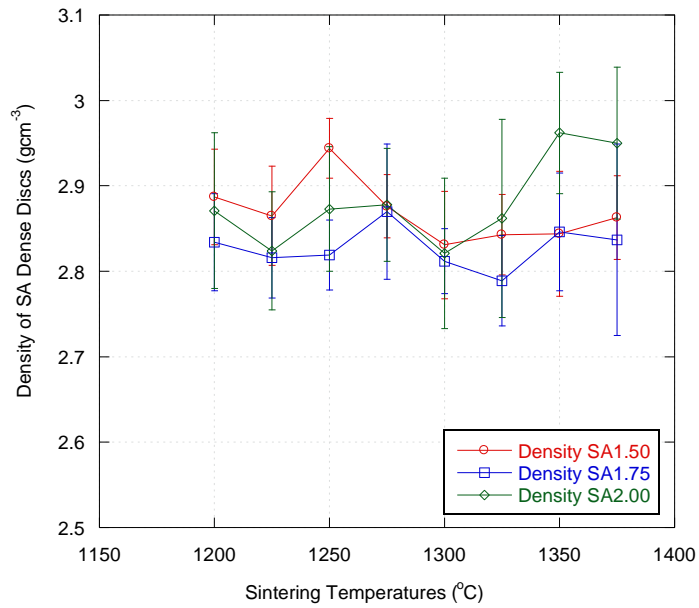
Figure 31 – Density of sintered SA at different pressures 75.8 (1.50), 90.9 (1.75) and 101.1 (2.00) MPa, calculated using a micrometer

Appendix 4
Table 15 – SA-DD dimensions, weight and density at all sintering temperature pressed at 90.9 MPa, using micrometer

Sintering Temperature / °C	Diameter (±σ) / cm	Thickness (±σ) / cm	Weight (±σ) / g	Density (±σ) / gcm⁻³
1200	11.98 (±0.08)	2.99 (±0.07)	0.9458 (±0.006)	2.834 (±0.06)
1225	11.86 (±0.07)	3.04 (±0.07)	0.9446 (±0.007)	2.816 (±0.05)
1250	11.85 (±0.09)	3.02 (±0.02)	0.9374 (±0.003)	2.819 (±0.05)
1275	11.95 (±0.07)	2.91 (±0.07)	0.9362 (±0.0030	2.870 (±0.08)
1300	11.95 (±0.04)	2.96 (±0.04)	0.9340 (±0.003)	2.812 (±0.04)
1325	11.99 (±0.01)	2.97 (±0.05)	0.9343 (±0.005)	2.789 (±0.05)
1350	11.95 (±0.05)	2.97 (±0.07)	0.9375(±0.001)	2.846 (±0.07)
1375	11.97 (±0.03)	2.94 (±0.09)	0.9357 (±0.008)	2.837 (±0.11)

Appendix 5
Table 16 – SA-DD dimensions, weight and density at all sintering temperature pressed at 101.1 MPa, using micrometer

Sintering Temperature / ^{o}C	Diameter ($\pm\sigma$) / cm	Thickness ($\pm\sigma$) / cm	Weight ($\pm\sigma$) / g	Density ($\pm\sigma$) / gcm^{-3}
1200	12.06 ($\pm$0.05)	2.88 ($\pm$0.10)	0.9431 ($\pm$0.008)	2.871 ($\pm$0.09)
1225	12.03 ($\pm$0.05)	2.92 ($\pm$0.08)	0.9355 ($\pm$0.006)	2.824 ($\pm$0.07)
1250	12.04 ($\pm$0.04)	2.88 ($\pm$0.09)	0.9403 ($\pm$0.006)	2.873 ($\pm$0.07)
1275	12.02 ($\pm$0.02)	2.89 ($\pm$0.06)	0.9411 ($\pm$0.006)	2.878 ($\pm$0.07)
1300	12.04($\pm$0.04)	2.92 ($\pm$0.09)	0.9360 ($\pm$0.004)	2.821 ($\pm$0.09)
1325	12.05 ($\pm$0.04)	2.87 ($\pm$0.10)	0.9347 ($\pm$0.004)	2.862 ($\pm$0.12)
1350	12.07 ($\pm$0.05)	2.76 ($\pm$0.05)	0.9332 ($\pm$0.005)	2.962 ($\pm$0.07)
1375	12.07 ($\pm$0.02)	2.76 ($\pm$0.07)	0.9299 ($\pm$0.008)	2.950 ($\pm$0.09)

Appendix 6
Table 17 – HA-DD dimensions, weight and density at all sintering temperature pressed at 75.8 MPa, using micrometer

Sintering Temperature / ^{o}C	Diameter ($\pm\sigma$) / cm	Thickness ($\pm\sigma$) / cm	Weight ($\pm\sigma$) / g	Density ($\pm\sigma$) / gcm^{-3}
1150	12.07 ($\pm$0.04)	2.77 ($\pm$0.02)	0.9535 ($\pm$0.008)	3.008 ($\pm$0.04)
1175	12.02 ($\pm$0.04)	2.90 ($\pm$0.03)	0.9499 ($\pm$0.03)	2.893 ($\pm$0.10)
1200	12.02 ($\pm$ 0.04)	2.81 ($\pm$0.04)	0.9536 ($\pm$0.00)	2.900 ($\pm$0.03)
1225	12.00 ($\pm$0.06)	2.91 ($\pm$0.03)	0.9601 ($\pm$0.02)	2.926 ($\pm$0.07)
1250	12.00 ($\pm$0.03)	2.82 ($\pm$0.09)	0.9363 ($\pm$0.01)	2.945 ($\pm$0.09)
1275	11.99 ($\pm$0.03)	2.87 ($\pm$0.09)	0.9445 ($\pm$0.00)	2.922 ($\pm$0.09)
1300	11.98 ($\pm$0.03)	2.91 ($\pm$0.09)	0.9413 ($\pm$0.01)	2.874 ($\pm$0.08)

Appendix 7
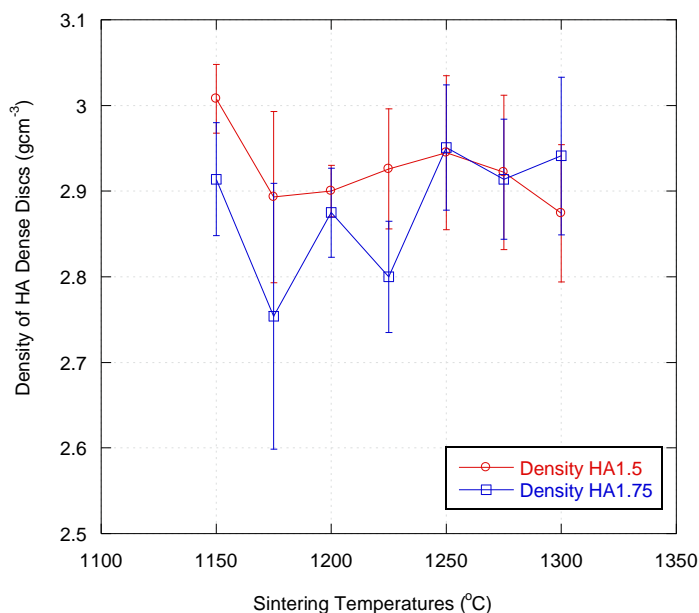
Figure 32 – Density of sintered HA at different pressures 75.8 (1.50) and 90.9 (1.75) MPa, calculated using a micrometer

Appendix 8

Table 18 – HA-DD dimensions, weight and density at all sintering temperature pressed at 90.9 MPa, using micrometer

Sintering Temperature / ^{o}C	Diameter ($\pm\sigma$) / cm	Thickness ($\pm\sigma$) / cm	Weight ($\pm\sigma$) / g	Density ($\pm\sigma$) / gcm^{-3}
1150	12.29 ($\pm$0.11)	2.81 ($\pm$0.06)	0.9686 ($\pm$0.007)	2.914 ($\pm$0.07)
1175	12.22 ($\pm$0.07)	2.80 ($\pm$0.22)	0.9372 ($\pm$0.05)	2.754 ($\pm$0.16)
1200	12.25 ($\pm$0.09)	2.81 ($\pm$0.050	0.9830 ($\pm$0.01)	2.875 ($\pm$0.05)
1225	12.20 ($\pm$0.09)	2.79 ($\pm$0.04)	0.9492 ($\pm$0.03)	2.800 ($\pm$0.07)
1250	12.12 ($\pm$0.05)	2.79 ($\pm$0.06)	0.9483 ($\pm$0.01)	2.951 ($\pm$0.07)
1275	12.07 ($\pm$0.04)	2.84 ($\pm$0.07)	0.9467 ($\pm$0.006)	2.914 ($\pm$0.07)
1300	12.07 ($\pm$0.04)	2.83 ($\pm$0.070	0.9518 ($\pm$0.009)	2.941 ($\pm$0.09)

Appendix 9
Table 19 – Average SA-DD dimensions, weight and density at optimum sintering
temperature of 1300 ^{o}C, using micrometer

Pressure / MPa	Diameter (±σ) / cm	Thickness (±σ) / cm	Weight (±σ) / g	Density (±σ) / gcm^{-3}
75.8	11.77 (±0.03)	3.06 (±0.07)	0.9408 (±0.007)	2.831 (±0.06)
90.9	11.95 (±0.04)	2.96 (±0.04)	0.9340 (±0.003)	2.812 (±0.04)
101.1	12.04 (±0.04)	2.92 (±0.09)	0.9360 (±0.004)	2.821 (±0.09)

Appendix 10
Table 20 – Average HA-DD dimensions, weight and density at optimum sintering
temperature of 1250 ^{o}C, using micrometer

Pressure / MPa	Diameter (±σ) / cm	Thickness (±σ) / cm	Weight (±σ) / g	Density (±σ) / gcm^{-3}
75.8	12.00 (±0.03)	2.82 (±0.09)	0.9363 (±0.01)	2.945 (±0.09)
90.9	12.12 (±0.05)	2.79 (±0.06)	0.9483 (±0.01)	2.951 (±0.07)

Chapter 3

Appendix 11
Table 21 - Tabulated representations of attempted synthetic routes
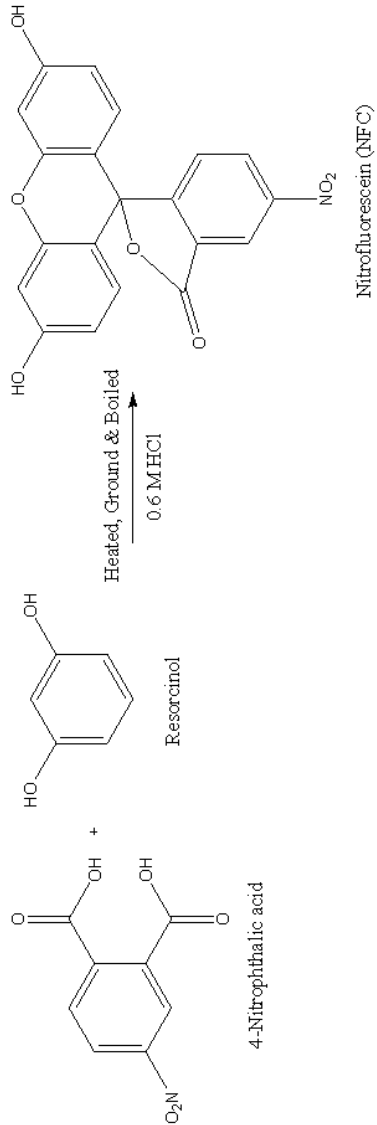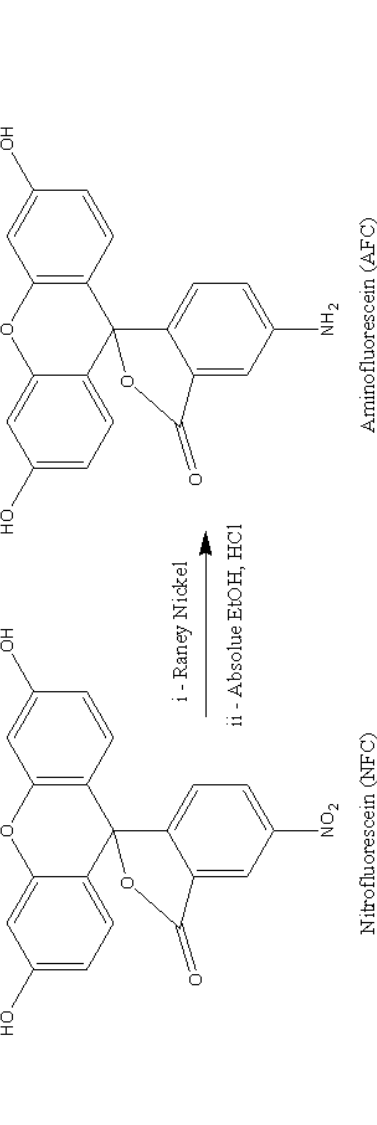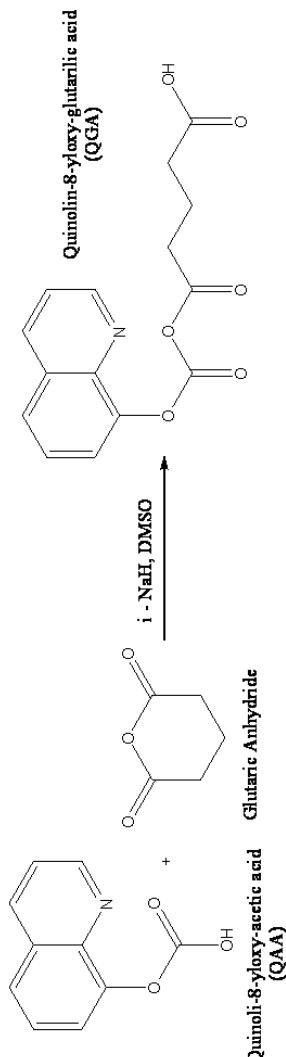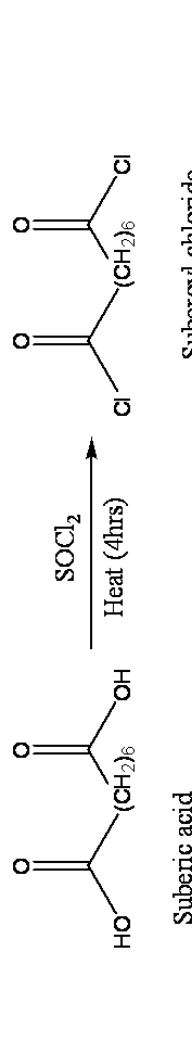
Expt no.	Synthetic Routes-Compounds & Reagents	References
2A		(Coons and Kaplan 1950)
2B		(Coons and Kaplan 1950)

Table 22 - Tabulated representations of attempted synthetic routes (continued)

Expt. no.	Synthetic Routes -Compounds & Reagents	References
7		(Collman, Yan et al. 2006)
9A		(Oikawa, Sugano et al. 1978)
9B		(Adamczyk, Mattingly et al. 1996)

Table 23 – Synthetic route (continued)

Expt no.	Synthetic Routes-Compounds & Reagents	References
10	Quinoli-8-yloxy-acetic acid (QAA) + Glutaric Anhydride → (i - NaH, DMSO) → Quinolin-8-yloxy-glutanilic acid (QGA)	(Abd-Alla, Ahmed et al. 1992)
13	Suberic acid → (SOCl₂, Heat (4hrs)) → Suberoyl chloride	(Kubicova, Waisser et al. 2000) (Stevens and Vanderhoydonck 2001)
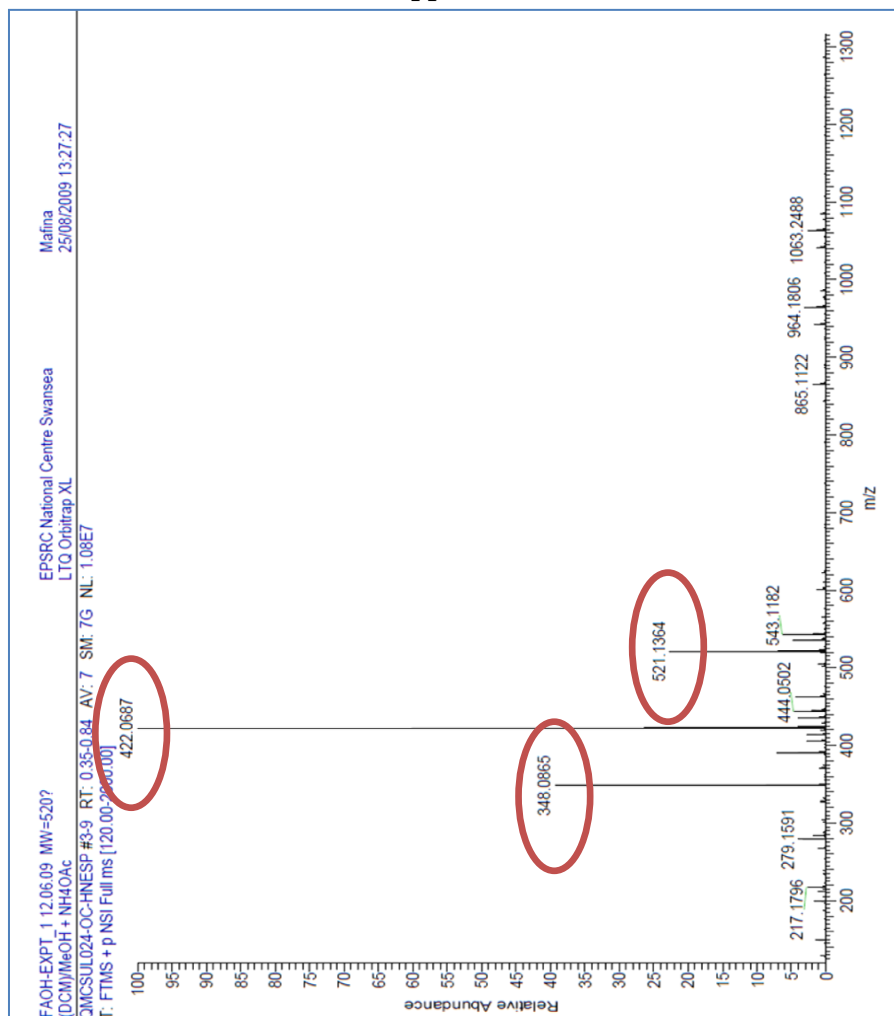
Appendix 12

Figure 33- Mass spectrum of the synthesised FTCA

Appendix 13
Table 24 – Tabulated Excitation & Emission of the FTCA in spectroscopic grade ethanol

Concentration / M	Excitation / nm	Emission in Ethanol / nm	Emission in Water / nm
2.845×10^{-8}	494	522	518
2.845×10^{-7}	494	523	516
2.845×10^{-8}	494	524	516

Appendix 14
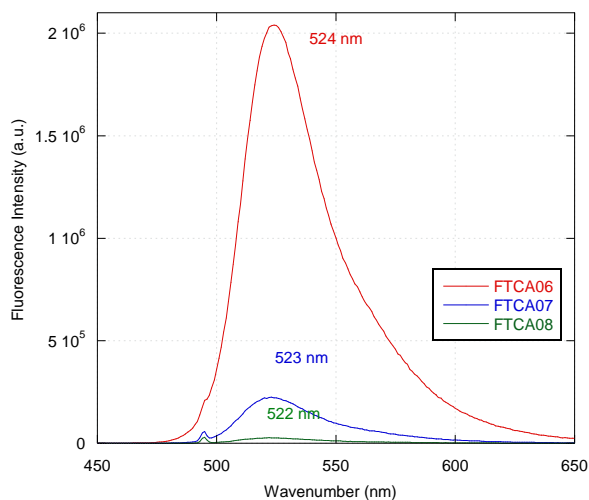
Figure 34 - The emission Spectra at 3 distinct concentrations of the FTCA compound in ethanol

Appendix 15
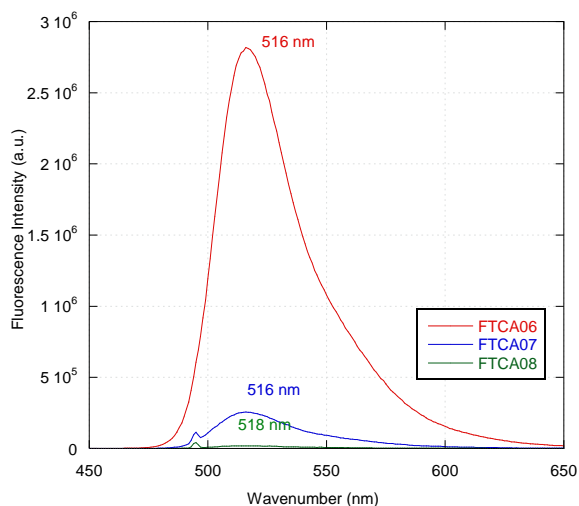
Figure 35 - Emission Spectra at 3 distinct concentrations of the FTCA compound in water

Appendix 16
Table 25- Absorbance of the FTCA compound related to the concentration used in Ethanol

Concentration / M	Absorbance (A.U.)	Extinction Coefficient / L mol^{-1}cm^{-1}
2.845×10^{-8}	0.06534 ($\lambda=501$ nm)	23,000
2.845×10^{-7}	-0.03269 ($\lambda=500$ nm)	-115,000
2.845×10^{-8}	-0.007385 ($\lambda=486$ nm)	-260,000

Appendix 17

Table 26- Absorbance of the FTCA compound related to the concentration used in Water

Concentration / M	Absorbance (A.U.)	Extinction Coefficient / L mol^{-1}cm^{-1}
2.845×10^{-8}	0.09057 (λ=489 nm)	32,000
2.845×10^{-7}	0.01812 (λ=490 nm)	64,000
2.845×10^{-8}	0.007744 (λ=486 nm)	272,000

Appendix 18

Figure 36– Structure of the Texas Red (TXR)

Chapter 4
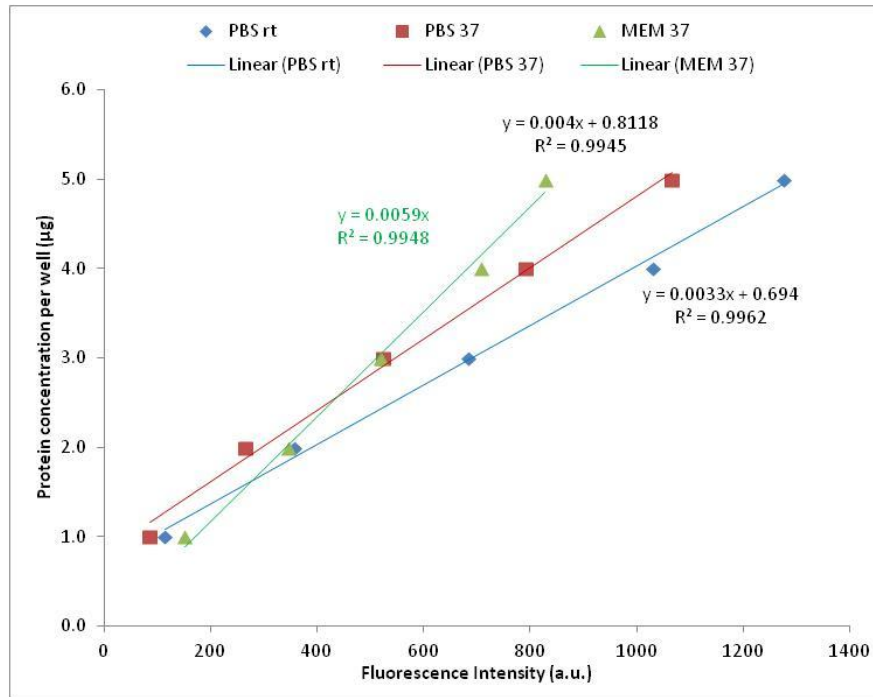
Figure 37– Calibration curves for the 0-5 μg range concentration in all media and temperature using the Quant-it kit
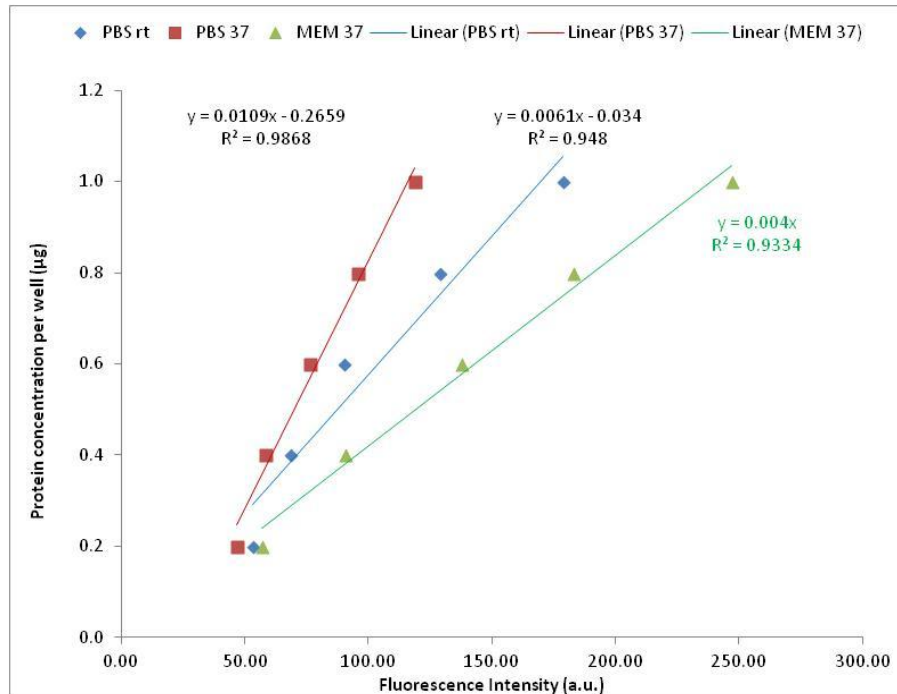
Figure 38 – Calibration curves for the 0-1 μg range concentration in all media and temperature using the Quant-it kit

Appendix 21
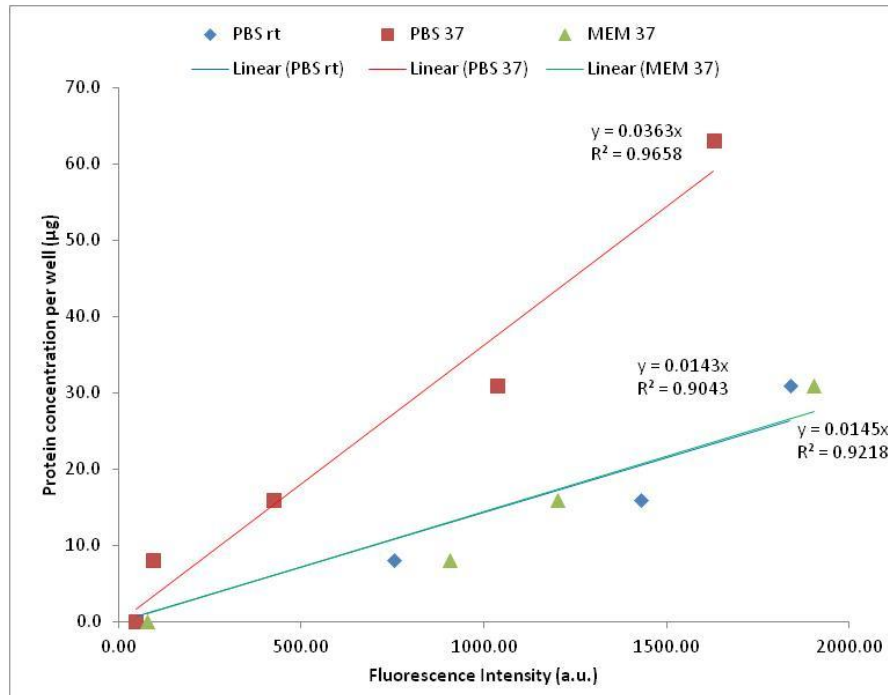
Figure 39 - Calibration curves for the 0-500 µg range concentration in all media and temperature using the Quant-it kit

Appendix 22
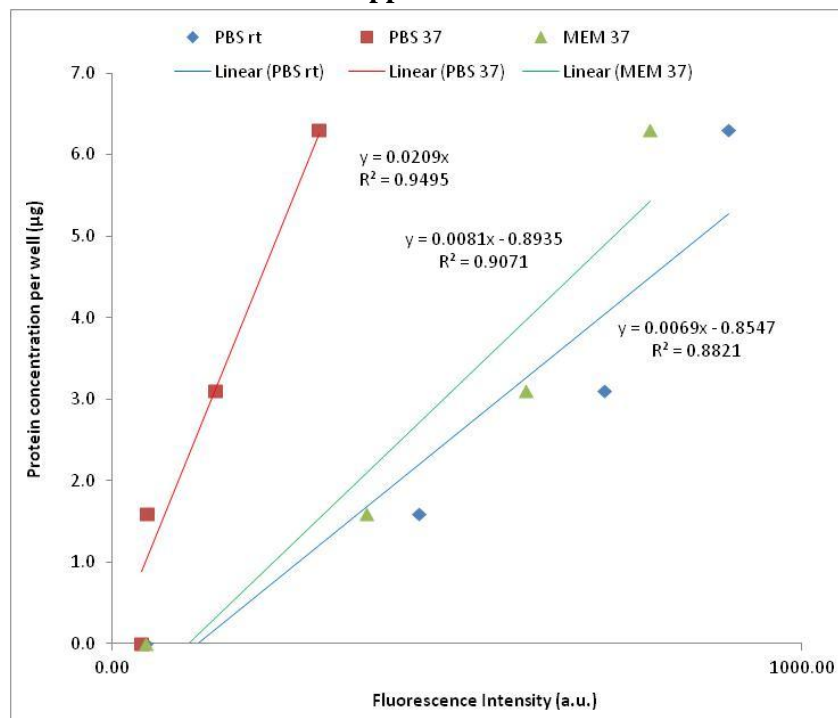
Figure 40- Calibration curves for the 0-100 µg range concentration in all media and temperature using the Quant-it kit

Appendix 23
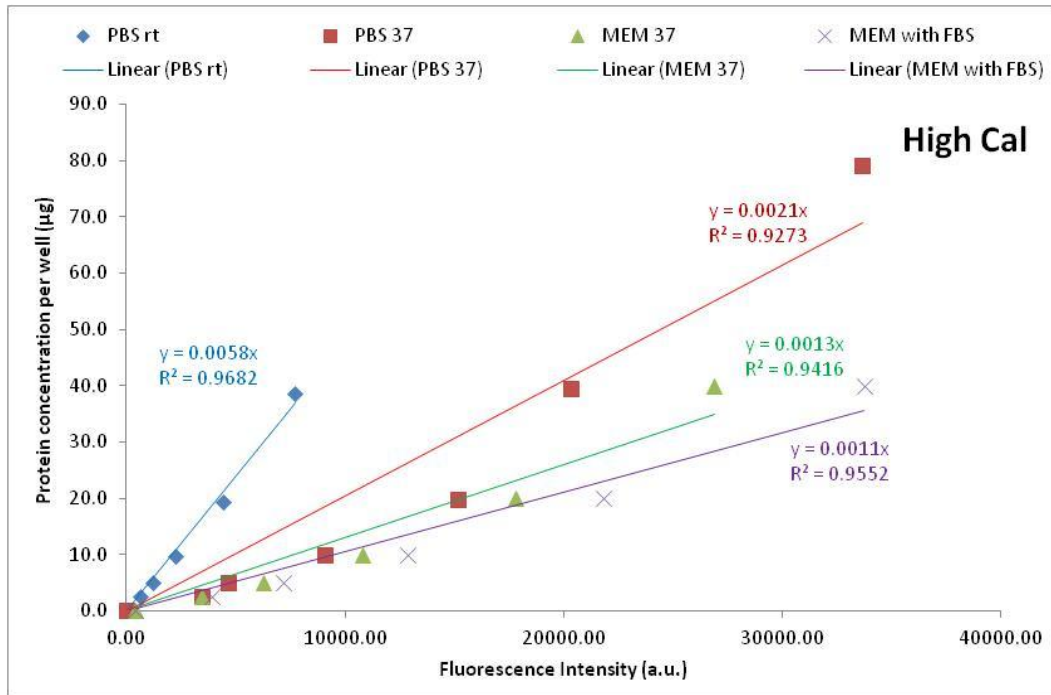
Figure 41– Calibration curves for the high range concentration in all media and temperature using FTCA-BSA

Appendix 24
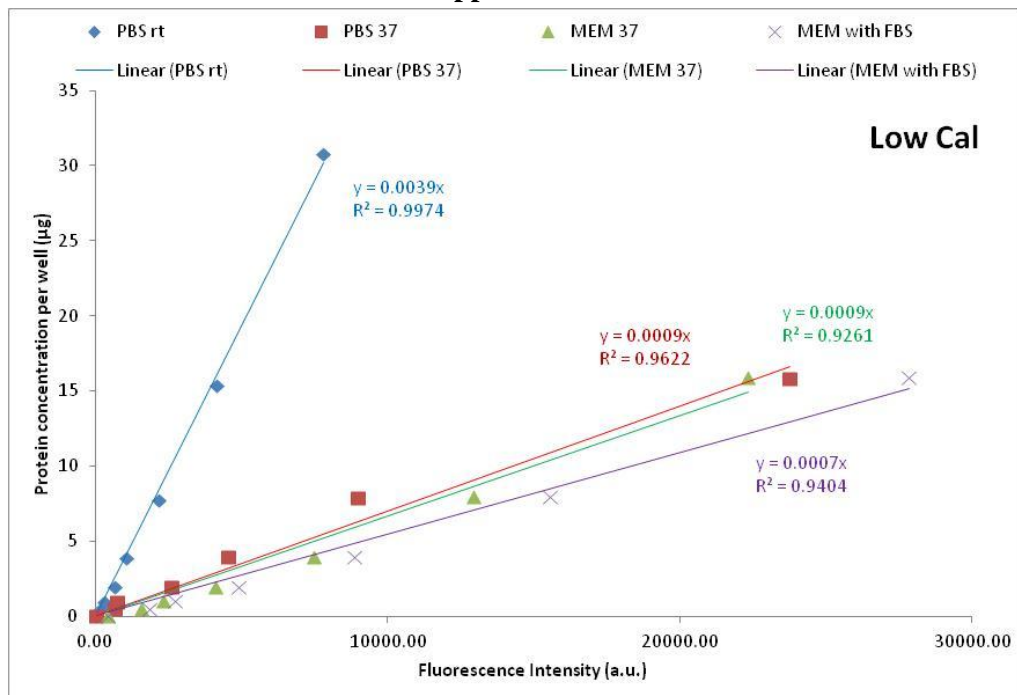
Figure 42– Calibration curves for the low range concentration in all media and temperature using FTCA-BSA

Chapter 5
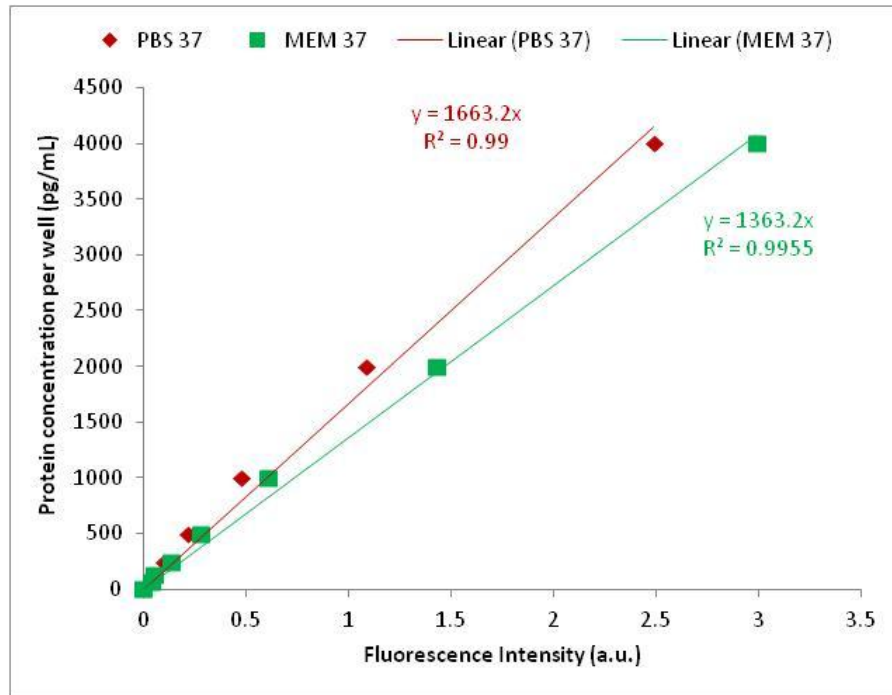
Figure 43 – Calibration curves for the BMP-2 standards in all media at 37 ^{o}C using Quantikine kit
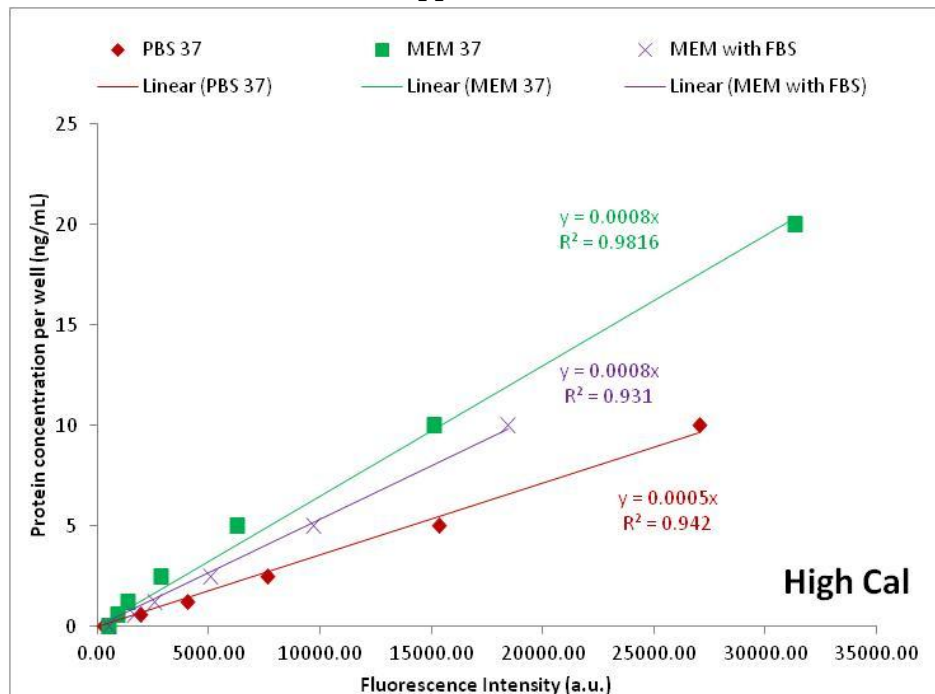
Figure 55 – Calibration curves for the high BMP-2 range in all media at 37 ^{o}C using FTCA-BMP-2

Appendix 27
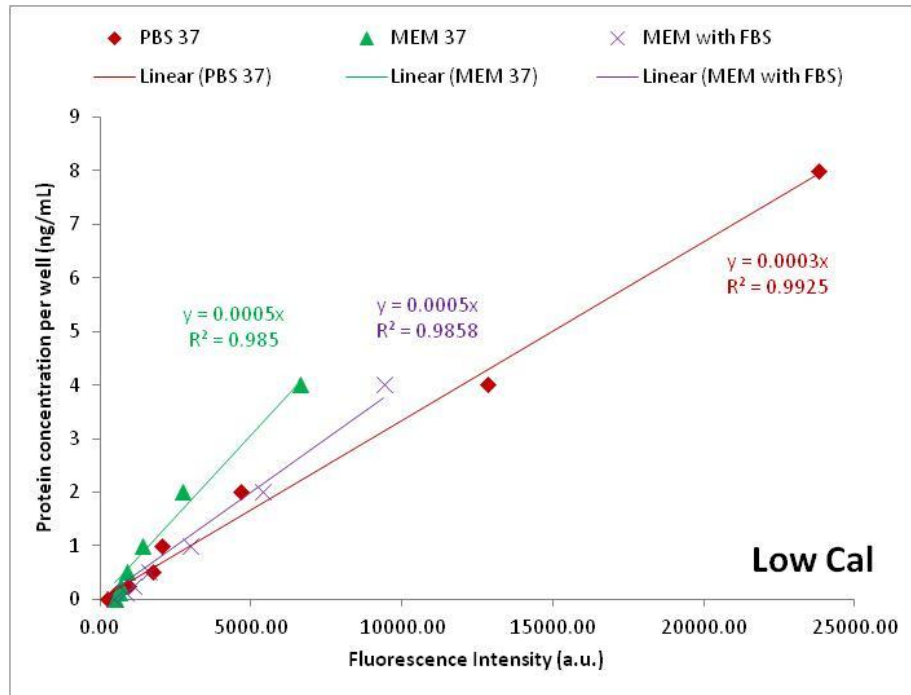
Figure 56 – Calibration curves for the low BMP-2 range in all media at 37 ^{o}C using FTCA-BMP-2

Chapter 6
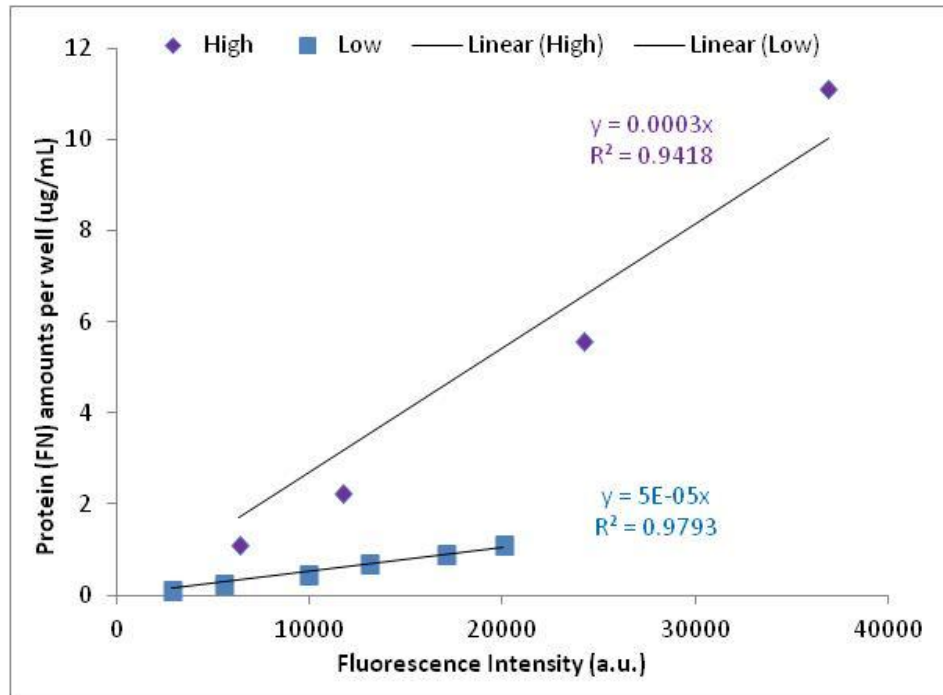
Figure 46 – Calibration curves for the high and low FN range in PBS at 37 $^{\circ}$C using FTCA-FN
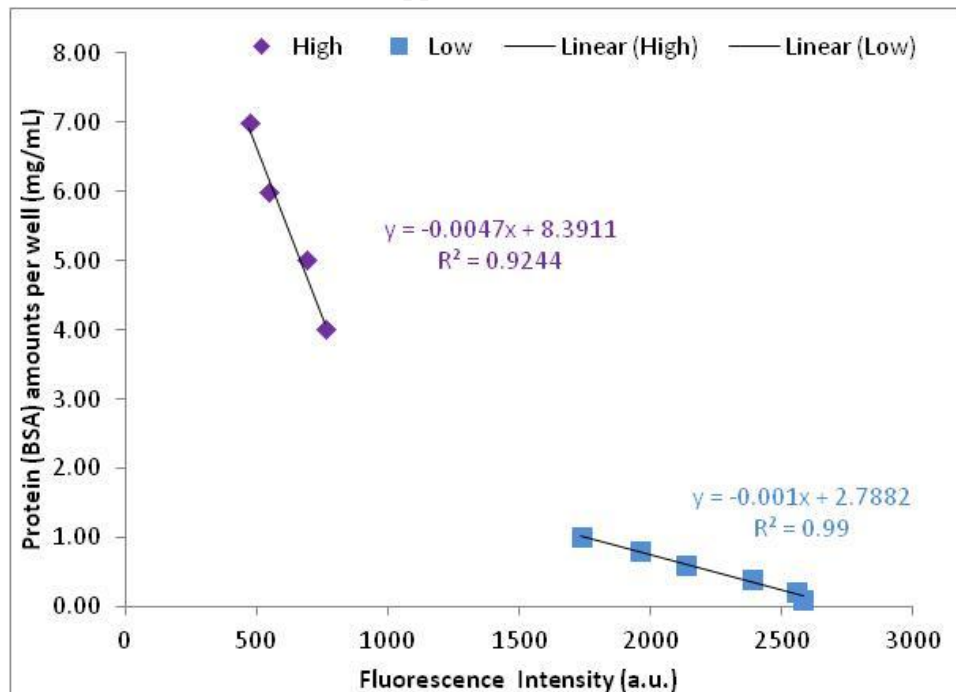
Figure 47 – Calibration curves for the high and low BSA range in PBS at 37 $^{\circ}$C using SR101-BSA

Appendix 30
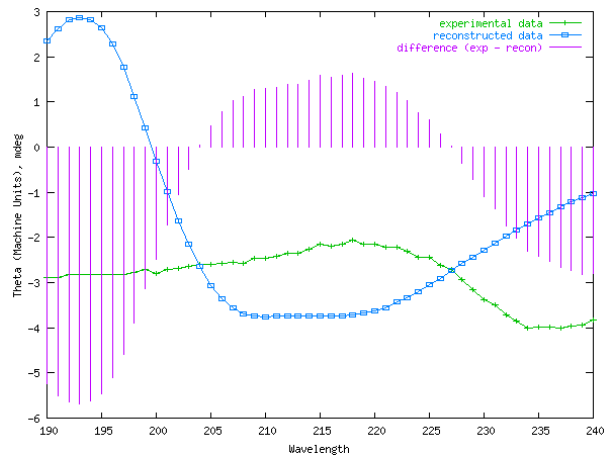
Figure 48 - Dichroweb data for FN in PBS

Appendix 31
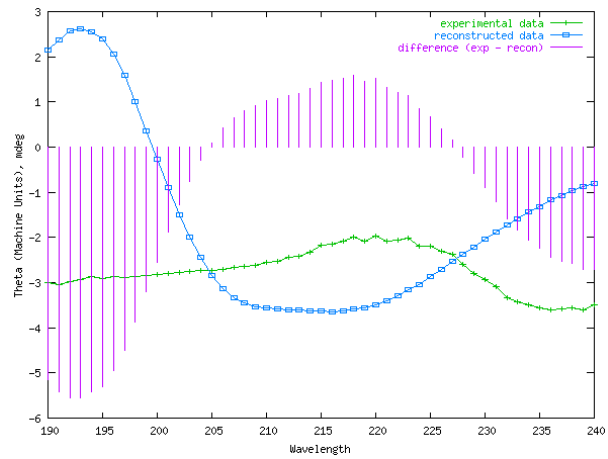
Figure 49 - Dichroweb data for HA-FN in PBS

Appendix 32
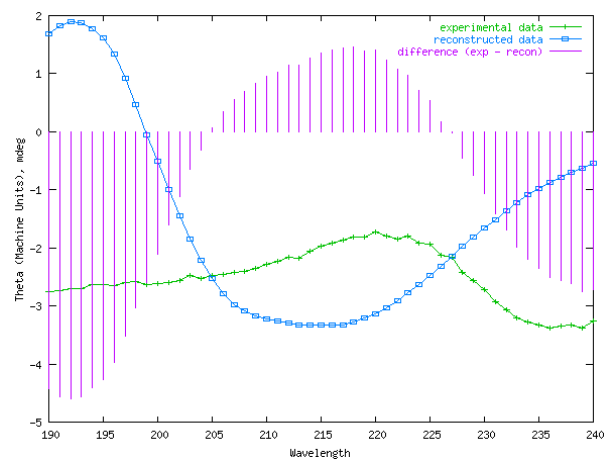
Figure 50 - Dichroweb data for SA-FN in PBS

Appendix 33
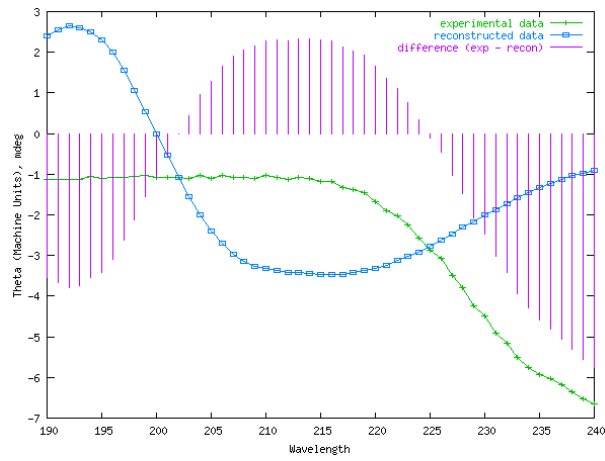
Figure 51 - Dichroweb data for FN in MEM

Appendix 34
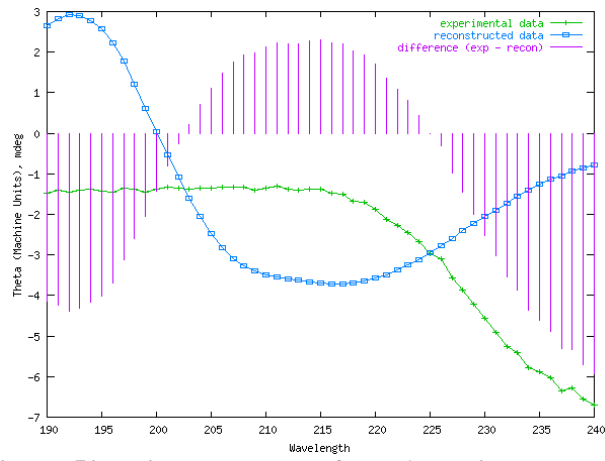
Figure 52 - Dichroweb data for HA-FN in MEM

Appendix 35
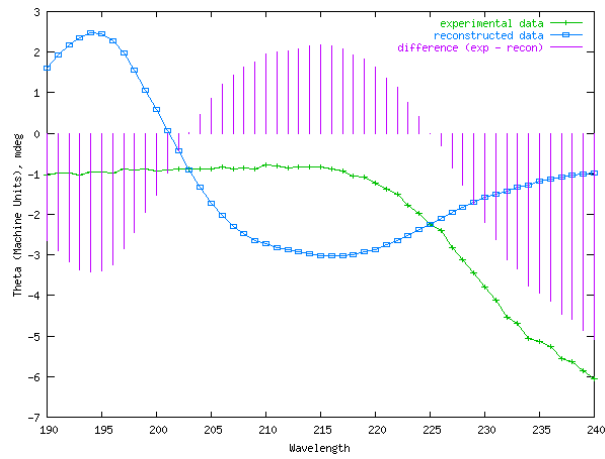
Figure 53 - Dichroweb data for SA-FN in MEM

Appendix 36
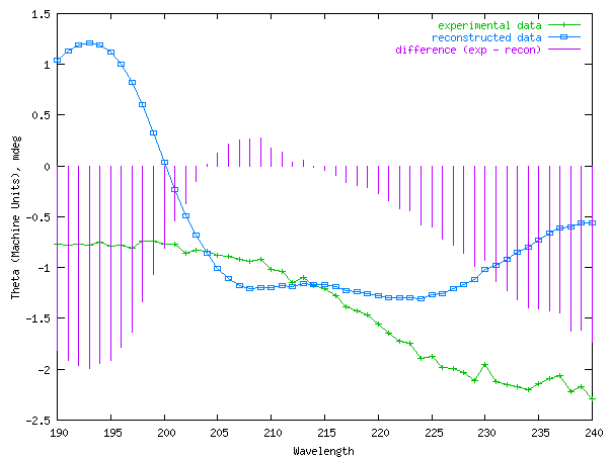
Figure 54 - Dichroweb data for rhBMP-2 in PBS

Appendix 37
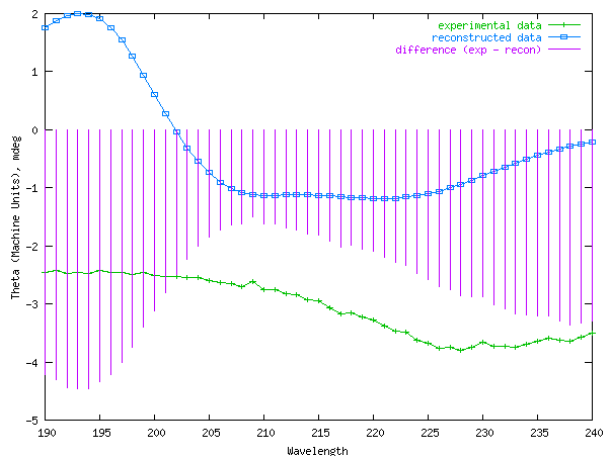
Figure 55 - Dichroweb data for HA-rhBMP-2 in PBS

Appendix 38
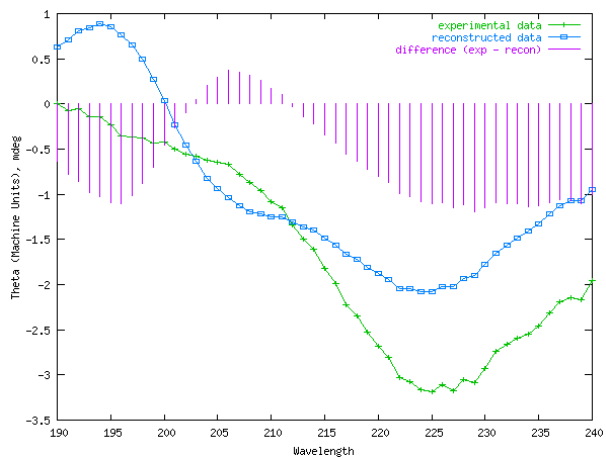
Figure 56 - Dichroweb data for SA-rhBMP-2 in PBS

Appendix 39
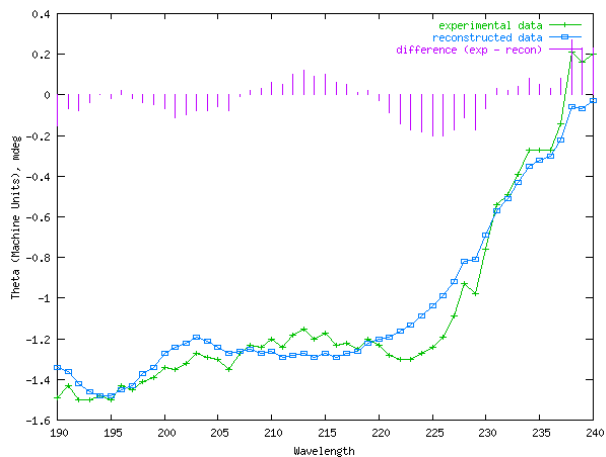
Figure 57 – Dichroweb data for rhBMP-2 in MEM

Appendix 40
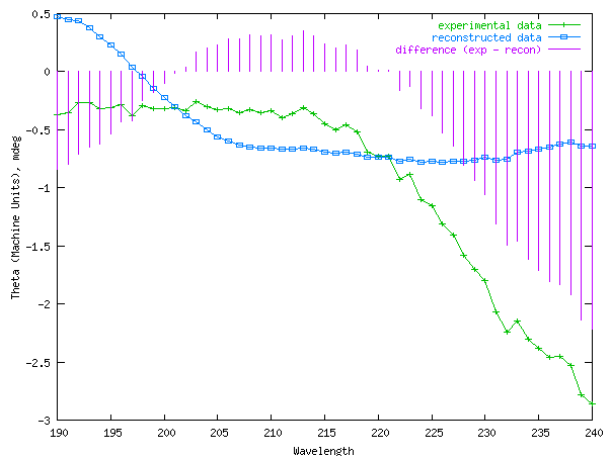
Figure 58 – Dichroweb data for HA-rhBMP-2 in MEM

Appendix 41
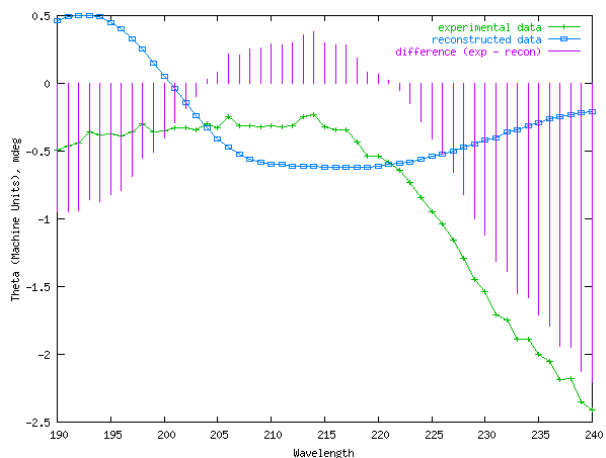
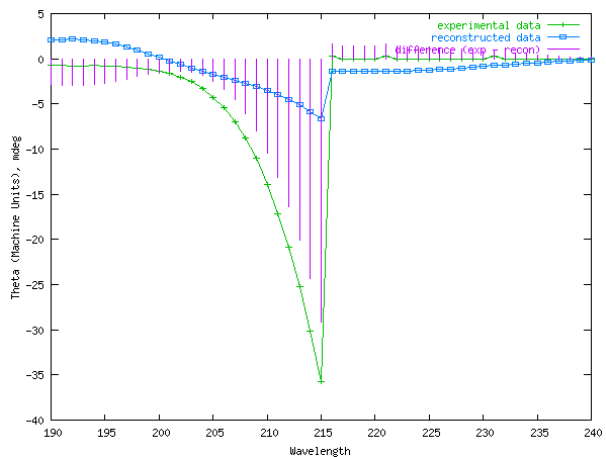**Figure 59 – Dichroweb data for SA-rhBMP-2 in MEM**

Appendix 42
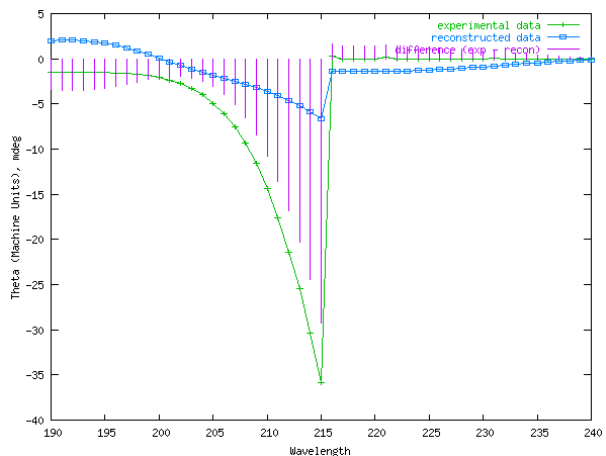

Figure 60 – Dichroweb data for rmOPN in PBS

Appendix 43

Figure 61 – Dichroweb data for HA-rmOPN in PBS
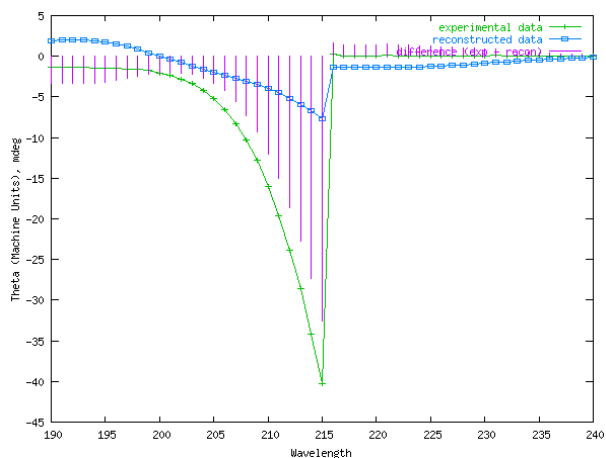
Appendix 44

Figure 62 – Dichroweb data for SA-rmOPN in PBS
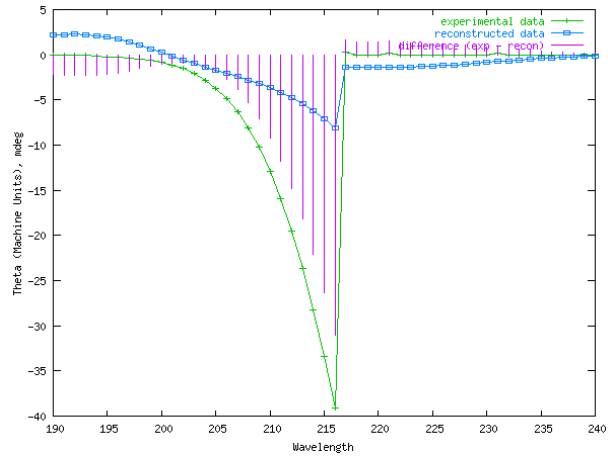
Appendix 45

Figure 63 – Dichroweb data for rmOPN in MEM
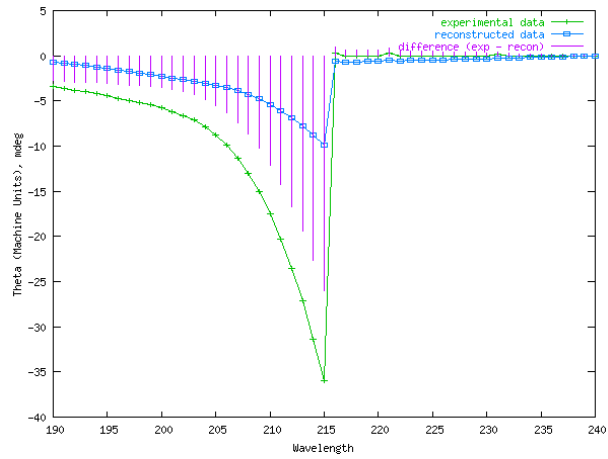
Appendix 46

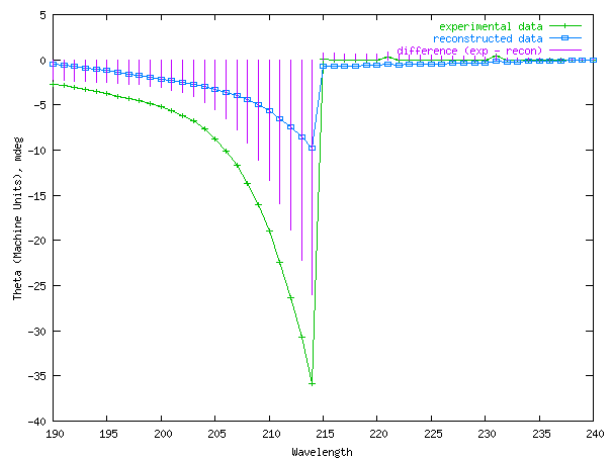**Figure 64 – Dichroweb data for HA-rmOPN in MEM**

Appendix 47

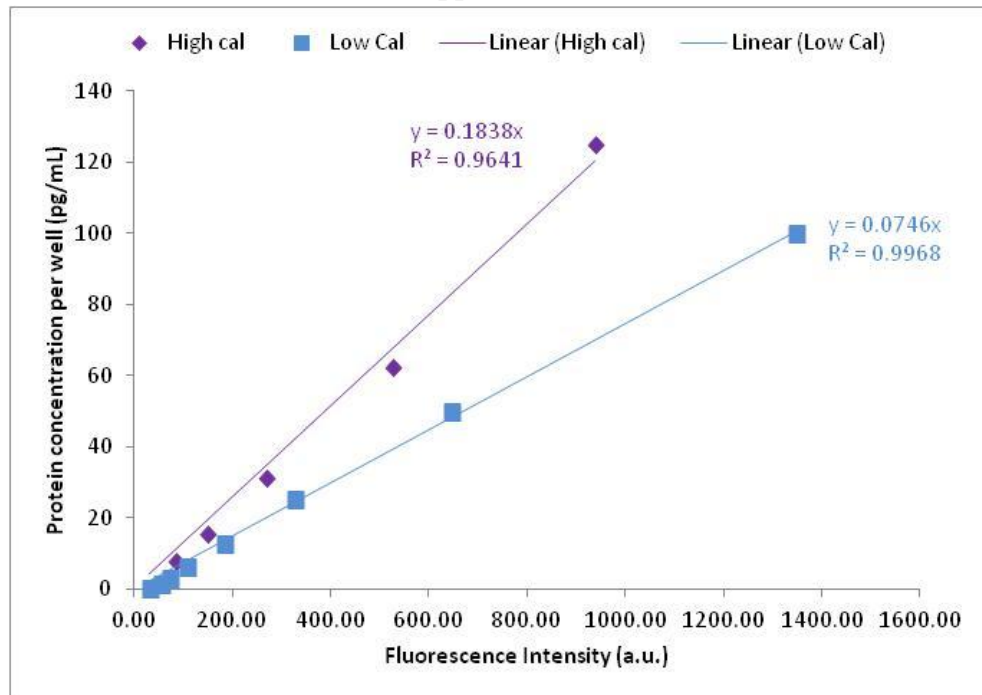**Figure 65 – Dichroweb data for SA-rmOPN in MEM**

Appendix 48

Figure 66 – Calibration curves for the high and low OPN range in MEM with 10 % FBS at 37 $^{\circ}$C using SR101-OPN

Chapter 7

<div align="center">

Appendix 49

</div>

- European Cells & Materials, Vol. 18, Suppl. 2, 2009, page 73, ISSN: 1473-2262 for the poster presentation in Glasgow at TCES 2008

<div align="center">

Monitoring the Effect of Silicate Substitution on Protein Adsorption/Desorption to Hydroxyapatite

</div>

<div align="center">

M.-K. Mafina[1,2], A.C. Sullivan[2] and K.A. Hing[1]

[1]School of Engineering and Materials & IRC, [2]School of Biological & Chemical Sciences
Queen Mary, University of London, London, E1 4NS, UK

</div>

INTRODUCTION: The aim of this study was to develop a method which would facilitate the evaluation and comparison of competitive protein adsorption on silicate-substituted hydroxyapatite (SA) and stoichiometric hydroxyapatite (HA). The initial objective was to synthesise a fluorescent label, fluorescein isothiocyanate (FITC), for covalent attachment to individual target proteins (albumin, fibronectin) and to use fluorescence to monitor competitive binding at equilibrium.

METHODS: SA and HA powders (Apatech Ltd, UK) were pressed and sintered at 1300 and 1250 °C, respectively. FITC was extended with a methyl-aminocaproate ester (Sigma-Aldrich, UK) spacer to provide covalent bonding to bovine serum albumin, BSA, (Sigma-Aldrich, UK). BSA solutions (1.5 ml in phosphate buffered saline, PBS) were placed in clean glass vials, and samples (1 dense **D** disc or 0.50 g 2-5 mm porous granules G, Apatech Ltd, UK) were added to analyse **adsorption**, aliquots of the solution was removed at time intervals. After 15 minutes, the materials were removed, placed in clean vials with PBS (1.5 ml) and gently agitated to remove loosely bound BSA. Test materials were then placed in fresh PBS (1.5 ml) to analyse **desorption**, aliquots were removed at time intervals. Additionally, a binding constant-type study was performed on dense SA discs, where the amount of protein adsorbed was determined for a range of equilibrium concentrations. Protein concentrations in the studies were independently analysed using the Quant-it assay (Invitrogen) and the FITC-labelled protein fluorescence intensity (excitation/emission, nm) to verify accuracy of the technique.

RESULTS & DISCUSSION: Dense SA & HA materials with densities of 98.1 and 99.1 % were formed, respectively. Analysis *via* X-Ray diffraction and FT-IR spectroscopy verified phase purity in both materials, and the presence of silicate groups in SA only, in accordance with previous findings[1,2]. Scanning electron microscopy of surfaces demonstrated SA and HA to have similar surface morphology. Good correlation was found between Quant-it and FITC data, validating this approach as a method to quantitatively analyse an individual protein species' interaction with a bioceramic substrate. Studies confirmed that porous specimens adsorb more BSA per µg than the dense (Fig 1a) and that BSA is more readily desorbed from HA than SA (Fig 1b)
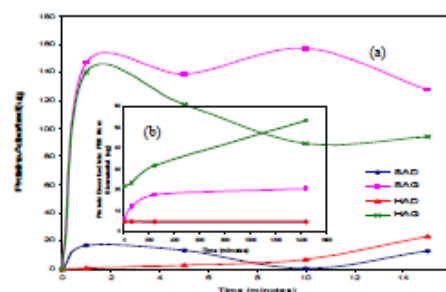

Fig. 1: (a) Adsorption and (b) desorption of BSA on dense (SAD, HAD) and porous (SAG, HAG) materials

Binding constant-type study revealed two distinct regions (Fig 2), suggesting that a monolayer-like layer may be established on SAD at an average of 1.37×10^{-14} mol/0.9 g of disc, but as the BSA solution concentration is increased a more complex multi-layer developed.
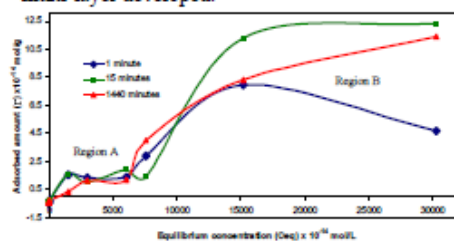

Fig 1: BSA adsorption on SAD with concentration

CONCLUSIONS Protein-surface interactions may be monitored by covalent binding of FITC to a specific target protein (BSA). Binding constant-type studies were performed. Further work will determine whether this approach will work under conditions of competitive binding.

REFERENCES: [1]I.R. Gibson, *et al.* (1999) *J. Biomed Mater Res* **44**: 422-8. [2]K.A. Hing, *et al.* (2006) *Biomaterials* **27**: 5014-26.

http://www.ecmjournal.org

- European Cells & Materials, Vol. 22, Suppl. 2, 2011, page 15, ISSN: 1473-2262 for the talk given in Manchester at TCES 2010

Recording & Evaluating the Effect of Silicon-substitution on Protein Adsorption/Desorption to Hydroxyapatite

M.-K. Mafina[12], A.C.Sullivan[2] & K.A. Hing[1]
[1] School of Engineering and Materials & IRC, and [2] School of Biological & Chemical Sciences
Queen Mary & Westfield College, University of London, E1 4NS, UK

INTRODUCTION: The aim of this study was to develop a method which would facilitate the evaluation & comparison of individual & competitive protein adsorption on silicate-substituted hydroxyapatite (SA) & stoichiometric hydroxyapatite (HA). The initial objective was to evaluate whether it was possible to synthesise a fluorescent label fluorescein isothiocyanate (FITC) for covalent attachment to individually target proteins (albumin-BSA, fibronectin & osteopontin) and to use fluorescence to monitor individual & competitive binding.

METHODS: SA & HA powders (Apatech Ltd, UK) were calcined at 700 °C, pressed into 12 mm diameter dense discs (DD) at a pressure of 88.4 MPa, and sintered at 1300 & 1250 °C, respectively. Porous granules (PG) were also investigated. FITC was extended with a methyl-aminocaproate ester (ACA-OMe, Sigma-Aldrich, UK) spacer to provide covalent bonding to bovine serum albumin (BSA, Sigma-Aldrich, UK) via the lysine residue. BSA & FTCA-BSA solutions (1.5 ml) were placed in glass vials, and samples (1 DD /0.50 g PG) were added to analyse **adsorption**, 100 μl aliquot of the solution was removed at time intervals of 1, 5, 10 and 15mins. After 15 minutes, the test materials were placed in another vial to remove loosely bound BSA. Test materials were then placed in fresh PBS (1.5 ml) to analyse **desorption**, 100 μl aliquots were removed at time intervals of 5, 60, 240 and 1440mins. Protein concentrations in adsorption and desorption studies were doubly analysed (in triplicate) using the Quant-it kit assay (Invitrogen) and by measurement of FTCA-labelled protein fluorescence intensity (excitation/emission, nm) to verify accuracy of the technique.

RESULTS: Good correlation was found between Quant-it and FTCA-BSA data on HAD (*Fig.1*). Data obtained for FTCA-BSA adsorption and desorption at 37°C (*Fig.2*) showed BSA adsorption to be sensitive to temperature, chemistry and porosity of biomaterials.

DISCUSSION & CONCLUSIONS: This data indicates that FTCA-labelled proteins may be used to monitor protein adsorption & desorption. Initially, the data indicates that both substrate chemistry and its morphology affect the protein the

adsorption and desorption profiles, especially when porosity is introduced. Delayed adsorption is initially observed, which may reflect time for BSA diffusion to occur into the pore structure.
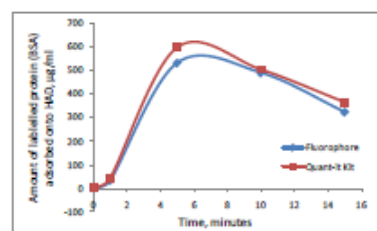

Fig. 1: Amount of FTCA-BSA adsorbed onto HAD calculated using the Quant-it kit & Fluorophore at RT
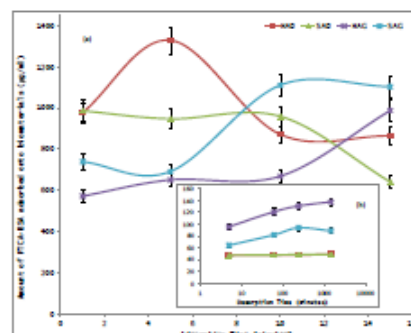

Fig. 2: (a) Adsorption & (b) desorption profiles of FTCA-BSA onto biomaterials at 37°C

Desorption, however, was instantaneous from PG with greater desorption from HA, suggesting protein is more tightly bound to SA-PG. Very little desorption occurred from DD, suggesting flat surfaces may facilitate tighter bonding of BSA.

REFERENCES: [1] A.S. Abuelyaman, et al. (1994) *Bioconjugate Chem* 5:400-405 [2] D.J. Fabrizius-Homan, et al (2000) *J Biomatter Sci Polymer Edn* 3:27-47.

- Central Research Fund (CRF) from University London awarded in January 2010 for the sum of £2,900 for the work on BMP-2 adsorption and desorption study.
- Impact QM Scholarship awarded October 2010 to work three months at CERAM Research (24/01/11-24/04/11), Stoke-on-Trent £ 3,890

Appendix 50
Table 27- Courses and Seminars

Date	Title/Description
31/10/07	Starting your PhD R100
01/11/07	Demonstrating in laboratory R180
21/11/08	Labelling Proteins
21/01/08	Managing a research Project from Start to Finish R121
23/01/08	Writing development R168
02/07/08	A symposium for Postgraduates in Inorganic & Material Chemistry (ASPIC08)
11/12/08	RSC Seminars with speaker such as Catherine Housecroft
26/11/09	Relax about Writing R202

Appendix 51
Table 28- Training, Conferences and Presentations

Date	Title/Description
24/10/07	FTIR (Photoacoustic) training with Monisha Phillips
28/11/07	Grinding & Polishing with Dr Karin
14/12/07	SBCS 1st year Postgraduate talk (15 minutes)
10&11/03/08	SEM training with Dr Zofia Luklinska
16/04/08	Visit to Apatech Ltd, followed by 2 months industrial work May 2008 & October 2009
25/08/08	60th Anniversary Summer Symposium IAESTE-UK at Imperial College
14/11/08	SEMS 2nd year symposium: Winner of the Becker prize
8-10/07/09	TCES 10th Conference in Glasgow: Poster presentation
15,20&29/05/09	AFM training with Dr Barber
03/09/09	AxioVision training at Charterhouse campus with Dr Paul Browne supervised by Dr Alex Sullivan
7-11/09/09	ESB 22nd Conference in Lausanne: Poster presentation & workshops
24/03/10	SEMS Industrial Forum: Poster presentation
24/06/10	Presentation to Apatech: Chaman Chander
28-30/07/10	TCES 11th Conference in Manchester: Talk
11-15/09/10	ESB 23rd Conference in Tampere: Talk & Poster presentations
24/01-24/04/2011	ImpactQm at CERAM research trained on the Zetasizer (Electroacoustic) Stoke-on-Trent
01-06/06/2012	9th World Congress of Biomaterial in China, Chendgu: Talk presentation